Towards high-fidelity modeling of turbulent reactive systems using highly-resolved and simplified simulation techniques

Von der Fakultät für Ingenieurwissenschaften
Abteilung Maschinenbau und Verfahrenstechnik der
Universität Duisburg-Essen
Zur Erlangung des Grades eines

Doktors der Ingenieurwissenschaften
(Dr.-Ing.)

genehmigte Dissertation

von

Linus Engelmann

aus
Dortmund

1. Gutachter: Prof. Dr.-Ing. Andreas Kempf

2. Gutachter: Prof. Dr.-Ing. Markus Klein

Tag der Disputation: 13. Juli, 2023

Acknowledgements

This thesis was developed during my time as a doctoral candidate at the Chair of Fluid Dynamics at the University of Duisburg-Essen. I am very grateful to Prof. Andreas Kempf for giving me the opportunity to pursue my Ph.D. under his supervision, for the support and inspiration he gave me during this time, and for the opportunity to present my work at international conferences, which led to many helpful contacts with other researchers.

I am equally grateful to Prof. Markus Klein of the University of the Federal Armed Forces in Munich, not only for his willingness to report on this work, but also for the guidance he has given me and for treating me as one of his own students since our first meeting.

This work would not have been possible without my colleagues at the EMPI/CFD. I would like to thank Sylvia Helwig for the many conversations about work and family life, Irenaeus Wlokas for the trivia knowledge he provided in numerous pub quizzes, Seungjin Baik for his pure heart and mind, and for introducing me to the Korean culture, Max Schäfer for mixing the deadliest gin tonics, Johannes Sellmann for life-inspiring quotes from gossip magazines, Timo Lipkowicz for discussions about work and exotic leisure activities, Pascal Gruhlke for his edgy humor, Patrick Wollny for claiming to be the best at everything, Andreas Unterberger for showing why there is a little Swabian in all of us, Robert Externbrink for representing sanity in academia, Jonas Eigemann for enforcing law and order in Vancouver, Monika Nanjaiah for her ability to laugh even at inappropriate times, Piotr Cwiek for almost hurting himself every time he uses the coffee machine, Amir Karimi for spending more time at the office than at home, Guannan Liu for the occasional Mandarin lesson, and finally, Tyan Foo for the many discussions about food and enforcing the lunch tradition.

Among them, a special mention must go to my dear friend Dominik Meller for all our work and non-work related discussions, for making our office the most memorable institution in the NETZ building's history, for crashing every possible conference in 2022, and for the countless pickle jars won in quizzes.

I am deeply grateful to my family for their unconditional support and motivation during difficult times.

Finally, I would like to thank my beloved Eunlak for being the person she is. You fill my life with confidence and joy and make every single day unforgettable. Being with you gives me the strength and motivation to be the best version of myself.

"I never read reviews. I'm not interested."

宮崎 駿 (Hayao Miyazaki)

This work would not have been possible without the life's work of Hans Zimmer. ...

Abstract

This work evaluates methods and models for Large-Eddy Simulation (LES) using Direct Numerical Simulation (DNS) data, with a specific focus on two aspects: grid resolution and subgrid modeling, and their influence on simulation quality. Recent model developments are assessed and applied to LES of turbulent reactive systems. The work is divided into two parts.

The first part assesses the performance and quality of LES results for a canonical configuration and a numerically well-studied laboratory experiment. Different subgrid models, as well as DNS, are employed and compared. A workflow is proposed to assess the fidelity of the simulations performed, and the investigated models are recently developed subgrid models proposed in previous studies. The grid resolution is evaluated in a separate study, attempting to formulate an indicator to quantify resolution quality based solely on the performed LES, without the need for high-resolution reference data. The predictive ability of the indicator is validated using reference data from DNS, and a wide range of grid qualities are evaluated.

The second part of this work applies high-fidelity models and numerical schemes to the investigation of reciprocating engines, representing as a turbulent reactive system. A back-tracing algorithm is proposed using Lagrangian tracers to trace the causes of physical events in technical systems in time and space. The method is shown to be applicable to both steady-state and transient engineering processes, providing insight into the convective transport behavior of fluid parcels involved in the physical events studied. Any desired data obtained from the simulation can be targeted and recorded in spatial and temporal protocols by the particles. Finally, the proposed tools are also used for the case of a piston engine exhibiting cyclic variability, demonstrating that high-order numerical models and methods can replace complicated supplementary models for ignition and early flame evolution.

Zusammenfassung

Diese Arbeit bewertet numerische Methoden und Modelle für die Grobstruktursimulation anhand von Daten aus Feinstruktursimulationen. Dabei werden insbesondere zwei Aspekte, die Gitterauflösung und die Turbulenzmodellierung, hinsichtlich ihres Einflusses auf die Simulationsqualität untersucht. Neuere Modellentwicklungen werden evaluiert und auf die Grobstruktursimulation turbulenter reaktiver Systeme angewendet. Die Arbeit gliedert sich in die folgenden zwei Teile.

Im ersten Teil werden Grobstruktursimulationen hinsichtlich ihrer Leistungsfähigkeit und Ergebnisqualität für eine kanonische Konfiguration sowie für ein numerisch gut validiertes Laborexperiment untersucht. Es werden Grobstruktursimulationen mit verschiedenen Turbulenzmodellen sowie eine Feinstruktursimulation durchgeführt und verglichen. Ein Schema zur Bewertung der Qualität der durchgeführten Simulationen wird vorgeschlagen und angewendet. Bei den in den Simulationen eingesetzten Modellen handelt es sich um kürzlich entwickelte Turbulenzmodelle, die in vorausgegangenen Studien vorgeschlagen wurden und in direktem Zusammenhang mit dieser Arbeit stehen. Die Gitterauflösung wird in einer separaten Studie bewertet, in der ein Indikator formuliert wird, der die Auflösungsqualität allein auf der Grundlage der durchgeführten Grobstruktursimulation quantifiziert, ohne dass hochaufgelöste Referenzdaten benötigt werden. Zur Validierung der Vorhersagekraft des Indikators werden Referenzdaten aus Feinstruktursimulationen verwendet und ein breites Spektrum von Gittern unterschiedlicher Qualität ausgewertet.

Im zweiten Teil werden die Ergebnisse des ersten Teils angewendet, indem Modelle und numerische Schemata höherer Ordnung für die Simulation von Hubkolbenmotoren, die ein turbulentes reaktives System darstellen, eingesetzt werden. Unter Verwendung der im ersten Teil bewerteten Methoden wird ein Algorithmus vorgeschlagen, der Lagrangesche Partikel verwendet, um Ursachen physikalischer Ereignisse in technischen Systemen zeitlich und räumlich zurückzuverfolgen. Die Methode erweist sich sowohl in stationären als auch in instationären technischen Prozessen als aufschlussreich und liefert detaillierte Einblicke in das konvektive Transportverhalten von Fluidpaketen, die an zu untersuchenden physikalischen Ereignissen beteiligt sind. Darüber hinaus können jegliche, von der Simulation generierte Daten durch die Partikel erfasst und in zeitlich-räumlicher Korrelation protokolliert werden. Darüber hinaus können jegliche von der Simulation generierten Daten von den Partikeln erfasst

und in räumlich-zeitlicher Korrelation aufgezeichnet werden. Die vorgeschlagenen Methoden und Modelle werden auch für die Simulation eines zyklisch schwankenden Hubkolbenmotors eingesetzt. Es wird gezeigt, dass Methoden und Modelle höherer Ordnung in der Lage sind, aufwendige Zusatzmodelle für die Zündung und die frühe Flammenausbreitung zu ersetzen.

Contents

List of Figures

List of Tables

Nomenclature

Lower case latin symbols

a_{ij}	coefficients of the Runge-Kutta matrix	-
b	arbitrary quantity to be averaged in a mixture of species	$[b]$
b	exponent of the temperature in the Arrhenius law	m/s
b_{i}	weights of a numerical scheme or filter	-
c	speed of sound	m/s
c_{i}	nodes of the Runge-Kutta stages	-
c_{p}	heat capacity at constant pressure	$\mathrm{J/(kg \cdot K)}$
c_{v}	heat capacity at constant volume	$\mathrm{J/(kg \cdot K)}$
d	diameter	m
e	energy	J
g_{ij}	grid-scale velocity gradient tensor	1/s
g_{i}	gravitational acceleration	$\mathrm{m/s^2}$
h	enthalpy	J/kg
h_{f}^{0}	heat of formation	J/kg
h_{s}	sensible enthalpy	J/kg
k	turbulent kinetic energy	$\mathrm{m^2/s^2}$
k	wave number	1/m
k_{i}	slope at stage i of the Runge-Kutta scheme	$[k_{\mathrm{i}}]$
k_{rb}	backward reaction rate	$\mathrm{mol/(m^3 \cdot s)}$
k_{rf}	forward reaction rate	$\mathrm{mol/(m^3 \cdot s)}$
l	length	m
l_{t}	turbulent length scale	m
m	mass	kg
n_{α}	number of molecules of species α	mol
n_{i}	face normal vector	-
p	pressure	Pa
p_{mod}	modified pressure including the isotropic subgrid stresses	Pa
r	reaction rate	$\mathrm{mol/(m^3 \cdot s)}$

r_m	randomized data	-
s	stages of the Runge-Kutta scheme	-
s_l	laminar flame speed	m/s
t	time	s
u_i	velocity vector	m/s
u_m	filtered signal	-
x_i	spatial coordinate vector	m
y	distance from the wall	m

Upper case latin symbols

A	area	m^2
A	pre-exponential coefficient	1/s
A^+	parameter of the van Driest model	-
C	normalized reaction progress variable	-
C_m	constant of static eddy-viscosity subgrid models	-
C_sensor	constant of the sensor-enhanced Smagorinsky model	-
D	diffusion coefficient	m^2/s
D	dissipation matrix	-
D_m	differential operator of an eddy-viscosity subgrid model	m^4/s
E	magnitude of the 2nd invariant of the velocity-gradient tensor	1/s
E	total non-chemical energy	J/m^3
E_A	activation energy in the Arrhenius equation	J/mol
F_CS	coherent structure function	-
F_D	thickening factor in the ATF approach	-
G	filtering kernel	-
G_ij	positive semidefinite grid-scale velocity gradient tensor	$\mathrm{m}^2/\mathrm{s}^2$
I	invariant of a tensor	-
K_C	equilibrium constant	-
L	amplitude of a mathematical wave	-
L_ij	residual of the Germano identity / Leonard stress tensor	N/m^2
L_v	latent heat of vaporization	J/kg
N	number concentration of particles	$1/\mathrm{m}^3$
N_R	number of reactions	-
N_S	number of species	-
Q	2nd invariant of the velocity-gradient tensor	1/s
Q	heat source term in energy equation	J/kg
R	specific gas constant	$\mathrm{J}/(\mathrm{kg}\cdot\mathrm{K})$
R_ij	subgrid-scale anisotropy term	N/m^2

R_{uu}	normalized auto-correlation	-
S_{ij}	strain rate tensor	1/s
T	temperature	K
T_{ij}	test-filtered subgrid stress	$\mathrm{N/m^2}$
T_0	reference temperature	K
U	maximum velocity component in the domain	m/s
U_{i}	velocity signal obtained from the digital filtering technique	m/s
V_{c}	diffusion correction velocity	m/s
V_{k}	diffusion velocity	m/s
W	molecular weights	kg/mol
W_{ij}	rotation rate tensor	1/s
X_α	molar fraction of species α	-
Y_P	non-normalized progress variable	-
Y_α	mass fraction of species α	-
Z	mixture fraction	-

Lower case greek symbols

α	angle	rad
α_{D}	pre-factor of the dissipation matrix	-
α_{ij}	modified stress tensor in the Germano procedure	$\mathrm{N/m^2}$
βij	modified test-filtered stress tensor in the Germano procedure	$\mathrm{N/m^2}$
δ_{ij}	Kronecker delta	-
δ_{l}^0	thermal flame thickness	m
ϵ	rate of dissipation	$\mathrm{m^2/s^3}$
η_{k}	Kolmogorov scale	m
γ	heat capacity ratio	-
γ	ratio of the resolved and total turbulent kinetic energy	-
κ	thermal conductivity	$\mathrm{W/(K \cdot m)}$
λ	propagation speed of a mathematical wave	m/s
λ_{B}	Batchelor scale	1/m
μ	dynamic viscosity	$\mathrm{Pa \cdot s}$
ν	kinematic viscosity	$\mathrm{m^2/s}$
ϕ	general quantity	-
ρ	density	$\mathrm{kg/m^3}$
σ_{i}	singular values	-
τ	discretization error	$[\phi]$
τ_{d}	droplet relaxation time	s
τ_{ij}	subgrid stress tensor	$\mathrm{N/m^2}$

τ_j	subgrid scalar flux vector for transport of the scalar ϕ	$[\phi]$m/s
χ	formula of a chemical species	-
$\dot{\omega}$	source term for species/progress variable	kg/(m$^3 \cdot$ s)
$\dot{\omega}$	specific rate of dissipation	1/s
$\dot{\omega}_\alpha$	chemical source term for species α	kg/(m$^3 \cdot$ s)

Upper case greek symbols

$\dot{\Gamma}_\phi$	volumetric source term for ϕ	$[\phi]$ /(m$^3 \cdot$ s)
Δx	cell size	m
$\overline{\Delta}$	filter width	m
Φ	general quantity in the context of filtering	-
Ψ	flux limiter function in the TVD schemes	-
Ω	flame sensor	-

Subscripts to an arbitrary quantity ϕ

ϕ_A	averaged over area
ϕ_a	vector in index notation, $a = 1, 2, 3$
ϕ_b	value on bottom cell face
ϕ_b	vector in index notation, $b = 1, 2, 3$
ϕ_e	value on eastern cell face
ϕ_ij	two dimensional tensor in index notation, $i, j = 1, 2, 3$
ϕ_i	vector in index notation, $i = 1, 2, 3$
ϕ_j	vector in index notation, $j = 1, 2, 3$
ϕ_k	vector in index notation, $k = 1, 2, 3$
ϕ_max	maximum of ϕ
ϕ_min	minimum of ϕ
ϕ_n	value on north cell face
ϕ_p	at constant pressure
ϕ_res	resolved contribution
ϕ_s	value on south cell face
ϕ_t	turbulent
ϕ_t	value on top cell face
ϕ_V	averaged over volume
ϕ_v	at constant volume
ϕ_w	value on western cell face
ϕ_0	initial / reference state
ϕ_α	value for species α

Superscripts to an arbitrary quantity ϕ

ϕ^{d}	deviatoric part
ϕ^{sgs}	subgrid-scale
ϕ^{+}	wall normalized
ϕ'	fluctuating part of a quantity

Operators to an arbitrary quantity ϕ

$\Delta\phi$	finite difference of quantity ϕ
$\mathrm{d}\phi$	total differential of quantity ϕ
$\partial\phi$	partial differential of quantity ϕ
$\nabla\phi$	gradient of quantity ϕ
$\dot{\phi}$	time derivative of quantity ϕ
$\overline{\phi}$	averaged part of quantity ϕ in RANS context
$\overline{\phi}$	filtered part of quantity ϕ in LES context
$\widehat{\overline{\phi}}$	test-filtered quantity ϕ
$\widetilde{\phi}$	Favre filtered quantity ϕ
$\check{\phi}$	Favre- and test-filtered quantity ϕ
ϕ'	sub-filter part of fluctuating quantity ϕ in LES context
ϕ''	fluctuating part of Reynolds-decomposed quantity ϕ in RANS context

Dimensionsless numbers

$\mathrm{B_h}$	Spalding number for heat transfer: ratio of potential heat transfer from gas phase to droplet to latent heat
$\mathrm{B_m}$	Spalding number for mass transfer: ratio of the transferable vapor mass from droplet surface to the free gas to the total evaporated mass
CFL	Courant-Friedrichs-Lewy number: ratio of physical to numerical velocity
Kn	Knudsen number: ratio of mean free path of the gas molecules to characteristic length of the flow
Le	Lewis number: ratio of thermal diffusion to mass diffusion
Ma	Mach number: ratio of fluid velocity to speed of sound
Nu	Nusselt number: ratio of total heat transfer to conductive heat transfer
Pr	Prandtl number: ratio of momentum diffusion to thermal diffusion

Re	Reynolds number: ratio of inertial forces to viscous forces
Sc	Schmidt number: ratio of momentum diffusion to mass diffusion
Sh	Sherwood number: ratio of convective mass transfer to diffusive mass transfer

Physico-chemical constants

k_b	Boltzmann constant	$1.381 \cdot 10^{-23} \cdot \mathrm{J/K}$
N_A	Avogadro constant	$6.022 \cdot 10^{23} \cdot 1/\mathrm{mol}$
R_m	ideal gas constant	$8.314 \cdot \mathrm{J}/(\mathrm{K} \cdot \mathrm{mol})$

Abbreviations

1D	One Dimensional
2D	Two Dimensional
3D	Three Dimensional
ADM	Approximate Deconvolution Model
ANN	Artificial Neural Network
ATF	Artificial Thickened Flame
CCSS	Center for Computational Sciences and Simulation
CDS	Central Differencing Scheme
CFD	Computational Fluid Dynamics
CV	Control Volume
DNS	Direct Numerical Simulation
EVM	Eddy Viscosity Model
FDM	Finite Difference Method
FEM	Finite Element Method
FGM	Flamelet Generated Manifolds
FVM	Finite Volume Method
GA	Genetic Algorithm
GEP	Gene Expression Programming
HAB	Height Above Burner
HOT	Higher-Order Terms
IB	Immersed Boundary
KKK1	Klein-Ketterl-Kobayashi model 1
KKK2	Klein-Ketterl-Kobayashi model 2
LES	Large-Eddy Simulation
LHS	Left Hand Side

LODI	Local One Dimensional Inviscid
MIB	Moving Immersed Boundary
MPI	Message Passing Interface
NPFGM	Non-Premixed Flamelet Generated Manifolds
NSCBC	Navier-Stokes Characteristic Boundary Conditions
NSE	Navier-Stokes Equations
PDE	Partial Differential Equation
PFGM	Premixed Flamelet Generated Manifolds
PINN	Physically Informed Neural Network
QUICK	Quadratic Upstream Interpolation for Convective Kinematics
RANS	Reynolds Averaged Navier-Stokes
RHS	Right Hand Side
RMS	Root Mean Square
SES	Sensor-Enhanced Smagorinsky model
SGS	Subgrid-Scale
SI	Sigma model
SM	Smagorinsky model
SST	Scale Similarity Type model
TV	Total Variation
TVD	Total Variation Diminishing
UDS	Upwind Differencing Scheme
URANS	Unsteady Reynolds Averaged Navier-Stokes

1 Introduction

1.1 Motivation

Turbulence is a phenomenon that has a direct impact on numerous processes and is ubiquitous in modern engineering systems and processes operating at macro-scales. In these engineering applications, the effects of turbulent flows can be either desirable or undesirable, and sometimes both. Applications include reactors for chemicals and material synthesis, wind and gas turbines for power generation, piston- and turbo-engines for vehicles, as well as heating, ventilation and air conditioning for buildings. Large-scale environmental flows, such as the transport of pollutants in urban areas or meteorological dynamics, add to this spectrum. Numerical simulation has matured into a reliable tool for predicting and analyzing these flows, and is an essential instrument in the design process of technical devices involving turbulence. Different strategies for simulating turbulent flows exist, each with its own strengths and weaknesses. Large-Eddy Simulation and Direct Numerical Simulation are particularly relevant as research tools. Direct Numerical Simulation is typically suitable for fundamental studies at moderate levels of turbulence, while Large-Eddy Simulation can employ a wide range of models at arbitrary levels of turbulence. In general, Direct Numerical Simulation is used to validate of Large-Eddy Simulation results.

The motivation of this study is the advancement of state-of-the-art simulation techniques in computational fluid dynamics, which entail a plethora of models for different applications ranging from the description of turbulence [216], multi-phase flows [10], chemical reactions [212] to magneto-hydrodynamics [51]. Numerical solvers with varying levels of accuracy and stability are applied to subsonic and supersonic flow regimes, independently from the fluid simulation paradigm [291, 123, 237]. Typically, the resolution is set as high as possible, with respect to a certain cost threshold. However, depending on the combination of solver aspects, the outcome of a simulation may vary considerably. This is not only due to the employed tools but also to the way they interact with each other. Therefore, evaluating these tools can be challenging and expensive, and it can only be done successfully if their influence is isolated and compared with a reference simulation of high quality. One fundamental aspect of this analysis, which is of importance to this study, is that a comparison to a reference simulation is only valid if the reference simulation was performed using otherwise identical

numerics. Thus, the reference simulation must be executed using the same code as the one used for the analyzed simulation. In this study, we propose strategies for investigating models and required resolution using highly-resolved and simplified simulation techniques.

1.2 Outline

The numerical simulation of turbulent reactive flows aims to provide a mathematically accurate representation of the physical phenomena inherent in such flows. This work presents modeling approaches and numerical methods relevant to this objective, which are explained in the Chapters 2 to 5. The fundamentals of the mathematical treatment of fluid flow are laid out in Chapter 2, while Chapter 3 will delve into turbulence, its effects, and related simulation techniques. Chapter 4 will outline the fundamentals of reactive flows and their modeling, followed by an overview of numerical methods to handle the governing equations in Chapter 5.

After establishing the theoretical foundations, subsequent chapters will introduce the developed strategies for high-fidelity modeling assessment and classification. These descriptions comprise reprints of the reports published in leading international journals in the field of turbulent and reactive flows.

Chapter 6 investigates subgrid closures for Large-Eddy Simulation with respect to their ability to model scalar transport. For this purpose, a Direct Numerical Simulation of a free turbulent jet featuring scalar transport and well-defined boundary conditions was performed. In contrast to several comparable works, this study assesses the discretization of the respective subgrid closure in addition to its formulation.

In Chapter 7, the evaluation of subgrid closures is extended by a novel comparison of their performance in a turbulent reactive case. The range of subgrid closures was expanded to include recent developments, facilitating an investigation of the interaction between chemistry and turbulence modeling.

Chapter 8 aims to directly quantify simulation quality using the concept of information entropy. The study intends to generate low- and high-quality simulation results to systematically evaluate their impact on simulation quality estimators.

The goal of this research work is to contribute to the improvement of simulation by highlighting the strengths and weaknesses of established and recent modeling frameworks. The results of Chapters 6 through 8 are demonstrated and applied to the challenging and highly turbulent case of a thermochemical energy converter in Chapters 9 and 10.

Finally, a concluding remark and outlook are given in Chapter 11.

2 Fundamentals of fluid-motion and thermodynamics

In engineering problems, fluids are typically described using macroscopic properties such as density, momentum, pressure and temperature to represent the ensemble behavior of molecules. These properties are considered to be well defined within infinitesimal volume elements, which, by definition, are small compared to the characteristic length scale of the examined problem, but large compared to the motion scale of molecules – this is also referred to as *continuity*. Thus, these properties are defined to be continuous since only infinitesimal changes in properties may occur over an infinitesimal change in space. Ultimately, this allows for the treatment of fluids using a handful of spatial and temporal functions, instead of dealing with equations for a plethora of individual molecules. The assumption of continuity remains valid as long as the average distance traveled by a molecule is small compared to the characteristic length scale of the given problem – this ratio is also known as the Knudsen number.

Within this work, the Knudsen number remains small and the assumption of continuity is made. The mathematical description of fluid-mechanics and -thermodynamics is based on laws of conservation, which particularly balance the gain, loss and redistribution of the properties mass, momentum, energy and chemical species. These laws are written down in the form of *Partial Differential Equations* (*PDE*) which contain the temporal and spatial information of the corresponding conserved property.

2.1 Conservation of a general quantity

The conservation of a general quantity ϕ in the context of fluid-dynamics is a balance equation, which accounts for the quantities generation, transport and removal in time t and space x_{j}. The temporal change of the general quantity is represented by an accumulation term whose calculation is typically the main objective when solving these equations. Generation and removal are described by source terms that add-to or subtract-from the balance equation, depending on any possible mathematical law. The transport of a quantity can be of convective or diffusive nature. The convective contribution refers to the transport of a quantity due

to the actual motion of the flow. This requires the presence of a flow field, which can be either forced (e.g. by ventilation) or free (e.g. by thermal lift). Diffusion is a consequence of the motion of the individual molecules within the fluid due to their thermal energy. This motion is also referred to as Brownian motion and is generally considered to be random at the macroscopic level. Thus, diffusion is a statistical process that results in a decrease in the concentration of a property. Although it is a microscopic process by definition, the diffusive transport is summarized in a diffusion rate, characterizing the speed of this process on a macroscopic scale. It should be noted that this terminology may vary slightly depending on the field of science. In some cases, the terms advective and diffusive transport are used, while the term convection refers to both means of transport. In this work, however, the terms convection and diffusion will be used. Considering all aforementioned terms, the conservation equation of a general quantity ϕ is as follows:

$$\underbrace{\frac{\partial \rho \phi}{\partial t}}_{\text{accumulation}} + \underbrace{\frac{\partial \rho u_\mathrm{j} \phi}{\partial x_\mathrm{j}}}_{\text{convection}} = \underbrace{\frac{\partial}{\partial x_\mathrm{j}} \left(D_\phi \frac{\partial \phi}{\partial x_\mathrm{j}} \right)}_{\text{diffusion}} + \underbrace{\dot{\Gamma}_\phi}_{\text{source}} \tag{2.1}$$

With the density ρ, the velocity field u_j, the diffusion coefficient of the quantity ϕ within the fluid D_ϕ and the source term $\dot{\Gamma}_\phi$. The conserved quantity is typically expressed in its specific formulation and is thus converted to a volumetric quantity by multiplication with the density contained in the conservation law. This yields the mass-independent value of the conserved quantity when solving the equation for a given control volume.

A conservation law can be formulated for a wide variety of quantities. These can include conventional quantities such as mass or energy, but also more abstract properties such as an electric charge or even probability-distributions. In the following section, the conserved quantities relevant to this work are discussed in more detail and the characteristic aspects of their transport are presented.

2.2 Navier-Stokes equations

The *Navier-Stokes Equations* (*NSE*) are the central object of desire in *Computational Fluid Dynamics* (*CFD*) as their solutions yield the density and velocity fields ρ and u_j. The set of equations developed by Navier and Stokes describes the conservation of mass and momentum for Newtonian fluids. The NSE form a nonlinear set of PDEs with mixed parabolic-elliptic character, implying that the solution of the initial/boundary-value problem might not always yield a smooth solution. This question of the guaranteed existence of smooth solutions remains unsolved to this day and is part of the most important unsolved problems in mathematics: the Millenium Prize Problems [67]. The NSE are capable of fully describing any Newtonian flow, but their solution is difficult to obtain. While analytical solutions exist for only a very limited number of cases, the general solution approach requires numerical methods.

2.2.1 Conservation of mass

The conservation of mass, also referred to as the equation of continuity, accounts for the local and total changes in mass. The conservation of mass is formulated under the premise that all relative effects are negligible and thus, the energy is independent of the mass. While typically in classical mechanics, mass cannot be created or destroyed, source terms can occasionally be found for multi-phase problems where phase-changes such as evaporation or condensation occur. The conservation of mass contains no diffusion term. A flow consisting of a completely homogeneous mixture of molecules and diffusion as a statistical process effects can be considered. In this case, the effects of diffusion vanish as each molecule moving due to Brownian motion is replaced by an identical one. In the case of an inhomogeneous mixture different types of molecules will move around, resulting in differences in quantities such as concentration. However, since each large molecule is replaced by a number of smaller ones, no diffusive effects on mass can be observed. The conservation of mass is formulated as:

$$\frac{\partial \rho}{\partial t} + \frac{\partial \rho u_\mathrm{j}}{\partial x_\mathrm{j}} = \dot{\Gamma}_\rho \tag{2.2}$$

With $\dot{\Gamma}_\rho$ being the mass source term. This term is zero for single-phase flows. For flows involving gases and liquids or vapors, the source term is equal to the evaporation or condensation rate in cases relevant to this work. In the absence of the source term $\dot{\Gamma}_\rho = 0$ and for the case of a constant density $\rho = \text{const.}$, the equation yields a divergence-free condition for the velocity field $\nabla u_\mathrm{j} = 0$.

2.2.2 Conservation of momentum

The conservation of momentum is an extension of Newton's second law of motion by assuming that the stress acting on the fluid is equal to the sum of the pressure term and the viscous diffusion term. The momentum equation as present in the NSE is an expansion of Euler's equation – which is typically used in aerodynamics – by the effects of viscosity. The conservation of momentum is expressed as:

$$\frac{\partial \rho u_\mathrm{i}}{\partial t} + \frac{\partial \rho u_\mathrm{i} u_\mathrm{j}}{\partial x_\mathrm{j}} = -\frac{\partial p}{\partial x_\mathrm{i}} + \frac{\partial}{\partial x_\mathrm{j}} \left(\mu \left(\frac{\partial u_\mathrm{i}}{\partial x_\mathrm{j}} + \frac{\partial u_\mathrm{j}}{\partial x_\mathrm{i}} \right) - \frac{2}{3} \mu \frac{\partial u_\mathrm{k}}{\partial x_\mathrm{k}} \delta_\mathrm{ij} \right) + \rho g_\mathrm{i} + \dot{\Gamma}_{\rho u_\mathrm{i}} \tag{2.3}$$

With the pressure p, the dynamic viscosity μ and ρg_i as the gravitational source term. This term is commonly neglected in problems where the buoyant force is considered small, which is typically the case for gas flows due to low densities. The term $\dot{\Gamma}_{\rho u_\mathrm{i}}$ represents the exchange of momentum between different phases and is zero in single-phase flows.

2.3 Conservation of energy

The conservation of energy is of importance in non-isothermal flows, especially in reacting flows. The quantity of interest while solving the energy equation is the temperature, which is thermodynamically related to the energy. Therefore, the energy equation is usually accompanied by additional modeling of the thermodynamic state. Energy can be formulated in several ways and the choice can simplify the respective problem. In many works the term *energy*-equation is a placeholder that refers to either the actual energy or the enthalpy. Since a transport equation for either of these can be formulated using its non-chemical, chemical, total non-chemical or total chemical formulation, there are a total of eight equations to choose from. For a complete overview of the respective definitions and full transport equations the reader is referred to Poinsot and Veynante [212]. In this work, only the total non-chemical energy formulation is employed, which is also the most common choice for non-reactive flows. Therefore, the conservation of energy within this work is formulated as:

$$\frac{\partial \rho E}{\partial t} + \frac{\partial \rho u_\mathrm{j} \left(E + p/\rho\right)}{\partial x_\mathrm{j}} = \kappa \frac{\partial^2 T}{\partial x_\mathrm{j}^2} + \frac{\partial}{\partial x_\mathrm{j}} u_\mathrm{j} \left(\mu \left(\frac{\partial u_\mathrm{i}}{\partial x_\mathrm{j}} + \frac{\partial u_\mathrm{j}}{\partial x_\mathrm{i}} - \frac{2}{3} \frac{\partial u_\mathrm{k}}{\partial x_\mathrm{k}} \delta_\mathrm{ij} \right) \right) + \dot{Q} \tag{2.4}$$

With the total non-chemical energy E, the thermal conductivity κ, the temperature T and the heat source term $\dot{Q}$. The heat source term represents the effects of external heating – in this formulation this strictly excludes chemical reactions – and can represent, e.g., heating through walls. The total non-chemical energy is defined as:

$$E = \int_{T_0}^{T} c_\mathrm{v} dT - RT_0 + \frac{1}{2} u_\mathrm{i} u_\mathrm{i} \tag{2.5}$$

In this equation, c_v is the isochoric specific heat and R indicates the specific gas constant. In the following, some thermodynamic context will be given to clarify the quantities mentioned in the energy equation.

2.3.1 Thermodynamics of the energy equation

While all transport equations mentioned above hold for both gaseous and liquid fluids, the calculation of the material properties mentioned – especially those of the conservation of energy – is phase-dependent. This work focuses on the investigation of gaseous flows, and thus, all formulations given in the following will be made for gases without further emphasis.

Most mathematical relations used for the description of gas-physics rely on the assumption of an *ideal gas* behavior. The concept of an ideal gas originates from statistical mechanics and describes a gas-like composition of randomly moving point-particles that are not subject

to interparticle interaction. The three assumptions of an ideal gas can be summarized as follows:

- Ideal gas particles are free of attractive as well as repellent forces, and only collide elastically with other molecules or walls
- Ideal gas particles do not occupy any volume
- Ideal gas particles are considered monoatomic and hence, do not vibrate or rotate

The ideal gas assumption is only valid for pressures that are relatively low compared to the critical pressure and temperatures that are relatively high compared to the critical temperature (this temperature threshold is also referred to as the Boyle temperature), as this is where the interparticle interaction starts to show a stronger effect. If these conditions are satisfied, the ideal gas model can be applied and the corresponding ideal gas law reads:

$$p = \rho \frac{R_\mathrm{m}}{W} T \tag{2.6}$$

With the ideal gas constant R_m and the molecular weight W – these can be converted into the specific gas constant for a given gas following:

$$R = \frac{R_\mathrm{m}}{W} \tag{2.7}$$

The ideal gas law forms the presumably most prominent *equation of state* as it links the temperature to the pressure. This link is required to solve the conservation equation of momentum and energy (Eqs. 2.3 and 2.4). The internal energy of an ideal gas solely depends on its temperature and is defined as:

$$e = \int_{T_0}^{T} c_\mathrm{v} dT \tag{2.8}$$

And its enthalpy as:

$$h = \int_{T_0}^{T} c_\mathrm{p} dT \tag{2.9}$$

Where T_0 is the temperature of the thermodynamic reference state and c_p is the isobaric specific heat. The isochoric and isobaric specific heats c_v and c_p are related by the specific gas constant as $R_\mathrm{m} = c_\mathrm{p} - c_\mathrm{v}$.

The model of the ideal gas can also be applied to gas mixtures by taking into account the composition of the mixture. A mixture can be described by the contribution of each component to the total number of molecules or mass of the mixture. This contribution to a mixture of N_S species can be quantified in terms of mole fractions X_α or mass fractions Y_α

as follows:

$$X_\alpha = \frac{n_\alpha}{\sum_{\alpha=1}^{N_\mathrm{S}} n_\alpha} \tag{2.10}$$

With n_α being the number of molecules of a species α. The mass fraction can be defined accordingly using the mass m_α of each species α:

$$Y_\alpha = \frac{m_\alpha}{\sum_{\alpha=1}^{N_\mathrm{S}} m_\alpha} \tag{2.11}$$

The mole/mass fractions are of fundamental value for characterizing a mixture. The mean molecular weight of a mixture is calculated as:

$$W = \sum_{\alpha=1}^{N_\mathrm{S}} W_\alpha X_\alpha \tag{2.12}$$

As the transport equations are typically density-based and hence, require specific quantities, the mass fractions are preferred for the calculation of mean material properties. For a general property b, the mixture average is calculated as:

$$b = \sum_{\alpha=1}^{N_\mathrm{S}} b_\alpha Y_\alpha \tag{2.13}$$

With the property contribution b_α of each species α. It has to be noted, that molecular averages are commonly written as $\overline{b}$. In this work however, b will be used to avoid confusion with the filtering that will be introduced later. The property b for instance can represent, e.g., the internal energy e, the enthalpy h, the isochoric specific heat c_v or the isobaric specific heat c_p. Material properties are commonly tabulated or fitted using the *NASA*-polynomials [117, 176].

2.4 Flow regimes and predictability of flows

The mathematical foundation for the description of flows satisfying the assumption of a continuum was established. It is of interest to evaluate the physical behavior reflected in these equations and to provide a basis for interpreting their respective solutions. Although the assumption of continua holds, it should be noted that there is an influence acted from the molecular level to the larger and more relevant scales for the given problem. In particular, this influence is most prominently due to the Brownian motion which is superimposed on the advective flow direction and will be referred to as *perturbations* in the following.

Different examples of flows from technology and nature such as vortex structures behind ships, strong currents in a river or windstorms come to mind when thinking of the word flow.

By definition, flows begin when resting fluid is set in motion and relative to a stationary reference frame. The resulting flow regime is typically considered a direct consequence of the inertial and shear forces – commonly also referred to as viscous forces – acting on the fluid. While inertial forces lead to the acceleration of fluid parcels, the shear forces represent the resistance of the fluid to relative motion between its parcels. These forces are interacting, and their ratio is of critical importance in fluid dynamics. In particular, this ratio will indicate how much the perturbations will affect the flow. The ratio is quantified by the *Reynolds* number Re and is given as:

$$\mathrm{Re} = \frac{\rho U l}{\mu} \tag{2.14}$$

Where U is the mean flow velocity and l is the characteristic linear dimension of the problem. The characteristic linear dimension is a geometric length that is representative of the flow and depends on the geometry of the given problem, such as the diameter of a pipe or nozzle or the height of a channel. For many canonical studies of internal flows with constant cross-sections the linear dimension can be covered by the hydraulic diameter, which can be obtained as the ratio of the cross-sectional area to the wetted perimeter.

The Reynolds number is commonly used to distinguish between different flow regimes. These regimes are discussed below in terms of their physical behavior.

2.5 Laminar and transient flows

Creeping flows or *Stokes* flows occur when the magnitude of the viscous forces significantly exceeds the inertial forces, resulting in small Reynolds numbers $\mathrm{Re} \ll 1$. These conditions are met for fluids of high viscosity, slow flow velocities, or for length scales that are small. Linearizing the Navier-Stokes equations facilitates mathematical description of creeping flows, significantly simplifying their solution by neglecting the inertial terms in the momentum balance.

Laminar flows are characterized by the orderly motion of fluid in layers or filaments, with each layer behaving in isolation from the others, precluding any interaction. The strong viscous forces typically present in laminar flows are effective in damping out any perturbations that may induce interaction between layers.

Within the *transient* flow regime, the dampening effects of viscous forces on small perturbations are no longer present. Rather, the flow becomes highly sensitive to such perturbations and amplifies them, resulting in their growth and eventual breakdown into seemingly random behavior. This dynamic interplay often leads to spontaneous switching between laminar and turbulent fluid motion, making it exceedingly challenging to accurately describe flows in this regime.

2.6 Turbulent flows

Turbulence is widely recognized as one of the most significant unsolved challenges in contemporary physics. To date, no comprehensive mathematical derivation exists that links the Navier-Stokes equations to the framework of turbulence theory [75]. Despite this, the foundations of turbulence theory were first established by Reynolds and subsequently extended by Richardson and Kolmogorov, whose contributions remain of paramount importance to the current understanding of this complex phenomenon.

As the Reynolds number increases and the inertial forces govern the flow, the regime of fully developed turbulence is reached. Viscous forces now are no longer able to dampen out the perturbations, which maintain the laminar flow structure. Small perturbations grow and notably affect the flow by inducing crosscurrents to the main flow direction, which ultimately lead to the characteristic flow structures of turbulence: the eddies. Eddies are commonly referred to as vortices, but should generally be treated as a turbulent structure that is coherent in the region of size l, is characterized by a velocity of magnitude $u(l)$, and therefore has the timescale $\tau(l) = l/u(l)$. The eddies interact with the main flow, producing the characteristic unsteady and disordered fluid motion found in turbulent flows. Due to the severe fluid interaction caused by turbulence, the eddies ultimately increase the exchange of energy within the flow. Eddies are born and kept alive by draining the energy from the main flow. These eddies have sizes equal to the largest turbulent scale of the flow, which is referred to as the integral scale l_t. As an undirected structure embedded in a flow field with many of its kind, its lifetime is limited and it will eventually break down. The kinetic energy stored in its motion will be conserved and distributed to newly forming eddies. It is evident that when breaking down, an eddy can only form smaller eddies as the energy is distributed, and consequently the inertial forces it exerts are reduced. The newly formed smaller eddies again interact with the remaining flow and due to their overall lower energy content feature a shorter longevity. Now equipped with a shorter lifetime, the eddies will break up again and spread their energy, ultimately forming even smaller eddies. This process is repetitive and is therefore referred to as the *turbulent energy cascade*. The main characteristic of this cascade is the conservation of the energy held by the eddies. No energy is lost or created during the breakup and reformation of the eddies, but solely transported between eddies of decreasing size. After a large number of breakup and reformation steps, eddies will eventually reach a size where the viscous forces are comparable in magnitude to the inertial forces. From this point on, the viscous forces will progressively drain and dissipate the rotational energy from the eddies, with the eddies becoming more susceptible to the viscous forces with decreasing size. The rate of energy dissipation is determined at the beginning of the cascade, as the energy fed into the cascade will eventually dissipate. The rate is given by $\epsilon = u(l_\mathrm{t})^3/l_\mathrm{t}$. Since the smallest eddy ultimately dissipates into heat and thus cannot form any smaller eddies, a lowest possible eddy size exists. Typically, the energy cascade is represented in the form of a

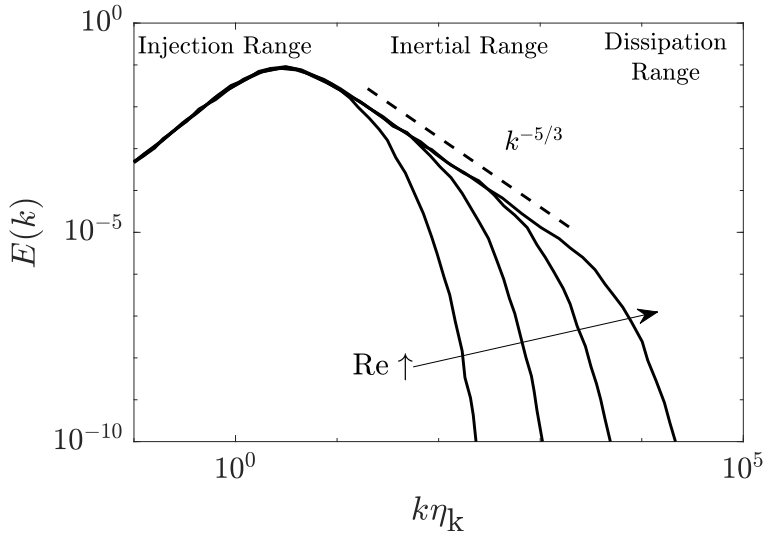

Figure 2.1 Turbulent energy spectra obtained from Reynolds number variation following the idea of the model spectrum given by Pope [216] and Klein [132].

wavenumber-based double-logarithmic diagram. In physics, a frequency can be thought of as a measure converted from time to timescale. In analogy to the frequency, the wavenumber represents the inverse of a length, thus converting a geometric length into a lengthscale. The wavenumber-based diagram is henceforth also referred to as the turbulent energy spectrum, as it shows the distribution of energy over the different lengthscales within the problem. An example of an energy spectrum can be found in Fig. 2.1, showing the energy density E versus the wavenumber k. Since the geometrical extension of the given problem is typically limited, it can be concluded that there must be a largest lengthscale. In particular, this scale is referred to as the integral or the injection scale. It refers to the scale at which the eddies form and feed on the energy of the main flow: the energy is injected into the turbulent energy cascade. The largest eddies that form will always be comparable in size to the integral scale – common examples for this are the vortices behind a ship's propeller or the tumble vortex in piston engines scaling with the respective diameters. The breakup of the largest eddies initiates the cascade, which is called the inertial range. In the double-logarithmic representation, the inertial range features a characteristic linear decrease of energy. This is also referred to as the Kolmogorov $-5/3$-law [147]. The law dictates the energy density within the inertial range following:

$$\mathrm{E(k)} \approx C\epsilon^{2/3}k^{-5/3} \tag{2.15}$$

With the wavenumber k, the dissipation rate ϵ and C, which is a universal constant. It is found that the spectrum begins to deviate from this law progressively as one approaches higher wavenumbers, and this is when the viscous forces gain importance. These wavenumbers mark

the beginning of the dissipation range and bear the name *Kolmogorov* scale. The Kolmogorov scale can be derived from the Reynolds number at the integral scale $\mathrm{Re}_\mathrm{t} = u(l_\mathrm{t})l_\mathrm{t}/\nu$, which is typically representative of the flow problem. Dimensional analysis reveals the Kolmogorov scale to be calculated from the dissipation rate and the viscosity $\eta_\mathrm{k} = (\nu^3/\epsilon)^{1/4}$, which can be rewritten using the identity for the dissipation rate as:

$$\eta_\mathrm{k}/l_\mathrm{t} \propto \mathrm{Re}_\mathrm{t}{}^{-3/4} \tag{2.16}$$

Which is of crucial importance for the computational study of turbulent flows as it allows for the calculation of the Kolmogorov scale from the basic parameters of the given problem.

Eddies occur as a spectrum of sizes ranging from the scale of the flow geometry down to the smallest eddy size mentioned above. As stated by Kolmogorov, the characteristic velocity and timescale of the eddies decrease with decreasing eddy size. With the energy injection occurring on the scale of the flow geometry, it is implied that these quantities are directly influenced by the main flow and its geometry. With the ongoing scale-reduction process imposed by the cascade, it can be observed however, that the information inherited from the geometry scale is lost and therefore the small eddies behave universally and are statistically isotropic. This ultimately means that the statistics of the small-scale turbulence is universal for all high Reynolds number flows.

The physical phenomena present in the turbulent energy cascade are fundamental to the development and use of mathematical models. Three paradigms for the computational study of turbulent flows exist at the current state and will be introduced in the following chapter.

3 Paradigms of turbulence simulation

Although used frivolously in modern times, the term simulation – especially in the context of fluid dynamics – remains non-trivial. Simulation aims for the imitation of real-world physical processes using mathematically constructed modeling strategies. A wide variety of models and strategies exist for simulating fluid flow, and the choice must be carefully considered for the problem at hand. Each model comes with strengths and limitations, and choosing the appropriate model is crucial for achieving accuracy. While accuracy is generally an attractive feature of a model, another important factor which goes in hand are the expenses. Powerful and expensive models can be used, however, but their yield must be weighed against the computational budget at hand. Although computational power has in fact increased over the last decades, three different paradigms for the analysis of turbulent systems will be introduced offering different levels of accuracy and cost. Figure 3.1 gives a first visual insight into the three main paradigms of turbulent flows in computational fluid dynamics. The three paradigms *Direct Numerical Simulation* (*DNS*), *Large-Eddy Simulation* (*LES*) and *Reynolds-Averaged Navier-Stokes Simulation* (*RANS*) involve a progressive degree of modeling in this very order, which allows for less computational cost but also less accuracy. Hence, the complexity of the physical phenomena as well as the geometry of the problem ultimately dictate the paradigm used to solve the problem.

3.1 Direct Numerical Simulation

The Direct Numerical Simulation is considered the purest paradigm of turbulence simulation as it fully resolves the turbulent energy spectrum without any additional modeling. The Navier-Stokes equations are solved using a sufficient number of spatial points to fully cover all turbulent scales from the integral down to the Kolmogorov scale. Hence, the DNS provides the highest accuracy out of all three paradigms at the price of immense computational effort.

Equation 2.16 established the relationship between the Reynolds number and the Kolmogorov scale. Given the requirement that the Kolmogorov scale must be resolved within the DNS, it can be concluded that the resolution requirements of the DNS become more stringent as the Reynolds number increases. Since the resolution is a direct – indeed, the primary – driver of the computational cost, the computational cost also scale alike. Furthermore,

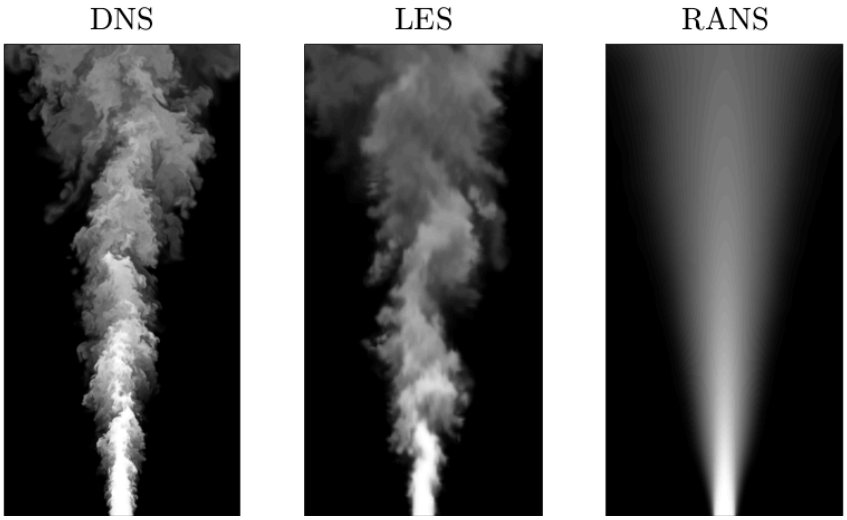

Figure 3.1 Simulation results of a planar free turbulent jet flow at a Reynolds number of $10,000$ by applying the three paradigms of turbulence simulation.

additional transport equations or models, such as for reacting or multiphase flows, may further increase this computational effort.

In the case of problems involving scalar transport, it has to be noted that the resolution of the Kolmogorov scale may not be sufficient for the simulation to be considered fully resolved. While the dissipation of the smallest eddy gives the resolution limit for the mechanics of the flow, the full resolution of the scalar transport is achieved when scalar parcels of the smallest eddies' size dissipate as fast as the smallest eddies themselves [18]. This scale is referred to as the *Batchelor* scale and can be obtained using the Schmidt number of the scalar:

$$\lambda_{\mathrm{B}} = \eta_{\mathrm{k}}/\mathrm{Sc}^{1/2} \tag{3.1}$$

Here, Sc represents the Schmidt number, which quantifies the ratio between diffusive momentum and diffusive scalar transport:

$$\mathrm{Sc} = \nu/D \tag{3.2}$$

While the diffusion coefficient of the scalar D is often unknown, the Schmidt number is typically known from experience and used to determine the latter. The Batchelor scale can be interpreted as the smallest length scale of fluctuations in the transported scalar that can exist before being dissipated by the molecular diffusion. Depending on the scalar, it has to be considered that the Schmidt number can be greater than one, leading to even higher resolution requirements.

In summary, DNS is a powerful tool with the potential to provide detailed insight into the physics of a flow. Its power, however, comes at the price of high cost which rise even further with increasing Reynolds number. State-of-the-art DNS is typically performed for

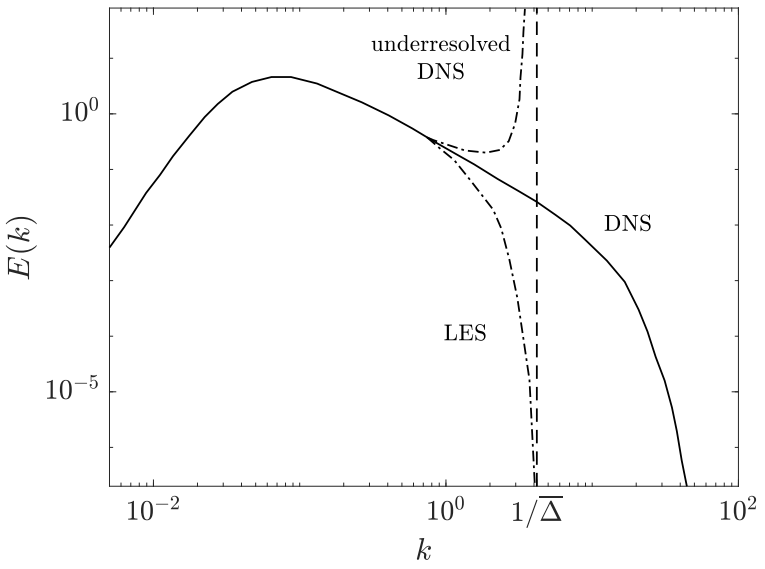

Figure 3.2 Turbulent energy spectra of a Large-Eddy Simulation as well as under- and fully resolved Direct Numerical Simulation.

Reynolds numbers up to the order of $10,000$ and in canonical cases (e.g., homogeneous isotropic turbulence, free jet flows, pipe flows or turbulent channel flows [111, 133, 57, 185]), which are typically considered low compared to real-world engineering systems. Therefore, DNS remains applicable only for selected small-scale systems to either validate or generate model data, but not yet to provide a detailed description of full technical processes.

3.2 Large-Eddy Simulation

Large-Eddy Simulation is a hybrid paradigm that includes both resolution and modeling of the turbulent energy cascade. LES has its roots in meteorology and aims to overcome the Reynolds number limitations of DNS. As the name implies, Large-Eddy Simulation attempts to resolve the largest turbulent structures within the flow while modeling the effects of the smaller scales. The LES theory is based on Kolmogorov's hypothesis of universal and isotropic small scales. While RANS modeling must cover the entire cascade and the highly geometry-dependent turbulent eddies, LES modeling takes place only at the scales where the information of the flow geometry has already decayed, thus, allowing for accurate and comparatively simple LES models.

To separate these desired scales, a filtering operation is introduced using the filter width $\overline{\Delta}$ as suggested by Leonard [160]. The filter width marks the scale before which the cascade is resolved and after which modeling of the cascade takes place. This effectively cuts off the wavenumbers beyond the filter scale from the turbulent energy spectrum.

The introduction of the cut-off scale and its effect on the turbulent energy cascade are portrayed in Fig. 3.2 and compared to the previously introduced full spectrum of a DNS introduced earlier. By filtering out the smaller scales – and thus the energy dissipation – from the spectrum, the process of energy dissipation is removed from the energy cascade. In particular, if there is no energy dissipation at the small scales, energy will accumulate at the lowest possible scale as it is dictated by the energy cascade. This will be the case for an underresolved DNS which is not experiencing dissipative effects from the solver. As the accumulation of energy at the lowest scale is not physical, LES aims to improve this behavior by introducing a subfilter model that effectively removes the energy up to the finest resolved scale. Hence, the true character of a LES is always defined by the particular model used.

The mathematical basis for LES lies within the filtering operation:

$$\overline{\Phi}(\boldsymbol{x},t) = \int_{D^3} \Phi(\breve{\boldsymbol{x}},t)\, G(\boldsymbol{x}-\breve{\boldsymbol{x}};\overline{\Delta})\, d\breve{\boldsymbol{x}} \tag{3.3}$$

Where the transported variable Φ is convolved with the filtering kernel G and the filter width $\overline{\Delta}$ to obtain the filtered quantity $\overline{\Phi}$. The filtering is applied spatially in the three-dimensional domain D^3. To ensure that the filter does not change the solution integral – which is easily noticed in the case of a constant function – integrating the filter kernel G must yield unity:

$$\int_{D^3} G(\boldsymbol{x}-\breve{\boldsymbol{x}};\overline{\Delta})\, d\breve{\boldsymbol{x}} = 1 \tag{3.4}$$

The achieved separation of scales is expressed mathematically by the decomposition of the unfiltered quantity Φ into the filtered part $\overline{\Phi}$ and the suppressed part (or subfilter part) Φ', leading to the identity:

$$\Phi = \overline{\Phi} + \Phi' \tag{3.5}$$

Along with the convolution integral come a few rules for the handling of the filtered terms. The first rule dictates, that introducing a new filter level to a filtered quantity does not lead to the same result:

$$\overline{\overline{\Phi}}(\boldsymbol{x},t) \neq \overline{\Phi}(\boldsymbol{x},t) \tag{3.6}$$

As the filter smooths out the original field of Φ rather than converting it to a constant value. The second rule states that filtering of the subfilter contribution will not result in values of zero:

$$\overline{\Phi}'(\boldsymbol{x},t) \neq 0 \tag{3.7}$$

Which is intuitive, since filtering is designed to reduce amplitude rather than remove it.

It can be concluded that the filter is of crucial importance since it is directly merged with the Navier-Stokes equations and thus takes control of their solution. To fully understand the concept of LES and to interpret its results, it is necessary to know the effect of the filter and to deal with its choice.

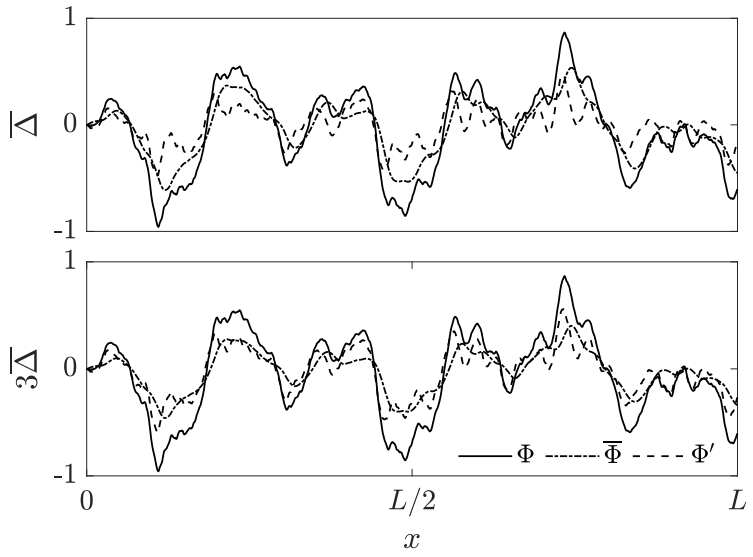

Figure 3.3 Effects of low-pass filtering on a randomly generated signal using two different filter widths.

Although filters are ubiquitous in the modern world, the effect of applying a filter to a spatially-resolved quantity shall be revised. Filters are typically classified as low-pass, band-pass and high-pass variants. Low-pass filters remove the small scale contribution to a recorded signal and high-pass filters remove the large scale contribution, respectively. Band-pass filters can be obtained by combining both low- and high-pass filtering, thus, narrowing down the scales to a limited range. As the removal of the small scales is of interest for LES theory, only low-pass filters will be considered in this work.

The effects of a low-pass filter on a spatially resolved arbitrary signal are demonstrated in Fig. 3.3. Applying a filter to a known signal obtained from all scales allows for the decomposition of the signal into the filtered $\overline{\Phi}$ and the suppressed contribution Φ'. It can be seen that the (low-pass) filter removes the small scale contribution in the signal and thus, smooths the signal. In a three-dimensional problem this will ultimately lead to the desired disappearance of the small turbulent structures for LES. To give a further insight, a variation of the filter width Δ is performed. Increasing the filter width leads to a progressive vanishing of the small scales and hence, must be chosen carefully for the respective problem.

The mathematical foundations of filtering have been laid in the previous paragraphs. In the following, the gap between the theory and the application of the filter within the equations shall be closed. Filters are typically given as a mathematical instruction, specifically in the form of an equation. While most of these equations are written down in a continuous domain, it must be considered that simulation techniques for turbulent flows operate in a discrete domain. Hence, filters applied to LES are typically of discrete nature.

The discretization of the domain depends on the given problem and introduces a smallest possible scale due to the computational limitations. In fact, the discretization dictates the smallest scale that can be found in the computational problem. By effect the discretization can be seen as a filter that suppresses the smallest scales of the given problem. Therefore, the discretization may adopt this function and replace the definition of a separate filter. This approach to filtering is referred to as *implicit* filtering and was introduced by Schumann [254]. Implicit filtering is the most commonly applied form of filtering within LES [68]. This is not only due to savings of computational effort but also because employing a filter width coarser than the discretization introduces a loss of resolution that is typically not considered worth to afford. In this context, the question arises as to why a separate filter was originally proposed. The true purpose of the filter is to draw a line between separation of scales and discretization, which was shown to vanish in the case of implicit filtering. This also led to the remaining inappropriate choice of terminology within LES and to the common use of both, the terms *subfilter* and *subgrid*. The separation results in the control of wavenumbers resulting from the nonlinear (convective) term that cannot be resolved on the computational grid, which may lead to aliasing contamination of the solution. In contrast to its implicit counterpart, the employment of an actual filter is also referred to as *explicit* filtering.

In order to further elaborate the influence of the filter, the concept and structure of LES – or paradigms of turbulence simulation in general – needs to be discussed in more detail. Following the theory, a paradigm of turbulence simulation is nothing but a set of equations waiting to be solved for a certain set of boundary conditions dictated by the respective problem. To actually obtain a solution from these equations in the case of an LES, the following tools or frameworks may be employed:

- Spatial discretization
- Numerical procedure
- Filtering
- Subfilter/subgrid modeling

When performing LES, the solution obtained from it is a direct result of the coupling and interaction of all the aspects included in the solver. Although usually being mathematically complicated and computationally expensive, there are approaches to uncouple the effects of these aspects. This is particularly important in the method development and evaluation step, where only the effects of the newly implemented model are relevant. In the case of implicit filtering no distinction is being made between the filter and the discretization. Hence, their effects merge and become practically inseparable. While this is of rather little concern in technical applications of CFD, it is considered a severe problem in the study of model performance – especially in the area of LES quality-assessment. A more recent approach to

reduce the coupling of solver-aspects is the implicit-LES, which omits the filtering as well as the corresponding sub-filter modeling and employs specifically designed numerical schemes to compensate for the lack of the latter [2, 98].

It can be seen that due to its hybrid nature LES requires special care in the choice of models and methods. Furthermore the use of terminology within the community may appear somewhat hypocritical – especially regarding the use of filter and subfilter-models. Although a plethora of LES studies use implicit filtering, the use of explicitly filtered LES equations is given at the beginning of most scientific documentation. For the sake of completeness of this work, the derivation of the filtered LES equations shall be presented.

The filtering of the source-free conservation equation of mass and momentum will be given to demonstrate the effect of the filter. Applying the filtering operation following Eq. 3.3 and employing a constant filtering width – indicated as $\overline{(\cdot)}$ – yields:

$$\overline{\frac{\partial \rho}{\partial t} + \frac{\partial \rho u_\mathrm{j}}{\partial x_\mathrm{j}}} = 0 \tag{3.8}$$

Per definition the filtering integral is linear:

$$\overline{\frac{\partial \rho}{\partial t}} + \overline{\frac{\partial \rho u_\mathrm{j}}{\partial x_\mathrm{j}}} = 0 \tag{3.9}$$

Following the Schwarz rule, the filter and the derivative are commutable:

$$\frac{\partial \overline{\rho}}{\partial t} + \frac{\partial \overline{\rho u_\mathrm{j}}}{\partial x_\mathrm{j}} = 0 \tag{3.10}$$

It can be seen that incorporating the filtering operation into the equation produces a merged filtered term $\overline{\rho u_\mathrm{j}}$ that contains the product of two variables at the subfilter level. A major objective of LES is to avoid these terms, since by definition they cannot be obtained at the LES resolution. Therefore, for the case of flows with variable density, the concept of Favre-filtering is introduced [66]. The Favre-filtering – indicated as $\widetilde{(\cdot)}$ – aims at avoiding coupled terms by replacing the conserved quantity Φ as follows:

$$\widetilde{\Phi} = \frac{\overline{\rho \Phi}}{\overline{\rho}} \tag{3.11}$$

And thus allows for the replacement of the unknown subfilter terms:

$$\frac{\partial \overline{\rho}}{\partial t} + \frac{\partial \overline{\rho} \widetilde{u}_\mathrm{j}}{\partial x_\mathrm{j}} = 0 \tag{3.12}$$

The filtered equation has the same structure as its counterpart. Therefore, it can be concluded that the conservation of mass still holds for the filtered quantities. In the next step, the filter

is applied to the source-free conservation of momentum:

$$\overline{\frac{\partial \rho u_\mathrm{i}}{\partial t} + \frac{\partial \rho u_\mathrm{i} u_\mathrm{j}}{\partial x_\mathrm{j}}} = \overline{-\frac{\partial p}{\partial x_\mathrm{i}} + \frac{\partial}{\partial x_\mathrm{j}} \left(\mu \left(\frac{\partial u_\mathrm{i}}{\partial x_\mathrm{j}} + \frac{\partial u_\mathrm{j}}{\partial x_\mathrm{i}} \right) - \frac{2}{3} \mu \frac{\partial u_\mathrm{k}}{\partial x_\mathrm{k}} \delta_\mathrm{ij} \right)} \tag{3.13}$$

Again the terms within the filter are decomposed:

$$\overline{\frac{\partial \rho u_\mathrm{i}}{\partial t}} + \overline{\frac{\partial \rho u_\mathrm{i} u_\mathrm{j}}{\partial x_\mathrm{j}}} = -\overline{\frac{\partial p}{\partial x_\mathrm{i}}} + \overline{\frac{\partial}{\partial x_\mathrm{j}} \left(\mu \left(\frac{\partial u_\mathrm{i}}{\partial x_\mathrm{j}} + \frac{\partial u_\mathrm{j}}{\partial x_\mathrm{i}} \right) - \frac{2}{3} \mu \frac{\partial u_\mathrm{k}}{\partial x_\mathrm{k}} \delta_\mathrm{ij} \right)} \tag{3.14}$$

The application of the Schwarz rule allows for the commutation of the filtering operation and the derivative:

$$\frac{\partial \overline{\rho u_\mathrm{i}}}{\partial t} + \frac{\partial \overline{\rho u_\mathrm{i} u_\mathrm{j}}}{\partial x_\mathrm{j}} = -\frac{\partial \overline{p}}{\partial x_\mathrm{i}} + \frac{\partial}{\partial x_\mathrm{j}} \overline{\rho \nu \left(\left(\frac{\partial u_\mathrm{i}}{\partial x_\mathrm{j}} + \frac{\partial u_\mathrm{j}}{\partial x_\mathrm{i}} \right) - \frac{2}{3} \frac{\partial u_\mathrm{k}}{\partial x_\mathrm{k}} \delta_\mathrm{ij} \right)} \tag{3.15}$$

With the Favre-filtering the equation can be rewritten as:

$$\frac{\partial \overline{\rho} \widetilde{u_\mathrm{i}}}{\partial t} + \frac{\partial \overline{\rho} \widetilde{u_\mathrm{i}} \widetilde{u_\mathrm{j}}}{\partial x_\mathrm{j}} = -\frac{\partial \overline{p}}{\partial x_\mathrm{i}} + \frac{\partial}{\partial x_\mathrm{j}} \overline{\rho} \overline{\nu \left(\left(\frac{\partial u_\mathrm{i}}{\partial x_\mathrm{j}} + \frac{\partial u_\mathrm{j}}{\partial x_\mathrm{i}} \right) - \frac{2}{3} \frac{\partial u_\mathrm{k}}{\partial x_\mathrm{k}} \delta_\mathrm{ij} \right)} \tag{3.16}$$

It is found that the viscous stresses have a structure that is difficult to assess using the filter-scale quantities. Hence, it is assumed that for the Favre-filtering – for all i and j – the kinematic viscosity ν and the velocity gradient $\frac{\partial \widetilde{\rho} \widetilde{u_\mathrm{i}}}{\partial x_\mathrm{j}}$ are uncorrelated. While this holds only true for the case of constant viscosity flows, the introduced error is assumed to be small, in particular compared to the error introduced by the modeling of the subfilter scales. This is especially the case for high Reynolds numbers where the turbulent dissipation is significantly stronger than the laminar dissipation. It can then be argued that, due to the dominance of the turbulent dissipation, the treatment of the viscosity within the filter is an error introduced by the subgrid modeling. A simplification of the equations can be formulated as:

$$\overline{\rho} \widetilde{\nu \frac{\partial u_\mathrm{i}}{\partial x_\mathrm{j}}} \approx \overline{\rho} \widetilde{\nu} \frac{\partial \widetilde{u_\mathrm{i}}}{\partial x_\mathrm{j}} \tag{3.17}$$

It can be seen that the Favre-filtering yields an unclosed term $\partial \rho \widetilde{u_\mathrm{i}} \widetilde{u_\mathrm{j}} / \partial x_\mathrm{j}$, which again consists of subfilter variables that cannot be obtained. This is the linchpin of LES theory, as this term represents the compromise of information by the filter. To preserve the original structure of the equation, a zero-sum addition is proposed:

$$\frac{\partial \overline{\rho} \widetilde{u_\mathrm{i}} \widetilde{u_\mathrm{j}}}{\partial x_\mathrm{j}} = \frac{\partial \overline{\rho} \widetilde{u_\mathrm{i}} \widetilde{u_\mathrm{j}}}{\partial x_\mathrm{j}} + \frac{\partial \overline{\rho} \widetilde{u_\mathrm{i}} \widetilde{u_\mathrm{j}}}{\partial x_\mathrm{j}} - \frac{\partial \overline{\rho} \widetilde{u_\mathrm{i}} \widetilde{u_\mathrm{j}}}{\partial x_\mathrm{j}} \tag{3.18}$$

The term mimics the original convective transport term but produces another term as a byproduct:

$$\frac{\partial \overline{\rho}\widetilde{u}_\mathrm{i}\widetilde{u}_\mathrm{j}}{\partial x_\mathrm{j}} + \frac{\partial \overline{\rho}\widetilde{u_\mathrm{i}u_\mathrm{j}}}{\partial x_\mathrm{j}} - \frac{\partial \overline{\rho}\widetilde{u}_\mathrm{i}\widetilde{u}_\mathrm{j}}{\partial x_\mathrm{j}} = \frac{\partial \overline{\rho}\widetilde{u}_\mathrm{i}\widetilde{u}_\mathrm{j}}{\partial x_\mathrm{j}} - \frac{\partial \overline{\rho}(\widetilde{u}_\mathrm{i}\widetilde{u}_\mathrm{j} - \widetilde{u_\mathrm{i}u_\mathrm{j}})}{\partial x_\mathrm{j}} \tag{3.19}$$

Resulting from the filtering of the NSE, this term represents the influence of the removed scales on the resolved scales. Hence, it is of crucial importance for the preservation of the turbulent energy spectrum, since this term removes the energy at the smallest scale found in the LES domain. This term retains the name subfilter stresses, although mostly being referred to as *Subgrid Stresses* (*SGS*) due to the common use of implicit filtering. For the sake of clarity, and due to this work employing implicit filtering, the stresses will be referred to as subgrid stresses in the following. One of the defining aspects of LES is the treatment of this unclosed term, the respective approaches of which are discussed in detail in this work. Following the above derivation, the subgrid stresses are defined as:

$$\tau_\mathrm{ij}^\mathrm{sgs} = \widetilde{u}_\mathrm{i}\widetilde{u}_\mathrm{j} - \widetilde{u_\mathrm{i}u_\mathrm{j}} \tag{3.20}$$

Using the newly derived term, the LES-filtered equation of momentum conservation can be composed:

$$\frac{\partial \overline{\rho}\widetilde{u}_\mathrm{i}}{\partial t} + \frac{\partial \overline{\rho}\widetilde{u}_\mathrm{i}\widetilde{u}_\mathrm{j}}{\partial x_\mathrm{j}} = -\frac{\partial \overline{p}}{\partial x_\mathrm{i}} + \frac{\partial}{\partial x_\mathrm{j}}\left(\overline{\rho}\widetilde{\nu}\left(\frac{\partial \widetilde{u}_\mathrm{i}}{\partial x_\mathrm{j}} + \frac{\partial \widetilde{u}_\mathrm{j}}{\partial x_\mathrm{i}}\right) - \frac{2}{3}\overline{\rho}\widetilde{\nu}\frac{\partial \widetilde{u_\mathrm{k}}}{\partial x_\mathrm{k}}\delta_\mathrm{ij}\right) + \frac{\partial \overline{\rho}\tau_\mathrm{ij}^\mathrm{sgs}}{\partial x_\mathrm{j}} \tag{3.21}$$

As the filtering of the momentum equation yields an additional term to account for the suppressed scales, it is of interest to investigate the effect of the filtering on the scalar transport equations. The source-free scalar transport equation from Sec. 2.1 will be used to demonstrate the filtering:

$$\overline{\frac{\partial \rho\phi}{\partial t} + \frac{\partial \rho\phi u_\mathrm{j}}{\partial x_\mathrm{j}}} = \overline{\frac{\partial}{\partial x_\mathrm{j}}\left(\rho D_\phi \frac{\partial \phi}{\partial x_\mathrm{j}}\right)} \tag{3.22}$$

Decomposing the filtered term yields:

$$\overline{\frac{\partial \rho\phi}{\partial t}} + \overline{\frac{\partial \rho\phi u_\mathrm{j}}{\partial x_\mathrm{j}}} = \overline{\frac{\partial}{\partial x_\mathrm{j}}\left(\rho D_\phi \frac{\partial \phi}{\partial x_\mathrm{j}}\right)} \tag{3.23}$$

Further change the order of the derivative and filter convolution:

$$\frac{\partial \overline{\rho\phi}}{\partial t} + \frac{\partial \overline{\rho\phi u_\mathrm{j}}}{\partial x_\mathrm{j}} = \frac{\partial}{\partial x_\mathrm{j}}\left(\overline{\rho D_\phi \frac{\partial \phi}{\partial x_\mathrm{j}}}\right) \tag{3.24}$$

Favre-filtering is employed to decouple the merged quantities. The simplification as demonstrated in Eq. 3.17 is applied assuming that the diffusion coefficient is uncorrelated with the

scalar gradient $\frac{\partial \phi}{\partial x_\mathrm{j}}$ for all j:

$$\frac{\partial \overline{\rho}\widetilde{\phi}}{\partial t} + \frac{\partial \overline{\rho}\widetilde{\phi u_\mathrm{j}}}{\partial x_\mathrm{j}} = \frac{\partial}{\partial x_\mathrm{j}} \left(\overline{\rho D_\phi \frac{\partial \phi}{\partial x_\mathrm{j}}} \right) \tag{3.25}$$

Again, the convective term cannot be obtained from the LES filtered quantities and is rewritten:

$$\frac{\partial \overline{\rho}\widetilde{\phi u_\mathrm{j}}}{\partial x_\mathrm{j}} = \frac{\partial \overline{\rho}\widetilde{\phi u_\mathrm{j}}}{\partial x_\mathrm{j}} + \frac{\partial \overline{\rho}\widetilde{\phi}\widetilde{u}_\mathrm{j}}{\partial x_\mathrm{j}} - \frac{\partial \overline{\rho}\widetilde{\phi}\widetilde{u}_\mathrm{j}}{\partial x_\mathrm{j}} \tag{3.26}$$

The zero-sum within this term can be treated analogous to the step taken in Eq. 3.19:

$$\frac{\partial \overline{\rho}\widetilde{\phi u_\mathrm{j}}}{\partial x_\mathrm{j}} = \frac{\partial \overline{\rho}\widetilde{\phi}\widetilde{u}_\mathrm{j}}{\partial x_\mathrm{j}} - \frac{\partial \overline{\rho}(\widetilde{\phi}\widetilde{u}_\mathrm{j} - \widetilde{\phi u_\mathrm{j}})}{\partial x_\mathrm{j}} \tag{3.27}$$

A structure similar to that of Eq. 3.20 is found. The resulting term represents the influence of the subfilter scalar transport on the resolved transport. Due to their similar structure and physical interpretation, this term is also referred to as the *subfilter* scalar flux. In this work, the term *subgrid* scalar transport is used specifically due to the employment of implicit filtering:

$$\tau_\mathrm{j}^\mathrm{sgs} = \widetilde{u}_\mathrm{j}\widetilde{\phi} - \widetilde{u_\mathrm{j}\phi} \tag{3.28}$$

By embedding the subgrid scalar flux into the LES-filtered scalar transport equation, the structure of the scalar LES equations can be derived:

$$\frac{\partial \overline{\rho}\widetilde{\phi}}{\partial t} + \frac{\partial \overline{\rho}\widetilde{\phi}\widetilde{u}_\mathrm{j}}{\partial x_\mathrm{j}} = \frac{\partial}{\partial x_\mathrm{j}} \left(\overline{\rho D_\phi \frac{\partial \phi}{\partial x_\mathrm{j}}} \right) + \frac{\partial \overline{\rho}\tau_\mathrm{j}^\mathrm{sgs}}{\partial x_\mathrm{j}} \tag{3.29}$$

Again, a coupling – this time between the scalar gradient and the diffusion coefficient – can be observed. This is approached in the same manner as for the viscosity in Eq. 3.17 and hence, in the scalar case reads:

$$\overline{\rho D_\phi \frac{\partial \phi}{\partial x_\mathrm{j}}} \approx \overline{\rho}\widetilde{D}_\phi \frac{\partial \widetilde{\phi}}{\partial x_\mathrm{j}} \tag{3.30}$$

Leading to the final formulation of the scalar transport equation:

$$\frac{\partial \overline{\rho}\widetilde{\phi}}{\partial t} + \frac{\partial \overline{\rho}\widetilde{\phi}\widetilde{u}_\mathrm{j}}{\partial x_\mathrm{j}} = \frac{\partial}{\partial x_\mathrm{j}} \left(\overline{\rho}\widetilde{D}_\phi \frac{\partial \widetilde{\phi}}{\partial x_\mathrm{j}} \right) + \frac{\partial \overline{\rho}\tau_\mathrm{j}^\mathrm{sgs}}{\partial x_\mathrm{j}} \tag{3.31}$$

A further decomposition of the obtained subgrid stresses was proposed by Leonard [160] and gives room for a better interpretation of the structure of the stresses. The decomposition may be performed by inserting the separation of the velocity into a resolved scale and the

subgrid scale contribution into the definition of the subgrid stresses $u_\mathrm{i} = \widetilde{u}_\mathrm{i} + u'_\mathrm{i}$:

$$\tau_\mathrm{ij}^\mathrm{sgs} = \widetilde{u_\mathrm{i} u_\mathrm{j}} - \widetilde{u}_\mathrm{i}\widetilde{u}_\mathrm{j} = \underbrace{\widetilde{\widetilde{u}_\mathrm{i}\,\widetilde{u}_\mathrm{j}} - \widetilde{u}_\mathrm{i}\,\widetilde{u}_\mathrm{j}}_{L_\mathrm{ij}} + \underbrace{\widetilde{\widetilde{u}_\mathrm{i} u'_\mathrm{j}} + \widetilde{u'_\mathrm{i}\widetilde{u}_\mathrm{j}}}_{C_\mathrm{ij}} + \underbrace{\widetilde{u'_\mathrm{i} u'_\mathrm{j}}}_{R_\mathrm{ij}} \tag{3.32}$$

The decomposition yields the components L_ij – the Leonard stresses –, C_ij – the cross stresses – and R_ij – the Reynolds subgrid stresses. Here, the Leonard term represents the interaction between the resolved scales, the cross-stress term describes the interaction between the resolved and subgrid scales and the Reynolds subgrid term quantifies the interaction between the subgrid scales. While the Leonard term can be calculated directly using an explicit filter, the Reynolds subgrid stresses must be modeled. The Leonard stress term will be relevant for some closure-approaches of the subgrid stresses.

The effect of the filtering on the different laws of conservation was discussed. It has been revealed that filtering leads to the formation of an additional flux term within the transport equation, which takes into account the suppressed scales. The closure of this term relies on additional models. In the following, an introduction to different modeling strategies will be given.

The closure of the subgrid stresses and fluxes can be seen as the heart of LES – especially in the context of implicit filtering – and aims at modeling the effects of the suppressed scales using resolved quantities. There is a plethora of approaches, the most important of which will be discussed in the following pages. There are two sets of requirements that are generally taken for granted and have been summarized by Sagaut [244]. The employed subgrid model must comply with the following types of constraints:

- Physical constraints: consistency with the modeled physics
  - Conserve the mathematical properties of the equation it is embedded in
  - Vanishing contribution locally where no small scales occur
  - Induce an effect of the same kind as the modeled terms
  - Do not alter the dynamics of the resolved scales and do not interfere with the flow driving mechanism
- Numerical constraints: consistency with the numerical algorithm
  - Acceptable numerical costs
  - Results produced local in time and space
  - Maintain or improve numerical stability
  - Insensitivity to the discretization

Two different types of approaches have emerged to satisfy the above mentioned constraints. The first type are the *functional models*, which follow a more empirical approach, as they

aim to provide a similar effect using resolved quantities without maintaining the same mathematical structure as the true subgrid stresses. The second type is the *structural models*, which aim at a precise representation of the subgrid stresses, ultimately yielding an exact mathematical expression of the subgrid stresses employing deconvolution or series expansion. The two approaches require different knowledge of the dynamics of the treated equations and provide a different quality of results. Functional models typically rely on information about the nature of the interscale interaction, while structural models require sufficient information about the structure of the small scales. In the following, the most relevant models in the context of this work will be discussed.

3.3 Functional models

The first class of LES subgrid models are the functional models, the most prominent group of which are the *Eddy-Viscosity Models* (*EVM*). The basis of this group of models is the approximation of Boussinesq [25], which states that the suppressed small scales act as an additional viscosity leading to the removal of energy from the resolved scales. In particular, the subgrid stresses can be related to the resolved stresses due to the assumed viscosity, as follows:

$$\tau_{\mathrm{ij}}^{\mathrm{sgs,d}} = \tau_{\mathrm{ij}}^{\mathrm{sgs}} - \frac{1}{3}\tau_{\mathrm{kk}}^{\mathrm{sgs}}\delta_{\mathrm{ij}} = -\bar{\rho}\widetilde{\nu}_{\mathrm{t}}\left(\left(\frac{\partial\tilde{u}_{\mathrm{i}}}{\partial x_{\mathrm{j}}} + \frac{\partial\tilde{u}_{\mathrm{j}}}{\partial x_{\mathrm{i}}}\right) - \frac{2}{3}\frac{\partial\tilde{u}_{\mathrm{k}}}{\partial x_{\mathrm{k}}}\delta_{\mathrm{ij}}\right) \tag{3.33}$$

Where ν_{t} is the turbulent viscosity. It is the target of all EVM to calculate the turbulent viscosity. The formulation of the Boussinesq hypothesis demonstrates the standard treatment of the subgrid stresses. Typically, the subgrid stresses are decomposed into an isotropic and a deviatoric (also referred to as anisotropic) part.

The scalar fluxes are treated respectively by assuming gradient-driven diffusion [297]:

$$\tau_{\mathrm{j}}^{\mathrm{sgs}} = -\frac{\widetilde{\nu}_{\mathrm{t}}}{\mathrm{Sc}_{\mathrm{t}}}\frac{\partial\widetilde{\phi}}{\partial x_{\mathrm{j}}} \tag{3.34}$$

Where Sc_{t} is the turbulent (or subgrid) Schmidt number. From the structure of the equations it can be seen that the isotropic part remains untreated. In fact, its treatment depends on the strategy of solving the LES-filtered equations. One procedure is to take advantage of the isotropic nature and to treat the term as an addition to the pressure resulting in a *modified* pressure, reading:

$$\overline{p}_{\mathrm{mod}} = \overline{p} + \frac{1}{3}\tau_{\mathrm{kk}}^{\mathrm{sgs}}\delta_{\mathrm{ij}} = \overline{p} + \frac{1}{3}\overline{\rho}\left(\widetilde{u_{\mathrm{k}}^2} - \widetilde{u}_{\mathrm{k}}^2\right) \tag{3.35}$$

This is the case for low Mach number solver architectures; the unknown isotropic subgrid stresses are determined together with the pressure. For high Mach number solver architectures, the isotropic part requires additional modeling and respective strategies have been proposed, e.g. by Yoshizawa [311], Moin [184] and Speziale [264]. It can be mentioned that Erlebacher

[63] found that the influence of the isotropic contribution remains comparatively small up to turbulent Mach numbers below a value of 0.4.

The eddy viscosity is generally defined as:

$$\nu_\mathrm{t} = \left(C_\mathrm{sgs}\overline{\Delta}\right)^2 \overline{D}_\mathrm{m} \tag{3.36}$$

Where C_sgs is the respective model constant and $\overline{D}_\mathrm{m}$ is the term which is characteristic of each EVM. While commonly being referred to as the differential operator, strictly mathematically seen $\overline{D}_\mathrm{m}$ is not a differential operator. Different EVM provide procedures for the calculation of the operator required for the turbulent viscosity. While all produced turbulent viscosities can ultimately be cast into equation Eq. 3.33, their calculation may strongly differ. A crucial aspect of EVM models is that the turbulent viscosity is always bounded to positive values $\nu_\mathrm{t} > 0$. This strictly limits the subgrid model to dissipative behavior, which favors numerical stability, but at the same time prohibits backscattering, which leaves the prediction of the energy cascade incomplete and leads to an overall increase in dissipation. In fact, early studies by Bardina [15] show generally poor alignment between the subgrid stresses produced by the EVM and the true stresses. At this point it also has to be stressed that the very basis of the EVM models – the Boussinesq hypothesis – has never been demonstrated to be fully valid experimentally or in DNS [250].

3.3.1 Smagorinsky model

The most commonly employed subgrid model is also the first subgrid model ever to be developed. The Smagorinsky model originates from the very motivation of LES which is meteorology and where it is still a popular choice – it bears the name of its creator Smagorinsky [259]. Common reasons for its use are its robustness, its efficiency and its simplicity.

Despite the advantages that lead to its popularity, the Smagorinsky model has some drawbacks that should be taken into account as they may pollute the solution obtained by LES. The drawbacks have already been discussed in detail by Launder and Sandham [154] and will be reviewed as an overview. A major discussion is the calibration of the model constant, the choice of which depends on the type of flow and geometry, the Reynolds number and the numerical discretization. The most general value proposed by Lilly [164] is $C_\mathrm{sgs} = 0.173$, while for wall bounded flows values of $C_\mathrm{sgs} = 0.065$ are suggested by Moin and Kim [183]. To overcome this issue, the dynamic procedure as developed by Germano [80] can be used. This procedure uses filtering to use information from the resolved scales near the cutoff scale and replaces the fixed constant with a value that varies in space and time. However, the model constant obtained from this procedure is overdetermined and fluctuates, which requires stabilization, e.g. by spatial averaging or temporal relaxation, as suggested by Breuer and

Rodi [26]. As with all EVMs, the stability of the Smagorinsky model comes at the cost of its strict dissipativity, and thus its inability to predict backscatter.

The Smagorinsky model calculates the operator $\overline{D}_{\mathrm{m}}$ as follows:

$$\overline{D}_{\mathrm{m}}^{\mathrm{Smagorinsky}} = \sqrt{2\widetilde{S}_{\mathrm{ij}}\widetilde{S}_{\mathrm{ij}}} \tag{3.37}$$

With the inner product of the grid-scale strain tensor $\widetilde{S}_{\mathrm{ij}}\widetilde{S}_{\mathrm{ij}}$, where the strain tensor $\widetilde{S}_{\mathrm{ij}}$ is defined as:

$$\widetilde{S}_{\mathrm{ij}} = \left(\frac{\partial \widetilde{u}_{\mathrm{i}}}{\partial x_{\mathrm{j}}} + \frac{\partial \widetilde{u}_{\mathrm{j}}}{\partial x_{\mathrm{i}}} \right) \tag{3.38}$$

It shall be revised that the inner product of a tensor in fact yields a scalar and must be seen as the sum of the products of all tensor elements. The full product can be written out as:

$$\begin{aligned} \widetilde{S}_{\mathrm{ij}}\widetilde{S}_{\mathrm{ij}} = \widetilde{S}_{11}\widetilde{S}_{11} + \widetilde{S}_{12}\widetilde{S}_{12} + \widetilde{S}_{13}\widetilde{S}_{13} \\ + \widetilde{S}_{21}\widetilde{S}_{21} + \widetilde{S}_{22}\widetilde{S}_{22} + \widetilde{S}_{23}\widetilde{S}_{23} \\ + \widetilde{S}_{31}\widetilde{S}_{31} + \widetilde{S}_{32}\widetilde{S}_{32} + \widetilde{S}_{33}\widetilde{S}_{33} \end{aligned} \tag{3.39}$$

A common problem with the use of the Smagorinsky model is the incorrect prediction of wall scaling for wall-bounded flows. Adequate damping of velocity fluctuations in EVM is achieved when $\widetilde{\nu}_{\mathrm{t}} \propto \left(y^{+}\right)^{3}$ holds sufficiently close to the wall. However, the standard Smagorinsky model does not scale the eddy viscosity, leading to increased dissipative behavior. This behavior can be improved by applying a damping correction to the model constant as suggested by van Driest [284]:

$$D\left(y^{+}\right) = 1 - e^{-y^{+}/A^{+}} \tag{3.40}$$

Where A^{+} is a parameter to adjust the damping behavior. In general, the van Driest correction achieves a wall scaling of $\widetilde{\nu}_{\mathrm{t}} \propto \left(y^{+}\right)^{2}$, which significantly improves the standard Smagorinsky model, but is not completely correct. The true scaling can be found by further modifying the van Driest approach according to Launder and Sandham [154], such as:

$$D\left(y^{+}\right) = \left(1 - e^{-\left(y^{+}/A^{+}\right)^{3}}\right)^{1/2} \tag{3.41}$$

Another alternative is a dynamic procedure, which produces correct wall scaling behavior and will be discussed in more detail later. Finally, the Smagorinsky model struggles in the case of laminar-turbulent transition. By its very nature, the Smagorinsky model produces turbulent viscosities even in the case of laminar flow, exhibiting unphysical dissipation that makes it difficult to apply to this type of flow.

3.3.2 Sigma model

The shortcomings of the Smagorinsky model are discussed by Nicoud et al. [192], who posed a list of requirements for the operator $\overline{D}_\mathrm{m}$ to overcome these shortcomings. The most important properties of the operator are related to stability and therefore require local values for its calculation as well as positive values of the operator to suppress backscatter. To improve the accuracy of an EVM, it is desirable for the operator to vanish for laminar and two-dimensional flows, as well as near boundaries, where it is expected to scale with the cube of the wall distance. The same work proposes a formulation for the operator that satisfies all of the above requirements and forms a powerful model. It can be computed using the singular values of the grid-scale velocity gradient tensor:

$$\widetilde{g}_\mathrm{ij} = \frac{\partial \widetilde{u}_\mathrm{i}}{\partial x_\mathrm{j}} \tag{3.42}$$

Precisely this tensor was chosen in order to meet the previously stated requirements for the operator $\overline{D}_\mathrm{m}$ – thus, it may be argued that this leads to a mathematical rather than a physical definition. These singular values are by definition always non-negative, since G_ij is positive semidefinite. In particular, the smallest singular value will be zero only if a row or column of $\widetilde{g}_\mathrm{ij}$ is zero, which corresponds to the case of a two-dimensional flow. Furthermore, analysis using a Taylor series expansion of the resolved velocities as a function of the wall distance showed that for a suitable combination of the singular values in the definition of $\overline{D}_\mathrm{m}$, cubic behavior can indeed be obtained near the wall. The singular values are commonly denoted as σ_i, which is why the model is also called the Sigma model. The singular values are obtained as roots of the eigenvalues of the following tensor:

$$G_\mathrm{ij} = \widetilde{g}_\mathrm{ki}\widetilde{g}_\mathrm{kj} = \frac{\partial \widetilde{u}_\mathrm{k}}{\partial x_\mathrm{i}} \frac{\partial \widetilde{u}_\mathrm{k}}{\partial x_\mathrm{j}} \tag{3.43}$$

The invariants of G_ij must first be obtained to compute the singular values:

$$I_1 = \mathrm{tr}(G_\mathrm{ij}) \tag{3.44}$$

$$I_2 = (\mathrm{tr}(G_\mathrm{ij})^2 - \mathrm{tr}(G_\mathrm{ij}^2))/2 \tag{3.45}$$

$$I_3 = \det(G_\mathrm{ij}) \tag{3.46}$$

Here tr() denotes the trace and det() denotes the determinant operator, following the literature. In the next step, the angles are obtained from the invariants:

$$\alpha_1 = \frac{I_1^2}{9} - \frac{I_2}{3} \tag{3.47}$$

$$\alpha_2 = \frac{I_1^3}{27} - \frac{I_1 I_2}{6} + \frac{I_3}{2} \tag{3.48}$$

$$\alpha_3 = \frac{1}{3}\arccos(\alpha_1^{-3/2}\alpha_2) \tag{3.49}$$

The singular values of $\widetilde{g}_{\mathrm{ij}}$ can be calculated directly from the angle values:

$$\sigma_1 = \left(\frac{I_1}{3} + 2\alpha_1^{1/2}\cos\left(\alpha_3\right)\right)^{1/2} \tag{3.50}$$

$$\sigma_2 = \left(\frac{I_1}{3} - 2\alpha_1^{1/2}\cos\left(\frac{\pi}{3} + \alpha_3\right)\right)^{1/2} \tag{3.51}$$

$$\sigma_3 = \left(\frac{I_1}{3} - 2\alpha_1^{1/2}\cos\left(\frac{\pi}{3} - \alpha_3\right)\right)^{1/2} \tag{3.52}$$

Where $\sigma_1 \geq \sigma_2 \geq \sigma_3 \geq 0$ always holds. The operator $\overline{D}_{\mathrm{m}}$ is assembled:

$$\overline{D}_{\mathrm{m}} = \frac{\sigma_3(\sigma_1 - \sigma_2)(\sigma_2 - \sigma_3)}{\sigma_1^2} \tag{3.53}$$

Nicoud suggests a universal constant of $C_{\mathrm{sgs}} = 1.5$ for his model. The model has been shown to yield good results using static and dynamic procedures [192]. Overall, the Sigma model generally outperforms the standard Smagorinsky model due to its design, following the desired properties. However, it is occasionally argued that the turbulent viscosities ν_{t} are of a non-physical nature and exhibit strong scattering behavior due to the model following a strictly mathematical definition [60, 96].

3.3.3 Germano's dynamical procedure

The dynamical procedure by Germano forms a tremendous upgrade to parameter-based eddy viscosity models – although initially proposed to improve the standard Smagorinsky model – at the cost of increased computational effort. While originally proposed by Germano, several improvements and extensions exist such as by Lilly [165], Meneveau [178] and Moin [184]. As the advantages and the working principle were briefly discussed before, more light shall be shed on the mathematics of the dynamic procedure. The aim of the dynamic procedure is to construct a suitable model constant from the smallest resolved scales as they contain the most accurate information on the grid about the suppressed scales. For this purpose it is assumed that the model constant to be determined is only a weak function of the wavenumber and hence, all information for its construction may be taken from the smallest resolved scales. An

additional filtering level is introduced (typically at the double of the cut-off scale $\widehat{\Delta} = 2\overline{\Delta}$) leading to the formulation of a new but known test filter stress $T_{\mathrm{ij}}^{\mathrm{sgs}}$, which is fully known due to the information obtained from the cut-off scale resolved variables. This test filter stress is obtained by applying the test filter on the LES-filtered variables. In the following, the framework by Lilly [165] – allowing for variable densities – is presented for the sake of consistency with the LES-filtered equations. It has to be noted henceforth, that together with the test filtering a second Favre-filtering level is introduced, following Eq. 3.11, which dictates:

$$\breve{\widehat{\Phi}} = \frac{\widehat{\overline{\rho}\widetilde{\Phi}}}{\widehat{\overline{\rho}}} \tag{3.54}$$

And allows for simplification of mathematical terms used in the derivation process. The cut-off and test filter scale stresses can be formulated as:

$$\begin{aligned} \tau_{\mathrm{ij}}^{\mathrm{sgs}} &= \frac{\overline{\rho u_{\mathrm{i}}}\,\overline{\rho u_{\mathrm{j}}}}{\overline{\rho}} - \overline{\rho u_{\mathrm{i}} u_{\mathrm{j}}} \\ T_{\mathrm{ij}}^{\mathrm{sgs}} &= \frac{\widehat{\overline{\rho u_{\mathrm{i}}}}\,\widehat{\overline{\rho u_{\mathrm{j}}}}}{\widehat{\overline{\rho}}} - \widehat{\overline{\rho u_{\mathrm{i}} u_{\mathrm{j}}}} \end{aligned} \tag{3.55}$$

It has been stated earlier that the Leonard stress can be obtained directly in LES by applying an explicit filtering level to the grid-scale variables. Germano's procedure thereby employs the test filter to establish a relationship between the previously introduced Leonard stresses, the subgrid stresses and the test-filter stresses. This expression can be simplified using the additional Favre-filtering level from Eq. 3.54. Due to its relevance for the procedure, this relation is also referred to as the Germano identity:

$$L_{\mathrm{ij}} = T_{\mathrm{ij}}^{\mathrm{sgs}} - \widehat{\tau}_{\mathrm{ij}}^{\mathrm{sgs}} = \widehat{\overline{\rho}\widetilde{u}_{\mathrm{i}}\widetilde{u}_{\mathrm{j}}} - \frac{\widehat{\overline{\rho}\widetilde{u}_{\mathrm{i}}}\,\widehat{\overline{\rho}\widetilde{u}_{\mathrm{j}}}}{\widehat{\overline{\rho}}} \tag{3.56}$$

It can be seen that the Leonard stress consists only of known quantities and hence, casting the baseline Smagorinsky model into this identity serves as a basis for the determination of the model constant. To include the modeling constant in the identity, Smagorinsky's model is formulated at the cut-off and test-filter scale, leading to two expressions for the respective subfilter and subgrid stresses, which are assumed to be modeled by the same constant:

$$\begin{aligned} \tau_{\mathrm{ij}}^{\mathrm{sgs}} - \frac{1}{3}\tau_{\mathrm{kk}}^{\mathrm{sgs}}\delta_{\mathrm{ij}} &= \overline{\rho} C_{\mathrm{m}}^2 \overline{\Delta}^2 \overline{D}_{\mathrm{m}}(\widetilde{u}_{\mathrm{i}}) \left(\frac{2}{3}\frac{\partial \widetilde{u}_{\mathrm{k}}}{\partial x_{\mathrm{k}}}\delta_{\mathrm{ij}} - \left(\frac{\partial \widetilde{u}_{\mathrm{i}}}{\partial x_{\mathrm{j}}} + \frac{\partial \widetilde{u}_{\mathrm{j}}}{\partial x_{\mathrm{i}}} \right) \right) \\ T_{\mathrm{ij}}^{\mathrm{sgs}} - \frac{1}{3}T_{\mathrm{kk}}^{\mathrm{sgs}}\delta_{\mathrm{ij}} &= \widehat{\overline{\rho}} C_{\mathrm{m}}^2 \widehat{\overline{\Delta}}^2 \overline{D}_{\mathrm{m}}(\widehat{\widetilde{u}}_{\mathrm{i}}) \left(\frac{2}{3}\frac{\partial \widehat{\widetilde{u}}_{\mathrm{k}}}{\partial x_{\mathrm{k}}}\delta_{\mathrm{ij}} - \left(\frac{\partial \widehat{\widetilde{u}}_{\mathrm{i}}}{\partial x_{\mathrm{j}}} + \frac{\partial \widehat{\widetilde{u}}_{\mathrm{j}}}{\partial x_{\mathrm{i}}} \right) \right) \end{aligned} \tag{3.57}$$

To simplify the notation and to separate the unknown modeling constant C_m from the remaining terms, which can be computed directly, two variables α_ij and β_ij are introduced:

$$\begin{aligned}\beta_\mathrm{ij} &= C_\mathrm{m}^2 \left(\tau_\mathrm{ij}^\mathrm{sgs} - \frac{1}{3}\tau_\mathrm{kk}^\mathrm{sgs}\delta_\mathrm{ij} \right) \\ \alpha_\mathrm{ij} &= C_\mathrm{m}^2 \left(T_\mathrm{ij}^\mathrm{sgs} - \frac{1}{3}T_\mathrm{kk}^\mathrm{sgs}\delta_\mathrm{ij} \right)\end{aligned} \tag{3.58}$$

These variables are merged into the deviatoric part of the Germano identity given in Eq. 3.56, which yields a set of six equations in the case of variable density. An overdetermined system of equations is obtained, which reads:

$$L_\mathrm{ij} - \frac{1}{3}L_\mathrm{kk}\delta_\mathrm{ij} = \widehat{C_\mathrm{m}^2\beta_\mathrm{ij}} - C_\mathrm{m}^2\alpha_\mathrm{ij} = M_\mathrm{ij} \tag{3.59}$$

However, the desired constant C_m is convolved in the filter operator. Following the ideas of Germano [80], Moin [184] and Lilly [165], the modeling constant is assumed to be independent of the test filtering operation for at least one interval of the test filter cut-off length.

In general, it is desired to obtain one equation while solving for a scalar. Therefore, Germano [80] proposed to contract the tensor using the strain tensor $\widetilde{S}_\mathrm{ij}$:

$$C_\mathrm{m}^2 = \frac{\left(L_\mathrm{ij} - \frac{1}{3}L_\mathrm{kk}\delta_\mathrm{ij} \right)\widetilde{S}_\mathrm{ij}}{\left(\widehat{\beta}_\mathrm{ij} - \alpha_\mathrm{ij} \right)\widetilde{S}_\mathrm{ij}} \tag{3.60}$$

A common problem with determining C_m using this equation is the occurrence of numerical instabilities, since the denominator can become zero independently of the nominator. It is common practice to deal with this by assuming a spatially homogeneous constant C_m in several directions and applying filtering.

Lilly [165] suggested the use of a least squares approximation. In analyzing this method, it was found that M_ij provides a suitable contraction:

$$C_\mathrm{m}^2 = \frac{\left(L_\mathrm{ij} - \frac{1}{3}L_\mathrm{kk}\delta_\mathrm{ij} \right)M_\mathrm{ij}}{M_\mathrm{ij}M_\mathrm{ij}} \tag{3.61}$$

Another possibility is the use of a modified version of Piomelli and Liu [208], also referred to as a localized dynamic model which is considered even more robust than the work of Lilly [165]. This approach employs the value of C_m^* at the previous time iteration n_t^* and does not require the assumption of a partially spatially homogeneous constant. This is achieved by using the strain tensor with the difference of $(\widehat{\beta}_\mathrm{ij} - \alpha_\mathrm{ij})$ as the contraction:

$$C_\mathrm{m}^2 = \frac{\left(L_\mathrm{ij} - \frac{1}{3}L_\mathrm{kk}\delta_\mathrm{ij} - \widehat{C_\mathrm{m}^{*2}\beta_\mathrm{ij}} \right)\alpha_\mathrm{ij}}{\alpha_\mathrm{ij}\alpha_\mathrm{ij}} \tag{3.62}$$

In order to ensure a good performance of the dynamic procedure – regardless of the chosen way of calculating C_m –, an additional limitation of the obtained constant is performed. The most important one is the exclusion of backscattering, which might lead to numerical instability by prohibiting negative viscosities. While the choice of C_m such that $\nu + \nu_\mathrm{t} \geq 0$ is legitimate, it is more common to simply set $C_\mathrm{m} > 0$. Another possible limitation that can be applied are maximum values to avoid excessive dissipation or local numerical instability produced by the model $C_\mathrm{m} \leq C_\mathrm{m,max}$.

The dynamic procedure is a powerful extension to EVM-type models, which has been reported to greatly improve their performance [80, 216, 244]. However, along with the choice of the dynamical procedure come limitations and effects on the model behavior. One constraint that is theoretically relevant, but not always met, is the choice of grid size. Since the test filter uses a coarser level than the grid size, it must be ensured that both filter levels remain within the inertial subrange, which may not be the case for the test filter on coarser grids. It was shown a-posteriori that this is comparatively unimportant and that satisfactory results can be obtained without fulfilling this requirement [216]. While the dynamical procedure is able to correct the behavior of its host model to a certain degree, some properties of the model are preserved despite the dynamical procedure. In particular, for the Smagorinsky model, it was shown that there is only a weak correlation between the resolved and subgrid stresses in the a-priori tests, which can be considered as a reason for the highly fluctuating nature of the constant obtained from the dynamical procedure [216].

3.3.4 Sensor-enhanced Smagorinsky model

An elegant way to deal with the drawback of the standard Smagorinsky model is the *Sensor-Enhanced Smagorinsky* model (*SES*) proposed by Hasslberger [96]. The sensor-enhanced variant of the Smagorinsky model aims at dynamically controlling the subgrid-dissipation to improve the performance of the standard Smagorinsky model in the vicinity of walls and for transitional flows. An important aspect hereby is the correction of the wall scaling of ν_t by the sensor. The sensor can be understood as an additional multiplier to the stresses produced by the standard Smagorinsky model $\tau_\mathrm{ij}^\mathrm{Smagorinsky}$ and reads:

$$\tau_\mathrm{ij}^\mathrm{sgs} = \tau_\mathrm{ij}^\mathrm{Smagorinsky} |\hat{F}_\mathrm{CS} - F_\mathrm{CS}|^{3/2} C_\mathrm{sensor} \tag{3.63}$$

The coherent-structure function F_CS is a central concept within the sensor and was introduced by Kobayashi [141]. The structure function is defined as the ratio of the second invariant of the grid-scale velocity-gradient tensor Q and its magnitude E, i.e. with:

$$Q = \frac{1}{2}\left(\widetilde{W}_\mathrm{ij}\widetilde{W}_\mathrm{ij} - \widetilde{S}_\mathrm{ij}\widetilde{S}_\mathrm{ij}\right) \tag{3.64}$$

And:

$$E = \frac{1}{2}\left(\widetilde{W}_{\mathrm{ij}}\widetilde{W}_{\mathrm{ij}} + \widetilde{S}_{\mathrm{ij}}\widetilde{S}_{\mathrm{ij}}\right) \tag{3.65}$$

Where the grid-scale strain rate shall be repeated:

$$\widetilde{S}_{\mathrm{ij}} = \frac{1}{2}\left(\frac{\partial\widetilde{u}_{\mathrm{i}}}{\partial x_{\mathrm{j}}} + \frac{\partial\widetilde{u}_{\mathrm{j}}}{\partial x_{\mathrm{i}}}\right) \tag{3.66}$$

And the grid-scale rotation rate is:

$$\widetilde{W}_{\mathrm{ij}} = \frac{1}{2}\left(\frac{\partial\widetilde{u}_{\mathrm{i}}}{\partial x_{\mathrm{j}}} - \frac{\partial\widetilde{u}_{\mathrm{j}}}{\partial x_{\mathrm{i}}}\right) \tag{3.67}$$

Leading to the structure function being bounded between -1 and $+1$. In Eq. 3.63, the coherent-structure function $\hat{F}_{\mathrm{CS}}$ recruits an additional filtering level and the filtering operation as described by Anderson and Domaradzki [8] is recommended in the original work. The sensor constant C_{sensor} has to be chosen with respect to the numerical scheme treating the momentum equations and is calibrated for the test case of homogeneous isotropic turbulence. A sensor constant of $C_{\mathrm{sensor}} \approx 0.016$ was found for the use of central differences while the quadratic upstream interpolation should use a constant of $C_{\mathrm{sensor}} \approx 0.013$.

3.4 Structural models

3.4.1 Bardina's and Liu's models

As the EVM type models are of importance to the functional models, the presumably most important group of structural models are the *Scale-Similarity Models* (*SST*). The SST-type models aim to directly mimic the subgrid-stress tensor and root in the works of Bardina [15] and Liu [168]. The model of Bardina reads:

$$\tau_{\mathrm{ij}}^{\mathrm{sgs}} = \widetilde{\widetilde{u}_{\mathrm{i}}\widetilde{u}_{\mathrm{j}}} - \widetilde{\widetilde{u}}_{\mathrm{i}}\widetilde{\widetilde{u}}_{\mathrm{j}} \tag{3.68}$$

$$\tau_{\mathrm{j}}^{\mathrm{sgs}} = \widetilde{\widetilde{u}_{\mathrm{j}}\widetilde{\phi}} - \widetilde{\widetilde{u}}_{\mathrm{j}}\widetilde{\widetilde{\phi}} \tag{3.69}$$

And the approach by Liu is based directly on the work of Bardina and employs a separate cut-off filter so that:

$$\tau_{\mathrm{ij}}^{\mathrm{sgs}} = \widehat{\widetilde{u}_{\mathrm{i}}\widetilde{u}_{\mathrm{j}}} - \widehat{\widetilde{u}}_{\mathrm{i}}\widehat{\widetilde{u}}_{\mathrm{j}} \tag{3.70}$$

$$\tau_{\mathrm{j}}^{\mathrm{sgs}} = \widehat{\widetilde{u}_{\mathrm{j}}\widetilde{\phi}} - \widehat{\widetilde{u}}_{\mathrm{j}}\widehat{\widetilde{\phi}} \tag{3.71}$$

Both models were found to yield considerable correlation with the true subgrid stresses in an a-priori analysis. However, all a-posteriori tests revealed severe stability problems of the two models, emphasizing the need to use additional EVM-type models.

3.4.2 Clark's model

A model proposed independently by Clark [42] and Lele [159] can be derived by approximating the filter of the velocity $\overline{u}_\mathrm{i}$ as well as $\overline{u}_\mathrm{j}$ using Taylor-series expansion and inserting this approximation into the equations of Bardina and Liu, thus, yielding a second-order expansion of the subgrid-stress tensor [136, 244]. Although being classified as a gradient-type model, Clark's model is typically mentioned in the same breath as the scale-similarity models. The model reads:

$$\tau_\mathrm{ij}^\mathrm{sgs} = \frac{\Delta^2}{12}\frac{\partial\widetilde{u}_\mathrm{i}}{\partial x_\mathrm{k}}\frac{\partial\widetilde{u}_\mathrm{j}}{\partial x_\mathrm{k}} \tag{3.72}$$

$$\tau_\mathrm{j}^\mathrm{sgs} = \frac{\Delta^2}{12}\frac{\partial\widetilde{u}_\mathrm{j}}{\partial x_\mathrm{k}}\frac{\partial\widetilde{\phi}}{\partial x_\mathrm{k}} \tag{3.73}$$

Clark suggested combining his model with additional models to provide sufficient energy dissipation.

3.4.3 Mixed models

It can be concluded that the structural models exhibit a considerable correlation with the true subgrid stresses at the level of individual tensor components, while suffering from stability problems due to insufficient energy dissipation. This reduces their applicability. On the other hand, the functional models show only low correlation with the true subgrid stresses, but adequately model the energy transfer from the resolved scales to the subgrid scales. While the idea of combining these two approaches already emerged with the development of the first structural models [15, 42, 293, 312], it is well known that combining their strengths can lead to improved results [132]. In the scope of this work, the role of the functional model can be represented by an EVM-type model, leading to the general formulation of a mixed model being:

$$\tau_\mathrm{ij}^\mathrm{sgs} = C_\mathrm{SST}\tau_\mathrm{ij}^\mathrm{sgs,SST} + C_\mathrm{EVM}\tau_\mathrm{ij}^\mathrm{sgs,EVM} \tag{3.74}$$

3.4.4 Klein's scale-similarity type models

The models proposed by Klein are based on the ideas of Kobayashi [142] and Abe [1]. Kobayashi aimed to formulate scale-similarity type models by casting them into a mixed model-like structure, which aims to eliminate energy transfer against the direction of the Kolmogorov cascade in the case of backscatter. The elimination of backscatter provides the desired property of stability to the scale-similarity type models. Two terms are commonly used in the analysis and treatment of backscatter. The first is called interscale energy transfer and is defined as $-\tau_\mathrm{ij}^\mathrm{SST}\widetilde{S}_\mathrm{ij}$. The sign of this term directly indicates the direction of the energy transfer and thus the presence of backscatter. In the case of forward scattering $-\tau_\mathrm{ij}^\mathrm{SST}\widetilde{S}_\mathrm{ij}$ is positive, which corresponds to the Kolmogorov cascade process, while negative $-\tau_\mathrm{ij}^\mathrm{SST}\widetilde{S}_\mathrm{ij}$ occur in the case of backscattering. Note that the expression $\tau_\mathrm{ij}^\mathrm{SST}\widetilde{S}_\mathrm{ij}$ appears as a production

term within the conservation equation of the subgrid scale turbulent kinetic energy k_{sgs}, indicating that the energy transfer from the grid scale to the subgrid scale is equal to the energy transfer between the subgrid scales. The second term is the subgrid scale force and characterizes the effect of the subgrid scale stresses on the conservation equations and is defined as $\partial \tau_{\mathrm{ij}}^{\mathrm{SST}} / \partial x_{\mathrm{j}}$.

Kobayashi's model structure goes back to the ideas of Abe [1], who aimed at stabilizing Bardina's scale-similarity model [15]. Although not directly relevant to the present work, Abe's idea will be summarized below, as it allows for a better understanding of Klein's successor models. Abe tried to transfer the structure of the robust EVM models to an SST model. The anisotropic part of the EVM model is as introduced earlier:

$$\tau_{\mathrm{ij}}^{\mathrm{EVM,d}} = -2\nu_t \widetilde{S}_{\mathrm{ij}} \tag{3.75}$$

Abe assumed the existence of an SST-type model of the same form:

$$\tau_{\mathrm{ij}}^{\mathrm{SST,d}} = -2\nu_t \widetilde{S}_{\mathrm{ij}} \tag{3.76}$$

Multiplication by the resolved strain tensor $\widetilde{S}_{\mathrm{ij}}$ converts the tensor-products into scalars and the equation can be solved for the newly introduced viscosity:

$$\nu_t = -\frac{\tau_{\mathrm{ij}}^{\mathrm{SST,d}} \widetilde{S}_{\mathrm{ij}}}{2\widetilde{S}_{\mathrm{ij}} \widetilde{S}_{\mathrm{ij}}} \tag{3.77}$$

The residual of the newly crafted model and the original SST model is summarized as:

$$R_{\mathrm{ij}} = \tau_{\mathrm{ij}}^{\mathrm{SST,d}} - \left(-2\nu_t \widetilde{S}_{\mathrm{ij}}\right) \tag{3.78}$$

According to Abe, the EVM-type model used is typically recognized as an isotropic model, and thus R_{ij} is also referred to as the subgrid-stress anisotropy term. An SST-type model that emulates the idea of EVM-type models can be written as:

$$\tau_{\mathrm{ij}}^{\mathrm{SST,d}} = -2\nu_t \widetilde{S}_{\mathrm{ij}} + R_{\mathrm{ij}} \tag{3.79}$$

This structure implies that these particular models yield the entire subgrid stress tensor, as opposed to common models that target only its deviatoric part. Because of its relation to the turbulent viscosity, the subgrid turbulent kinetic energy k_{sgs} was the choice of Abe and Kobayashi to construct the unknown terms in this equation at the cost of incorporating a corresponding transport equation. Klein suggested a possible elimination of the need for a transport equation for the subgrid turbulent kinetic energy k_{sgs}, which drastically reduces the computational effort and thus provides an attractive reformulation of Kobayashi's model.

Work by Sagaut [244] and Klein [138] showed that it is a reasonable assumption to express the subgrid kinetic energy using the isotropic part of the subgrid stress $k_{\mathrm{sgs}} \approx \tau_{\mathrm{kk}}^{\mathrm{sgs,SST}}/2$.

Due to the nature of its development, the resulting model is not a stand-alone model, but rather can be seen as an extension of existing scale-similarity type models. Initially, Klein's models were proposed and analyzed in combination with Clark's model. The equations read:

$$\tau_{\mathrm{ij}}^{\mathrm{sgs}} = \frac{-\tau_{\mathrm{ab}}^{\mathrm{SST}}\widetilde{S}_{\mathrm{ab}} + |-\tau_{\mathrm{ab}}^{\mathrm{SST}}\widetilde{S}_{\mathrm{ab}}|}{-\tau_{\mathrm{ab}}^{\mathrm{SST}}\widetilde{S}_{\mathrm{ab}}}\tau_{\mathrm{ij}}^{\mathrm{SST}} + \left(\tau_{\mathrm{ij}}^{\mathrm{SST}} + \frac{-\tau_{\mathrm{ab}}^{\mathrm{SST}}\widetilde{S}_{\mathrm{ab}}}{\widetilde{S}_{\mathrm{ab}}\ \widetilde{S}_{\mathrm{ab}}}\widetilde{S}_{\mathrm{ij}}\right) \tag{3.80}$$

$$\tau_{\mathrm{j}}^{\mathrm{sgs}} = \frac{-\tau_{\mathrm{a}}^{\mathrm{SST}}\partial\widetilde{\phi}/\partial x_{\mathrm{a}} + |-\tau_{\mathrm{a}}^{\mathrm{SST}}\partial\widetilde{\phi}/\partial x_{\mathrm{a}}|}{-\tau_{\mathrm{a}}^{\mathrm{SST}}\partial\widetilde{\phi}/\partial x_{\mathrm{a}}}\tau_{\mathrm{j}}^{\mathrm{SST}} + \left(\tau_{\mathrm{j}}^{\mathrm{SST}} + \frac{-\tau_{\mathrm{a}}^{\mathrm{SST}}\partial\widetilde{\phi}/\partial x_{\mathrm{a}}}{\left(\partial\widetilde{\phi}/\partial x_{\mathrm{a}}\right)^2}\partial\widetilde{\phi}/\partial x_{\mathrm{j}}\right) \tag{3.81}$$

It becomes evident that the pre-factor in the first summand can only take values of 0 or 2. The second term was found to represent only the subgrid force and thus, is considered to be of no particular relevance. The simplified model reads:

$$\tau_{\mathrm{ij}}^{\mathrm{sgs}} = \tau_{\mathrm{ij}}^{\mathrm{SST}} - \max\left(\frac{\tau_{\mathrm{ab}}^{\mathrm{SST}}\tilde{S}_{\mathrm{ab}}}{\tilde{S}_{\mathrm{ab}}\ \tilde{S}_{\mathrm{ab}}}, 0\right)\tilde{S}_{\mathrm{ij}} \tag{3.82}$$

$$\tau_{\mathrm{j}}^{\mathrm{sgs}} = \tau_{\mathrm{j}}^{\mathrm{SST}} - \max\left(\frac{\tau_{\mathrm{a}}^{\mathrm{SST}}\partial\tilde{\phi}/\partial x_{\mathrm{a}}}{\left(\partial\tilde{\phi}/\partial x_{\mathrm{a}}\right)^2}, 0\right)\frac{\partial\tilde{\phi}}{\partial x_{\mathrm{j}}} \tag{3.83}$$

The stabilization mechanism of the model can be understood as follows. The central assumption is that instability is a consequence of backscattering rather than lack of dissipation. The model retains the properties of the $\tau_{\mathrm{ij}}^{\mathrm{SST}}$ baseline model in the case of forward scattering. In the case of backscattering, however, the baseline model $\tau_{\mathrm{ij}}^{\mathrm{SST}}$ is replaced by a projection onto an energy-transfer neutral tensor, which is the subgrid scale force. The interscale energy transfer expressed by $-\tau_{\mathrm{ij}}^{\mathrm{SST}}\widetilde{S}_{\mathrm{ij}}$, where its sign is an indicator of its direction – thus representing forward or backward scattering. The mechanism can be nicely illustrated in Eq. 3.82, where forward scattering is characterized by negative $\tau_{\mathrm{ij}}^{\mathrm{SST}}\widetilde{S}_{\mathrm{ij}}$ and thus yields the baseline scale similarity model. Positive $\tau_{\mathrm{ij}}^{\mathrm{SST}}\widetilde{S}_{\mathrm{ij}}$ indicate backward scattering and lead to an additional term to support the baseline model.

These models are a fundamental aspect of this work and will be elaborated further in Chapters 6 and 7.

3.5 Modern closure approaches

All of the approaches presented so far share a physical modeling philosophy. The presented models aim to model either the effects of suppressed turbulence or the energy cascade directly.

This modeling approach is sometimes referred to as classical LES subgrid modeling. However, many recent developments follow a purely mathematical basis.

An important mathematical approach is the *Approximate Deconvolution Model* (*ADM*) introduced by Stolz [271, 272], which approximates the deconvolution of a filtered quantity by repeated filtering. Another group of approaches are data-driven models. Data-driven models based on *Gene-Expression Programming* (typically *GEP* – or *GA* for *Genetic Algorithm*) methods assume a certain relationship between the data available within the LES and the unknown subgrid stresses. This relationship is improved iteratively, starting from a certain initial set of functions and parameters by generating new sets based on the combination of elements from the set given in the previous iteration [162, 226]. Therefore, GEP approaches are very suitable for in-the-loop application in LES. Another data-driven type of model that is typically not used in-the-loop are *Artificial Neural Networks* (*ANN*). ANN-based LES subgrid models feed on vast amounts of DNS data and then perform a fit to close the unknown subgrid stresses [199, 317, 246]. Such ANN need to be trained using a plethora of test cases to achieve a certain generality that makes them applicable to a-posteriori LES. Another important flavor of ANN are the *Physics Informed Neural Networks* (*PINN*), which can support the fitting performed by the ANN by physical laws, making the closure of the subgrid stresses more of a guided rather than a random guess [309, 74].

3.6 Remarks on subgrid modeling

An overview of different closures for the subgrid stresses is given. Various extensions and improvements worth mentioning exist, however, for the sake of brevity they cannot be listed here. The aim is to give an insight into the closures relevant for this work and to provide a basis for the contributions presented in this work.

The very fundamentals of LES and turbulence modeling were laid down. In theory, LES can be seen as an most optimal compromise between DNS and RANS. Especially for technical applications with high Reynolds numbers and large-scale unsteady characteristics, LES brings the tools for accurate simulation into the field. While after more than fifty years of research the theory of LES appears mature and the modeling approaches refined, several aspects remain unsolved and are summarized by Klein [132]:

- Use of explicit or implicit filtering procedure
- Improved subgrid modeling
- Suitable numerical discretization
- Transient boundary conditions
- Near wall treatment

- Simulation quality assessment
- Multiphysics problems
- Complex geometries

In fact, no LES procedure has established itself as standard and most of the questions posed are highly controversial within the scientific community. The relevance of each question varies from problem to problem and each case presents its own challenges and difficulties. A sobering truth was formulated by Klein [132] stating that LES will not reach the state of solving general technical problems in the near future. However, LES is a promising approach and should be applied to realistic problems while taking into account the uncertainty of the employed solver, as it will be further elaborated in this work.

3.7 Reynolds-Averaged Navier-Stokes Simulation

Although not being used in this work the very fundamentals of the Reynolds-Averaged Navier-Stokes Simulation shall be discussed. The basis for the RANS approach is the decomposition proposed by Reynolds, which separates turbulence into two terms of stationary and fluctuating nature. Given an arbitrary turbulent variable Φ, the decomposition reads:

$$\Phi = \overline{\Phi} + \Phi'' \tag{3.84}$$

Featuring the stationary term $\overline{\Phi}$ and the fluctuating term Φ''. For the sake of brevity, the bars $(\bar{\cdot})$ indicate averaging only within this section. The stationary term, by definition, can be obtained by time averaging the quantity Φ:

$$\overline{\Phi} = \lim_{T\to\infty} \frac{1}{T} \int_0^T \Phi(x_\mathrm{i}, t) dt \tag{3.85}$$

To obtain a stationary set of RANS equations the averaging interval is set to an infinitely long time of sampling. However, for processes where the process timescale is much larger than the turbulence timescale, a finite sampling time can be chosen and hence, allowing for the study of transient and non-stationary physical processes. In this case, one speaks of *Unsteady Reynolds Averaged Navier-Stokes* (*URANS*), which is commonly employed for the transient technical systems such as piston engines or turbomachinery. It is a requirement of the applicability of URANS that the turbulent timescales are short in comparison to the unsteady timescale.

The equations for the RANS simulation are obtained by inserting in the Reynolds decomposition from Eq. 3.84 into the Navier-Stokes equations and then applying the averaging. Two rules apply when performing the averaging that will simplify the derivation of the set

of RANS equations. The first one states that averaging a quantity that has already been averaged again yields the average itself:

$$\overline{\overline{\Phi}} = \lim_{T\to\infty} \frac{1}{T} \int_0^T \overline{\Phi}(x_\mathrm{i}, t) dt = \langle \Phi \rangle \lim_{T\to\infty} \frac{1}{T} \int_0^T dt = \overline{\Phi} \tag{3.86}$$

As the already averaged value $\overline{\Phi}$ is no longer a function of time, it does not need to be considered for time integration, hence, leading to this simple identity. The second rule can be derived from the result of the first rule. The rule dictates that averaging the fluctuation part will yield a signal of zero, which can be shown by inserting the identity from Eq. 3.84 into the filter operation given in Eq. 3.85 and then applying Eq. 3.86:

$$\overline{\Phi}'' = \overline{\Phi} - \overline{\overline{\Phi}} = \overline{\Phi} - \overline{\Phi} = 0 \tag{3.87}$$

Given the previous findings for a general quantity Φ, it is now of interest to apply them within the desired equations. It has to be noted, however, that the quantity Φ always appears in the equations in its specific form as $\rho\Phi$, which adds complexity to the averaging procedure in the case of a variable density flow. It is of interest to obtain the solution of the variable Φ uncoupled from the density. The most common strategy to resolve this coupling is the so-called Favre density weighted averaging:

$$\tilde{\Phi} = \frac{\overline{\rho\Phi}}{\overline{\rho}} \tag{3.88}$$

And thus transports the density-weighted quantity $\tilde{\Phi}$ within the corresponding equation. This averaging is applied only within the definition of the variable in the transport equations and no additional processing is performed after their respective solution. Having established the mathematical framework necessary for the derivation of the source-free RANS equations, it is these equations that will be given here without step-by-step instructions. However, in order to stay within the scope of this work, only the conservation of mass and momentum will be presented:

$$\frac{\partial \overline{\rho}}{\partial t} + \frac{\partial \overline{\rho}\tilde{u}_\mathrm{j}}{\partial x_\mathrm{j}} = 0 \tag{3.89}$$

$$\frac{\partial \overline{\rho}\tilde{u}_\mathrm{i}}{\partial t} + \frac{\partial \overline{\rho}\tilde{u}_\mathrm{i}\tilde{u}_\mathrm{j}}{\partial x_\mathrm{j}} = -\frac{\partial \overline{p}}{\partial x_\mathrm{i}} + \frac{\partial}{\partial x_\mathrm{j}} \left(\mu \left(\frac{\partial \tilde{u}_\mathrm{i}}{\partial x_\mathrm{j}} + \frac{\partial \tilde{u}_\mathrm{j}}{\partial x_\mathrm{i}} \right) - \frac{2}{3}\mu \frac{\partial \tilde{u}_\mathrm{k}}{\partial x_\mathrm{k}} \delta_\mathrm{ij} \right) + \overline{\rho} g_\mathrm{i} - \frac{\partial \widetilde{\overline{\rho} u_\mathrm{i}'' u_\mathrm{j}''}}{\partial x_\mathrm{j}} \tag{3.90}$$

It can be seen that the conservation of mass given in Eq. 3.89 follows the same structure as its non-averaged counterpart from Eq. 2.2.1. The conservation of momentum, however, features an additional term with a structure similar to the convective flux, containing the turbulent fluctuations of the velocity field. This term is also referred to as the *Reynolds* stresses and is a direct result of the averaging procedure. Applying the average to the equations removes

all physical – and mathematical – information about the turbulence, leaving the equations with only the information about the stationary solution. To still include the influence of the turbulence on the averaged solution, the equations hold the Reynolds stresses as the solution of the original NSE is partially suppressed. This information remains to be closed by the Reynolds stresses and their respective models. Modeling the Reynolds stresses appears to be more challenging than LES modeling as RANS suppresses not only the smallest scales but the entire energy spectrum. A suitable RANS model therefore provides information on all scales within the turbulent flow, which is difficult to achieve.

The most commonly used turbulence model for free turbulence within the RANS framework is the k-ϵ model proposed by Jones and Launder [114]. The model is based on two additional transport equations – hence, being referred to as a two-equations model – for the turbulent kinetic energy k and the turbulent dissipation rate ϵ. The model produces a turbulent viscosity μ_t based on the turbulent kinetic energy and dissipation rate obtained from the transport equations. This turbulent viscosity is then used to calculate the Reynolds stresses following the Boussinesq hypothesis introduced in Sec. 3.2.

However, since it is calibrated for isotropic turbulence, the k-ϵ model has shortcomings in flows with anisotropy, which may be introduced by walls or swirling flow. A popular approach to problems involving these is the related k-ω model found independently by Kolmogorov [146] and Saffman [243]. Again, this model features two equations, this time including the turbulent kinetic energy k and the specific rate of dissipation ω.

In order to combine the advantages of both models, a blending of the k-ϵ and the k-ω model, also known as the SST-model, was proposed [179], leading to an overall good performance in the absence and presence of walls and thus earning the status of one of the most popular RANS models.

Overall RANS is typically considered to be the least expensive paradigm for turbulence simulation. However, its robustness and efficiency have made it very popular, especially for problems that require expensive additional modeling. This makes RANS, in its current state, the number one choice for turbulence problems in industry. Although computational power is increasing, RANS is expected to still maintain this status for the near future.

4 Treatment of reacting flows

The mathematical description of chemical reactions within a flow forms a common application in CFD. In particular, the modeling of exothermic reactions is relevant to this work. Since this work does not investigate the performance of these models, but rather their interaction with numerical methods and other modeling philosophies, the very basics of the reaction models used in this work are summarized.

4.1 Combustion as a reacting flow

Combustion is one of the most prominent reacting engineering flows and is of particular relevance to this work. In particular, combustion is a chain reaction characterized by the release of heat and light. To start this chain reaction, a mixture of a fuel and an oxidizer is required. The composition of this mixture is of crucial importance for the resulting combustion. Of particular relevance are the species that form the mixture as well as their relative amounts present in the mixture, as they control whether combustion of the mixture can occur and under what thermochemical conditions it will occur.

In the literature, two modes of combustion are typically distinguished on the basis of mixture formation: the *premixed* and the *non-premixed* (or diffusive) combustion. A visualization of a generic example for both modes can be found in Fig. 4.1. In premixed combustion the educts – fuel and oxidizer – are mixed prior to entering the reaction zone. The resulting flame can be considered as an interface between the mixture and the products of combustion. This flame propagates through a quiescent mixture at a characteristic velocity s_l, referred to as the laminar flame speed. As this velocity is driven solely by the chemical reactions, its value only depends on the mixture temperature, composition and pressure. Non-premixed combustion is characterized by the fuel and oxidizer entering the reaction zone separately and hence, mixture is formed directly at the flame.

Technical applications, however, typically operate under conditions ranging between premixed and non-premixed combustion modes. This condition is also referred to as *partially premixed* combustion. Flames of this combustion mode involve a mixing process between the fuel and the oxidizer, as these are commonly brought together inside the combustion

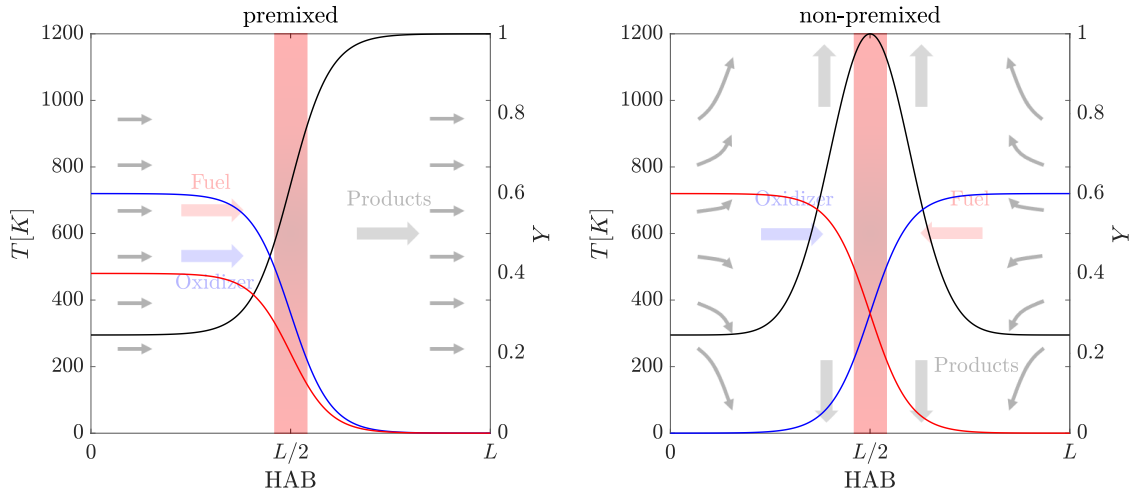

Figure 4.1 Generic example for the temperature, fuel and oxidizer mass-fraction profiles for the case of a one-dimensional premixed and non-premixed flame.

chamber for safety reasons. The completeness of the mixture formation varies spatially, thus, leaving premixed and non-premixed regions within the domain.

4.2 Mathematical description of reactive mixtures

The fundamentals of gas flows and thermodynamics given in Chp. 2 are now extended to describe reactive mixtures of different species. Conservation of species is introduced to take into account for the transport, consumption and generation of each species present in a reacting flow. The conservation of species states, that no mass contributed by the different species must be lost. Opposed to the previous transport equations, the conservation of species consists of a set of N_s equations, where each equation represents one species. The sum of all species transport equations employing the definition of the mass fractions (Eq. 2.11) yields the conservation of mass (Eq. 2.2). The transport equation for the species α reads:

$$\frac{\partial \rho Y_\alpha}{\partial t} + \frac{\partial \rho Y_\alpha u_\mathrm{j}}{\partial x_\mathrm{j}} + \frac{\partial \rho Y_\alpha V_{\mathrm{j},\alpha}}{\partial x_\mathrm{j}} = \dot{\omega}_\alpha + \dot{\omega}_{\rho Y_\alpha} \tag{4.1}$$

With α ranging between 1 and N_s, $V_{\mathrm{j},\alpha}$ being the diffusion velocity (relative to the flow velocity u_j) in the direction j of the species α due to interdiffusion and $\dot{\omega}_\alpha$ being the chemical source term describing the consumption or production of the species α due to chemical reactions. The term $\dot{\omega}_{\rho Y_\alpha}$ takes into account the generation or removal of chemical species apart from reactions, which can be, for instance, evaporation of droplets in the gas-phase.

4.2.1 Diffusion of chemical species

As introduced earlier, diffusion is a macroscopic summary of the microscopic motion of molecules. When considering the diffusion of chemical species, a complete description of diffusion requires to take into account all of the drivers of this microscopic motion. In particular, these can be gradients of concentration, temperature and pressure, as well as volume forces that act differently on the individual species. On the macroscopic scale, this motion is represented by the diffusion velocity. The diffusion velocity $V_{\mathrm{j},\alpha}$ of a species α is typically related to the aforementioned gradients – in the direction j – together with a constant which characterizes the mobility of the species α within the whole ensemble. This constant is typically referred to as the diffusion coefficient. The true nature of diffusion requires the consideration of the pairwise diffusion of a mixture's component α within another component β. The diffusion velocities are obtained by implicitly solving the following system of equations, which can be obtained from the conservation of momentum of the mixture's molecules after collision (for the full derivation the reader is referred to Williams [303]):

$$\frac{\partial X_\alpha}{\partial x_\mathrm{j}} = \sum_{\beta=1}^{N_\mathrm{S}} \frac{X_\alpha X_\beta}{D_{\alpha,\beta}}(V_\beta - V_\alpha) + (Y_\alpha - X_\alpha)\frac{1}{p}\frac{\partial p}{\partial x_\mathrm{j}} + \frac{\rho}{p}\sum_{\beta=1}^{N_\mathrm{S}} Y_\alpha Y_\beta (f_\alpha - f_\beta) \tag{4.2}$$

Where $D_{\alpha,\beta}$ is the binary diffusion coefficient – which is typically obtained from kinetic gas theory using the Chapman-Enskog theorem [35] – and f_α as well as f_β refer to external forces acting on the species. Considering the mixture to consist of N_s species, it becomes evident that a total of $N_\mathrm{s} \times N_\mathrm{s}$ equations has to be solved at each point in time. In fact, most computational applications avoid solving these equations [64, 151].

The presumably most common choice for the calculation of the species diffusion – especially in the field of combustion – is Fick's law of diffusion. Although the original formulation of Fick was found experimentally, it can be fully derived from Eq. 4.2 for the case of a binary mixture where the body forces do not differ for all species and the local pressure gradients are assumed to be small:

$$Y_\alpha V_{\mathrm{j},\alpha} = -D_{\alpha\beta}\frac{\partial Y_\alpha}{\partial x_\mathrm{j}} \tag{4.3}$$

Where $D_{\alpha\beta}$ refers to the diffusion coefficient characterizing the whole mixture consisting of the species α and β.

Typical mixtures, however, are of more complex composition and thus violate the binary-mixture simplification. As the solution of the full equations system above is not an option in the most cases, the solution matrix produced by this system can be approximated to the first-order by following Hirschfelder and Curtiss [101]. Instead of binary diffusion coefficients, this approach considers mixture-averaged diffusion coefficients D_α, which describe the diffusion

of a species α into the remaining components of the mixture:

$$Y_\alpha V_{\mathrm{j},\alpha} = -D_\alpha \frac{\partial Y_\alpha}{\partial x_\mathrm{j}} + Y_\alpha V_{\mathrm{c,j}} \tag{4.4}$$

Where the mixture-averaged diffusion coefficient D_α of the species α can be computed as:

$$\frac{1}{D_\alpha} = \sum_{\beta \neq \alpha}^{N_\mathrm{S}} \frac{X_\beta}{D_{\alpha\beta}} + \frac{X_\alpha}{1 - Y_\alpha} \sum_{\beta \neq \alpha}^{N_\mathrm{S}} \frac{Y_\beta}{D_{\alpha\beta}}. \tag{4.5}$$

However, the summation of all diffusive fluxes must yield zero to maintain continuity. A correction velocity $V_{\mathrm{c,j}}$ must be included to enforce continuity:

$$V_{\mathrm{c,j}} = -\sum_{\alpha=1}^{N_\mathrm{S}} Y_\alpha V_{\mathrm{j},\alpha} \tag{4.6}$$

Following Poinsot [212], it is a common approach to use the correction velocity and additionally solve the equations of only $N_\mathrm{s} - 1$ species to enforce continuity. Following the conservation of all species, the mass fraction of the remaining species must obey:

$$Y_{N_\mathrm{s}} = 1 - \sum_{\alpha=1}^{N_\mathrm{S}-1} Y_\alpha \tag{4.7}$$

It is recommended to choose $\alpha = N_\mathrm{s}$ as a non-sensitive species, which requires comparably high mass fractions. As it is desirable for $\alpha = N_\mathrm{s}$ to be chemically inert a common choice for this species is nitrogen, which also yields high mass fractions for chemical processes involving air.

A strong yet popular simplification is the assumption of a universal diffusion coefficient D for all species within the given problem. This assumption must be made with respect to the species present in the given problem as the diffusivity of a species is strongly dependent on its weight. While problems involving hydrocarbons such as methane can be treated with rather little concern using this assumption, species such as hydrogen are small and tend to diffuse much faster, and heavy hydrocarbons such as octane diffusive much slower than the rest of typical mixtures. The diffusion behavior of a species is often characterized using the Lewis number. By definition, the Lewis number gives the ratio of the thermal diffusivity to the mass diffusivity within a flow, which implies how fast heat is transported through a flow relative to the diffusion of chemical species. It is evident that the Lewis number hence, is of critical importance in the field of combustion where the flame is a result of heat and reactant diffusion through the flow [161]. The Lewis number is calculated as:

$$\mathrm{Le} = \frac{\kappa}{\rho D c_\mathrm{p}} \tag{4.8}$$

Where the isobaric specific heat and the heat conductivity are typically tabulated or calculated employing polynomials as mentioned in Sec. 2.3.1. In fact, it is common practice to extract the diffusion coefficient – either globally or for each species – using the Lewis number. Especially the assumption of a unity Lewis number for all species is a popular simplification, which is also known as the unity Lewis number assumption.

4.2.2 Closure of the chemical source term

The chemical source term $\dot{\omega}_\alpha$ is the result of chemical reactions within the flow and couples the species transport with the reaction kinetics and therefore yields the consumption or production of the species α by chemical reactions. The full chemical source term is a function of the chemical and thermodynamic state and as such can be challenging to assess. The full chemical conversion from educt to product species does not occur within a single step but in an ensemble of reactions between a plethora of species which may form during this process. In literature, the full conversion from educt to product species is referred to as a global reaction, while the different reactions ultimately leading to the formation of the product species are referred to as *elementary* reactions. The step-by-step sequence of chemical reactions leading to the conversion from educt to product species is called *reaction mechanism*. Typically a reaction then traverses through the following phases:

- Initiation: chemical bond breaks (e.g. due to heating or absorption of light) and creates a chain carrier molecule
- Progression: a chain carrier molecule is involved in a chemical reaction
  - Propagation: a chain carrier forms another chain carrier
  - Branching: a chain carrier forms multiple chain carriers
  - Retardation: a chain carrier does not form another chain carrier
- Termination: all chain carriers are consumed by reaction or by an external influence

A chemical reaction can be written down in the following form:

$$\sum_{\beta=1}^{N_\mathrm{S}} \nu'_{\beta,\mathrm{r}} \mathcal{X}_\beta \rightleftharpoons \sum_{\beta=1}^{N_\mathrm{S}} \nu''_{\beta,\mathrm{r}} \mathcal{X}_\beta \tag{4.9}$$

Where the reaction equations r from 1 to N_R balance the molar stoichiometric coefficients $\nu'_{\beta,\mathrm{r}}$ and $\nu''_{\beta,\mathrm{r}}$ – with $'$ indicating the educt and $''$ indicating the product species – of the species β with the chemical formula $\mathcal{X}_\beta$. It shall be noted that the indexing of species is written using β as all following considerations must be made for the calculation of each source term $\dot{\omega}_\alpha$.

A chemical reaction is a reversible thermodynamic process. Every chemical reaction features a forward and a reverse direction. All chemical reactions are driven by the urge of

reaching the chemical equilibrium and this equilibrium is reached when the forward reaction proceeds at the same rate as the reverse reaction. The rate of a reaction is quantified by the reaction rate q_r, which is typically calculated using the law of mass action, but can depend on the nature of the given reaction. The law of mass action reads:

$$q_\mathrm{r} = k_\mathrm{f,r} \prod_{\beta=1}^{N_\mathrm{S}} [\mathcal{X}_\beta]^{\nu'_{\beta r}} - k_\mathrm{b,r} \prod_{\beta=1}^{N_\mathrm{S}} [\mathcal{X}_\beta]^{\nu''_{\beta r}} \tag{4.10}$$

Where concentration of a species β can be obtained from its respective mass fraction and its molar weight:

$$[\mathcal{X}_\beta] = Y_\beta \frac{\rho}{W_\beta} \tag{4.11}$$

As the true rate of a reaction is the result of a counterplay between forward and backward reaction, two reaction rate constants $k_\mathrm{f,r}$ and $k_\mathrm{b,r}$ are required to characterize the respective directions. These constants are temperature dependent and the forward reaction rate constant can be obtained from the Arrhenius law [12, 13]:

$$k_\mathrm{f}(T) = A T^b \exp\left(-\frac{E_\mathrm{a}}{R_\mathrm{m}\, T}\right) \tag{4.12}$$

This law is an empirical relationship between the temperature and the reaction rate constant found by Arrhenius, who also provided a physical interpretation [45]. Strictly speaking, the herein introduced formulation is the so-called modified Arrhenius law, which is a more accurate description of this empirical relationship. The product AT^b is also referred to as the collision frequency, describing the total number of collisions between the molecules in the gas. These collisions are necessary for a reaction to take place. The pre-exponential factor A and the exponent b are characteristic of each specific chemical reaction. In gas kinetics, the temperature is defined as a measure of the kinetic energy of the molecules forming the gas. Multiplication by the universal gas constant – which is the molar equivalent of the Boltzmann constant, linking kinetic energy and temperature within a gas – yields the kinetic energy of the molecules $R_\mathrm{m}T$. With E_a describing the activation energy of a reaction, the ratio within the exponential function indicates whether the molecules can overcome the potential barrier that maintains the stable state of a molecule. Thus, the structure of the equation can be explained: AT^b is the number of collisions per time and $\exp\left(-E_\mathrm{a}/R_\mathrm{m}\, T\right)$ is the probability that any given collision will result in a reaction. It can be concluded that the reaction rate constant is the number of collisions that result in a reaction per time.

The backward reaction rate constant is linked to the forward reaction rate constant by the equilibrium constant:

$$K_\mathrm{C} = \frac{k_\mathrm{f}}{k_\mathrm{b}} \tag{4.13}$$

The equilibrium constant is obtained from the thermodynamic activities of the species present in the reaction equation.

This procedure is used unchanged for the treatment of *elementary* reactions. Elementary reactions are the first type of reactions that consist of a pair of reactants forming one or more products. Some reactions are characterized by an imbalance between the energies of the reactants and the products. A so-called third-body, which is potentially any species present in the gas but not involved in that particular reaction, serves as a compensation for this imbalance. These reactions are called *third-body* reactions. The respective reaction rate is simply calculated as for an elementary reaction and is then multiplied by the concentration of the third-body species. The last category of reactions are the *pressure-dependent* reactions. This type of reaction changes its behavior as a function of the pressure and typically requires a high-pressure and a low-pressure formulation of the reaction. This may differ in that the reaction at the one pressure-level requires a third-body in the reaction equation, while the reaction at the other pressure does not. The calculation of the corresponding reaction rate constant requires additional modeling and the reader is referred to the works of Lindemann [166], Gilbert [84] and Stewart [268] for further insight.

When the reaction rate is known, the chemical source term of the species α can be calculated considering all reactions r involving α:

$$\dot{\omega}_\alpha = W_\alpha \sum_{r=1}^{N_\mathrm{R}} \left(\nu''_{\alpha,\mathrm{r}} - \nu'_{\alpha,\mathrm{r}} \right) q_\mathrm{r} \tag{4.14}$$

4.3 Coupling of chemical reactions with flow solvers

Chemical reactions take place on atomic length-scales that are by a factor of more than a one-thousand smaller than the macroscopic length-scales present in CFD. It becomes evident that these processes cannot be resolved with current CFD techniques and therefore need to be modeled. Chemical reactions include a cascade of various reactions involving a plethora of chemical species with different lifetimes, further complicating the ability to directly incorporate these reactions in-situ into a simulation. Several approaches exist to cast the reaction chemistry into models that are digestible for a simulation.

The first group of approaches calculates the chemistry in-situ, however, with the strongly simplification of assuming single-step chemistry. Single-step chemistry reduces the entire reaction mechanism from a manifold to a single *global* conversion step from educts E to products P:

$$E \xrightarrow{k} P \tag{4.15}$$

Where the rate k of the global reaction is obtained from resolved data within the simulation or from additional models. The reduction of a reaction mechanism to a global reaction is a harsh simplification and hence, the accuracy of this modeling philosophy is very limited.

Despite their simplicity, single-step models are popular due to their low cost and numerical robustness.

The second group of models outsources the calculation of chemistry to the preprocessing and no chemical reaction is calculated during the simulation run. Instead, the chemical and thermodynamic variables of state calculated from all possible chemical reactions are arranged in the form of a look-up table. Based on certain indicator variables that are transported in the simulation, these tabulated quantities are then read and assigned during the simulation run. This allows for an arbitrary degree of detail in the chemical model, but results in a tremendous preprocessing effort to generate the look-up tables. Henceforth, the independent variables used to access the look-up table must be carefully chosen in order to reduce the complexity of the table and the simulation cost due to the additional transported variables.

The third group, describing chemistry in CFD, aims at the direct calculation of the chemical kinetics within the simulation. It was discussed earlier that this is not possible in a microscopic way and therefore the kinetics are calculated in a macroscopic framework using species mass fractions. It becomes evident that these approaches are highly expensive and are typically used only with reduced reaction mechanisms. Reduced mechanisms focus on the most important pathways within a full reaction mechanism and thus retain chemical significance at the cost of observability of the behavior of minor species. The main costs arise from the need for a separate additional transport equation to be solved for each chemical species and from the solution of the kinetic equations, which scale with the number of reactions present in the mechanism.

Due to its employment in the present work, one particular method of the second group will be explained in more detail.

4.4 Flamelet generated manifolds

The concept of Flamelet Generated Manifolds (*FGM*) goes back to van Oijen and de Goey [286], and aims at the description of turbulent flames. The very basis of FGM is the assumption that any three-dimensional flame may be considered as an ensemble of one-dimensional flames. These one-dimensional flames – also referred to as *flamelets* – are precomputed and the thermo-chemical variables obtained from their solution are stored in a low-dimensional table. The FGM approach can be formulated for *Premixed* (*PFGM*) and *Non-Premixed* (*NPFGM*) flame modes, and its application to partially premixed flames is still widely discussed. In particular, the works of Mueller [186], Noselov et al. [196] and Fiorina et al. [70] should be mentioned, which paradoxically state that no clear statements can be made and that the applicability of PFGM or NPFGM to partially premixed combustion is highly case dependent.

Flamelets are freely propagating (premixed) or counterflow (non-premixed) flames described using the one-dimensional form of the conservation laws as described in Chp. 2 for

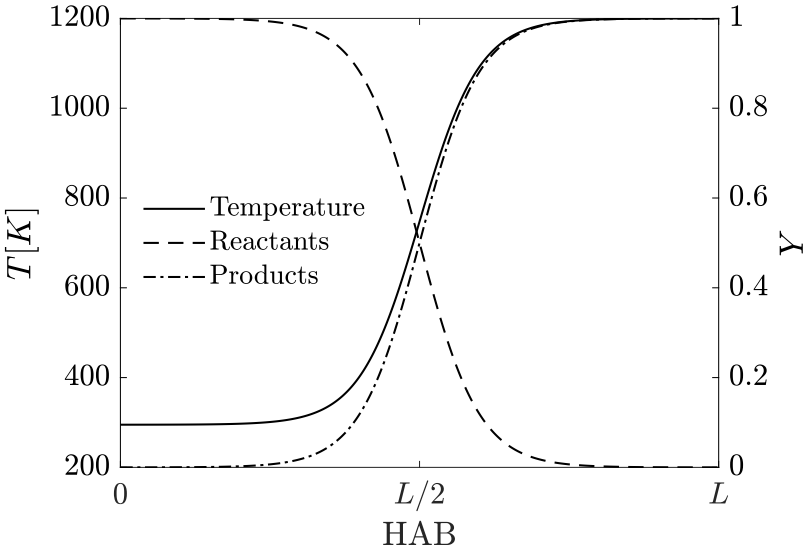

Figure 4.2 Generic example for the temperature, reactants and product mass fractions with the height above the burner (HAB) obtained from a one-dimensional freely propagation flame.

a steady state. Their boundaries are closed by a Dirichlet-type boundary condition on the unburnt side to ensure the inflow of fresh mixture and a von-Neumann-type boundary condition on the burnt side. A generic example is shown in Fig. 4.2. Each flamelet describes the conversion of a specific mixture from educts to products. The degree of conversion is typically described by a progress variable Y_C, whose definition is not unique. A plethora of definitions for the progress variable exists and can include, e.g., ratios of fuel and oxidizer mass fractions, weighted sums of element mass fractions or ratios of temperatures – and it is common practice to choose its definition by experience [107, 194, 223]. It has to be noted, that this progress variable does not necessarily require an upper bound of unity. As the progress variable is transported, it is normalized within the tabulation as $C = (Y_\mathrm{C} - Y_\mathrm{C}^{\min})/(Y_\mathrm{C}^{\max} - Y_\mathrm{C}^{\min})$. The flamelet itself is described by the mixture of fuel and oxidizer which quantifies their respective stoichiometries. These ultimately determine the heat release and thus, the evolution of the thermo-chemical variables through the flamelet. Again, several definitions for the mixture fraction Z exist and a common choice in the context of carbohydrate flames is the definition proposed by Bilger [22]. In addition, other variables may be added to access the table. These may include, e.g., multiple mixture fractions as in the case of multi-phase flows [177] or variances of the progress variable and mixture fraction [298, 38].

The approach involving a progress variable Y_C and a mixture fraction Z is a common choice – in particular in single-phase flows – and requires the solution of their respective

transport equations, in the DNS-case reading:

$$\frac{\partial \rho Y_{\mathrm{C}}}{\partial t} + \frac{\partial \rho Y_{\mathrm{C}} u_{\mathrm{j}}}{\partial x_{\mathrm{j}}} = \frac{\partial}{\partial x_{\mathrm{j}}} \left(\rho D \frac{\partial Y_{\mathrm{C}}}{\partial x_{\mathrm{j}}} \right) + \dot{\omega}_C \tag{4.16}$$

$$\frac{\partial \rho Z}{\partial t} + \frac{\partial \rho Z u_{\mathrm{j}}}{\partial x_{\mathrm{j}}} = \frac{\partial}{\partial x_{\mathrm{j}}} \left(\rho D \frac{\partial Z}{\partial x_{\mathrm{j}}} \right) \tag{4.17}$$

The chemical reactions induced in the flow by the flame are incorporated in the transport equation by the reaction source-term $\dot{\omega}_C$. The corresponding value is obtained from the table.

The generation of tables with thermo-chemical data is performed by solving the previously mentioned equations for flamelets. While this is possible using custom-built frameworks, a toolkit worth mentioning and of particular importance for this work is the Cantera library developed by Goodwin [86].

5 Numerical methods

The previous chapter discussed the mathematical foundations of the key physical phenomena. To accomplish this, computational fluid dynamics aims to predict flow phenomena using complex equations, which are highly nonlinear and have no analytical solutions for non-trivial cases. Numerical methods provide the means to translate these equations into an algorithm and extract information from physical laws. Therefore, the choice of numerical method is critical in determining the outcome of a CFD simulation. This section discusses basic and advanced numerical tools and their impact on the simulation performance.

5.1 Discretization

Computational fluid dynamics aims to solve problems of flow physics using computers. However, computers can only handle a finite amount of data, which limits the information that can be processed when solving a CFD problem. Therefore, the information stored in the equations defined in a continuous time and space domain has to be extracted on a discrete domain. Several approaches exist and the most relevant spatial and temporal discretizations are presented below. Examples are given using the general transport equation as introduced in Eq. 2.1. Some of the most important advances in this field were made by Euler [65], who laid the foundation for modern computational mathematics, although he was far from having access to these computational tools in his time.

5.1.1 Spatial discretization

Spatial discretization is essential to extract space-dependent information from the equations describing the given problem. There are different strategies and the most prominent ones are the *Finite Difference Method* (*FDM*), the *Finite Element Method* (*FEM*) and the *Finite Volume Method* (*FVM*). Within this work, the FVM is of great importance as it is suitable for problems based on conservation laws and therefore will be described in more detail.

The Finite Volume Method decomposes a physical domain into a discrete set of volumes of finite size, called *Control Volumes* (*CV*). The conservation laws describing the given problem are then solved for each individual CV. The center coordinates of each CV are mapped onto a data structure called a mesh. FVM relies heavily on the center-point rule, which assumes

that the volume-averaged value of a conserved quantity is representative of the distribution of that quantity within the CV and is located at the center of that CV [68]. The mathematical application of FVM will be demonstrated for the case of conservation of a general quantity. The conservation law is repeated for convenience:

$$\frac{\partial \rho\phi}{\partial t} + \frac{\partial \rho u_\mathrm{j}\phi}{\partial x_\mathrm{j}} = \frac{\partial}{\partial x_\mathrm{j}}\left(D_\phi \frac{\partial \phi}{\partial x_\mathrm{j}}\right) + \dot{\Gamma}_\phi \tag{5.1}$$

The first step in FVM is to integrate this equation over the CV of the volume V:

$$\iiint\limits_V \frac{\partial \rho\phi}{\partial t} dV + \iiint\limits_V \frac{\partial \rho u_\mathrm{j}\phi}{\partial x_\mathrm{j}} dV = \iiint\limits_V \frac{\partial}{\partial x_\mathrm{j}}\left(D_\phi \frac{\partial \phi}{\partial x_\mathrm{j}}\right) dV + \iiint\limits_V \dot{\Gamma}_\phi dV \tag{5.2}$$

To reduce the mathematical effort, the Gauss theorem can be used to relate the divergence in a closed volume V to a flux of the vector field through the closed surface S of the respective volume. The Gauss divergence theorem reads:

$$\iiint\limits_V \frac{\partial f_\mathrm{j}}{\partial x_\mathrm{j}} dV = \iint\limits_S f_\mathrm{j} n_\mathrm{j} dS \tag{5.3}$$

With the vector field f_j and the surface normal vector n_j. The theorem is used to simplify the convective and diffusive contributions in this transport equation:

$$\iiint\limits_V \frac{\partial \rho\phi}{\partial t} dV + \iint\limits_S \rho u_\mathrm{j}\phi n_\mathrm{j} dS = \iint\limits_S \left(D_\phi \frac{\partial \phi}{\partial x_\mathrm{j}}\right) n_\mathrm{j} dS + \iiint\limits_V \dot{\Gamma}_\phi dV \tag{5.4}$$

Applying the rule of Schwarz allows for alternating the order of integration and spatial derivative:

$$\frac{\partial}{\partial t}\iiint\limits_V \partial\rho\phi dV + \iint\limits_S \rho u_\mathrm{j}\phi n_\mathrm{j} dS = \iint\limits_S \left(D_\phi \frac{\partial \phi}{\partial x_\mathrm{j}}\right) n_\mathrm{j} dS + \iiint\limits_V \dot{\Gamma}_\phi dV \tag{5.5}$$

The design of the mesh typically depends on the solver used and is usually composed of cuboids, tetrahedrons, or hexahedrons in the three-dimensional case. Each CV must not overlap with neighboring CVs. Two types of meshes are distinguished in the literature: structured and unstructured meshes. Structured meshes have a repetitive topology and its CV are positioned in a homogeneous grid so that each CV can be indicated by indices. The advantages of structured meshes are the unambiguous indication of cells, lower memory requirements due to the absence of identification tables, more accurate results if the CV align well with the flow, and easy implementation of all numerical algorithms. Unstructured meshes, on the other hand, are a tessellation of simple geometric shapes in an irregular pattern. The mesh is not periodic and cannot be easily referenced. The unstructured approach allows

extremely fast generation of meshes even for complex geometries, which can even be locally refined without further drawbacks.

This work relies on structured cubic-equidistant meshes only and the CV indication is visualized in Fig. 5.1. The basis for each presented numerical stencil is the cell center (C),

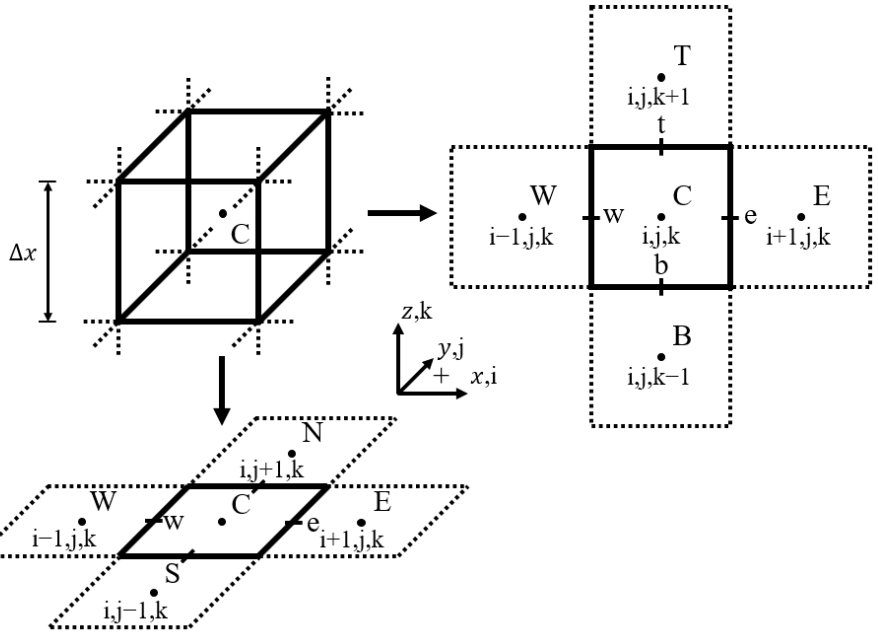

Figure 5.1 Indexing and nomenclature on a cubic equidistant grid in three dimensions.

thereby, following the coordinate system, the cells in the positive x, y and z directions are referred to as the eastern (E; i+1,j,k), northern (N; i,j+1,k) and top (T; i,j,k+1) neighboring cells and in the negative directions as the western (W; i-1,j,k), southern (S; i,j-1,k) and bottom (B; i,j,k-1) cells respectively. The corresponding cell interfaces are referenced by the same lowercase letters for the eastern (e; i+1/2,j,k), western (w; i-1/2,j,k), northern (n; i,j+1/2,k), southern (s; i,j-1/2,k), top (t; i,j,k+1/2) and bottom (b; i,j,k-1/2) cells.

The treatment of the volume and surface integrals is greatly simplified by the midpoint rule, e.g. the volume integral over the cell C is approximated as:

$$\iiint_{V_\mathrm{C}} \phi dV \approx \phi_\mathrm{C} V \tag{5.6}$$

And the surface integral over the interface e between C and E respectively as:

$$\iint_{S_\mathrm{e}} \phi dS \approx \phi_\mathrm{e} A \tag{5.7}$$

Considering the equidistant cubic mesh used in this study, the cell volume and surface area can be calculated as $V = \Delta x^3$ and $A = \Delta x^2$. Thus, the fully spatially discretized form of the

general transport equation reads:

$$\frac{\partial}{\partial t}\left(\rho\phi\right)\Delta x^3 \approx -\sum_S (D_\phi \frac{\partial \phi}{\partial x_\mathrm{j}} n_\mathrm{j})\Delta x^2 + \sum_S (\rho u_\mathrm{j} \phi n_\mathrm{j})\Delta x^2 + \dot{\Gamma}_\phi \Delta x^3 = \mathrm{RHS} \tag{5.8}$$

Application of the FVM to the general transport equation reveals the true objects of interest to be the transported variables on the CV surfaces. While information about these variables is known at the cell centers, their respective values on the surfaces have to be derived. Thus, interpolation techniques are utilized to determine the surface values. Many techniques exist that provide different levels of accuracy and stability, and the choice of interpolation technique often depends on the solver framework and the given problem. In fact, several of the approaches discussed in the following include the term *differencing* in their names, as these schemes were developed in FDM to approximate differencing quotients. Thus, the term *interpolation* appears more suitable in the context of this work, however, is not chosen to maintain the nomenclature of the literature within this work [69]. The techniques for handling convective and diffusive fluxes are discussed below.

Spatial discretization reduces a continuous domain to a finite number of data points, resulting in a loss of information and introducing an error known as the discretization error. This error arises from approximating a derivative $d\phi/dx$ by a finite difference quotient $\Delta\phi/\Delta x$ due to the finite gridsize Δx. Numerical consistency is a prerequisite for discretization techniques. This property is fulfilled if, for the discretization width Δx, $\Delta\phi/\Delta x$ approaches the continuous differential $d\phi/dx$ and thus the discretization error vanishes. The consistency of a discretization scheme ensures that the numerical algorithm solves the discretized problem and not a problem modified due to the introduction of discretization.

While the discretization error decides over the general applicability of a discretization scheme, the truncation error characterizes its respective solution behavior. The spatial discretization error is defined as $\tau = d\phi/dx - \Delta\phi/\Delta x$ and depends on the employed scheme, the discretization width Δx and the gradients within the analyzed variable. The truncation error may occur in two different forms.

A diffusive leading truncation error smoothes gradients and dampens small perturbations and fluctuations in the solution. Diffusion errors are commonly tolerated, since the damping of perturbations improves the numerical stability of the employed scheme. However, numerical diffusion can easily outweigh the effects of physical diffusion, which eventually leads to inaccurate solutions.

A dispersive leading truncation error on the other hand leads to numerical oscillations – especially at locations where sharp gradients occur in the solution. These oscillations amplify as the algorithm proceeds and eventually lead to unphysical solutions. Hence, a dispersion error causes numerical instability and is generally undesirable. However, the low-dissipative nature of such schemes is desirable, and oscillations can be treated by adding

artificial dissipation, to dampen the growth of the oscillations, which is the reason that certain dispersive discretization schemes are still usable within a suitable numerical algorithm.

To quantify the truncation error, a Taylor series of the function f can be computed and modified to construct the expression of the respective discretization scheme. The truncation error is given by the *Higher-Order Terms* (*HOT*) that are not included in the discretized expression. The truncation error is dissipative if the order of the derivative in the first HOT is even. The truncation error appears dispersive when the order of the first HOT is odd. The order of the first HOT is relevant because all terms of even higher order vanish faster with refinement of the discretization width [9].

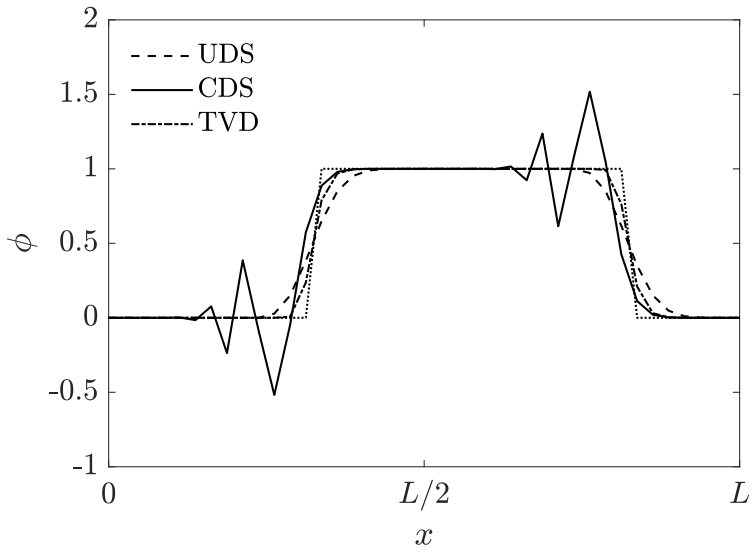

Figure 5.2 Solution of a one-dimensional linear convection equation employing three common discretization schemes visualizing the two different forms of the discretization error.

The nature of the discretization error is visualized in Fig. 5.2. The profiles are obtained from solving the linear convection equation $\partial\phi/\partial t + u \cdot \partial\phi/\partial x = 0$ and employing three different discretization schemes for the convective term. The initial solution is a simple top-hat function which features strong gradients to demonstrate the nature of the error. The true solution is indicated by shifting the initial solution in the transport direction with the simulation run time. The mathematics of the employed schemes will be explained in greater detail later on.

Two of the presented schemes flatten the initially steep gradients of the top hat profile. The observed behavior will progressively alter the profile by reduction of the gradients in the profile until no gradients are left in the computational domain. The remaining scheme features numerical oscillations that lead to the formation of new steep gradients. These oscillations will grow progressively and ultimately result in a crash of the simulation run. While the diffusive error can be generally tolerated, the dispersive error will always introduce

instability. It can be concluded, however, that a combination of both errors may lead to improved solution behavior.

The family of the *Central Differencing Schemes* (*CDS*) is one of the most prominent discretization techniques and aims for the linear interpolation of the neighboring cell face value using symmetrical stencils. The order of the CDS can be increased almost arbitrarily and the respective stencils can be crafted using Taylor-series expansion. The standard second-order CDS reads:

$$\phi_{\mathrm{i}+1/2} = \frac{1}{2}\phi_{\mathrm{i}} + \frac{1}{2}\phi_{\mathrm{i}+1} \tag{5.9}$$

The FDM formulation of the FVM CDS can be obtained by casting its stencil into a finite difference coefficient describing the differential $d\phi/dx \approx (\phi_{\mathrm{e}} - \phi_{\mathrm{w}})/\Delta x$ leading to:

$$\frac{d\phi}{dx} \approx \frac{\frac{\phi_{\mathrm{C}}+\phi_{\mathrm{E}}}{2} - \frac{\phi_{\mathrm{W}}+\phi_{\mathrm{C}}}{2}}{\Delta x} = \frac{\phi_{\mathrm{E}} - \phi_{\mathrm{W}}}{2\Delta x} \equiv \frac{\phi_{\mathrm{i}+1} - \phi_{\mathrm{i}\text{-}1}}{2\Delta x} \tag{5.10}$$

To assess the order of a discretization scheme, its expression has to be reconstructed using a Taylor-series expansion:

$$\phi(x) = \phi(x_{\mathrm{i}}) + \frac{1}{1!}\frac{d\phi}{dx}|_{x_{\mathrm{i}}}(x - x_{\mathrm{i}}) + \frac{1}{2!}\frac{d^2\phi}{dx^2}|_{x_{\mathrm{i}}}(x - x_{\mathrm{i}})^2 + \frac{1}{3!}\frac{d^3\phi}{dx^3}|_{x_{\mathrm{i}}}(x - x_{\mathrm{i}})^3 + \dots \tag{5.11}$$

Which can be evaluated at the two respective locations $x_{\mathrm{i}\text{-}1}$ and $x_{\mathrm{i}+1}$:

$$\phi(x_{\mathrm{i}\text{-}1}) = \phi(x_{\mathrm{i}}) - \frac{1}{1!}\frac{d\phi}{dx}|_{x_{\mathrm{i}}}\Delta x + \frac{1}{2!}\frac{d^2\phi}{dx^2}|_{x_{\mathrm{i}}}\Delta x^2 - \frac{1}{3!}\frac{d^3\phi}{dx^3}|_{x_{\mathrm{i}}}\Delta x^3 + \dots \tag{5.12}$$

$$\phi(x_{\mathrm{i}+1}) = \phi(x_{\mathrm{i}}) + \frac{1}{1!}\frac{d\phi}{dx}|_{x_{\mathrm{i}}}\Delta x + \frac{1}{2!}\frac{d^2\phi}{dx^2}|_{x_{\mathrm{i}}}\Delta x^2 + \frac{1}{3!}\frac{d^3\phi}{dx^3}|_{x_{\mathrm{i}}}\Delta x^3 + \dots \tag{5.13}$$

Subtracting and rearranging these two series expansions will lead to an expression for the difference quotient:

$$\frac{d\phi}{dx}|_{x_{\mathrm{i}}} = \frac{\phi(x_{\mathrm{i}+1}) - \phi(x_{\mathrm{i}\text{-}1})}{2\Delta x} + \frac{1}{3}\frac{d^3\phi}{dx^3}|_{x_{\mathrm{i}}}\Delta x^2 + \mathrm{HOT}(\Delta x^4) \tag{5.14}$$

It can be seen that the first higher-order term vanishes at a rate of Δx^2, which yields an order of 2 for the standard CDS scheme. The third-order derivative implies an error of odd order for the truncation error, leading to a dispersive nature of the error as observed in Fig. 5.2.

The respective stencils are not unique and can be customized e.g., by rearranging the Taylor-series expansion following the example given above. The stencils relevant to this work were chosen following Kennedy and Carpenter [123] and are summarized in Tab. 5.1.

The accuracy of CDS was shown and it can be concluded that CDS is a powerful scheme with the disadvantage of amplifying oscillations near steep gradients. These oscillations can be suppressed by pressure solvers, dissipative subgrid models or additional procedures to detect and remove numerical oscillations, such as the combination of schemes or self-adaptive

Table 5.1 Coefficients of the CDS discretization of different order. Only the right half of the symmetric stencil is written.

order	$i+1$	$i+2$	$i+3$	$i+4$
2	1/2			
4	27/48	−3/48		
6	5859/10000	−977/10000	177/10000	
8	5981/10000	−1196/10000	239/10000	−24/10000

methods, e.g. by Ciardi et al. [41]. It is common practice to support the CDS stencils, especially in the context of density-based solvers, by applying filtering of even higher order to suppress numerical oscillations [37]. The interested reader is referred to the works of Kennedy et al. [124] and Ray et al. [225]. Due to their relevance to this work, the stencil suggested by Kennedy et al. [124] and its corresponding notation is explained in the following for the one-dimensional case. Given the commutativity of the filter, multidimensional filtering is achieved by applying the filter in sequentially in the respective dimensions. The filtering stencil consists of the dissipation matrix D – this matrix is chosen to have negative eigenvalues to ensure the dissipative nature of the filter. The digital filter is convolved as:

$$\overline{u} = ((1 + \alpha_D D) * u) \tag{5.15}$$

Where for a $2n$-th order filter, the prefactor α_D is calculated as:

$$\alpha_D = (-1)^{n+1} 2^{-2n} \tag{5.16}$$

Approaching physical or computational boundaries within the domain poses a challenge as the filter stencil is not supported with enough cells in the respective direction of the boundary. To maintain the order of the filter in that direction, the stencil is skewed and included in the dissipation matrix. The upper portion of the dissipation matrix for a tenth-order filter is given as:

$$\begin{pmatrix}
\mathbf{+1} & -5 & +10 & -10 & +5 & -1 & & & & & \\
-5 & \mathbf{+26} & -55 & +60 & -35 & +10 & -1 & & & & \\
+10 & -55 & \mathbf{+126} & -155 & +110 & -45 & +10 & -1 & & & \\
-10 & +60 & -155 & \mathbf{+226} & -205 & +120 & -45 & +10 & -1 & & \\
+5 & -35 & +110 & -205 & \mathbf{+251} & -210 & +120 & -45 & +10 & -1 & \\
-1 & +10 & -45 & +120 & -210 & \mathbf{+252} & -210 & +120 & -45 & +10 & -1
\end{pmatrix} \tag{5.17}$$

The structure of the matrix is to be read as follows. The rows give the one-dimensional stencil to be applied to the desired variable. The different rows give the progressively skewed stencils with the first row being fully skewed and the last row being fully unskewed. The

mathematical center of the stencil and hence, the cell to be filtered, lies on the main diagonal $D_{\mathrm{i,i}}$ – this center is highlighted in Eq. 5.17. Thus, the first row $D_{1,\mathrm{j}}$ is the fully skewed and one-sided stencil. The second row gives the stencil with a distance of one cell to the boundary and the last row shows the stencil without any necessary modifications due to boundaries – this is the fully symmetric stencil. The minor diagonals are continued from each entry $D_{\mathrm{i},5}$ with the respective value found in $D_{\mathrm{i},5}$. The filtering approach is extended in this work by reducing the order of both the interpolation scheme and the numerical filter near the boundaries successively by two, until the highest possible order stencil fits to the corresponding cell.

The *Upwind Differencing Scheme* (*UDS*) is an unconditionally stable scheme that directly assigns the center values of a neighboring cell to the cell surface based on the flow direction – thus, it is called upwind scheme. The UDS is of first order accuracy and reads:

$$\phi_{\mathrm{i+1/2}} = \begin{cases} \phi_{\mathrm{i}} & u_{\mathrm{i+1/2}} \geq 0 \\ \phi_{\mathrm{i+1}} & u_{\mathrm{i+1/2}} < 0 \end{cases} \tag{5.18}$$

The accuracy of the UDS can be analyzed using Taylor-series expansion in the same manner as for the CDS. The first row assumes a non-negative velocity and the second row assumes a positive velocity:

$$\frac{d\phi}{dx} \approx \frac{\phi_{\mathrm{C}} - \phi_{\mathrm{W}}}{\Delta x} \equiv \frac{\phi_{\mathrm{i}} - \phi_{\mathrm{i\text{-}1}}}{\Delta x} \tag{5.19}$$

$$\frac{d\phi}{dx} \approx \frac{\phi_{\mathrm{E}} - \phi_{\mathrm{C}}}{\Delta x} \equiv \frac{\phi_{\mathrm{i+1}} - \phi_{\mathrm{i}}}{\Delta x} \tag{5.20}$$

Reusing the Taylor-series expansion from Eq. 5.12 and 5.13, as well as rearranging yields the full form of the UDS discretization:

$$\frac{d\phi}{dx}|_{x_{\mathrm{i}}} = \frac{\phi(x_{\mathrm{i}}) - \phi(x_{\mathrm{i\text{-}1}})}{\Delta x} + \frac{1}{2}\frac{d^2\phi}{dx^2}|_{x_{\mathrm{i}}}\Delta x + \mathrm{HOT}(\Delta x^2) \tag{5.21}$$

$$\frac{d\phi}{dx}|_{x_{\mathrm{i}}} = \frac{\phi(x_{\mathrm{i+1}}) - \phi(x_{\mathrm{i}})}{\Delta x} - \frac{1}{2}\frac{d^2\phi}{dx^2}|_{x_{\mathrm{i}}}\Delta x + \mathrm{HOT}(\Delta x^2) \tag{5.22}$$

The resulting expression immediately indicates that the UDS is of first order accuracy. The numerical error is diffusive, which is the main reason for the numerical stability. Fig. 5.2 confirms that UDS provides the strongest smoothing among the schemes compared. Thus, UDS is able to capture even discontinuities such as shock waves and always maintains the boundedness of the transported quantity. However, the strong dissipative nature of UDS is a common reason for choosing other numerical schemes that provide similar stability with less dissipation [100].

A common alternative is therefore to use higher-order interpolation methods instead, which are bounded using a suitable limiter function. These methods dynamically blend the

previously introduced CDS and UDS methods in order to achieve better accuracy through a higher CDS contribution and, if necessary, to increase stability through a higher UDS contribution. These blends form a family of schemes that are characterized by their ability to reduce the *Total Variation* (TV) that occurs while solving a PDE, as introduced by Harten [94]:

$$\mathrm{TV}(\phi^n) = \sum_j |\phi^n_{\mathrm{j+1}} - \phi^n_{\mathrm{j}}| \tag{5.23}$$

Where the total variation TV diminishes if:

$$\mathrm{TV}(\phi^{n+1}) \leq \mathrm{TV}(\phi^n) \tag{5.24}$$

Due to their shared property of being *Total Variation Diminishing*, this family of schemes is also referred to as *TVD* schemes.

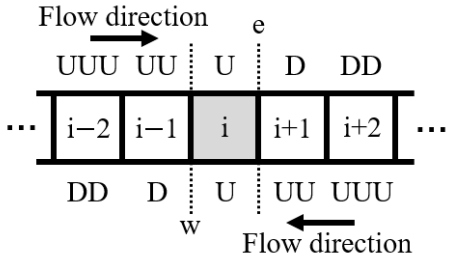

Figure 5.3 Nomenclature for the upstream and downstream cells involved in the TVD stencil.

TVD schemes rely heavily on flow-oriented indexing due to their upwind nature. Figure 5.3 shows the indexing of the cells involved as a function of flow direction. To quantify the mixing of the UDS and CDS nature, the ratio r is used, which relates the downstream gradient to the upstream gradient:

$$r = \frac{\phi_{\mathrm{D}} - \phi_{\mathrm{U}}}{\phi_{\mathrm{U}} - \phi_{\mathrm{UU}}} \tag{5.25}$$

So that the blending is built as:

$$\phi_{\mathrm{i+1/2}} = \phi_{\mathrm{U}} + \frac{1}{2}\Psi\left(r\right)\left(\phi_{\mathrm{U}} - \phi_{\mathrm{UU}}\right) \tag{5.26}$$

Given this definition, it can be concluded that the nature of the TVD scheme strongly depends on the used limiter function $\Psi(r)$. Looking closely at the formulation in Eq. 5.26, it can be seen that the choice of the limiter at 0 or r leads to the definitions of UDS and CDS according to the above nomenclature, which are therefore also part of the TVD family. There is a wide range of limiter functions, and some of the most commonly used limiters are summarized in Tab. 5.2.

Due to the nature of the blending, it becomes evident that the order of accuracy of the TVD schemes is not straightforward and heavily depends on the limiter function $\Psi(r)$.

Table 5.2 Commonly employed flux limiters $\Psi(r)$ and their bounds within the $r - \Psi(r)$ space.

Limiter	$\Psi(r)$	$\Psi(r) \in$	Reference
UDS	0	$\{0\}$	
MINMOD	$\max(\min(r, 1), 0)$	$[0, 1]$	Roe [238]
VAN-LEER	$(r + \lvert r\rvert)/(1 + \lvert r\rvert)$	$[0, 2)$	van Leer [285]
EXP	$2(1 - \exp(\log(0.5) \cdot \max(r, 0)))$	$[0, 2)$	Proch [219]
CHARM	$\max(r, 0) \cdot (3\max(r, 0) + 1)/(\max(r, 0) + 1)^2$	$[0, 3)$	Zhou [317]
SUPERBEE	$\max(\min(r, 2), \min(2r, 1), 0)$	$[0, 2]$	Roe [238]
CDS	r	$[0, \infty)$	

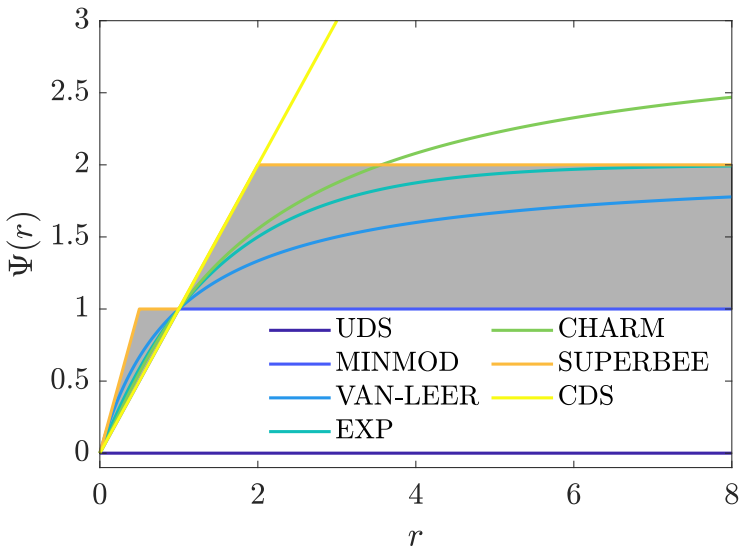

Figure 5.4 Comparison of selected flux limiters $\Psi(r)$ as a function of the ratio of successive gradients r. The second-order region as introduced by Sweby [274] is marked by the shaded area.

Sweby [274] assessed the values of r and $\Psi(r)$ for which the CDS contribution achieves a maximum while maintaining stability. The result is an area in the $r - \Psi(r)$ space, shaded in Fig. 5.4, which is also referred to as the second-order region.

A limiter function that lies entirely within the gray shaded area results in a fully second order TVD scheme. This requirement is met by the *MINMOD*, *VAN-LEER*, *EXP*, and *SUPERBEE* limiters, which lie either inside or at the boundaries of the second order region. It is of interest to evaluate the performance of the different limiters in a-posteriori simulation. A one-dimensional linear transport equation with periodic bounds for a scalar quantity was solved and compared to the shifted initial solution.

Following the findings of Kempf [119], Klein [132] and Stein [266] it is not sufficient to demonstrate the different limiters with a top-hat-like function. Instead, a top-hat function and a sine-function are transported to investigate the influence of gradients on the limiters.

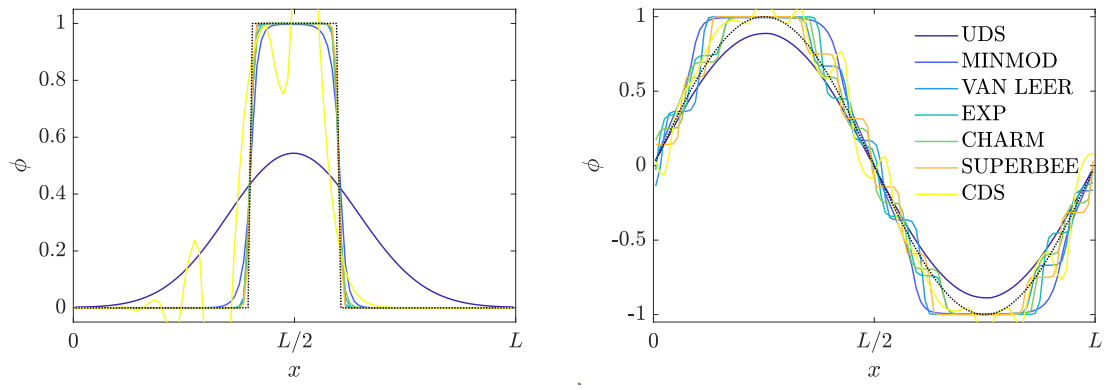

Figure 5.5 Solution of a linear convection equation employing the limiter functions $\Psi(r)$ as presented in Tab. 5.2 and two different initial solutions: top-hat and sine function.

A detailed study of the limiters was performed by Kemm [118] and the interested reader is referred to the respective work. Furthermore, the simulation run time was chosen long enough to reveal the effects of the different limiters.

The results, including the shifted initial solution, can be seen in Fig. 5.5. In the absence of blending, one obtains the pure UDS, which is always stable and does not exhibit any over-compressive behavior. However, it can be seen that this comes at the cost of strong diffusion, which changes the shape and magnitude of the transported profiles. The MINMOD limiter is located at the lower limit of the stable second-order region, which implies the lowest possible CDS contribution while maintaining second-order accuracy – or in other words, the highest possible UDS contribution. Hence, the MINMOD limiter is the most dissipative second-order limiter, as can be seen from the strongly smoothed top-hat. The transported sine function reveals that the MINMOD limiter has a tendency to maintain plateaus while being dissipative, as shown by the very pronounced plateaus at the extrema, as well as the poor results for the slopes.

On the upper limit of the stable second-order region lies the SUPERBEE limiter, which is the least dissipative limiter due to the maximum CDS contribution. The low dissipativeness makes the limiter theoretically very attractive as it is capable of preserving sharp gradients, which is also seen in the top-hat profile. However, the SUPERBEE exhibits the most over-compressive behavior among the presented limiters. Over-compression is the tendency of a scheme to steepen gradients, which can be observed in most limiter functions. This leads to the characteristic formation of plateaus, as present for the sine profile.

The VAN-LEER limiter lies in the second-order stable region and hence compromises between the MINMOD and SUPERBEE limiter. This can be seen by reasonable results for both transport cases, where it reveals moderate dissipation for the top-hat but also moderate over-compression for the sine case. Another limiter partially lying in the second-order stable region is the CHARM limiter. The CHARM limiter, like the VAN-LEER limiter, shows

degressive growth but does not converge within the second-order stable region, leading to instabilities in the case of strong gradients. However, this implies that the CHARM limiter overall includes a higher CDS contribution, leading to slightly better results in the case of smooth transported profiles. The CHARM limiter is the standard choice for TVD in this work.

The EXP limiter is not a conventional limiter formulation from the literature and was developed by Proch [219] to mimic the behavior of the CHARM limiter while remaining in the second-order stable region at the same time, as shown in Fig. 5.4. The EXP limiter reveals similar results to the CHARM limiter, with slightly better symmetry-preserving properties than the remaining limiters.

In the case of CDS, the scheme is of second order accuracy, but it only marginally falls within the stable second-order region. Not surprisingly, the CDS exhibits strong oscillations when transporting the top-hat function due to its steep gradients. The oscillations present in the transported sine function are comparatively small due to the overall smoother profile. Therefore, it takes longer for oscillations to develop. A common problem for the CDS can be observed within the top-hat function. Compared to all other profiles, the CDS features a phase-shifted profile, which is a consequence of the dispersive error. This has to be considered when using dissipation-supported CDS, and for a detailed investigation the reader is referred to Klein [132].

After common techniques for the determination of the cell face values were given above, it is finally of interest to describe differential quotients in an appropriate way, especially for assessing diffusive fluxes. A differential quotient on a surface can be written as the change in value between adjacent cells:

$$\frac{\partial \phi}{\partial x}|_{\mathrm{i}+1/2} \approx \frac{\phi_{\mathrm{i}+1} - \phi_{\mathrm{i}}}{\Delta x} \tag{5.27}$$

Which is the most common approach to deal with differential quotients occurring in transport equations [68] – typically in the form of diffusive fluxes. While the above formulation is employed within this work, the reader is referred to the work of Pletcher et al. [211] for more details on higher-order closures of diffusive fluxes.

5.1.2 Temporal discretization

The spatial discretization has been shown to decompose the physical domain into a finite number of points at which solutions of the fundamental equations can be obtained and which are representative for the given problem. The temporal discretization aims at advancing the solution at these points in time, again using discrete time intervals. The spatial discretization provides instructions on how to handle the spatial derivatives within the transport equation at a given point in time, and the temporal discretization connects these points in time using the current time as initialization to predict the state after the next interval.

Mathematical properties of temporal discretization

It is evident that the simplest approach to connect two points in time from a given initialization is linear extrapolation. This idea was proposed and further analyzed by Euler, which is why it is often referred to as the Euler method. The Euler method reads:

$$\frac{\partial \rho\phi}{\partial t} = \text{RHS} \approx \frac{(\rho\phi)^{\text{n}+1} - (\rho\phi)^{\text{n}}}{\Delta t} \tag{5.28}$$

Where the indices n and n+1 denote the steps at initial- t^{n} and target-time $t^{\text{n}+1}$ framing the interval of interest. Hence, the length of the interval denoted as Δt is defined as $\Delta t = t^{\text{n}+1} - t^{\text{n}}$. From an accounting point of view, it is not far-fetched to think that large stepping intervals are desirable in order to advance quickly in time and to save iterations and thus costs. However, the size of the interval is limited by numerical stability, which can vary greatly from problem to problem. An important property of the equation to be solved that characterizes its stability is the so-called stiffness. While generally non-trivial in its definition, stiffness can be simply described as the sensitivity of the equation to timestep widths due to the presence of a broad range of timescales. This is due to individual terms in the equation leading to potentially large variations in the solution over small increments, which can contaminate or ruin its solution properties. Thus, a stiff equation is typically considered one where the timestep size must be extremely small to maintain numerical stability. The stiffness of an equation can be analyzed or, in the case of CFD, it can be known from experience and must be taken into account when choosing the time discretization scheme. It should be noted that the use of an explicit scheme for a stiff PDE is not necessarily inappropriate if the physics involved in the problem already requires high temporal resolution.

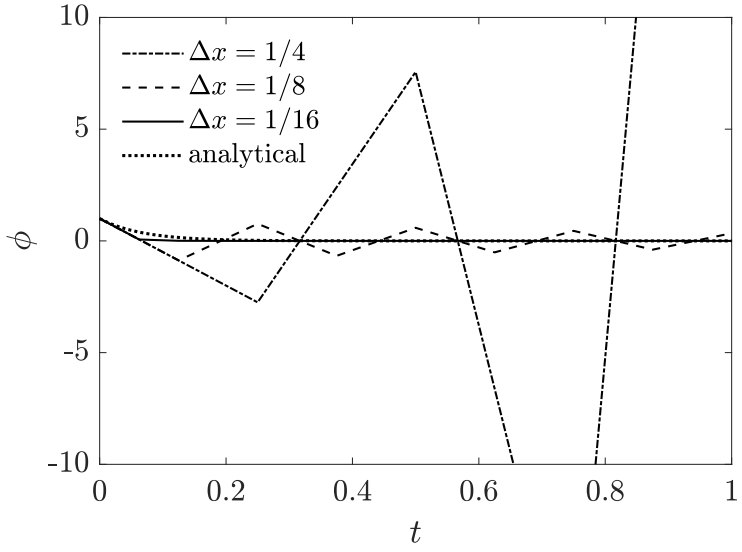

Figure 5.6 Solution behavior of a stiff differential equation for different step sizes.

The effects of stiffness are visualized in Fig. 5.6. The lines represent the solutions of $dy/dx = -15y$ employing the explicit Euler method as well as the analytical solution. The different solutions exhibit a strong dependency on the numerical step size, illustrating the concept of stiffness. Step sizes of 1/4 reveal divergent behavior, while the solution for a step size of 1/8 remains bounded but does not converge to the true solution. Only a step size of 1/16 succeeds in reproducing the true solution behavior. The difference between the analytical and numerical solution is further reduced by using even finer step sizes. For a detailed study of a chemical problem, the interested reader is referred to the work of Robertson [236].

One remaining question is the time dependence of the sum of the flux terms, also called the *Right-Hand Side* (*RHS*). It comes to mind that the RHS can be defined for both ends of the interval as $\mathrm{RHS}^{\mathrm{n}}$ or $\mathrm{RHS}^{\mathrm{n+1}}$. The first definition, $\mathrm{RHS}^{\mathrm{n}}$, results in all terms within the equation being fully known, and thus forms the simplest temporal discretization, referred to as the explicit Euler method:

$$\phi^{\mathrm{n+1}} = \phi^{\mathrm{n}} + \Delta t \cdot \mathrm{RHS}^{\mathrm{n}} \tag{5.29}$$

The other possible option is to treat the right-hand side as a function of the unknown time step $\mathrm{RHS}^{\mathrm{n+1}}$. This leads to the similar definition:

$$\phi^{\mathrm{n+1}} = \phi^{\mathrm{n}} + \Delta t \cdot \mathrm{RHS}^{\mathrm{n+1}} \tag{5.30}$$

Since the term $\mathrm{RHS}^{\mathrm{n+1}}$ is now unknown, the solution is not as easy to compute as before. Since the solution $\phi^{\mathrm{n+1}}$ can no longer be recovered explicitly, this method is called the implicit Euler method. Instead, the solution $\phi^{\mathrm{n+1}}$ appears on both sides of the equation and must be obtained by solving an additional algebraic equation.

Both variants of Euler's method are of first order accuracy. The numerical accuracy is defined by the local truncation error τ_{n}. This error characterizes the deviation between the time discretization and the true solution within a single time step. For a better understanding, the procedure for obtaining this error will be demonstrated using the example of the explicit Euler method. The Taylor-series expansion is used to formulate and reconstruct the definition of the investigated method:

$$\phi\left(t\right) = \phi^{\mathrm{n}} + \frac{\dot{\phi}^{\mathrm{n}}}{1!}\left(t - t^{\mathrm{n}}\right) + \frac{\ddot{\phi}^{\mathrm{n}}}{2!}\left(t - t^{\mathrm{n}}\right)^2 + \ldots \tag{5.31}$$

Inserting $t^{\mathrm{n+1}}$ for t and using $\Delta t = t^{\mathrm{n+1}} - t^{\mathrm{n}}$ allows for the rearrangement of the equation into:

$$\dot{\phi}^{\mathrm{n}} = \frac{\phi^{\mathrm{n+1}} - \phi^{\mathrm{n}}}{\Delta t} - \frac{\ddot{\phi}^{\mathrm{n}}}{2}\Delta t + \mathrm{HOT}(\Delta t^2) \tag{5.32}$$

From this identity it can be concluded that the deviation between the true derivative $\dot{\phi}^{\mathrm{n}}$ and the approximation reduces with the order of one, as the slowest decreasing residual term has the prefactor Δt. Thus, the explicit Euler method is of first order accuracy. The same result

can be found for the implicit Euler scheme by altering the Taylor-series expansion around t^{n+1} and inserting t^n and inverting the sign in front of the higher-order terms. An example for the analysis of numerical accuracy was given. Now it is of interest to characterize the numerical stability.

The Euler method will serve as an example of the effects of treating the time dependence of the RHS, allowing for a discussion of the stability of the time discretization. In general, the term numerical stability refers to a broad field, and most commonly the concept of *A-stability* is meant when speaking of numerical stability of the time discretization. A-stability of a numerical method is investigated by means of the so-called test equation, which is defined as $\dot{\phi} = -\alpha\phi$ with $\alpha \in \mathbb{R}^+$ and features the analytical solution $\phi = \phi_0 e^{-\alpha t}$ with $\phi_0 > 0$. The first step is to rewrite the explicit Euler scheme from Eq. 5.29 as $\phi^{n+1} = \phi^n + \Delta \cdot \mathrm{RHS}^n$. The test equation is inserted into this formulation, resulting in the expression:

$$\phi^{n+1} = (1 - \alpha\Delta t)\,\phi^n \tag{5.33}$$

The expression $g(\alpha\Delta t) = (1 - \alpha\Delta t)$ is typically referred to as the stability function, which is by definition a complex function. The true solution of the test equation remains positive and converges to zero. These conditions are equivalent to $|g(\alpha\Delta t)| < 1$. The region of absolute stability can thus be defined as $\{\alpha\Delta t \in \mathbb{C}, |g(\alpha\Delta t)| < 1\}$. The investigated method is called A-stable if $\{\alpha\Delta t \in \mathbb{C}, \mathrm{Re}(\alpha\Delta t) > 0\}$ is satisfied.

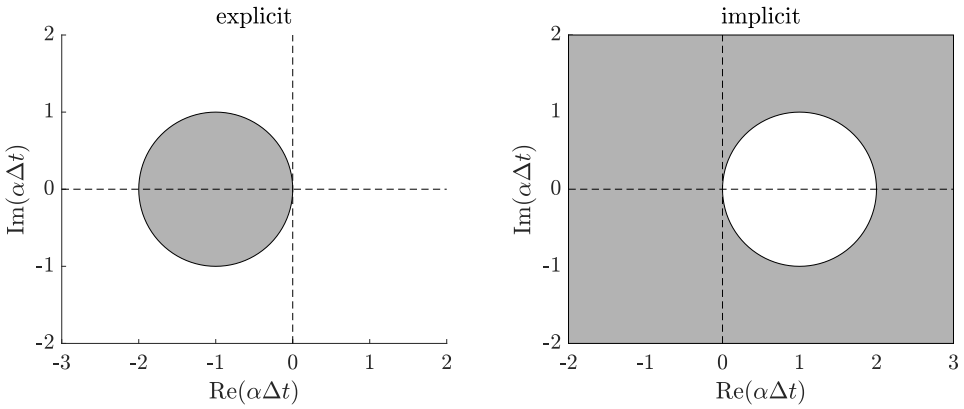

Figure 5.7 Stability planes obtained for the explicit and implicit Euler method.

The extent of the stability region of the explicit and implicit Euler methods obtained from the test equation is shown in Fig. 5.7. The stability plane of the explicit Euler method shows a disk located in the left half of the complex half-plane, indicating that the explicit Euler method is not A-stable. For the implicit Euler method, the region of absolute stability is the complement in the complex half-plane of the disk with a radius of unity centered at $\mathrm{Re}(\alpha\Delta t) = 1$, thus including the entire left half of the complex half-plane, making it particularly suitable for solving stiff differential equations [29].

As the stability of the Euler method was discussed in a general manner it shall be elaborated in the direct context of solving the conservation laws given in Sec. 2. The most crucial condition for the stability of the time discretization scheme when solving the NSE is the Courant-Friedrichs-Lewy number CFL [46]. Its importance and origin can be demonstrated using a simplified form of the general conservation law from Eq. 2.1 for a simple one-dimensional convection problem at constant density and transport velocity thus, consider:

$$\frac{\partial \phi}{\partial t} + u\frac{\partial \phi}{\partial x} = 0 \tag{5.34}$$

The equation shall be discretized using the explicit Euler method for time as well as the UDS for space – for simplicity, it is assumed that transport occurs only in the positive direction. Inserting the respective formulations for the explicit Euler method and the UDS yields:

$$\frac{\phi_{\mathrm{i}}^{\mathrm{n+1}} - \phi_{\mathrm{i}}^{\mathrm{n}}}{\Delta t} + u\frac{\phi_{\mathrm{i}}^{\mathrm{n}} - \phi_{\mathrm{i\text{-}1}}^{\mathrm{n}}}{\Delta x} = 0 \tag{5.35}$$

While this equation is formally a PDE and is usually solved numerically, a heuristic analysis as performed by Hirt [102] sheds more light on the true mathematical nature of this discretized formulation. Therefore, a Taylor-series expansion is employed once more around t^{n} and x_{i}. The value of $t^{\mathrm{n+1}}$ is inserted into the corresponding Taylor series right away, and the resulting equation is solved for the discretization expression:

$$\frac{\phi_{\mathrm{i}}^{\mathrm{n+1}} - \phi_{\mathrm{i}}^{\mathrm{n}}}{\Delta t} = \frac{1}{1!}\frac{\partial \phi}{\partial t} + \frac{1}{2!}\frac{\partial^2 \phi}{\partial t^2}\Delta t + \dots \tag{5.36}$$

For the spatial discretization a value of $x_{\mathrm{i\text{-}1}}$ is inserted, yielding:

$$\frac{\phi_{\mathrm{i}}^{\mathrm{n}} - \phi_{\mathrm{i\text{-}1}}^{\mathrm{n}}}{\Delta x} = \frac{1}{1!}\frac{\partial \phi}{\partial x} - \frac{1}{2!}\frac{\partial^2 \phi}{\partial x^2}\Delta x + \dots \tag{5.37}$$

Rewriting and deriving Eq. 5.35 in time establishes the following relationship between the spatial and temporal derivatives:

$$\frac{\partial^2 \phi}{\partial t^2} = -u^2\frac{\partial^2 \phi}{\partial x^2} \tag{5.38}$$

Reforming the discretized transport equation leads to:

$$\frac{\phi_{\mathrm{i}}^{\mathrm{n+1}} - \phi_{\mathrm{i}}^{\mathrm{n}}}{\Delta t} + u\frac{\phi_{\mathrm{i}}^{\mathrm{n}} - \phi_{\mathrm{i\text{-}1}}^{\mathrm{n}}}{\Delta x} = \frac{1}{1!}\frac{\partial \phi}{\partial t} + \frac{1}{2!}\frac{\partial^2 \phi}{\partial t^2}\Delta t + \mathcal{O}(\Delta t^2) + u\frac{1}{1!}\frac{\partial \phi}{\partial x} + u\frac{1}{2!}\frac{\partial^2 \phi}{\partial x^2}\Delta x + \mathcal{O}(\Delta x^2) \tag{5.39}$$

Which can be rewritten as:

$$\frac{\phi_{\mathrm{i}}^{\mathrm{n+1}} - \phi_{\mathrm{i}}^{\mathrm{n}}}{\Delta t} + u\frac{\phi_{\mathrm{i}}^{\mathrm{n}} - \phi_{\mathrm{i\text{-}1}}^{\mathrm{n}}}{\Delta x} = \frac{\partial \phi}{\partial t} + u\frac{\partial \phi}{\partial x} + \frac{1}{2}\left(\frac{\partial^2 \phi}{\partial t^2}\Delta t + u\frac{\partial^2 \phi}{\partial x^2}\Delta x\right) + \mathcal{O}(\Delta t^2, \Delta x^2) \tag{5.40}$$

Employing the new found identity:

$$\frac{\phi_{\mathrm{i}}^{\mathrm{n}+1}-\phi_{\mathrm{i}}^{\mathrm{n}}}{\Delta t}+u\frac{\phi_{\mathrm{i}}^{\mathrm{n}}-\phi_{\mathrm{i\text{-}1}}^{\mathrm{n}}}{\Delta x}=\frac{\partial\phi}{\partial t}+u\frac{\partial\phi}{\partial x}+\frac{1}{2}u\Delta x\left(1-\mathrm{CFL}\right)\frac{\partial^2\phi}{\partial x^2}+\mathcal{O}(\Delta t^2,\Delta x^2) \tag{5.41}$$

It is evident that the choice of discretization resulted in the formation of a convection-diffusion equation, which was not the true object of interest. Instead, the problem now exhibits diffusive behavior, which is one of the major challenges in CFD numerics. In this particular case, the numerical diffusion coefficient is given as $u\Delta x\left(1-\mathrm{CFL}\right)/2$. Numerical stability is maintained if this coefficient remains positive, which is true as long as $\mathrm{CFL}<1$, which is the stability condition for the explicit Euler method in time and UDS in space.

The CFL number is defined as:

$$\mathrm{CFL}=\frac{U\Delta t}{\Delta x}\leq\mathrm{CFL}_{\max} \tag{5.42}$$

Where U is the maximum velocity component in the domain and $\mathrm{CFL}_{\max}$ is the maximum allowed value for CFL for maintaining stability dictated by the employed temporal and spatial discretization. The CFL number gives a ratio between a physical velocity U and a numerical velocity $\Delta x/\Delta t$ and can be interpreted as follows. The ratio indicates how fast physical information is transported through the numerical grid. In particular, ratios less than one indicate that the physical information is transported more slowly than the information propagates from cell to cell. In this sense, the CFL number can be interpreted as how many cells the physical information travels per timestep. It may seem intuitive that the physical information should propagate on the order of one cell per timestep to maintain stability. The most commonly encountered value for $\mathrm{CFL}_{\max}$ is unity, which is the limit for the case of the explicit Euler method, while for some methods – such as the later introduced Runge-Kutta methods – a $\mathrm{CFL}_{\max}$ beyond unity is allowed.

Runge-Kutta methods

Runge-Kutta methods are state-of-the-art time integration methods of great relevance to this work. Occasionally called *the* Runge-Kutta method, Runge-Kutta refers to a family of multi-stage single-step methods of explicit or implicit nature [240, 152]. In fact, the explicit Euler method is the simplest Runge-Kutta method. For convenience and to study the structure of Runge-Kutta methods, the simplified equation to be solved in time discretization will be rewritten:

$$\frac{\partial\phi}{\partial t}=\mathrm{RHS} \tag{5.43}$$

Runge-Kutta methods aim to solve the equation by introducing a manifold of s stages to decompose the timestep Δt and ultimately find a better estimate for the slope connecting

the given and desired point in time [218]. The general form of a Runge-Kutta scheme reads:

$$\phi^{\mathrm{n}+1} = \phi^{\mathrm{n}} + \Delta t \sum_{i=1}^{s} b_{\mathrm{i}} k_{\mathrm{i}} \tag{5.44}$$

Here, k_{i} denotes the slopes obtained from the staging which are then averaged using the weights b_{i} to compose the estimate of the slope used for the final time integration step. The slopes k_{i} at the different stages i are calculated as follows:

$$k_1 = \mathrm{RHS}\left(t^{\mathrm{n}}, \phi^{\mathrm{n}}\right) \tag{5.45}$$

$$k_2 = \mathrm{RHS}\left(t^{\mathrm{n}} + c_2 \Delta t, \phi^{\mathrm{n}} + \Delta t \left(a_{21} k_1\right)\right) \tag{5.46}$$

$$k_3 = \mathrm{RHS}\left(t^{\mathrm{n}} + c_3 \Delta t, \phi^{\mathrm{n}} + \Delta t \left(a_{31} k_1 + a_{32} k_2\right)\right) \tag{5.47}$$

$$\vdots \tag{5.48}$$

$$k_{\mathrm{s}} = \mathrm{RHS}\left(t^{\mathrm{n}} + c_{\mathrm{s}} \Delta t, \phi^{\mathrm{n}} + \Delta t \left(a_{\mathrm{s}1} k_1 + a_{\mathrm{s}2} k_2 + \cdots + a_{\mathrm{s,s-1}} k_{\mathrm{s}-1}\right)\right) \tag{5.49}$$

To fully characterize the Runge-Kutta scheme, the number of stages s, the Runge-Kutta matrix a_{ij}, the weights b_{i}, and the nodes c_{i} must be given. It is common practice to visualize these coefficients in a mnemonic structure known as the Butcher tableau [110]. In general, an explicit Runge-Kutta scheme of s stages can have a maximum order of s. The coefficients can be found empirically or using Butcher trees to obtain a desired compromise between accuracy, stability, and consistency.

The foundations of the stability of time discretization were laid using the example of the Euler method. Since there are a large number of Runge-Kutta schemes, not all of them can be discussed here. However, because of its relevance to this work, the low-storage three-stage Runge-Kutta scheme proposed by Williamson [304] will be introduced in some detail. It should be noted that this scheme was developed at a time when memory problems were more severe. However, since it has the same accuracy compared to regular three-stage Runge-Kutta schemes, it is still state of the art. To achieve the low memory requirements, the structure of the scheme is slightly modified:

$$\phi_1^{\mathrm{n}} = \phi^{\mathrm{n}} + \left(b_1 \mathrm{RHS}\left(t^{\mathrm{n}}, \phi^{\mathrm{n}}\right)\right) \Delta t \tag{5.50}$$

$$\phi_2^{\mathrm{n}} = \phi_1^{\mathrm{n}} + \left(a_2 b_2 \mathrm{RHS}\left(t^{\mathrm{n}}, \phi^{\mathrm{n}}\right) + b_2 \mathrm{RHS}\left(t_1^{\mathrm{n}}, \phi_1^{\mathrm{n}}\right)\right) \Delta t \tag{5.51}$$

$$\phi_3^{\mathrm{n}} = \phi_2^{\mathrm{n}} + \left(a_2 a_3 b_3 \mathrm{RHS}\left(t^{\mathrm{n}}, \phi^{\mathrm{n}}\right) + a_3 b_3 \mathrm{RHS}\left(t_1^{\mathrm{n}}, \phi_1^{\mathrm{n}}\right) + b_3 \mathrm{RHS}\left(t_2^{\mathrm{n}}, \phi_2^{\mathrm{n}}\right)\right) \Delta t = \phi^{\mathrm{n}+1} \tag{5.52}$$

The equations contain the reduced matrix $a_{\mathrm{s}} = (0, -5/9, -153/128)$, the weights $b_{\mathrm{s}} = (1/3, 15/16, 8/15)$ and the nodes $c_{\mathrm{s}} = (1/3, 5/12, 1/4)$ to compute the Runge-Kutta times $t_{\mathrm{s}} = t_{\mathrm{s\text{-}1}} + c_{\mathrm{s}} \Delta t$.

An example of an implicit Runge-Kutta method (without further discussion) is the Crank-Nicolson method. While it is only second-order accurate, it has the advantage of

being unconditionally stable [47]. The Crank-Nicolson method is commonly used within the OpenFOAM framework [301].

5.2 Pressure-Velocity coupling

While general approaches to deal with the discretization of the equations of fluid motion were given above, a fundamental distinction is made between two states of flow which dictates the solver architecture. In thermodynamics, this distinction is made based on the dependence of the density of the flow medium on the pressure and is referred to as *compressibility*. While variation of density can have multiple sources, only the pressure-induced variation defines the compressibility. From a numerical point of view, compressibility is a harsh boundary that strictly determines whether the density of a medium is pressure dependent or not. Thus, in CFD, a flow medium is typically either compressible or incompressible. It becomes obvious that along with this distinction, different models and solver frameworks become necessary. Furthermore, in CFD this separation is linked to the Mach number Ma, which characterizes the ratio of flow velocity to sonic velocity. Gas dynamics dictates a direct relationship between the changes of velocity, changes of density and the Mach number, which can be obtained from the differential form of the conservation laws. This relation reads:

$$-\frac{d\rho}{\rho} = \mathrm{Ma}^2 \frac{du}{u} \tag{5.53}$$

It is observed from this relationship that the Mach number serves as a sensitivity parameter that links the variation of the density to the variation of the velocity, and this relationship becomes stronger as the Mach number increases. However, the relationship does not imply a strict separation, which is thus up to the designer of the CFD algorithm. The most common limit to distinguish between incompressible and compressible solvers is chosen to be $\mathrm{Ma} = 0.3$. This limit does not result from theoretical arguments but from the willingness to accept a certain error, as incompressibility is an idealization after all. Due to the Mach number serving as the indicator for distinguishing between the required solver architecture the terms *low-Mach* and *high-Mach* solvers are used.

5.2.1 Compressible solver framework

Also known as density-based or high-Mach solvers, compressible solver frameworks do not assume that the density is independent of the pressure. Instead, they incorporate a thermodynamic equation of state, denoted as $f(p, T, \rho) = 0$, which couples the density to the pressure. This equation of state must be included in the solver framework to access the pressure from the transported variables. Common choices for the equation of state are the ideal gas law (as shown in Eq. 2.6) or the van-der-Waals equation. The ideal gas law can be

expressed as follows for the purpose of this discussion:

$$p = \rho \frac{R_\mathrm{m}}{W} T \tag{5.54}$$

The van-der-Waals equation is a thermodynamic model that accounts for intermolecular forces and the volume occupied by gas particles, which the ideal gas law neglects. It introduces two parameters, the cohesion pressure parameter a and the molar volume parameter b, to capture the effects of intermolecular forces and particle volume, respectively. In many engineering applications, the van-der-Waals equation can be simplified by neglecting a and b at pressures below 10 bar. The van-der-Waals equation is typically formulated in terms of the amount of substance n and can be expressed as follows:

$$\left(p + \frac{n^2 a}{V^2} \right) (V - b) = n R_\mathrm{m} T \tag{5.55}$$

The equation of state requires a temperature T to complete the coupling between pressure and density. Since the equation of state is already reserved for the calculation of the pressure, a conservation law for the energy is incorporated in addition with a caloric equation of state to derive the temperature from the energy. It can be concluded so far that the compressible solver framework requires an additional transport equation, which is not necessarily needed in a comparable incompressible framework.

Another aspect of compressible solvers is their ability to resolve the pressure-dependent variation of the density. These pressure-induced variations of the density are also referred to as weak perturbations, which ultimately are pressure waves. Pressure waves spread through space at the speed of sound – which, by definition, is the speed of pressure waves. It was discussed earlier that it is of crucial importance for maintaining stability to limit the speed at which information propagates through the grid. Due to the presence of acoustic phenomena, however, this speed is not only the convective speed of the flow, but also the speed at which sound waves propagate. Therefore, in a compressible solver framework, it is necessary to include the speed of sound in the calculation of the timestep, which typically reduces the timestep width by at least one order of magnitude. In this context, the CFL number is also referred to as the acoustic CFL number.

5.2.2 Incompressible solver framework

The so-called pressure-based, low-Mach, or incompressible solver frameworks rely on the idealization of the density being independent of the pressure. Therefore, a coupling between pressure and density through a thermodynamic law is not possible as $\rho \neq f(p)$. The incompressible solver instead assumes a static background pressure – which in most works is given by the atmospheric pressure – and superimposes on this pressure with the corresponding

pressure gradient required for the conservation of momentum. This pressure gradient is implicitly dictated by the conservation of mass. For the general case of a varying density – e.g. due to thermal effects – the conservation of mass can be rewritten as a target-divergence condition:

$$\frac{\partial \rho u_\mathrm{j}}{\partial x_\mathrm{j}} = -\frac{\partial \rho}{\partial t} \tag{5.56}$$

This can also be understood in the following way: at the beginning of each new timestep, the momentum field must satisfy the divergence dictated by the density field. Employing a simple explicit Euler method, the procedure is further elaborated. This procedure is still valid when using Runge-Kutta methods, but the pressure must be corrected at each Runge-Kutta stage and the timestep width must be adapted to the Runge-Kutta method. The conservation of momentum can be rewritten as:

$$(\rho u_\mathrm{i})^{n+1} = (\rho u_\mathrm{i})^{n} + \Delta t \left(-\frac{\partial \rho u_\mathrm{i} u_\mathrm{j}}{\partial x_\mathrm{j}} - \frac{\partial p}{\partial x_\mathrm{i}} + \frac{\partial \tau_\mathrm{ij}}{\partial x_\mathrm{j}} \right) \tag{5.57}$$

It is now of interest to obtain the pressure gradient, which serves to complete the time iteration. Hence, the new momentum field is decomposed:

$$(\rho u_\mathrm{i})^{n+1} = (\rho u_\mathrm{i})^{n} + \Delta t \left(-\frac{\partial \rho u_\mathrm{i} u_\mathrm{j}}{\partial x_\mathrm{j}} + \frac{\partial \tau_\mathrm{ij}}{\partial x_\mathrm{j}} \right) - \Delta t \frac{\partial p}{\partial x_\mathrm{i}} = (\rho u_\mathrm{i})^{*} - \Delta t \frac{\partial p}{\partial x_\mathrm{i}} \tag{5.58}$$

Where $(\rho u_\mathrm{i})^{*}$ denotes the predicted momentum using only the convective and diffusive contributions. Applying the divergence operator to this equation yields:

$$\left(\frac{\partial \rho u_\mathrm{i}}{\partial x_\mathrm{i}} \right)^{n+1} = \frac{\partial}{\partial x_\mathrm{i}} \left((\rho u_\mathrm{i})^{*} - \Delta t \frac{\partial p}{\partial x_\mathrm{i}} \right) \tag{5.59}$$

This finding can be combined with the divergence condition found from the conservation of mass:

$$-\left(\frac{\partial \rho}{\partial t} \right)^{n+1} = \left(\frac{\partial \rho u_\mathrm{i}}{\partial x_\mathrm{i}} \right)^{*} - \Delta t \frac{\partial}{\partial x_\mathrm{i}} \left(\frac{\partial p}{\partial x_\mathrm{i}} \right)^{n+1} \tag{5.60}$$

Which yields the following identity for the pressure:

$$\frac{\partial}{\partial x_\mathrm{i}} \left(\frac{\partial p}{\partial x_\mathrm{i}} \right)^{n+1} = \frac{1}{\Delta t} \left(\left(\frac{\partial \rho}{\partial t} \right)^{n+1} + \left(\frac{\partial \rho u_\mathrm{i}}{\partial x_\mathrm{i}} \right)^{*} \right) \tag{5.61}$$

This equation is a Poisson-type equation that can be solved implicitly using an appropriate algorithm. The solver used must be chosen with respect to the case and boundary conditions. Typical candidates are the successive-overrelaxation Gauss-Seidel solver, the Jacobi solver, or the conjugate gradient method – all of which are well established, and for details on their algorithmic structure the reader is referred to the appropriate literature [218]. It may now be argued that the inclusion of an iterative solver will add a significant amount of computational

cost, which may not encourage the use of incompressible frameworks. However, it should be noted that incompressible solvers do not require the resolution of acoustic phenomena, which greatly increases the possible time step size. Finally, the pressure obtained is not of thermodynamic nature, but only the dynamic pressure of the fluid motion, and therefore must not be used for further thermodynamic analysis.

The present work employs an density based on the thermochemical state and referred to as target density, for providing the temporal derivative of the density based on the work of Kempf [119] – for open access the reader is referred to the related work of Stein [266] and Pierce [207]. The stages for a single timestep included in the present algorithm are summarized as follows:

1. Calculate the predicted momentum $(\rho u_\mathrm{i})^*$ at the present timestep n using all known contributions to the momentum equation except the pressure:

$$(\rho u_\mathrm{i})^* = (\rho u_\mathrm{i})^n + \Delta t \left(-\frac{\partial \rho u_\mathrm{i} u_\mathrm{j}}{\partial x_\mathrm{j}} + \frac{\partial \tau_\mathrm{ij}}{\partial x_\mathrm{j}} \right) \tag{5.62}$$

   and applying the respective boundary conditions.

2. Solve all scalar transport equations besides the momentum equation using u_i^n to obtain the conserved variables $(\rho\phi_\mathrm{m})^{n+1}$ (where $m = 1 \ldots N$). The density is potentially a function of ϕ_m and hence, the additional transport equation is included to give a prediction of ρ^{n+1} to be used to extract ϕ_m^{n+1} from $(\rho\phi_\mathrm{m})^{n+1}$. Thus, the density based on the reactive models can be calculated as $\rho_\mathrm{s} = f\left(\phi_\mathrm{m}^{n+1}\right)$. The respective boundary conditions for the conserved scalars need to be applied.

3. Use the target density to calculate the density gradient as:

$$\frac{\partial \rho}{\partial t} \approx \frac{\rho_\mathrm{s} - \rho^{n+1}}{\Delta t} \tag{5.63}$$

   The target divergence is inserted into the Poisson-type equation and is implicitly solved for the pressure. The respective boundary conditions for the pressure are applied.

4. Assemble the correct momentum field $(\rho u_\mathrm{i})^{n+1}$ using the pressure gradient and apply the respective boundary conditions for the momentum field.

As the pressure is obtained using this procedure and then merged into the momentum equation, some aspects of the spatial discretization gain even more relevance. For demonstration purposes, an excerpt of the momentum conservation law is presented:

$$\frac{\partial \rho u_\mathrm{i}}{\partial x_\mathrm{i}} = -\frac{\partial p}{\partial x_\mathrm{i}} + \ldots \tag{5.64}$$

This structure can be used to identify the nature of the pressure. The pressure is a scalar field and acts as an additional acceleration away from the pressure peaks as dictated by the gradient. The equation is treated using Euler's explicit time and CDS spatial discretization for the one-dimensional case:

$$\frac{(\rho u)_{\mathrm{C}}^{n+1} - (\rho u)_{\mathrm{C}}^{n}}{\Delta t} = \frac{p_{\mathrm{w}}^{n} - p_{\mathrm{e}}^{n}}{\Delta x} \tag{5.65}$$

The CDS discretization then estimates the face values of the pressure by the center values of the neighboring cells $\mathrm{w} = (\mathrm{W} + \mathrm{C})/2$ and $\mathrm{w} = (\mathrm{C} + \mathrm{E})/2$ ultimately yielding:

$$(\rho u)_{\mathrm{C}}^{n+1} = (\rho u)_{\mathrm{C}}^{n} + \frac{\Delta t}{2\Delta x}\left(p_{\mathrm{W}}^{n} - p_{\mathrm{E}}^{n}\right) \tag{5.66}$$

The potential problems with this equation become apparent. The change in momentum in a cell C due to pressure gradients depends only on its neighboring values, but not on the pressure value within the same cell. Hence, decoupling between the momentum and the pressure field may occur, which potentially leads to unphysical pressures as not the absolute values but the relative pressure values are now of importance. This is also referred to as checkerboarding due to the independence solutions of odd and even cell indices on a cubic grid [69]. The most common approach found in the literature to tackle checkerboarding is referred to as staggering [93]. While collocated meshes store all variables at the cell centers, staggered meshes compute the momentum equations at the cell-face centers of the volumes used for the other transported variables and the pressure. Staggered meshes typically come with increased computational cost and are more difficult to formulate on unstructured meshes. A more convenient method that does not depend on the architecture of the mesh has been proposed by Rhie and Chow [227]. This approach prevents the decoupling of momentum and pressure by applying a correction to the velocity obtained at the cell faces that emulates the effects of a staggered mesh. Ultimately, this leads to possible checkerboard patterns in the pressure field modifying the transport velocity at the cell faces in such a way, that these patterns are removed due to change of mass transport. Following the nomenclature from the example above, the modification for the eastern cell face reads:

$$u_{\mathrm{e}}^{n+1} = \frac{1}{2}\left(\frac{(\rho u)_{\mathrm{C}}^{*}}{\rho_{\mathrm{C}}^{n+1}} + \frac{(\rho u)_{\mathrm{E}}^{*}}{\rho_{\mathrm{E}}^{n+1}}\right) - \Delta t \frac{\left(p_{\mathrm{E}}^{n+1} - p_{\mathrm{C}}^{n+1}\right)/\Delta x}{\left(\rho_{\mathrm{C}}^{n+1} + \rho_{\mathrm{E}}^{n+1}\right)/2} \tag{5.67}$$

5.3 Boundary Treatment

5.3.1 Conventional boundary conditions

The NSE form a set of partial differential equations with an additional set of constraint, and is therefore considered a boundary value problem. The additional constraints serve

the purpose of finding a unique solution – the problem is then referred to as being well posed. The process of translating the physical problem into the computational domain was introduced. To incorporate the boundary values into the computing problem, an additional type of cells is introduced. While all conservation laws for the discretized domain are solved using physical cells, additional layers of cells – the *ghost cells* – are wrapped around the set of physical cells. The ghost cells are filled with values dictated by the boundary conditions which are used to complete the discretization at the outer physical cells and their values are updated at each timestep. The integration of ghost cells into the computational domain for a one-dimensional case is shown in Fig. 5.8. The ghost cells form layers around the physical domain and the number of layers typically depends on the spatial discretization. If higher order numerical schemes are employed, a larger number of ghost cell layers will be required.

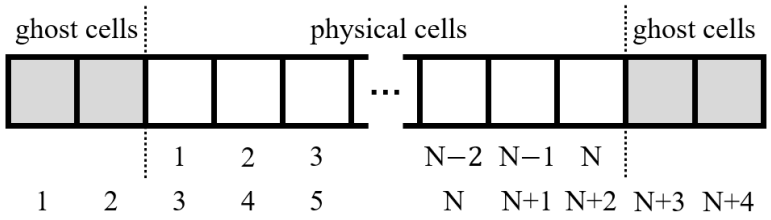

Figure 5.8 Location of ghost cells on the computational grid and the change of indexing for the one-dimensional case.

The most classical boundary conditions typically consist of two types, which either directly prescribe a certain value at the boundary or implicitly prescribe values by dictating a certain gradient. The Dirichlet condition dictates a value for the respective quantity directly at the boundary. The von-Neumann condition prescribes a gradient for the transported quantity at the boundary. In mathematical literature it is common practice to further generalize these two fundamental boundary conditions to the so called Robin condition, which aims at setting a weighted combination of a Dirichlet and a von-Neumann condition at the boundary [3]. The third fundamental boundary condition is the periodic boundary condition. As the name implies, the periodic boundary condition closes two opposite boundaries with each other. This causes the fluid to leave the domain on one side and re-enter on the corresponding opposite side. This boundary condition is very precise, but appears to be of more academic value. Hence, this boundary condition is heavily employed in benchmark cases for model development as well as in turbomachinery applications due to its rotational symmetry.

5.3.2 Navier-Stokes characteristic boundary conditions

It becomes evident that, due to the nature of the solver framework used, special care needs to be addressed to the boundary conditions, as they will interfere with the pressure waves traveling through the domain. This is particularly the case for pressure waves that travel out

Table 5.3 Summary of the most commonly employed boundary conditions in CFD problems.

Boundary Condition	Prescription
Dirichlet	$\phi\left(x_{\mathrm{GC}}\right) = f$
von Neumann	$\partial\phi/\partial\vec{n}\left(x_{\mathrm{GC}}\right) = f$
Periodic	$\phi\left(x_{\mathrm{GC}}\right) = \phi\left(x_{\mathrm{N}}\right)$

of the domain. Standard boundary conditions will typically lead to at least partial reflection of the pressure waves, resulting in contamination of the solution, and in the worst case, numerical instability. This is a consequence of the fact that conventional boundary conditions impose fixed or gradient-based values at the boundary, which do not exhibit compression and relaxation for sound waves approaching the boundary. Therefore, the boundary conditions must be designed in such a way that they do not interfere with the outgoing pressure waves. This desired property of boundary conditions is also referred to as non-reflecting boundary conditions. For the case of compressible NSE-based solvers, the concept was introduced by Poinsot and Lele [213] and is henceforth known as *Navier-Stokes Characteristic Boundary Conditions* (*NSCBC*). For a detailed overview in the context of reactive systems, the reader is referred to the work of Poinsot and Veynante [212].

The propagation of mathematical waves in a set of hyperbolic equations is typically described by the propagation velocity λ of the wave and the variation of its amplitude L in space. Assuming that the original equation is given in the common form of a conservation law, it is referred to as the primitive form of the equation with the vector of primitive state variables $\boldsymbol{U}$:

$$\frac{\partial \boldsymbol{U}}{\partial t} + A\frac{\partial \boldsymbol{U}}{\partial x} + C = 0 \tag{5.68}$$

Using characteristic analysis, the propagation velocity and amplitude variation for the waves featured in the primitive set of equations can be obtained, leading to the *characteristic* form of the equation – which represents the propagation of waves. A detailed derivation for the case of the Euler equations was performed by Thompson [279, 280]. The same procedure is performed for the Navier-Stokes equations and leads to the following set of equations, which

is solved at a boundary normal to the direction x when using the NSCBC:

$$\frac{\partial \rho}{\partial t} + d_1 + \frac{\partial \rho v}{\partial y} + \frac{\partial \rho w}{\partial z} = 0 \tag{5.69}$$

$$\begin{aligned}\frac{\partial \rho E}{\partial t} + \frac{1}{2}\left(\sum_{k=1}^{3} {u_\mathrm{k}}^2\right) d_1 + \frac{d_2}{\gamma - 1} + \rho u d_3 + \rho v d_4 + \rho w d_5 \\ + \frac{\partial v\left(\rho E + p\right)}{\partial y} + \frac{\partial w\left(\rho E + p\right)}{\partial z} = \frac{\partial}{\partial x_\mathrm{i}}\left(\kappa \frac{\partial T}{\partial x_\mathrm{i}}\right) + \frac{\partial u_\mathrm{i} \tau_\mathrm{ij}}{\partial x_\mathrm{i}} + \dot{Q}\end{aligned} \tag{5.70}$$

$$\frac{\partial \rho u}{\partial t} + u d_1 + \rho d_3 + \frac{\partial \rho v u}{\partial y} + \frac{\partial \rho w u}{\partial z} = \frac{\partial \tau_\mathrm{1j}}{\partial x_\mathrm{j}} \tag{5.71}$$

$$\frac{\partial \rho v}{\partial t} + v d_1 + \rho d_4 + \frac{\partial \rho v v}{\partial y} + \frac{\partial \rho w v}{\partial z} + \frac{\partial p}{\partial y} = \frac{\partial \tau_\mathrm{2j}}{\partial x_\mathrm{j}} \tag{5.72}$$

$$\frac{\partial \rho w}{\partial t} + w d_1 + \rho d_5 + \frac{\partial \rho v w}{\partial z} + \frac{\partial \rho w w}{\partial z} + \frac{\partial p}{\partial z} = \frac{\partial \tau_\mathrm{3j}}{\partial x_\mathrm{j}} \tag{5.73}$$

$$\begin{aligned}\frac{\partial \rho Y_\mathrm{k}}{\partial t} + Y_\mathrm{k} d_1 + \rho d_{5+\mathrm{k}} + \frac{\partial \rho v Y_\mathrm{k}}{\partial y} + \frac{\partial \rho w Y_\mathrm{k}}{\partial z} = \frac{\partial}{\partial x_\mathrm{j}}\left(\rho D \frac{\partial Y_\mathrm{k}}{\partial x_\mathrm{j}}\right) - \dot{\omega}_\mathrm{k} \\ \text{for } k = 1 \ldots N\end{aligned} \tag{5.74}$$

The vector d_i is a result of the characteristic analysis and contains derivatives of the primitive variables featured in the Navier-Stokes equations [279, 280]. The terms are calculated as:

$$d_\mathrm{i} = \begin{pmatrix} d_1 \\ d_2 \\ d_3 \\ d_4 \\ d_5 \\ d_{5+\mathrm{k}} \end{pmatrix} = \begin{pmatrix} \frac{1}{c^2}\left[L_2 + \frac{1}{2}(L_5 + L_1)\right] \\ \frac{1}{2}(L_5 + L_1) \\ \frac{1}{2\rho c}(L_5 - L_1) \\ L_3 \\ L_4 \\ L_{5+\mathrm{k}} \end{pmatrix} = \begin{pmatrix} \frac{\partial \rho u}{\partial x} \\ \rho c^2 \frac{\partial u}{\partial x} + u \frac{\partial p}{\partial x} \\ u \frac{\partial u}{\partial x} + \frac{1}{\rho} \frac{\partial p}{\partial x} \\ u \frac{\partial v}{\partial x} \\ u \frac{\partial w}{\partial x} \\ u \frac{\partial Y_\mathrm{k}}{\partial x} \end{pmatrix} \tag{5.75}$$

Since these derivatives d_i can be calculated directly from the characteristic wave amplitude variations L_i and the wave propagation velocity λ_i, rewriting the Navier-Stokes equations in this form allows direct control of the wave propagation through the boundaries. The characteristic velocities λ_i of the waves follow from the analysis of the eigenvalues of the system of equations:

$$\lambda_1 = u - c \; ; \quad \lambda_2 = \lambda_3 = \lambda_4 = \lambda_{5+\mathrm{k}} = u \; ; \quad \lambda_5 = u + c \tag{5.76}$$

Considering the velocity u to be surface-normal to the boundary and c being the local speed of sound given by $c^2 = \gamma p / \rho$ under the assumption of adiabatic sound wave propagation in an ideal gas at sufficiently high speed of the sound wave.

The eigenvalues and the gradients of the primitive variables are used to reconstruct the amplitude variation of the traveling waves L_i, which are calculated as:

$$L_1 = \lambda_1 \left(\frac{\partial p}{\partial x} - \rho c \frac{\partial u}{\partial x} \right) \tag{5.77}$$

$$L_2 = \lambda_2 \left(c^2 \frac{\partial \rho}{\partial x} - \frac{\partial p}{\partial x} \right) \tag{5.78}$$

$$L_3 = \lambda_3 \frac{\partial v}{\partial x} \text{ and } L_4 = \lambda_4 \frac{\partial w}{\partial x} \tag{5.79}$$

$$L_5 = \lambda_5 \left(\frac{\partial p}{\partial x} + \rho c \frac{\partial u}{\partial x} \right) \tag{5.80}$$

$$L_{5+k} = \lambda_{5+\mathrm{k}} \frac{\partial Y_\mathrm{k}}{\partial x} \tag{5.81}$$

The strategy of the NSCBC is to advance the solution at the boundary in time using a separate system of equations given in Eq. 5.69 - 5.74, which allows for control of the waves crossing the boundaries of the domain. All featured terms tangent to the boundary can be treated using the same numerical approximations as for the main computational domain. The terms L_i are aligned normal to the domain boundary, which requires one-sided differences for calculating L_i of the waves leaving the domain through the boundary. However, the amplitude variations L_i of the waves entering the domain from the outside are unknown. Although there is no exact approach to determine these amplitude variations in a general form for three-dimensional viscous problems, expressions can be found for inviscid one-dimensional equations. To fit these values to the NSE, the one-dimensional inviscid solutions are augmented with viscous terms and terms representing the neglected dimensions. This approach is widely known as the *Local One-Dimensional Inviscid* (*LODI*) relations. The procedure is not considered a physically correct boundary condition, but serves as a supplement to determine the characteristic wave amplitude variations L_i at the boundary.

The set of corresponding LODI equations is obtained by reducing the original Navier-Stokes equations at the boundary given in Eq. 5.69 - 5.74 by neglecting the transverse, viscous and reaction contributions. The LODI relations can be used to formulate equations that close the surface normal gradients of the primitive variables at the boundary using the

wave amplitude variations:

$$\frac{\partial \rho}{\partial x} = \frac{1}{c^2}\left[\frac{L_2}{u} + \frac{1}{2}\left(\frac{L_5}{u+c} + \frac{L_1}{u-c}\right)\right] \tag{5.82}$$

$$\frac{\partial p}{\partial x} = \frac{1}{2}\left(\frac{L_5}{u+c} + \frac{L_1}{u-c}\right) \tag{5.83}$$

$$\frac{\partial u}{\partial x} = \frac{1}{2\rho c}\left(\frac{L_5}{u+c} - \frac{L_1}{u-c}\right) \tag{5.84}$$

$$\frac{\partial v}{\partial x} = L_3 \tag{5.85}$$

$$\frac{\partial w}{\partial x} = L_4 \tag{5.86}$$

$$\frac{\partial T}{\partial x} = \frac{T}{\gamma p}\left[-\frac{L_2}{u} + \frac{1}{2}(\gamma - 1)\left(\frac{L_5}{u+c} + \frac{L_1}{u-c}\right)\right] \tag{5.87}$$

5.3.3 Static geometrical boundaries

A crucial aspect of most CFD frameworks is the design of the computational grid. The quality of the grid has a massive impact on the accuracy of the CFD framework and must be appropriate for the given problem. For CFD of technical systems, the computational grid is limited by boundaries that can allow or prohibit fluid transport. Boundaries with fluid transport properties were discussed in Sec. 5.3.1. Typically, the remaining boundaries of a technical system are given by walls of a certain geometry. Due to their ability to accurately represent even complicated geometries, unstructured meshes as described in Sec. 5.1.1 are the most common meshing-strategy in open-source CFD. The present work, however, employs a structured equidistant cubic mesh and hence, cannot arbitrarily refine or rotate the cells in order to satisfy geometric constraints. Instead, the constraining geometry of the given problem is incorporated by distinguishing the cells in the computational domain between fluid-type and wall-type cells, where the fluid-type cells store the solutions to the conservation equations and the wall-type cells are computed to mimic the effects of walls. This typically results in an overabundance of cells, which is accepted for the sake of the simplicity of the grid. The walls in this work are inelastic and enforce the zero-slip condition for the velocity field. The approach employed within this work is referred to as the *Immersed Boundary* (*IB*) method and was proposed by Peskin [202]. To maintain computational efficiency, the conservation equations are solved for all fluid-type cells. The wall-type cells are rewritten as such that no convective or diffusive fluxes occur at the fluid-wall cell interfaces. Convective fluxes will vanish because the convection velocity is forced to have a value of zero when a wall-type cell is adjacent to the fluid-type cell face. Velocities and momentum in the first layer of wall-type cells are mirrored with a negative sign to satisfy the zero-slip boundary condition.

The IB-method is applicable to the description of moving boundaries. The moving geometry is modeled in a Lagrangian framework and each cell occupied by the geometry

is treated as an immersed boundary. A key-aspect for this description is the concept of *mirror-flow* as introduced by Forrer and Berger [71]. This method imposes the values in the immersed boundary cells describing a moving geometry using an extrapolation between the kinematics of the moving geometry and the neighboring fluid cells. A disadvantage is the coupling between the resolution of the geometry and the domain. The given geometry must be decomposed into cells using a voxelizer prior to the simulation run, leading to an increased amount of preprocessing. This approach was pioneered and evaluated by Nguyen et al. [191].

5.3.4 Moving geometrical boundaries

The description of moving geometry is a desirable aspect in a variety of engineering applications and CFD problems. There are several approaches to incorporate a moving geometry into an existing solver and the most common approaches are: cell deformation, cell splitting and cell occupation. The previously introduced unstructured meshes typically describe the motion of the geometry by deforming existing cells, which is an attractive approach in these solvers because the tabulation and identification of cells does not need to be modified. Existing cell interfaces do not need to be modified, and during volume reduction, resolution near the moving boundary increases due to the formation of smaller cells. For solvers based on structured meshes, cell splitting is a common approach. Structured meshes generally require more elaborate workarounds for cell deformation. A common compromise is to split cells that are partially occupied by moving geometry, as this counteracts the loss of resolution when cells are occupied by both fluid and geometry. For structured meshes in solvers that cannot efficiently describe cell splitting, the approach proposed earlier by Nguyen [191] provides a powerful alternative. This approach combines the ideas of Forrer and Berger [71] with the concept of immersed boundaries of Peskin [202] and is particularly relevant for this work.

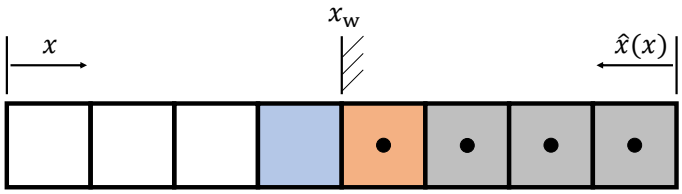

Figure 5.9 Visualization of the coordinate transformation performed for the mirror-flow approach as presented by Forrer and Berger [71].

Forrer and Berger base their method on the concept of *mirror flow*, which was formulated for inviscid flows [71]. The notion of mirror flow results from the introduction of a transformed coordinate linking each coordinate x outside the wall to a corresponding coordinate $\widehat{x}$ inside the wall, both having the same distance from the solid-fluid interface x_w. The transformation reads:

$$\widehat{x}(x,t) = 2x_\mathrm{w}(t) - x \tag{5.88}$$

And the respective velocity can be found by applying the time derivative:

$$\widehat{u} = 2\dot{x}_{\mathrm{w}} - u \tag{5.89}$$

With this identity being used in the following to correct the velocities within the immersed boundaries. The acceleration of the wall will be used to adjust the pressure values in the wall. The treatment of the density and pressure requires the application of a zero-gradient boundary condition at the moving interface. While the density does not require any further modifications, the pressure increment directly at the wall can be obtained from the acceleration of the moving wall $\ddot{x}_{\mathrm{w}}$ using the second law of Newton:

$$\Delta p = -\rho(x_{\mathrm{w}})\ddot{x}_{\mathrm{w}} \tag{5.90}$$

The approach of incorporating moving geometries into the solver is based on the ideas of Forrer and Berger [71] as well as Nguyen et al. [191] and necessarily requires knowledge of the thermodynamic pressure which is obtainable from the equation of state, e.g. given in Eq. 5.54 as $p = \rho R_{\mathrm{m}} T/W$. Due to the accessibility of the pressure, the original works based their ideas on the compressible solver-framework. The procedure embedded in the algorithm for one timestep can be summarized as follows:

1. Calculate the thermochemical state
2. Obtain the thermodynamic pressure and update all related boundary conditions
3. Update the density to take into account the changes in the boundary conditions of the pressure
4. Enforce a zero-gradient boundary condition at the wall cells for the density ρ
5. Move the respective boundaries; in particular within this framework: relocate the immersed boundary based on the new boundary location
6. Apply new values in the moving wall for:
   (a) Pressure p
   (b) Momentum u_{i}
   (c) Energy e

   At the respective fluid-structure interfaces using the framework presented by Forrer and Berger [71]
7. Enforce a zero-gradient boundary condition at the wall cells for all remaining transported quantities ϕ

8. Calculate additional source terms
9. Solve all transport equations for one timestep
10. Update all boundary conditions

In the *Moving Immersed Boundary* (*MIB*) method applied by Nguyen et al. [191], a geometric shape is decomposed into a cloud of data points. These data points are treated in a Lagrangian framework, also referred to as *Lagrangian particles*. Each particle is characterized by a location x_i, a velocity v_i and an acceleration a_i. The decomposition of a geometry into discrete Lagrangian particles for a given mesh can be achieved using a voxelizer. The acceleration, velocity and position of these particles can either be derived from the kinematic laws given by the problem, or can be obtained by applying Newton's theorem and integrating the acceleration and velocity to obtain the positions at each timestep. However, it is strongly recommended that these properties be tabulated or calculated analytically, if possible, to avoid any numerical error affecting the motion of the geometry. A decomposition of a geometry into a cloud of particles is shown in Fig. 5.10 for two different grid resolutions.

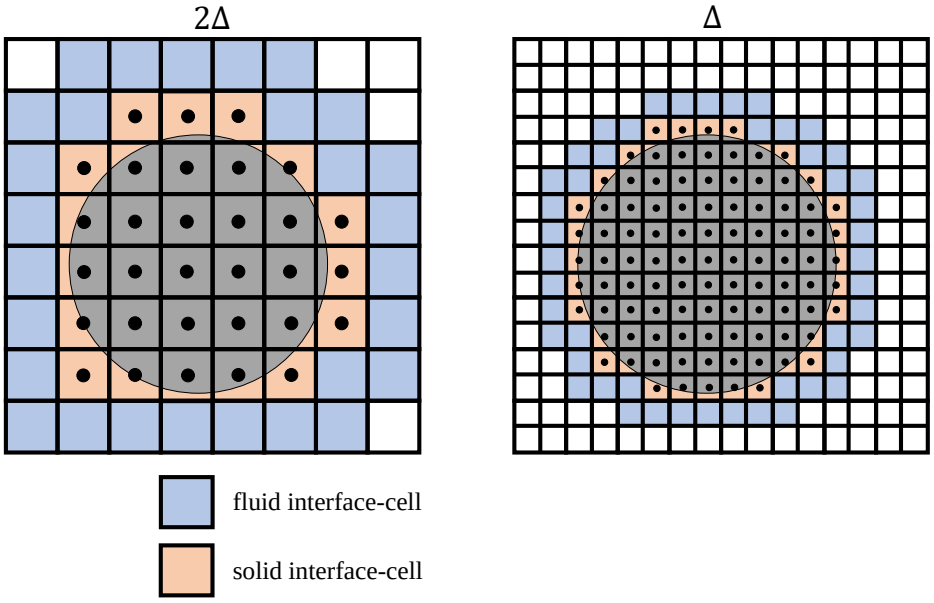

Figure 5.10 Decomposition of a geometrical shape into data points and their distribution on the numerical grid. Two gridsizes of the domain are presented two demonstrate the effect of voxelization on the grid.

It is evident that the description of the geometry is directly coupled to the grid resolution. The visualization shows that the shape of the geometry when projected onto the numerical grid depends on the treatment of the data points on cells containing fluid and geometry. Ultimately, there is no rule on how to treat these cells, but in the context of this work it was found that the geometry is better preserved on fine grids when the ratio of the cell volume

occupied by the geometry to the total cell volume is greater than zero, which is also applied in this work. On coarser meshes, it is recommended to define a case-dependent threshold for the treatment of these cells.

In this work, the particle acceleration, velocity and position are calculated analytically during the simulation run in order to avoid numerical errors due to integration when applying kinematic laws.

The velocity within the fluid-structure interface cells is adjusted based on the velocity of the moving boundary v_i and the average of the velocity values $u^\mathrm{n}_\mathrm{i,MIB}$ in all neighboring interface cells $\mathrm{n_{NB}}$ before their respective correction:

$$u^{\mathrm{n+1}}_\mathrm{i,MIB} = 2v^{\mathrm{n+1}}_\mathrm{i} - \sum^{\mathrm{n_{NB}}} u^\mathrm{n}_\mathrm{i,MIB}/\mathrm{n_{NB}} \tag{5.91}$$

A similar procedure is used for the pressure in the moving boundary. Based on the acceleration of the moving boundary, a pressure gradient is added to the fluid cells adjacent to the moving boundary. The pressure gradient is calculated from the acceleration of the moving boundary and the average of the density values $\rho^\mathrm{n}_\mathrm{MIB}$ in all neighboring boundary cells $\mathrm{n_{NB}}$:

$$u^{\mathrm{n+1}}_\mathrm{i,MIB} = -a^{\mathrm{n+1}}_\mathrm{i} \sum^{\mathrm{n_{NB}}} \rho^\mathrm{n}_\mathrm{MIB}/\mathrm{n_{NB}} \tag{5.92}$$

The energy in the moving wall is simply increased by the kinetic energy due to its movement. This kinetic energy is calculated from the velocity of the particle in each cell containing a moving boundary. While in static geometries the wall simply holds its respective internal energy, the energy value in the moving wall reads:

$$e_\mathrm{MIB} = \frac{1}{2} v^2_\mathrm{i} + c_\mathrm{v,MIB} T_\mathrm{MIB} \tag{5.93}$$

The advantage of the approach by Nguyen et al. [191] becomes evident. The equations to be introduced into the solver are of low complexity, since only Lagrangian particles need to be simulated and the values in the now moving immersed boundary need to be adjusted. The corrected values are calculated in such a way that the immersed boundary method works as before: the fluxes are blocked at static boundaries and modified at moving boundaries to account for the change in the conserved variables. It is important to note that the fluxes at the moving boundaries are not blocked, but instead fluxes are introduced to account for the displacement of the fluid at the boundary. This allows the method to be highly efficient with little additional computational time required.

The explained procedure allows for the movement of walls within the computational domain using Lagrangian particles. The particles are moved through the domain in steps smaller than the gridsize. All cells occupied by a Lagrangian particle are blocked by enforcing immersed boundary treatment. If a wall moves to another cell, that cell is blocked and

treated as an immersed boundary. The values of the conserved quantity within this cell are then adjusted to allow the description of the moving wall. When the wall leaves a cell, the cell is no longer treated as an immersed boundary and the conservation equations are solved again for this cell. The cell needs to be initialized with physically meaningful values. However, the true physical state in the released cell is unknown, so an average of the values in all neighboring cells is used.

5.3.5 Turbulent inflow generation

The turbulent inflow generator is a powerful method to artificially induce turbulent-like behavior at the inflow boundary of the domain. This is of crucial importance for almost all LES or DNS of technical applications due to their mostly turbulent nature. While the simulation of laminar-turbulent transition can be achieved by an appropriate choice of the inlet geometry, the additional cost of including it in the computational domain can be enormous. Due to their general importance and, in particular, their relevance in this work, the digital inflow generator of Klein [133] and its modification by Kempf [120] are discussed. For related work following a similar philosophy, the reader is referred to the work of Glaze, Lee, and Smirnov [85, 157, 261].

The aim of a turbulence generator is to provide a velocity signal u_i with certain desired statistical properties such as averages, fluctuations, cross-correlations or energy-spectra. The first step in obtaining this signal is to generate a signal U_i with two-point statistics characterizing the length scale and the energy spectrum. The digital filtering technique creates the signal U_i based on a series of randomized data r_m with $\langle r_\mathrm{m} \rangle = 0$, $\langle r_\mathrm{m} r_\mathrm{m} \rangle = 1$ and $\langle r_\mathrm{m} r_\mathrm{n} \rangle = 0$ for $m \neq n$. Applying a digital filter on this data yields:

$$u_\mathrm{m} = \sum_{n=-N}^{N} b_\mathrm{n} r_\mathrm{m+n} \tag{5.94}$$

With the kernel size $2N + 1$ and the filter coefficients b_n. To extend this definition to the desired three dimensions, the proposed one-dimensional approach is convolved, yielding the three-dimensional filter $b_\mathrm{ijk} = b_\mathrm{i} b_\mathrm{j} b_\mathrm{k}$. By applying the filter to the randomized data, a nonlinear implicit relationship between the filter coefficients and the autocorrelation of the filtered signal u_m can be found [133]. The filter coefficients can be obtained from the implicit relation if the auto-correlation is given, which in the discussed works is assumed to be a Gaussian function based on the length scale L. So far, it can be noted that this provides an elegant way to include the length scale of the inflowing turbulent structures. Thus, the autocorrelation for the one-dimensional stencil at cell k is given by:

$$R_\mathrm{uu}(k) = \exp\left(-\frac{k^2 \Delta x^2}{4L^2} \right) \tag{5.95}$$

Thus, following Klein [133], the coefficients of the digital filter can be reconstructed as:

$$b_\mathrm{k} \approx \widetilde{b}_\mathrm{k} / \left(\sum_{j=-N}^{N} \widetilde{b}_\mathrm{j}^2 \right)^{0.5} \text{ with } \widetilde{b}_\mathrm{k} = \exp\left(-\frac{k^2 \Delta x^2}{2L^2} \right) \tag{5.96}$$

It was the idea of Kempf [120], who suggested to use the separability of this filter formulation and to perform three consecutive one-dimensional filters instead of one three-dimensional filtering operation. This approach reduces the computational complexity from $(2N+1)^3$ cells to $3\,(2N+1)$, resulting in a highly efficient implementation of the digital filter-based inflow generator.

In the second step, the cross-correlations between the different velocity components are established, which is not necessary in the case of homogeneous isotropic turbulence. The cross-correlations are typically obtained following the idea of Lund [172]. First, the signal from the first step is generated in such a way that $\langle U_\mathrm{i} \rangle = 0$ and $\langle U_\mathrm{i} U_\mathrm{i} \rangle = \delta_\mathrm{i}$, so that the desired velocity signal reads $u_\mathrm{i} = \langle u_\mathrm{i} \rangle + a_\mathrm{ij} U_\mathrm{j}$. The desired mean $\langle u_\mathrm{i} \rangle$ depends on the problem under investigation. The correlations are obtained from the tensor a_ij, which is defined as follows:

$$a_\mathrm{ij} = \begin{pmatrix} (R_{11})^{1/2} & 0 & 0 \\ R_{21}/a_{11} & (R_{22} - a_{21}^2)^{1/2} & 0 \\ R_{31}/a_{11} & (R_{32} - a_{21} a_{31})/a_{22} & (R_{33} - a_{31}^2 - a_{32}^2)^{1/2} \end{pmatrix} \tag{5.97}$$

Where R_ij is the Reynolds stress-tensor to be prescribed.

5.3.6 Interblock boundaries – Message-Passing Interface

Based on the findings of the previous sections, it is clear that LES and DNS of engineering applications require fine grid resolutions, which leads to a large number of computational cells. Such a number cannot be handled by a single processor core, but by multiple cores. Therefore, the domain needs to be decomposed into subdomains, each identified by a unique rank and handled by a separate core. The number of cores is equal to the number of ranks. Due to the decomposition, each rank will have cells at the outer boundaries that lack neighboring cells to close the numerical discretization. To counteract this problem, the parallelization in this work relies on a distributed memory approach that exchanges information about each rank and its neighbors. The technique used to exchange this information is called the *Message Passing Interface* (*MPI*).

A major strength of the MPI employed within this work is achieved by the so-called non-blocking communication. This form of communication allows for the exchange of data in the background while subsequent tasks are performed simultaneously. Another aspect of saving computational costs time is the sequential evaluation of diffusive fluxes, convective fluxes and time integration for each conserved variable. The communication for one conserved variable is started after the time integration, followed by the solution process for the next

conserved variable. Another aspect of the iterative solver required for the later introduced projection method is the need to communicate only the cells adjacent to the rank boundary. This allows the iterative solver to be designed in such a way that the cells adjacent to the boundary are communicated while the computation of the remaining cells is already started.

Although MPI is a parallelization technique, it comes with a set of boundary conditions. However, these boundary conditions do not address the boundaries of the physical domain, but rather the inner boundaries between the ranks. Fig. 5.11 illustrates the use of ghost cells for the decomposition of the domain into ranks.

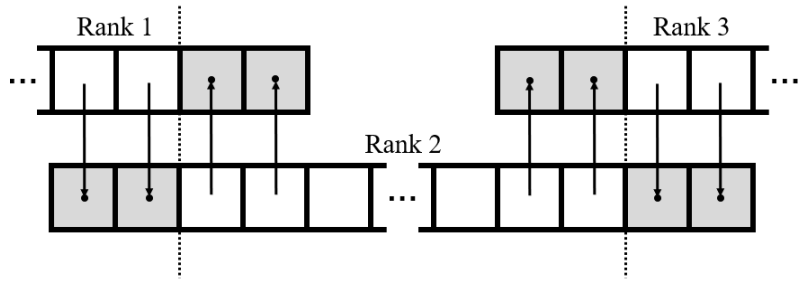

Figure 5.11 Arrangement of ghost cells for the one-dimensional parallelization case based on three ranks.

For each transported quantity, the ghost cells of a rank need to be filled with the values of the respective quantity within the cells on the neighboring rank adjacent to the boundary of this particular ranks. As the three-dimensional case is most commonly encountered, this communication between the rank has to be performed with up to eight neighboring ranks depending on the location of the rank within the whole ensemble of ranks. In this particular work the exchange occurs at least once during each Runge-Kutta stage. Hence, it is only of interest to design the communication operation as efficient as possible, especially with respect to highly-parallelized simulations and also to avoid unnecessary communication.

6 A-posteriori Large-Eddy Simulation assessment of subgrid-scale closures for bounded passive scalars

Authors: L. Engelmann, M. Klein, A. Kempf

This chapter including all figures and tables was previously published in *Computers and Fluids, L. Engelmann, M. Klein, A. Kempf, A-posteriori Large-Eddy Simulation assessment of subgrid-scale closures for bounded passive scalars, 2021; 218: 104840* and is reprinted with permission from Elsevier. L. Engelmann developed the software for the presented simulations and the post-processing, performed all calculations, wrote the manuscript and generated all figures and tables. M. Klein and A. Kempf contributed corrections, discussions and proofreading.

Abstract

Scale similarity or gradient models represent attractive, functionally simple expressions for large eddy simulation (LES) subgridscale (SGS) models, showing excellent behaviour in a-priori LES studies for small to moderate filter sizes. However, when applied a-posteriori to real LES calculations, they frequently suffer from numerically unstable behavior. A recent regularization approach revealed promising results for both wall-bounded and free turbulent flows. One attractive feature of this modelling strategy is that it can potentially be applied in many different contexts, such as momentum transport in single or two phase flows, different fluids such as non-Newtonian fluids, etc. The aim of the present study is to test the application of this regularisation technique to turbulent transport of bounded passive scalars. The performance of the model together with suitable discretization strategies will be assessed for turbulent plane free jet simulations. LES results will be benchmarked against DNS calculations of the same configuration obtained with the same code. The new model exhibits good results for momentum and scalar transport, outperforming standard eddy-viscosity models particularly with respect to the prediction of second order moments. Further, they provide good stability and are easy to implement. While the influence of the

This chapter was previously published in Computers and Fluids [59] and is reprinted with permission of the journal.

SGS model for scalar transport is not negligible, it is shown that an appropriate momentum SGS-closure is likely to be more important.

6.1 Introduction

Large-Eddy Simulation (LES) can be considered a state-of-the-art technique for detailed simulations of turbulent flows. Taking account of the growing efficiency of modern CFD-methods and rising computing power, an increase of LES-usage in research and industrial applications can be expected. While LES aims for the resolution of the energy-carrying scales of the flow, a universal behavior of the smaller scales is assumed and henceforth, grids are chosen coarse enough to resolve large-scale turbulent structures only, applying a filter-like effect on the remaining resolved scales. The influence of the unresolved motion on the resolved flow is unknown and has to be expressed by a closure-model based on the resolved quantities, which strongly determines the overall quality of the simulation results. Besides the transport of momentum, the transport of scalars is very important in many applications involving mixing or chemical reactions. Scalars are often bounded between zero and unity, and numerical discretization as well as physical modeling have to obey this constraint. As a result of this, despite the existence of high fidelity SGS closures for scalar transport [293, 184, 192], the gradient diffusion assumption is mostly employed [316].

As a recurring configuration in both natural and technical flows turbulent jet flows have been the subject of numerous experimental and numerical studies. Although the flow-setup is comparatively simple, turbulent jet flows feature flow-phenomena that are challenging to measure and to model, conferring jet flows the status of an important benchmark case. While it is common to compare simulation results with experimental data, the assessment of numerical techniques and modeling strategies in the LES context is preferably performed using DNS reference data. In spite of their apparent simplicity, jet flows are demanding when it comes to proper modelling of the boundary conditions, turbulent inflow, lateral entrainment and turbulent backflow at the outlet boundary. In order to eliminate any systemic errors, model development should ideally be done using DNS data obtained with the same numerical code employing exactly the same boundary conditions. This approach is followed in this work by first establishing a DNS database for a turbulent plane jet at $Re = 10,000$ based on the nozzle width $D = 0.01$m, including scalar transport. This dataset is subsequently used for benchmarking a variety of LES simulations with different combinations of momentum and scalar SGS closures and by employing different discretization techniques. The main goal of the present study is the testing of a recently proposed scale-similarity type model [140] to scalar transport and a scrutinizing assessment of its performance.

This chapter was previously published in Computers and Fluids [59] and is reprinted with permission of the journal.

6.2 Modeling strategy

Even in modern LES, eddy-viscosity models (EVM) remain the most commonly used closures for the subgrid-contribution in the filtered Navier-Stokes equations

$$\tau_{\mathrm{ij}} = \overline{u_{\mathrm{i}} u_{\mathrm{j}}} - \overline{u}_{\mathrm{i}}\ \overline{u}_{\mathrm{j}} \tag{6.1}$$

and share the following form

$$\tau_{\mathrm{ij}}^{EVM} = -2\nu_{\mathrm{t}} \left(\overline{S}_{\mathrm{ij}} - \frac{1}{3} \overline{S}_{\mathrm{kk}} \delta_{\mathrm{ij}} \right) \tag{6.2}$$

with the filtered strain-tensor $\overline{S}_{\mathrm{ij}} = \frac{1}{2}\left(\frac{\partial \overline{u}_{\mathrm{i}}}{\partial x_{\mathrm{j}}} + \frac{\partial \overline{u}_{\mathrm{j}}}{\partial x_{\mathrm{i}}} \right)$. To close the subgrid scalar transport

$$\tau_{\mathrm{j}} = \overline{\phi u_{\mathrm{j}}} - \overline{\phi}\ \overline{u}_{\mathrm{j}} \tag{6.3}$$

the gradient-diffusion hypothesis (GDH) based on the turbulent viscosity ν_{t} and the subgrid Schmidt-number $\mathrm{Sc}_{\mathrm{sgs}}$ is often used

$$\tau_{\mathrm{j}}^{GDH} = -\frac{\nu_{\mathrm{t}}}{\mathrm{Sc}_{\mathrm{sgs}}} \frac{\partial \overline{\phi}}{\partial x_{\mathrm{j}}} \tag{6.4}$$

Generally, the turbulent viscosity ν_{t} is defined as

$$\nu_{\mathrm{t}} = (C_{\mathrm{m}} \Delta)^2 \overline{D}_{\mathrm{m}} \tag{6.5}$$

with the model constant C_{m} and the gridsize Δ (filter-width for LES with explicit filtering). The actual type of eddy-viscosity model aims for an expression of the inverse timescale $\overline{D}_{\mathrm{m}}$. For the well-known Smagorinsky model [259], $\overline{D}_{\mathrm{m}}$ can be expressed with the resolved characteristic rate of strain as

$$\overline{D}_{\mathrm{m}} = \sqrt{2 \overline{S}_{\mathrm{ab}}\ \overline{S}_{\mathrm{ab}}}. \tag{6.6}$$

Nicoud's Sigma-model relies on the ordered singular values $\sigma_1 \geq \sigma_2 \geq \sigma_3$ of the resolved velocity gradient tensor $\overline{g}_{\mathrm{ij}} = \partial \overline{u}_{\mathrm{i}} / \partial x_{\mathrm{j}}$ [192, 230]. The singular values can be calculated as the square roots of the eigenvalues of $\overline{g}_{\mathrm{ik}}\ \overline{g}_{\mathrm{kj}}$ and lead to

$$\overline{D}_{\mathrm{m}} = \frac{\sigma_3 \left(\sigma_1 - \sigma_2\right) \left(\sigma_2 - \sigma_3\right)}{\sigma_1^2} \tag{6.7}$$

The static Smagorinsky and Sigma model will be referred to as SM and SI respectively. The dynamic procedure to determine the Smagorinsky constant by Germano et. al. [80] will be denoted as DSM.

Even though both the Smagorinsky and Sigma models are numerically stable and give satisfactory results in LES, it is known that the underlying gradient-diffusion leads to a

This chapter was previously published in Computers and Fluids [59] and is reprinted with permission of the journal.

poor alignment with the true stresses [250, 16]. This led researchers to the development of scale similarity [16, 169] and gradient models [42, 244]. As these are prone to numerical instability, different regularization techniques have been suggested [244, 1, 142] and a recently proposed methodology - the *KKK* model - by Klein et al. [140] will be employed. For deeper insight, the authors refer to the studies by [1, 142, 138] and only a brief overview of the model equations and model assumptions will be given here. The fundamental idea is that backscatter is likely to cause stability problems. To avoid this problem in the event of backscatter, the subgrid-scale tensor produced by the model is projected onto a tensor that has no energy transfer but can be considered a SGS force. In the following text structural models (such as scale similarity or gradient type models) will be referred to as scale similarity type models (SST). A possible regularization is now introduced. The subgrid momentum-contribution of the first model reads

$$\begin{aligned}\tau_{\mathrm{ij}}^{KKK1} = & \frac{-\tau_{\mathrm{ab}}^{SST}\overline{S}_{\mathrm{ab}} + |-\tau_{\mathrm{ab}}^{SST}\overline{S}_{\mathrm{ab}}|}{-\tau_{\mathrm{ab}}^{SST}\overline{S}_{\mathrm{ab}}}\tau_{\mathrm{ij}}^{SST} \\ & + \left(\tau_{\mathrm{ij}}^{SST} + \frac{-\tau_{\mathrm{ab}}^{SST}\overline{S}_{\mathrm{ab}}}{\overline{S}_{\mathrm{ab}}\ \overline{S}_{\mathrm{ab}}}\overline{S}_{\mathrm{ij}}\right)\end{aligned} \tag{6.8}$$

with the following counterpart of subgrid-contribution to transport of the scalar $\overline{\phi}$

$$\begin{aligned}\tau_{\mathrm{j}}^{KKK1} = & \frac{-\tau_{\mathrm{a}}^{SST}\partial\overline{\phi}/\partial x_{\mathrm{a}} + |-\tau_{\mathrm{a}}^{SST}\partial\overline{\phi}/\partial x_{\mathrm{a}}|}{-\tau_{\mathrm{a}}^{SST}\partial\overline{\phi}/\partial x_{\mathrm{a}}}\tau_{\mathrm{j}}^{SST} \\ & + \left(\tau_{\mathrm{j}}^{SST} + \frac{-\tau_{\mathrm{a}}^{SST}\partial\overline{\phi}/\partial x_{\mathrm{a}}}{\left(\partial\overline{\phi}/\partial x_{\mathrm{a}}\right)^2}\partial\overline{\phi}/\partial x_{\mathrm{j}}\right)\end{aligned} \tag{6.9}$$

The second model is given by

$$\tau_{\mathrm{ij}}^{KKK2} = \tau_{\mathrm{ij}}^{SST} - \max\left(\frac{\tau_{\mathrm{ab}}^{SST}\overline{S}_{\mathrm{ab}}}{\overline{S}_{\mathrm{ab}}\ \overline{S}_{\mathrm{ab}}}, 0\right)\overline{S}_{\mathrm{ij}} \tag{6.10}$$

for momentum transport, while the scalar transport reads

$$\tau_{\mathrm{j}}^{KKK2} = \tau_{\mathrm{j}}^{SST} - \max\left(\frac{\tau_{\mathrm{a}}^{SST}\partial\overline{\phi}/\partial x_{\mathrm{a}}}{\left(\partial\overline{\phi}/\partial x_{\mathrm{a}}\right)^2}, 0\right). \tag{6.11}$$

Here, τ_{ij}^{SST} denotes an arbitrary baseline scale similarity type model. In the present study Clark's tensor-diffusivity model [42] is chosen for its good performance in a-priori testing, which provides for momentum transport

$$\tau_{\mathrm{ij}}^{CTM} = \frac{\Delta^2}{12}\frac{\partial\overline{u}_{\mathrm{i}}}{\partial x_{\mathrm{k}}}\frac{\partial\overline{u}_{\mathrm{j}}}{\partial x_{\mathrm{k}}} \tag{6.12}$$

This chapter was previously published in Computers and Fluids [59] and is reprinted with permission of the journal.

and for scalar transport

$$\tau_{\mathrm{j}}^{CTM} = \frac{\Delta^2}{12} \frac{\partial \overline{u}_{\mathrm{j}}}{\partial x_{\mathrm{k}}} \frac{\partial \overline{\phi}}{\partial x_{\mathrm{k}}} \tag{6.13}$$

Liu's model, reading $\tau_{\mathrm{ij}}^{LSS} = \widehat{\overline{u}_{\mathrm{i}}\overline{u}_{\mathrm{i}}} - \widehat{\overline{u}}_{\mathrm{i}}\ \widehat{u}_{\mathrm{i}}$ and $\tau_{\mathrm{j}}^{LSS} = \widehat{\overline{u}_{\mathrm{j}}\overline{\phi}} - \widehat{\overline{u}}_{\mathrm{j}}\ \widehat{\phi}$ respectively, can be used alternatively, but requires an additional filtering level $\widehat{(\cdot)}$ [169].

6.3 Numerical methods

The in-house code *PsiPhi* has been used to perform all simulations. It has been developed at the Imperial College London and the University of Duisburg-Essen. *PsiPhi* was utilized in many LES calculations – some of them highly resolved up to DNS resolution – of reactive and non-reactive flows [232, 221, 108]. A finite volume method (FVM) and a cubic, equidistant grid allow for the solution of mass, momentum and a variable number of scalar transport equations. This study is based on the solution of the incompressible Navier-Stokes equations, which, for constant density, viscosity and diffusivity, takes the form:

$$\frac{\partial \overline{u}_{\mathrm{j}}}{\partial x_{\mathrm{j}}} = 0 \tag{6.14}$$

$$\frac{\partial \rho\ \overline{u}_{\mathrm{i}}}{\partial t} + \frac{\partial \rho\ \overline{u}_{\mathrm{i}}\ \overline{u}_{\mathrm{j}}}{\partial x_{\mathrm{j}}} + \frac{\partial \overline{p}}{\partial x_{\mathrm{i}}} = \frac{\partial}{\partial x_{\mathrm{j}}} \left(\mu \left(\frac{\partial \overline{u}_{\mathrm{i}}}{\partial x_{\mathrm{j}}} + \frac{\partial \overline{u}_{\mathrm{j}}}{\partial x_{\mathrm{i}}} \right) - \rho\ \tau_{\mathrm{ij}}^{\mathrm{sgs}} \right) \tag{6.15}$$

$$\frac{\partial \rho\ \overline{\phi}}{\partial t} + \frac{\partial \rho\ \overline{\phi}\ \overline{u}_{\mathrm{j}}}{\partial x_{\mathrm{j}}} = \frac{\partial}{\partial x_{\mathrm{j}}} \left(D_\phi \left(\frac{\partial \rho \overline{\phi}}{\partial x_{\mathrm{j}}} \right) - \rho\ \tau_{\mathrm{j}}^{\mathrm{sgt}} \right) \tag{6.16}$$

Using a convolutional filter to allow for the separation of scales

$$\overline{Z}(\vec{x}, t) = \iiint_{-\infty}^{+\infty} Z(\vec{r}, t) \cdot g(\vec{x} - \vec{r}, t)\ \mathrm{d}\vec{r} \tag{6.17}$$

$\tau_{\mathrm{ij}}^{\mathrm{sgs}}$ denotes the subgrid-stresses and $\tau_{\mathrm{j}}^{\mathrm{sgt}}$ refers to the subgrid scalar transport. The momentum transport equations are spatially discretized using fourth-order central differencing (CDS - strictly speaking called linear interpolation in the context of FV) for the LES and DNS calculations. The additional scalar transport equation is discretized using fourth-order central differencing in the DNS, while the resolved convective scalar transport in the LES calculations is treated with a total variation diminishing (TVD-CHARM) scheme [317].

It is common in literature for eddy-viscosity models to use the same numerical discretization for diffusive and subgrid fluxes [182]. However in this study, the effect of the discretization scheme of the scalar subgrid fluxes $\tau_{\mathrm{j}}^{\mathrm{sgt}}$ in the LES calculations is investigated by comparing different approaches: a treatment of the scalar subgrid fluxes using the TVD-CHARM flux limiter, using a second order CDS method and using a fourth order CDS method, leading

This chapter was previously published in Computers and Fluids [59] and is reprinted with permission of the journal.

to possibly different forms of discretization for the resolved scalar convective and subgrid fluxes - e.g. treatment of convective scalar fluxes with second order CDS and treatment of subgrid scalar fluxes with TVD. To achieve the discretization of the turbulent scalar fluxes, the Gaussian divergence theorem is used:

$$\iiint_V \frac{\partial \overline{\rho}\tau_{\mathrm{j}}^{\mathrm{sgt}}}{\partial x_{\mathrm{j}}} dV = \iint_S \overline{\rho}\tau_{\mathrm{j}}^{\mathrm{sgt}} n_{\mathrm{j}} dA \tag{6.18}$$

Using the midpoint-rule on a equidistant cubic mesh with n_{j} being the surface normal vector, the integral can be decomposed into

$$\iint_S \overline{\rho}\tau_{\mathrm{j}}^{\mathrm{sgt}} n_{\mathrm{j}} dA = \sum_m^S \left(\overline{\rho}\tau_{\mathrm{j}}^{\mathrm{sgt}} n_{\mathrm{j}} A\right)_{\mathrm{m}} \tag{6.19}$$

The values of $\tau_{\mathrm{j}}^{\mathrm{sgt}}$ are stored in the cell centers and have to be obtained on the cell-surfaces m by using the aforementioned discretization methods. Given - for instance - the TVD-CHARM approach, $\left(\tau_{\mathrm{j}}^{\mathrm{sgt}}\right)_{\mathrm{m}}$ is calculated using the values $\left(\tau_{\mathrm{j}}^{\mathrm{sgt}}\right)_C$ of a cell C, as well as its values $\left(\tau_{\mathrm{j}}^{\mathrm{sgt}}\right)_U$ in the cell upstream U and $\left(\tau_{\mathrm{j}}^{\mathrm{sgt}}\right)_D$ in the cell downstream depending on the flow velocity, using:

$$\left(\tau_{\mathrm{j}}^{\mathrm{sgt}}\right)_{\mathrm{m}} = \left(\tau_{\mathrm{j}}^{\mathrm{sgt}}\right)_C + \frac{B}{2}\left(\left(\tau_{\mathrm{j}}^{\mathrm{sgt}}\right)_C - \left(\tau_{\mathrm{j}}^{\mathrm{sgt}}\right)_U\right) \tag{6.20}$$

Where $B = r\left(3r+1\right)/\left(r+1\right)^2 \wedge r > 1$ is the limiter function for a CHARM-limiter and r is the gradient-ratio

$$r = \frac{\left(\tau_{\mathrm{j}}^{\mathrm{sgt}}\right)_D - \left(\tau_{\mathrm{j}}^{\mathrm{sgt}}\right)_C}{\left(\tau_{\mathrm{j}}^{\mathrm{sgt}}\right)_C - \left(\tau_{\mathrm{j}}^{\mathrm{sgt}}\right)_U} \tag{6.21}$$

If $\left(\tau_{\mathrm{j}}^{\mathrm{sgt}}\right)_C = \left(\tau_{\mathrm{j}}^{\mathrm{sgt}}\right)_U$, the operator fails and one forces $\left(\tau_{\mathrm{j}}^{\mathrm{sgt}}\right)_{\mathrm{m}} = \left(\tau_{\mathrm{j}}^{\mathrm{sgt}}\right)_C$.

Timestepping is achieved by a low-storage, third-order Runge-Kutta scheme and continuity is enforced by a fractional-step method [129], while the Poisson-equation is solved using a conjugate gradients method [283].

6.4 Case description

A plane turbulent jet based on previous work by Klein et al. [133] and Stanley et al. [265] is the basis for the present test case. A computational domain of $20D \times 20D \times 6.4D$ in streamwise (x), normalwise (y) and spanwise (z) direction with a nozzle width D is chosen. The homogeneous direction is treated by periodic boundary conditions and boundaries in normalwise direction use Dirichlet conditions with velocity data from the DNS of Klein [133]. Hence, the normalwise velocity component $\overline{v}$ at the normalwise boundaries is defined as constant $+3.3\%$ of U_0 at $y = 0$ and -3.3% of U_0 at $y = 20D$ over the boundary, while stream- and spanwise velocity components are set to zero, which is based on the averaged velocity

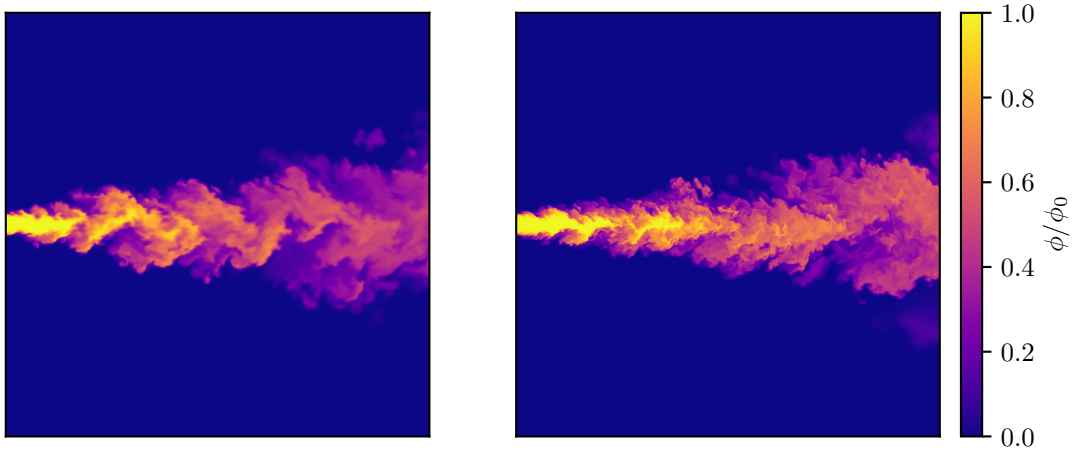

Figure 6.1 Instantaneous snapshot of the normalized passive scalar distribution ϕ/ϕ_0 of a plane jet LES without turbulence model (left) together with the benchmark DNS (right) in the $x-y$ midplane.

values observed at the boundary in the DNS of Klein. In addition to the von-Neumann conditions for pressure and velocity (clipping for negative velocities), filtering by Anderson and Domaradzki is applied in a thin buffer layer of thickness $D/4$ at the streamwise outlet to ensure unperturbed turbulent outflow and to avoid the formation of unwanted artifacts at the boundary [8]. The three-dimensional filter is the product of the convolution of three one-dimensional filters with coefficients $(b_{-1}, b_0, b_1) = (C, 1-2C, C)$, given by

$$\widehat{\overline{\phi}}_{\mathrm{ijk}} = \sum_{l=-1}^{1} \sum_{m=-1}^{1} \sum_{n=-1}^{1} b_{\mathrm{l}} \cdot b_{\mathrm{m}} \cdot b_{\mathrm{n}} \cdot \overline{\phi}_{\mathrm{i+l,j+m,k+n}} \tag{6.22}$$

The constant C is set to $C = 1/12$ but can vary between $0 < C \leq 1/3$ [127]. The inflow velocity U_0 is chosen in order to achieve a Reynolds number of $Re = 10,000$ at the nozzle and the initial passive scalar value ϕ_0 is set to unity for incoming fluid and $\phi = 0$ for the surrounding ambient fluid. The Schmidt-number is set to $Sc = 0.2$, allowing for an accurate and efficient solution of convective scalar transport using central schemes in the DNS. Turbulent inflow data is generated at the streamwise inlet using an efficient, low-storage implementation [120] of the inflow generator developed by Klein et al. [133] and setting the inflow-lengthscale to the product of the von-Karman constant and the maximum wall distance in the nozzle. The velocity profile prescribed at the inflow is approximated using a hyperbolic-tangent relation based on findings of Thomas and Goldschmidt [278]

$$\overline{u} = \frac{U_0}{2} + \frac{U_0}{2} \tanh\left(\frac{-|z| + 0.5D}{2\Theta}\right), \tag{6.23}$$

This chapter was previously published in Computers and Fluids [59] and is reprinted with permission of the journal.

with the shear layer momentum thickness Θ being set to $D/20$ according to Ribault [155]. The normal- and spanwise mean velocity components $\overline{v}$ and $\overline{w}$ are chosen as zero. For the DNS, the nozzle width D is discretized by 80 cells, while the LES uses 20 cells for the nozzle. Consistent with the plane jet DNS of Stanley at al. [265] and Klein et al. [133], the DNS grid provides a resolution of approximately $\Delta x/\eta \approx 3$ where η denotes the Kolmogorov scale. The LES resolution was chosen to allow for a sufficient scale separation between LES and DNS and at the same time for a sufficient resolution of the shear layer dictated by the mean inlet velocity profile. Both setups rely on an equidistant cubic grid, which leads to a total number of 1.3 billion cells for the DNS and 20 million cells for the LES respectively. While the new scale-similarity models are free of any parameters, the Sigma model uses $C_\mathrm{s} = 1.5$ [192] and the static Smagorinsky model features $C_\mathrm{s} = 0.173$ [163].

The instantaneous scalar field in Fig. 6.1 demonstrates the capability of DNS to resolve fine structures in the flow field compared to the LES without turbulence modelling (underresolved DNS / implicit LES).

The computational time needed for the LES calculations using the different turbulence models is shown in Tab. 6.1, indicating a very moderate computational overhead of the *KKK* models (13%) relative to the Smagorinsky model, compared to the Sigma model (35%) and the DSM model. (109%).

Table 6.1 Comparison of computational costs for the used models in thousand CPU-hours.

Model	Cost [kCPUh]
SM	160.4
SI	217.0
KKK1	182.5
KKK2	181.7
DSM	336.0
none	124.4

The nomanclature for the presented combinations of turbulence model and discretization schemes are given in Tab. 6.2.

6.5 Results

6.5.1 Influence of scalar subgrid discretization

The scalar subgrid closure has a crucial influence on LES simulation quality and interacts with the numerical scheme [82]. While central differencing methods are the most common approach for subgrid momentum fluxes due to their kinetic energy preserving properties, numerical oscillations have been observed for transport of bounded scalars before jet break-up when using models without limiter. Close to the nozzle, the steep gradients of the mean

Table 6.2 Configuration of turbulence models and discretization schemes.

Configuration	SGS-Model		Convective Discretization		SGS Discretization	
	$\rho\vec{u}$	$\rho\phi$	$\rho\vec{u}$	$\rho\phi$	$\rho\vec{u}$	$\rho\phi$
SI-CDS2	Sigma	Sigma	CDS4	TVD	CDS2	CDS2
SI-CDS4	Sigma	Sigma	CDS4	TVD	CDS2	CDS4
KKK1-CDS2	KKK1	KKK1	CDS4	TVD	CDS2	CDS2
KKK1-CDS4	KKK1	KKK1	CDS4	TVD	CDS2	CDS4
SI	Sigma	Sigma	CDS4	TVD	CDS2	TVD
SM	Smag. stat.	Smag. stat.	CDS4	TVD	CDS2	TVD
DSM	Smag. dyn.	Smag. dyn.	CDS4	TVD	CDS2	TVD
KKK1	KKK1	KKK1	CDS4	TVD	CDS2	TVD
KKK2	KKK2	KKK1	CDS4	TVD	CDS2	TVD
none	none	none	CDS4	TVD	none	none
SI-KKK1	Sigma	KKK1	CDS4	TVD	CDS2	TVD
KKK1-SI	KKK1	Sigma	CDS4	TVD	CDS2	TVD

scalar flux profiles feature high frequency modes and this results in large dispersion errors for central differencing schemes. It appears that such problems cannot be removed by SST-type models and it turned out that also the regularization technique suggested in Eq. 6.9 or 6.11 was not able to eliminate this problem. Further, it has been speculated in combustion literature, that models that feature counter gradient transport, result in instabilities of the flame [156]. It has been observed that a possible solution is to write the SGS model within the flux limiter as described at the end of section 6.3, which successfully prevents any over- or undershoots. The use of this approach for the scalar subgrid-fluxes $\tau_{\mathrm{j}}^{\mathrm{sgt}}$ will be indicated by adding $\mathrm{TVD}^{\tau(\phi)}$ to the model name in the figure-key.

To investigate the effects of the discretization of scalar subgrid fluxes, results using second- and fourth-order central differencing schemes, and the TVD scheme for scalar subgrid-fluxes are compared, while in all cases the convective term for scalar transport has been discretized using the TVD scheme. In this subsection, the *SI* and *KKK1* model are used to represent eddy-viscosity and scale-similarity approaches.

Figure 6.2 shows the results for the deviations from the mean passive scalar due to oscillations using central differencing before jet break-up. The *maximum allowed deviation* $\sigma_{\mathrm{alwd.}}$ is defined as the maximum deviation of the local mean value $\langle\phi\rangle$ within the physically meaningful range of the bounded scalar ϕ and is calculated as $\sigma_{\mathrm{alwd.}} = min\left((1-\langle\phi\rangle/\phi_0), \langle\phi\rangle/\phi_0\right)$. Comparing the maximum allowed deviation $\sigma_{\mathrm{alwd.}}$ to the observed standard deviation of the instantaneous passive scalar σ_{true} in a statistical sense physically allowed oscillations if $\sigma_{\mathrm{true}} \leq \sigma_{\mathrm{alwd.}}$. The dotted curves show the maximum allowed deviation from the mean profile to avoid over- or undershoots while sampling over ten flow-through times, together with the standard deviation of ϕ as a measure for the mean deviation shown in dashed lines. As the passive scalar is constructed to range between values of 0 and 1, a standard deviation

This chapter was previously published in Computers and Fluids [59] and is reprinted with permission of the journal.

σ_{true} exceeding the physically meaningful value $\sigma_{\text{alwd.}}$ indicates numerical oscillations. Both models show dispersion errors resulting in over- or undershoots as the allowed deviation is exceeded in the range of $y/D = 0.5$ and 0.75 for all curves. Differences between CDS2 and CDS4 remain small, even negligible for the *SI* model. The differences of discretization for the *KKK1* model are small, but more distinct compared to the Sigma model with the CDS4 scheme showing slightly larger deviations.

The dispersion errors vanish for all streamwise distances from the nozzle beyond jet break-up. The influence of the discretization on the statistics are shown in Tab. 6.3 and 6.4 for $x/D = 3$ and 11. Overall, central differencing improves the results of the Sigma model, where the improvement using fourth-order exceeds the second-order CDS. The SI model does not promote over- or undershoots and there is no necessity to write it inside the flux limiter. Hence, the combination *SI-TVD* was investigated for completeness. The performance of the *KKK1* model with all three discretizations is comparable for both axial positions, but the *KKK1-TVD* scheme prevents over- and undershoots close to the nozzle. Hence, this TVD-CHARM discretization will be used for subgrid scalar fluxes for all following simulations.

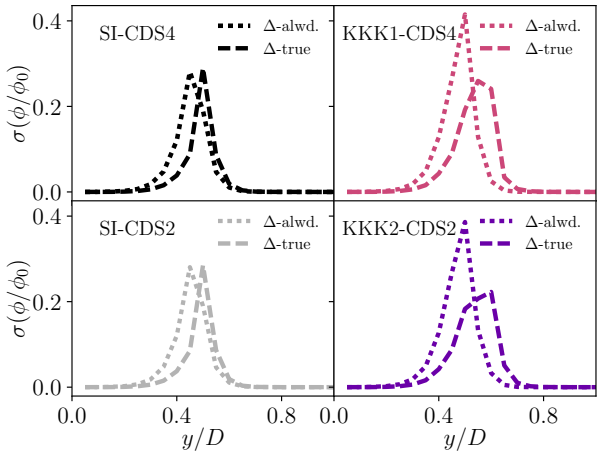

Figure 6.2 Averaged maximum allowed (*alwd.*) deviation (i.e. $min\left((1-\langle\phi\rangle/\phi_0), \langle\phi\rangle/\phi_0\right)$ of instantaneous passive scalar ϕ/ϕ_0 from mean value in order to avoid over- and undershoots (dotted lines) and standard deviation profiles with normalwise distance from the centerline y/D at a streamwise distance of $x/D \approx 0.5$ from the nozzle for CDS2 and CDS4 discretization schemes for the scalar turbulent subgrid-fluxes (dashed lines) and by employing the *SI* and $KKK1$ models

6.5.2 Standard configuration

The LES results include the newly proposed scale-similarity-type models by Klein et al. [140] (denoted as *KKK1* and *KKK2*), as well as the well known Smagorinsky (*static* denoted as *SM*, *dynamic* denoted as *DSM*) and Sigma (denoted *SI*) models (- these simulations use

Table 6.3 Quantitative error measure for the plane turbulent jet using $\|\phi_{\mathrm{DNS}} - \phi_{\mathrm{LES}}\|_2$ at $x/D = 3$ based on the present flow quantities. Object of investigation is the discretization of scalar subgrid flux.

	ϕ/ϕ_0	$\sqrt{\phi'\phi'}/\phi_0$	$\phi'u'/\phi_0 U_0$
SI-CDS2	0.03021	0.02509	0.00444
SI-CDS4	0.02993	0.02501	0.00429
SI-TVD	0.02968	0.02706	0.00496
KKK1-CDS2	0.02950	0.01955	0.00278
KKK1-CDS4	0.02996	0.01828	0.00253
KKK1-TVD	0.03068	0.01890	0.00252

Table 6.4 Quantitative error measure for the plane turbulent jet using $\|\phi_{\mathrm{DNS}} - \phi_{\mathrm{LES}}\|_2$ at $x/D = 11$ based on the present flow quantities. Object of investigation is the discretization of scalar subgrid flux.

	ϕ/ϕ_0	$\sqrt{\phi'\phi'}/\phi_0$	$\phi'u'/\phi_0 U_0$
SI-CDS2	0.02580	0.02340	0.00337
SI-CDS4	0.02641	0.02197	0.00298
SI-TVD	0.02668	0.02374	0.00326
KKK1-CDS2	0.02016	0.01564	0.00218
KKK1-CDS4	0.01899	0.01627	0.00227
KKK1-TVD	0.02020	0.01495	0.00212

the same turbulence model for momentum and scalar transport, while different models for momentum and scalar transport will be combined in section 6.5.3). Calculations without turbulence modeling (denoted *none*) are included to demonstrate the improvement of results by using a turbulence model. Further, crossover combinations using the Sigma model for momentum transport and KKK1 model for scalar transport (denoted as *SI-KKK1*) - and vice versa (denoted as *KKK1-SI*) - have been performed to assess the influence of the subgrid momentum contribution on the scalar transport and will be reported in the next section.

Two different axial locations have been evaluated - at $x/D = 3$ just upstream of the jet break-up and at $x/D = 11$, close to the fully-developed region of the flow. Profiles of the mean streamwise velocity u and passive scalar ϕ as seen in Fig. 6.3 and 6.5 exhibit negligible differences between the subgrid-models for both sampling locations, which suggests that for this configuration no turbulence modeling is needed if only mean profiles are of interest. Of course, the evaluation of fluctuation and shear-stress profiles is very important for unsteady resolving simulation techniques and these are more challenging to capture properly with LES.

More distinct differences between the subgrid-models can be observed for the averaged (in the following denoted without operator $\langle . \rangle$) streamwise $\langle\sqrt{u'u'}\rangle$ and normalwise $\langle\sqrt{v'v'}\rangle$ fluctuating velocity components, the averaged shear stress $\langle u'v'\rangle$, the passive scalar fluctuations $\langle\sqrt{\phi'\phi'}\rangle$ as well as $\langle\phi'u'\rangle$, which are commonly described as challenging to simulate correctly

This chapter was previously published in Computers and Fluids [59] and is reprinted with permission of the journal.

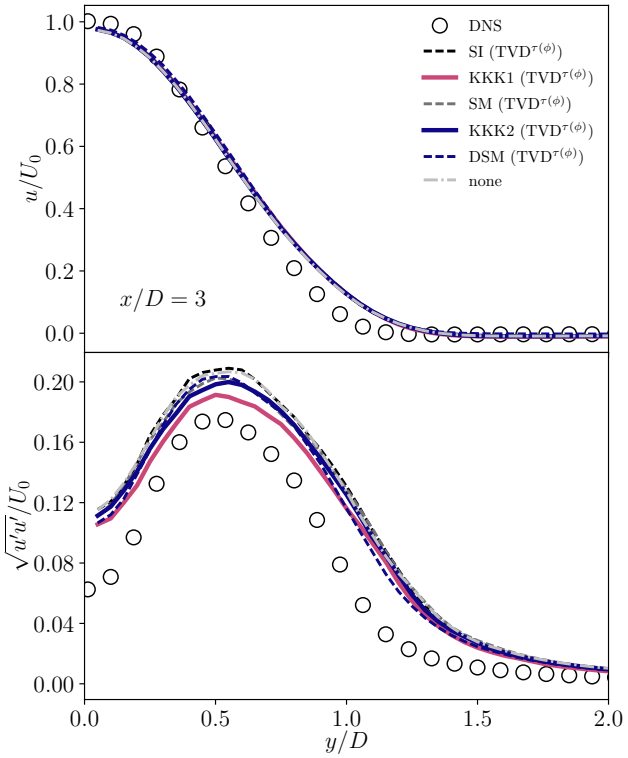

Figure 6.3 Normalized mean streamwise velocity u/U_0 and streamwise velocity fluctuation $\sqrt{u'u'}/U_0$ profiles with normalwise distance from the centerline y/D at a streamwise distance of $x/D = 3$ from the nozzle

This chapter was previously published in Computers and Fluids [59] and is reprinted with permission of the journal.

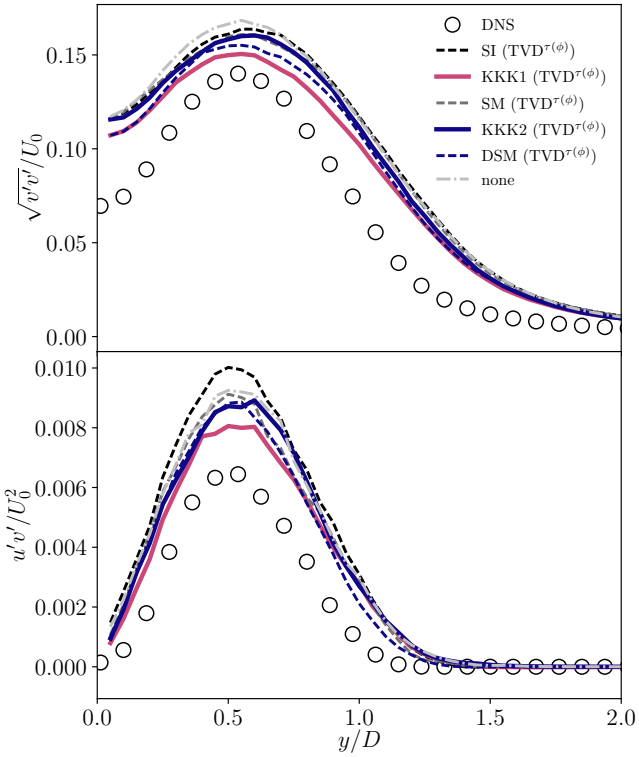

Figure 6.4 Normalized normalwise velocity fluctuation $\sqrt{v'v'}/U_0$ and shear-stress $u'v'/U_0^2$ profiles with normalwise distance from the centerline y/D at a streamwise distance of $x/D = 3$ from the nozzle

This chapter was previously published in Computers and Fluids [59] and is reprinted with permission of the journal.

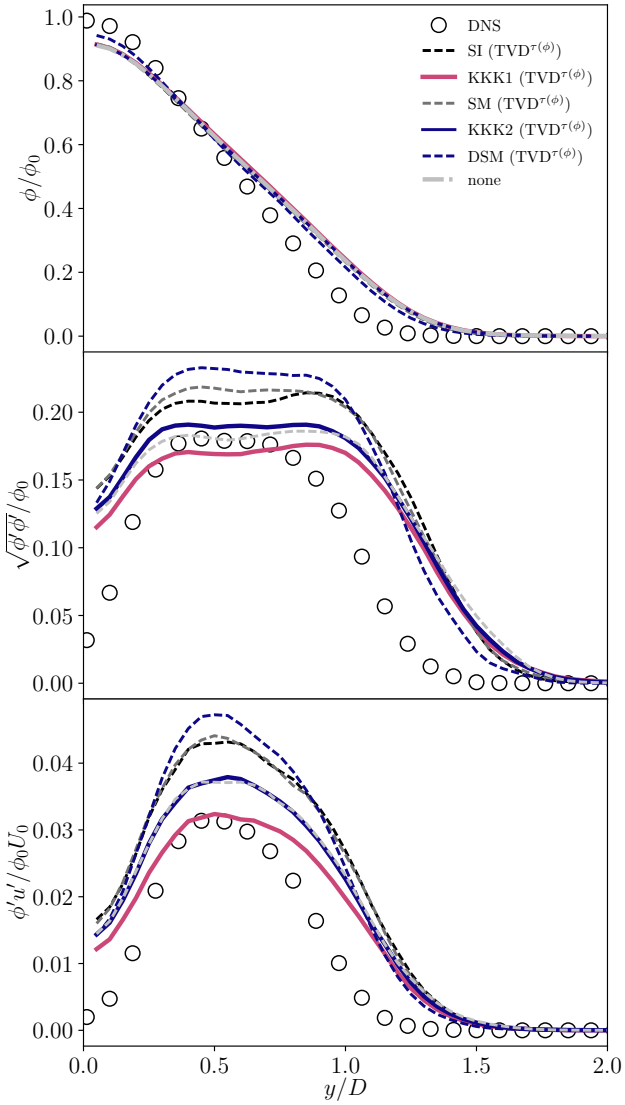

Figure 6.5 Normalized mean passive scalar ϕ/ϕ_0, passive scalar fluctuation $\sqrt{\phi'\phi'}/\phi_0$ and cross-correlation $u'\phi'/\phi_0 U_0$ profiles with normalwise distance from the centerline y/D at a streamwise distance of $x/D = 3$ from the nozzle

This chapter was previously published in Computers and Fluids [59] and is reprinted with permission of the journal.

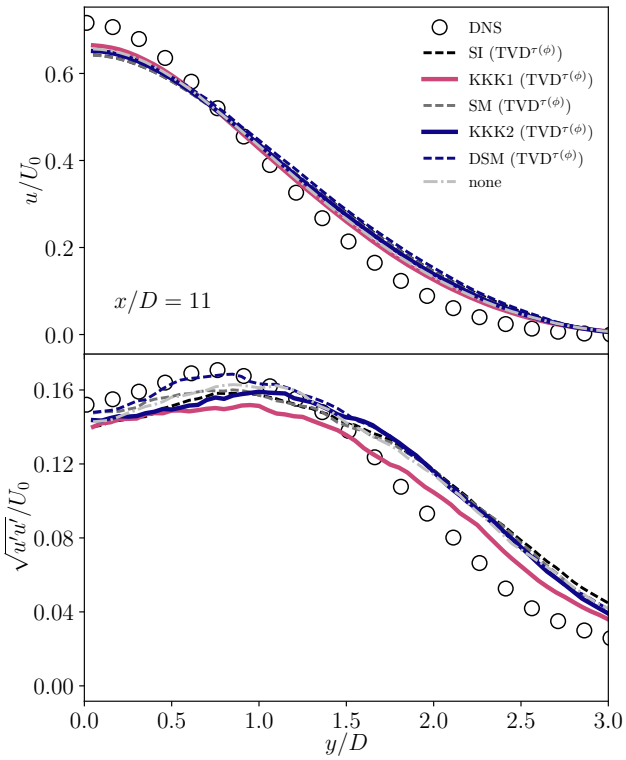

Figure 6.6 Normalized mean streamwise velocity u/U_0 and streamwise velocity fluctuation $\sqrt{u'u'}/U_0$ profiles with normalwise distance from the centerline y/D at a streamwise distance of $x/D = 11$ from the nozzle

in LES [155] and hence, serve as good reference for the model performance. The Sigma, static Smagorinsky and no-model calculation show the strongest deviations from the DNS data at $x/D = 3$ for the velocity fluctuations. These profiles feature a constant offset until $y/D = 1$, which decreases rapidly and eventually vanishes for larger y/D. The best agreement is achieved by the KKK-models and the dynamic Smagorinsky model, with the KKK1 model outperforming the KKK2 and dynamic Smagorinsky model and showing the best results in resolving the peak height. The passive scalar profile at $x/D = 3$ reveals stronger deviations of the eddy-viscosity models. The simulation without model shows good results at the peak region, but is outperformed by the KKK1 model for the remaining y/D values, while all calculations fail to give a proper estimate of centerline fluctuations.

The normalized streamwise mean velocity and velocity fluctuation at $x/D = 11$ can be seen in Fig. 6.6. Minor differences between the LES models are observed. However, the KKK1 model reveals slightly better agreement with the DNS data than the remaining models. The profile of streamwise velocity fluctuations $\sqrt{u'u'}$ features only small differences between the models for $y/D < 1$, with the dynamic Smagorinsky model showing tendencies of better agreement for smaller and the KKK1 leading to better agreement for larger y/D. For the

This chapter was previously published in Computers and Fluids [59] and is reprinted with permission of the journal.

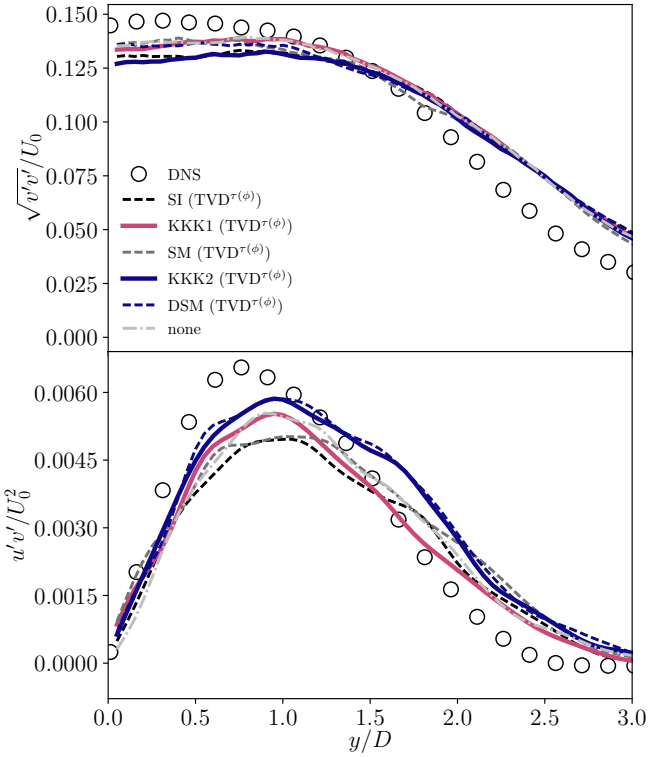

Figure 6.7 Normalized normalwise velocity fluctuation $\sqrt{v'v'}/U_0$ and shear-stress $u'v'/U_0^2$ profiles with normalwise distance from the centerline y/D at a streamwise distance of $x/D = 11$ from the nozzle

This chapter was previously published in Computers and Fluids [59] and is reprinted with permission of the journal.

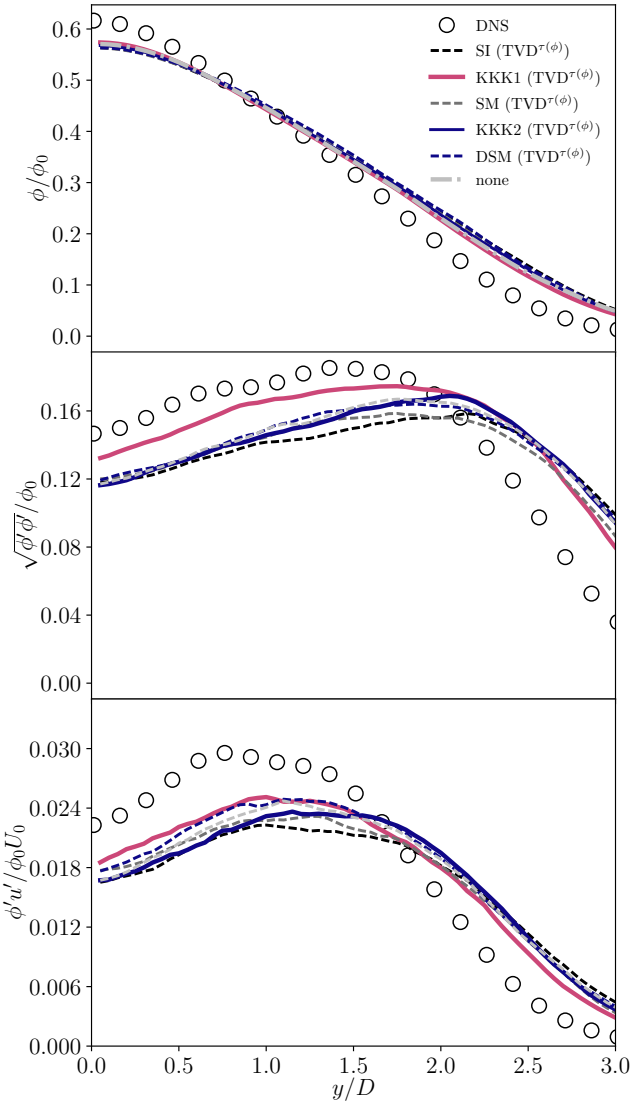

Figure 6.8 Normalized mean passive scalar ϕ/ϕ_0, passive scalar fluctuation $\sqrt{\phi'\phi'}/\phi_0$ and cross-correlation $u'\phi'/\phi_0 U_0$ profiles with normalwise distance from the centerline y/D at a streamwise distance of $x/D = 11$ from the nozzle

This chapter was previously published in Computers and Fluids [59] and is reprinted with permission of the journal.

Table 6.5 Quantitative error measure for the plane turbulent jet using $\|\phi_{\mathrm{DNS}} - \phi_{\mathrm{LES}}\|_2$ at $x/D = 3$ based on the present flow quantities. The smallest error is visualized in bold letters, the second smallest one in italics.

	u/U_0	$\sqrt{u'u'}/U_0$	$\sqrt{v'v'}/U_0$	$u'v'/U_0^2$	ϕ/ϕ_0	$\sqrt{\phi'\phi'}/\phi_0$	$\phi'u'/\phi_0 U_0$
SI	0.01944	0.01665	0.01493	0.00130	0.02968	0.02706	0.00496
SM	*0.01878*	0.01572	0.01437	0.00117	*0.02811*	0.02706	0.00493
DMS	0.01975	*0.01322*	*0.01163*	0.01111	**0.02318**	0.02642	0.00523
KKK1	0.01955	**0.01203**	**0.01042**	**0.00086**	0.03068	**0.01890**	**0.00252**
KKK2	0.01909	0.01460	0.01327	*0.00105*	0.02970	*0.02176*	*0.00358*
none	**0.01841**	0.01627	0.01519	0.00113	0.02971	0.02198	0.00365

Table 6.6 Quantitative error measure for the plane turbulent jet using $\|\phi_{\mathrm{DNS}} - \phi_{\mathrm{LES}}\|_2$ at $x/D = 11$ based on the present flow quantities. The smallest error is visualized in bold letters, the second smallest one in italics.

	u/U_0	$\sqrt{u'u'}/U_0$	$\sqrt{v'v'}/U_0$	$u'v'/U_0^2$	ϕ/ϕ_0	$\sqrt{\phi'\phi'}/\phi_0$	$\phi'u'/\phi_0 U_0$
SI	0.02651	0.01124	0.00892	0.00083	0.02668	0.02374	0.00326
SM	0.02950	0.01006	**0.00693**	0.00086	0.02525	*0.01922*	0.00282
DSM	0.02759	0.00972	0.00783	0.00069	0.02676	0.02043	0.00347
KKK1	**0.01815**	**0.00810**	0.00798	**0.00063**	**0.02020**	**0.01495**	**0.00212**
KKK2	0.02355	0.01024	0.00850	0.00078	0.02411	0.02102	0.00302
none	*0.02073*	*0.00957*	*0.00748*	*0.00067*	*0.02234*	0.02028	*0.00275*

normalwise velocity fluctuations $\sqrt{v'v'}$, the KKK1 and dynamic Smagorinsky model give equally good agreement, but are succeeded by the static Smagorinsky model. Again, the KKK1 model leads to good overall results for $u'v'$ and shows a clear improvement of the LES results for the passive scalar fluctuations compared to the remaining simulations. It may be concluded, that the new scale-similarity models lead to good results, with the KKK1 model showing the best overall agreement with the DNS data of the tested models.

The previous qualitative observations have been validated by applying quantitative error measures for the deviations from the DNS data. Since previous work has proven high correlations between a variety of error measures, the choice of Euclidean norm is considered to give sufficient insight [140]. Results of Tab. 6.5 and 6.6 confirm the KKK1 model to give the best overall agreement with the DNS data, as it leads to the smallest error for almost all quantities at both streamwise distances from the nozzle. The overall second best model appears to be the KKK2 model closer to the nozzle, and no turbulence model *OM* further downstream.

It is worth noting that the present configuration and numerics is not identical to the one investigated in Klein et al. [140]. Nevertheless, results for momentum transport are qualitatively consistent.

This chapter was previously published in Computers and Fluids [59] and is reprinted with permission of the journal.

While the present study features a moderate Reynolds number when thinking of technical applications [216], similar prediction quality for higher Reynolds numbers is expected. Since the DNS work by Klein et. al. [134] suggests Reynolds number independance of first- and second-order statistics of the plane jet at similar Reynolds numbers as in the present study, it can be speculated that the prediction quality for LES with higher Re will not become worse, unless the nozzle flow changes drastically.

6.5.3 Cross configuration

The foregoing investigation confirms the *KKK1* model as the most accurate option amongst the tested models for momentum and scalar transport. To investigate whether the improved scalar transport is a consequence of better momentum transport or actual scalar transport, a hybrid approach featuring momentum and scalar subgrid transport expressed by *KKK1* and Sigma model - and vice versa - is evaluated. Here, *SI-KKK1* refers to the *SI* model for momentum and *KKK1* model for scalar transport, whereas the opposite holds for the combination *KKK1-SI*. As the momentum transport remains uninfluenced by the different model for the passive scalar subgrid fluxes, only results of scalar quantities are shown. The results for $\phi' u'/\phi_0 U_0$ have to be considered with care in this context due to the influence of momentum transport on this quantity.

Results from the combined model approaches are shown in Fig. 6.9 at $x/D = 3$ and Fig. 6.10 at $x/D = 11$. The graphs reveal better results if *KKK1* is used for momentum transport for both distances from the nozzle, confirming that high fidelity modeling of momentum transport is crucial also for the prediction of scalar transport. For a more detailed analysis, quantitative error measures are utilized and shown in Tab. 6.7 and 6.8.

From the results of the previous section it can be concluded that the *SI* model results in a poorer prediction of momentum transport. The crossover-simulations exhibit better results for scalar transport if the *KKK1* model is used for subgrid momentum transport, while improvements due to scalar subgrid contribution remain small. The *KKK1* and *KKK1-SI* models lead to similar errors at $x/D = 3$, while the *KKK1* model shows the best results at $x/D = 11$. Hence, for larger distances from the nozzle, the influence of scalar subgrid-transport increases and the scalar *KKK1* model yields a notable improvement of the subgrid scalar transport.

The improvement from *KKK1-SI* to *KKK1* remains comparably small, which implies a stronger influence of momentum-closure on scalar statistics than the influence of scalar-closure. Still, to achieve optimal results for scalar-transport, a proper subgrid-closure for momentum and scalar subgrid-transport should be chosen.

This chapter was previously published in Computers and Fluids [59] and is reprinted with permission of the journal.

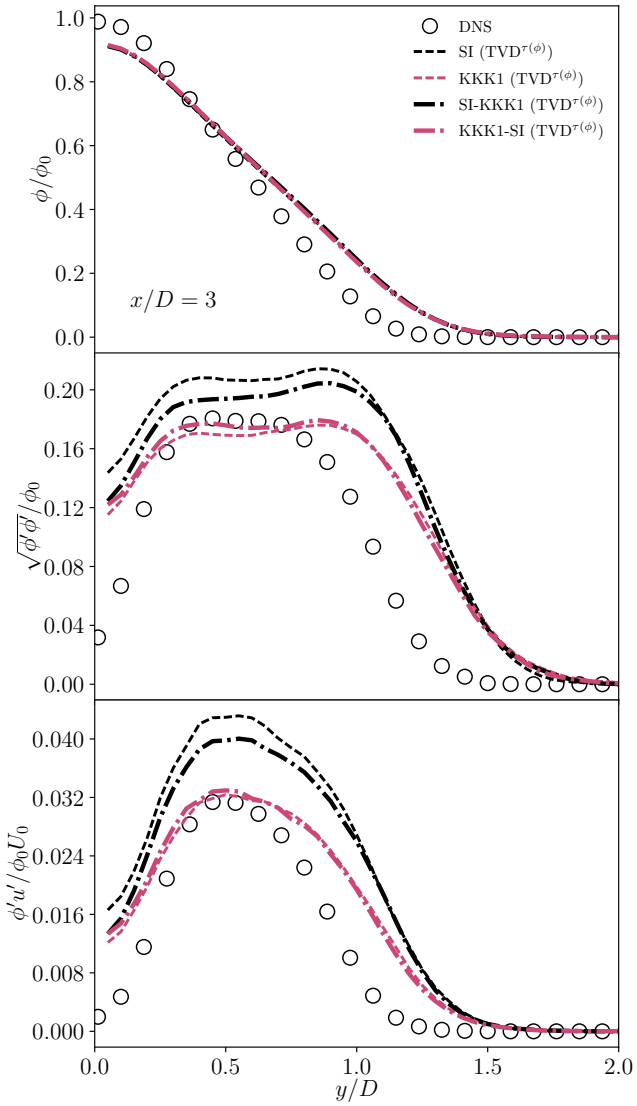

Figure 6.9 Mean passive scalar ϕ/ϕ_0, passive scalar fluctuation $\sqrt{\phi'\phi'}/\phi_0$ and normalized cross-correlation $u'\phi'/\phi_0 U_0$ profiles with normalwise distance from the centerline y/D at a streamwise distance of $x/D = 3$ from the nozzle

Table 6.7 Quantitative error measure for the plane turbulent jet using $\|\phi_{\mathrm{DNS}} - \phi_{\mathrm{LES}}\|_2$ at $x/D = 3$ based on the present flow quantities. Object of investigation is the performance of scalar transport using combined model approaches.

	ϕ/ϕ_0	$\sqrt{\phi'\phi'}/\phi_0$	$\phi'u'/\phi_0 U_0$
SI	0.02968	0.02706	0.00496
KKK1	0.03068	0.01890	0.00252
SI-KKK1	0.03115	0.02401	0.00427
KKK1-SI	0.02917	0.01841	0.00251

This chapter was previously published in Computers and Fluids [59] and is reprinted with permission of the journal.

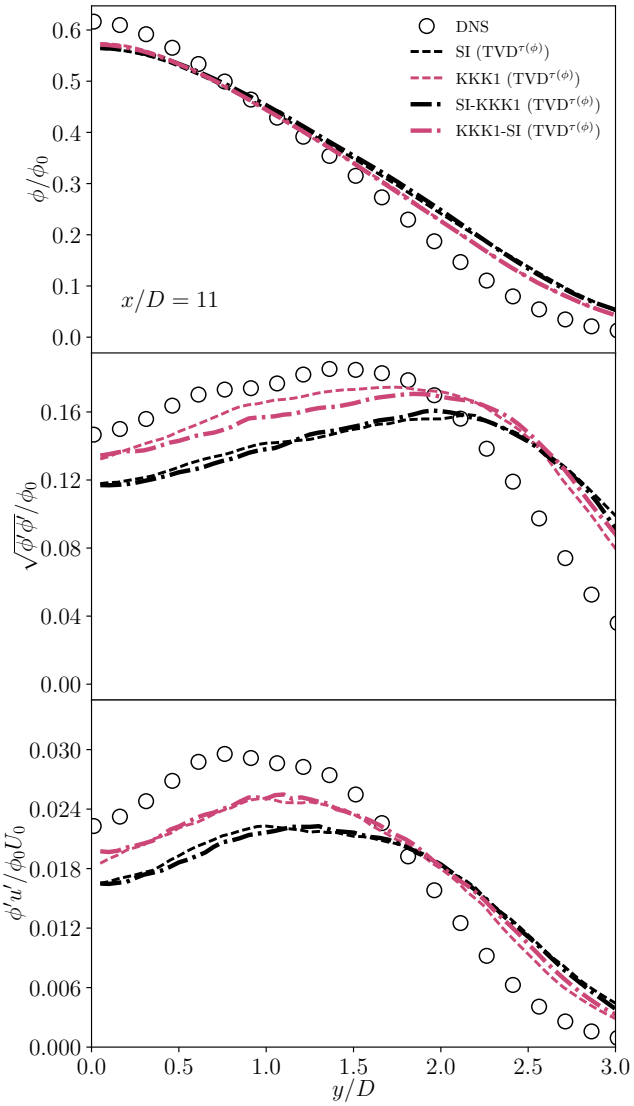

Figure 6.10 Mean passive scalar ϕ/ϕ_0, passive scalar fluctuation $\sqrt{\phi'\phi'}/\phi_0$ and normalized cross-correlation $u'\phi'/\phi_0 U_0$ profiles with normalwise distance from the centerline y/D at a streamwise distance of $x/D = 11$ from the nozzle

Table 6.8 Quantitative error measure for the plane turbulent jet using $\|\phi_{DNS} - \phi_{LES}\|_2$ at $x/D = 11$ based on the present flow quantities. Object of investigation is the performance of scalar transport using combined model approaches.

	ϕ/ϕ_0	$\sqrt{\phi'\phi'}/\phi_0$	$\phi' u'/\phi_0 U_0$
SI	0.02668	0.02374	0.00326
KKK1	0.02020	0.01495	0.00212
SI-KKK1	0.02729	0.02235	0.00332
KKK1-SI	0.02029	0.01732	0.00220

This chapter was previously published in Computers and Fluids [59] and is reprinted with permission of the journal.

6.6 Summary

In the present work, two newly proposed scale-similarity type models have been compared to standard eddy-viscosity (static and dynamic) Smagorinsky and Sigma models for a plane turbulent jet. A-posteriori calculations using different discretization methods for subgrid scalar fluxes and crossover model configurations have been considered as well to assess the influence of the scalar subgrid model and its discretization on the simulation quality. The simulations have been supplemented by calculations without a turbulence model, to demonstrate the models ability to improve the simulation results. It has been found that the use of a limiter for the scalar subgrid discretization eliminates dispersion errors and does not deteriorate the overall simulation results. All results have been compared to a DNS performed using the same code and setup to eliminate systematic errors not caused by the turbulence modeling. The new KKK1 model achieves good agreement with the DNS data for mean and fluctuation values. Quantitative analysis of the error revealed the best overall performance for the new model and the KKK2 model showing second best agreement with the DNS data closer to the nozzle and the no-model calculation in the fully developed region. Calculations using crossover model configurations reveal a stronger influence of the treatment of momentum subgrid transport on the results of scalar quantities than the treatment of scalar subgrid transport. In summary, the new model improves the overall performance of this shear flow LES, while being free of parameters and easy to implement.

6.7 Acknowledgements

The authors gratefully acknowledge the financial support through the state of North Rhine-Westphalia and the computational resources of the Center for Computational Sciences and Simulation (CCSS) of the University of Duisburg-Essen. Further computer resources for this project have been provided by the Gauss Centre for Supercomputing/Leibniz Supercomputing Centre under grant no. pn69ga.

This chapter was previously published in Computers and Fluids [59] and is reprinted with permission of the journal.

7 A-posteriori assessment of Large-Eddy Simulation subgrid-closures for momentum and scalar fluxes in a turbulent premixed burner experiment

Authors: L. Engelmann, J. Hasslberger, E. Inanc, M. Klein, A. Kempf

This chapter including all figures and tables was previously published in *Computers and Fluids: L. Engelmann, J. Hasslberger, M. Klein, A. Kempf, A-posteriori assessment of Large-Eddy Simulation subgrid-closures for momentum and scalar fluxes in a turbulent premixed burner experiment, 2022; 240: 105441* and is reprinted with permission from Elsevier. L. Engelmann developed the software for the presented simulations and the post-processing, performed all calculations, wrote the manuscript and generated all figures and tables. J. Hasslberger, E. Inanc, M. Klein and A. Kempf contributed corrections, discussions and proofreading.

Abstract

Although overall increasing computing power allows for higher resolution in Large-Eddy Simulation (*LES*), an appropriate choice of the subgrid-model is still decisive for the simulation quality. The relevance of the subgrid-model increases even further, if transported quantities are used in additional thermo-chemical models, which are coupled to the flow field. The present study investigates the impact of the choice of the subgrid-model for reactive flows in LES in the context of tabulated chemistry using well known and recently suggested modifications of eddy viscosity and scale-similarity-type models. LES calculations of the well investigated Cambridge stratified swirl burner have been performed with flamelet generated manifolds in combination with artificial flame-thickening. The simulations have been compared with flame-resolved results using the same numerical setup. Encouraging results have been obtained for a regularized scale-similarity-type model (applied to momentum- and scalar-fluxes). The sensor-enhanced Smagorinsky model outperforms well known eddy viscosity models while

This chapter was previously published in Computers and Fluids [60] and is reprinted with permission of the journal.

maintaining stability and being straight forward to implement with very low computational overhead compared to the static Smagorinsky model.

7.1 Introduction

Large-Eddy Simulation (*LES*) research experienced a major boost with the increase of computational power in recent decades. The development and improvement of numerical methods, subgrid-closures and boundary conditions led to an overall rise of simulation quality and confirms LES being a promising tool for scientific and industrial applications. The arguably most discussed aspect of LES since its early introduction remains the choice of the subgrid-closure for the LES-filtered Navier-Stokes equations [217]. As a plethora of subgrid-closures exists, it might become difficult to decide which closure satisfies the given requirements in the optimal manner. The class of eddy-viscosity approaches forms the oldest and - even today - the most popular group of closures featuring prominent models such as the Smagorinsky model [260] or Nicoud's Sigma model [192]. Based on the hypothesis of the interaction of small turbulent structures behaving like an additional viscosity, eddy-viscosity approaches provide excellent stability and satisfactory results. This hypothesis, however, has never been confirmed experimentally or by Direct Numerical Simulation (*DNS*; in particular in the context of reactive flows [135, 206]) and excessive dissipation is occasionally criticized, leading to the development of different approaches. Another well known class of LES turbulence models are the scale-similarity-type models with the model of Bardina [16] being the best known approach. Scale-similarity-type models gained attention due to its mathematically exact formulation of the subgrid-stresses while leading to excellent results in a-priori analysis. Still many of these models lack a sufficient amount of dissipation to be effectively used in a-posteriori LES. While the conceptual background of a model may already form a controversial basis, the actual value of a subgrid-closure is always judged by a-posteriori results. It is a consequential development, therefore, that subgrid-closures are evaluated for a broad variety of flow cases and conditions, such as Reynolds number and resolution. While canonical cases such as channel flows, homogeneous isotropic turbulence and jet flows form a frequently used benchmark repertoire [216], further cases are rarely reported either due to lack of reliable reference data or the case being rather exotic. The prediction of velocity profiles and stresses is a minimum requirement for many researchers to consider the use of a turbulence model and passive, as well as active scalar prediction is of great importance for multidisciplinary fields such as chemical modeling, multi-phase flows and hydroelectric flows. Most of these applications rely on the transported scalars to feed additional physical models, which may react upon the flow field and hence, interact with the subgrid-model.

In state-of-the-art combustion modeling, flamelet generated manifolds (*FGM*) gained popularity due to their ability to provide detailed chemical information in the form of tabula-

This chapter was previously published in Computers and Fluids [60] and is reprinted with permission of the journal.

tion at reasonable computational cost [286, 287, 294]. While originally being developed for premixed configurations, FGM has been further extended to account for stratified conditions. In the FGM approach it is assumed that the turbulent three-dimensional flame structure consists of an ensemble of one-dimensional laminar flames. Hence, one-dimensional freely propagating flames are computed using a detailed chemical mechanism. The results are mapped over a set of control variables (such as progress variable and fuel mixture fraction) and subsequently stored in a low dimensional lookup-table, which is accessed by the numerical solver. Common LES grids are usually too coarse to fully resolve the flame front. Hence, the flame needs to be spatially thickened in the flame-normal direction. This can be achieved by reducing the source term and increasing the diffusion term in the transport equations for the fuel mass fraction. This technique originally suggested by Colin et al. [44] is referred to as the artificially thickened flame (*ATF*) approach, which has been successfully applied in the LES context.

The influence of the subgrid-closure on the numerical overall model's behavior is a critical factor deciding on the subgrid-model's attractiveness. The aim of this study is the assessment of state-of-the-art turbulence models and recently proposed modifications based on momentum and active scalar quantities from DNS and LES calculations.

7.2 Modeling Approach

A set of five different LES subgrid-models is investigated. In addition to the well-established *Smagorinsky* and *Sigma* models, calculations using the *KKK1* and *KKK2* scale-similarity-type models by Klein et al. [140, 59] and a robust dynamic adaption of the *Smagorinsky* model by Hasslberger et al. [96] have been performed. The different approaches for the closure of the subgrid-stresses τ_{ij}^{sgs} and scalar subgrid fluxes τ_{j}^{sgs} are briefly presented below. For further details, the authors refer to the respective original publications.

The subgrid-stresses of the Favre-filtered equations arise from the filtering of the Navier-Stokes equations and represent the influence of the unresolved on the resolved scales

$$\tau_{ij} = \widetilde{u_i u_j} - \tilde{u}_i \, \tilde{u}_j. \tag{7.1}$$

Eddy-Viscosity models (denoted as *EVM*) aim for the expression of the stresses using an additional turbulent viscosity ν_t, which allows for calculation of the subgrid-stresses in the following form

$$\tau_{ij}^{EVM} - \frac{1}{3}\tau_{kk}^{EVM}\delta_{ij} = -2\nu_t \left(\tilde{S}_{ij} - \frac{1}{3}\tilde{S}_{kk}\delta_{ij} \right) \tag{7.2}$$

where

$$\tilde{S}_{ij} = \frac{1}{2}\left(\frac{\partial \tilde{u}_i}{\partial x_j} + \frac{\partial \tilde{u}_j}{\partial x_i} \right) \tag{7.3}$$

This chapter was previously published in Computers and Fluids [60] and is reprinted with permission of the journal.

corresponds to the Favre-filtered strain-rate tensor.

Accordingly, filtering the transport equation of a scalar variable ϕ leads to the scalar subgrid-fluxes

$$\tau_\mathrm{j} = \widetilde{\phi u_\mathrm{j}} - \tilde{\phi}\ \tilde{u}_\mathrm{j}. \tag{7.4}$$

The gradient-diffusion hypothesis (*GDH*) based on the turbulent viscosity ν_t and the subgrid Schmidt-number Sc_t is used in the context of eddy-viscosity models to express the unknown scalar subgrid-contribution

$$\tau_\mathrm{j}^\mathrm{GDH} = -\frac{\nu_\mathrm{t}}{Sc_\mathrm{t}} \frac{\partial \tilde{\phi}}{\partial x_\mathrm{j}} \tag{7.5}$$

The turbulent viscosity ν_t remains to be determined by the respective subgrid-model. A general form for calculating the turbulent viscosity reads

$$\nu_\mathrm{t} = (C_\mathrm{m}\Delta)^2 \tilde{D}_\mathrm{m} \tag{7.6}$$

with the model constant C_m and the filter-width Δ. The various eddy-viscosity models most commonly differ in the way of calculating the inverse timescale $\tilde{D}_\mathrm{m}$.

For the well-known *Smagorinsky* model [260], $\tilde{D}_\mathrm{m}$ can be expressed with the resolved characteristic rate of strain as

$$\tilde{D}_\mathrm{m} = \sqrt{2\tilde{S}_\mathrm{ab}\ \tilde{S}_\mathrm{ab}}. \tag{7.7}$$

Nicoud's *Sigma*-model relies on the ordered singular values $\sigma_1 \geq \sigma_2 \geq \sigma_3$ of the resolved velocity gradient tensor $\tilde{g}_\mathrm{ij} = \partial\tilde{u}_\mathrm{i}/\partial x_\mathrm{j}$ [192]. The singular values can be calculated as the square roots of the eigenvalues of $\tilde{g}_{ik}\ \tilde{g}_{kj}$ and lead to

$$\tilde{D}_\mathrm{m} = \frac{\sigma_3\,(\sigma_1 - \sigma_2)\,(\sigma_2 - \sigma_3)}{\sigma_1^2} \tag{7.8}$$

Within this study, a model constant of $C_\mathrm{m} = 0.173$ is used for the *Smagorinsky* model (i.e. the theoretical value [260]) and the *Sigma* calculations were performed using $C_\mathrm{m} = 1.5$ as suggested by Nicoud et al. [192]. The *KKK1* and *KKK2* models follow the idea of regularizing existing scale-similarity-type models to make them applicable in real LES. Hence, to avoid the stability-problems in the event of backscatter, the subgrid-scale tensor produced by the model is projected onto a tensor that has no energy transfer but can be considered a subgrid-scale force. In the following text, structural models (such as scale-similarity-type or gradient-type models) will be referred to as scale-similarity-type models (*SST*).

The regularized model require an arbitrary baseline scale-similarity-type model, denoted as $\tau_\mathrm{ij}^\mathrm{SST}$. In the present study Clark's tensor-diffusivity model (*CTM*) [42] is chosen for its good performance in a-priori testing, which provides for momentum transport

$$\tau_\mathrm{ij}^\mathrm{CTM} = \frac{\Delta^2}{12} \frac{\partial \tilde{u}_\mathrm{i}}{\partial x_\mathrm{k}} \frac{\partial \tilde{u}_\mathrm{j}}{\partial x_\mathrm{k}} \tag{7.9}$$

This chapter was previously published in Computers and Fluids [60] and is reprinted with permission of the journal.

and for scalar transport

$$\tau_{\mathrm{j}}^{\mathrm{CTM}} = \frac{\Delta^2}{12}\frac{\partial \tilde{u}_{\mathrm{j}}}{\partial x_{\mathrm{k}}}\frac{\partial \tilde{\phi}}{\partial x_{\mathrm{k}}} \tag{7.10}$$

The regularization reads

$$\begin{aligned}\tau_{\mathrm{ij}}^{\mathrm{KKK1}} = &\frac{-\tau_{\mathrm{ab}}^{\mathrm{SST}}\tilde{S}_{\mathrm{ab}} + |-\tau_{\mathrm{ab}}^{\mathrm{SST}}\tilde{S}_{\mathrm{ab}}|}{-\tau_{\mathrm{ab}}^{\mathrm{SST}}\tilde{S}_{\mathrm{ab}}}\tau_{\mathrm{ij}}^{\mathrm{SST}} \\ &+\left(\tau_{\mathrm{ij}}^{\mathrm{SST}} + \frac{-\tau_{\mathrm{ab}}^{\mathrm{SST}}\tilde{S}_{\mathrm{ab}}}{\tilde{S}_{\mathrm{ab}}\ \tilde{S}_{\mathrm{ab}}}\tilde{S}_{\mathrm{ij}}\right)\end{aligned} \tag{7.11}$$

($_{\mathrm{ab}}$ indicates an additional set of indices and $|-\tau_{\mathrm{ab}}^{\mathrm{SST}}\tilde{S}_{\mathrm{ab}}| = \mathrm{abs}(-\tau_{\mathrm{ab}}^{\mathrm{SST}}\tilde{S}_{\mathrm{ab}})$) and the subgrid-contribution for a scalar $\tilde{\phi}$ follows a similar form

$$\begin{aligned}\tau_{\mathrm{j}}^{\mathrm{KKK1}} = &\frac{-\tau_{\mathrm{a}}^{\mathrm{SST}}\partial\tilde{\phi}/\partial x_a + |-\tau_{\mathrm{a}}^{\mathrm{SST}}\partial\tilde{\phi}/\partial x_a|}{-\tau_{\mathrm{a}}^{\mathrm{SST}}\partial\tilde{\phi}/\partial x_a}\tau_{\mathrm{j}}^{\mathrm{SST}} \\ &+\left(\tau_{\mathrm{j}}^{\mathrm{SST}} + \frac{-\tau_{\mathrm{a}}^{\mathrm{SST}}\partial\tilde{\phi}/\partial x_a}{\left(\partial\tilde{\phi}/\partial x_a\right)^2}\partial\tilde{\phi}/\partial x_{\mathrm{j}}\right)\end{aligned} \tag{7.12}$$

The *KKK2* model is given as a further simplification of the *KKK1* model

$$\tau_{\mathrm{ij}}^{\mathrm{KKK2}} = \tau_{\mathrm{ij}}^{\mathrm{SST}} - \max\left(\frac{\tau_{\mathrm{ab}}^{\mathrm{SST}}\tilde{S}_{\mathrm{ab}}}{\tilde{S}_{\mathrm{ab}}\ \tilde{S}_{\mathrm{ab}}}, 0\right)\tilde{S}_{\mathrm{ij}} \tag{7.13}$$

for momentum transport, while the scalar transport parameterization reads

$$\tau_{\mathrm{j}}^{\mathrm{KKK2}} = \tau_{j}^{\mathrm{SST}} - \max\left(\frac{\tau_{\mathrm{a}}^{\mathrm{SST}}\partial\tilde{\phi}/\partial x_a}{\left(\partial\tilde{\phi}/\partial x_a\right)^2}, 0\right)\frac{\partial\tilde{\phi}}{\partial x_{\mathrm{j}}}. \tag{7.14}$$

Both SST models yield the same subgrid contribution in the case of back-scattering. If $\tau_{\mathrm{ab}}^{\mathrm{SST}}\tilde{S}_{\mathrm{ab}} > 0$, the first term of *KKK1* vanishes and the second term equals the formulation of *KKK2*. As the interscale energy transfer is $-\tau_{\mathrm{ij}}\tilde{S}_{\mathrm{ij}}$, the models exhibit no energy transfer and purely act as a subgrid-scale force. The major difference between the two SST models lies within their treatment of forward-scattering. Both terms of *KKK1* are active for the case of $\tau_{\mathrm{ab}}^{\mathrm{SST}}\tilde{S}_{\mathrm{ab}} < 0$ and the first term results in twice the dissipation of the baseline SST model in contrast to *KKK2* [140, 142].

The *sensor-enhanced Smagorinsky* (*SES*) model by Hasslberger et al. [96] aims for dynamical control of the subgrid-dissipation to improve the performance of the standard *Smagorinsky* model in the vicinity of walls and for transitional flows. Following Kobayashi, the sensor is based on a coherent structure function F_{CS}, defined as

$$F_{\mathrm{CS}} = Q/E \tag{7.15}$$

This chapter was previously published in Computers and Fluids [60] and is reprinted with permission of the journal.

The structure function F_{CS} includes the second invariant of the grid-scale velocity-gradient tensor Q and its magnitude E [141], i.e. with

$$Q = \frac{1}{2}\left(\tilde{W}_{\mathrm{ij}}\tilde{W}_{\mathrm{ij}} - \tilde{S}_{\mathrm{ij}}\tilde{S}_{\mathrm{ij}}\right) \tag{7.16}$$

and

$$E = \frac{1}{2}\left(\tilde{W}_{\mathrm{ij}}\tilde{W}_{\mathrm{ij}} + \tilde{S}_{\mathrm{ij}}\tilde{S}_{\mathrm{ij}}\right) \tag{7.17}$$

where the grid-scale strain rate $\tilde{S}_{\mathrm{ij}}$ is given in Eq. 7.3 and the grid-scale rotation rate is

$$\tilde{W}_{\mathrm{ij}} = \frac{1}{2}\left(\frac{\partial \tilde{u}_{\mathrm{i}}}{\partial x_{\mathrm{j}}} - \frac{\partial \tilde{u}_{\mathrm{j}}}{\partial x_{\mathrm{i}}}\right) \tag{7.18}$$

leading to the structure function being bounded between -1 and $+1$ following Kobayashi [141]. The final formulation of the sensor-enhanced model reads

$$\tau_{\mathrm{ij}}^{\mathrm{SES}} = \tau_{\mathrm{ij}}^{\mathrm{Smago.}} |\hat{F}_{\mathrm{CS}} - F_{\mathrm{CS}}|^{3/2} C_{\mathrm{sensor}} \tag{7.19}$$

The model includes a constant C_{sensor}, which is used to take account for the filter and the used numerical scheme for the momentum transport. For the suggested filter by Anderson and Domaradzki [8] and the central differencing schemes used within this study, the constant is set to a value of $C_{\mathrm{sensor}} = 1/0.16$. The proposed modification requires a spatially test-filtered coherent structure function $\hat{F}_{\mathrm{CS}}$. Hasslberger et al. [96] recommend explicit filtering as described by Anderson and Domaradzki [8], which reads

$$\hat{\tilde{\phi}}_{\mathrm{ijk}} = \sum_{\mathrm{l}=-1}^{1} \sum_{\mathrm{m}=-1}^{1} \sum_{\mathrm{n}=-1}^{1} b_{\mathrm{l}} \cdot b_{\mathrm{m}} \cdot b_{\mathrm{n}} \cdot \tilde{\phi}_{\mathrm{i+l,j+m,k+n}} \tag{7.20}$$

With the coefficients $(b_{-1}, b_0, b_{+1}) = (C, 1-2C, C)$ and the constant C being set to $C = 1/12$, however, values between $0 < C \leq 1/3$ are possible [127]. The indices i,j,k indicate the filtered cell within the x, y and z coordinate directions and m,n,l the filter-stencil within the respective direction. In the case of wall-bounded flows, the coherent structure function F_{CS} is set to zero directly at the wall, where $Q = 0$ holds.

7.3 Test Case

Ideally, the evaluation of LES-subgrid-models should be conducted with DNS and LES calculations performed with the same code, to avoid drawing the wrong conclusions due to inconsistent boundary conditions or numerical schemes. Hence, the DNS calculations of the Cambridge bluff-body burner by Proch et al. [221, 222] and Inanc et al. [109] are used for reference, as the present calculations have been performed using the same code and

This chapter was previously published in Computers and Fluids [60] and is reprinted with permission of the journal.

Table 7.1 Velocities and equivalence ratios of the inner ($U_\mathrm{i}, \phi_\mathrm{i}$) and outer ($U_\mathrm{o}, \phi_\mathrm{o}$) stream, as well as co-flow ($U_\mathrm{co}, \phi_\mathrm{co}$) at the investigated operating condition of the burner.

Case	U_i [m/s]	U_o [m/s]	U_co [m/s]	T [K]	ϕ_i [-]	ϕ_o [-]	ϕ_co [-]
SwB1	8.31	18.7	0.4	295	0.75	0.75	0
SwB5	8.31	18.7	0.4	295	1.0	0.5	0

setup, albeit on *LES*-grids. Earlier studies assessing the performance of the subgrid-closures presented in this study feature canonical cases covering laminar-turbulent transition (Taylor-Green vortex), wall dominated flows (turbulent channel flow) and a jet flow including passive scalar mixing (free planar jet) [140, 96, 59]. The Cambridge burner experiment features recirculation, swirl as well as chemical reaction under stratified conditions, offering a level of complexity that has not been covered by the previous cases. The context of combustion modeling provides a challenging case featuring transport of momentum and active scalars requiring an accurate subgrid-closure. Both calculations have revealed good agreement with the experimental evidence by Sweeney and Zhou [275, 276].

Statistics have been obtained by sampling over eight flow-through times, based on the inner streamwise velocity U_i. To ensure the removal of all roll-up vortices during the development of a stationary jet-flow, sampling is started after seven flow-through times. Hence, remaining artifacts from the initialization process are flushed out of the domain before the start of the sampling.

The present burner has been investigated within the well-known Cambridge stratified flame series by Sweeney and co-workers [275, 276, 318]. The burner consists of a bluff-body surrounded by two co-annular ducts transporting premixed methane and air with adjustable equivalence ratios at ambient conditions, allowing for the stratification of the flame. The flame is embedded in a co-flow of air.

Two different operating points *SwB1* and *SwB5* are investigated, representing two lean fuel jets (case *SwB1*) and a stratified flame with a stoichiometric inner and a lean outer fuel stream (case *SwB5*). The characteristic quantities are summarized in Tab. 7.1.

7.4 Numerical Methods

All numerical methods are used as described by Proch et al. [221, 222] and Inanc et al. [109]. The calculations were performed using the in-house code *PsiPhi*, which uses a pressure-based finite-volume approach to solve for the Navier-Stokes equations and has been used in numerous medium and highly resolved simulations of nanoparticle-synthesis, flames and canonical studies [167, 255]. The last 12 mm of the burner geometry were included in the simulation domain using the immersed boundary approach by Peskin [202]. A uniform Cartesian grid of 0.5 mm size has been chosen in order to achieve a sufficient scale separation

This chapter was previously published in Computers and Fluids [60] and is reprinted with permission of the journal.

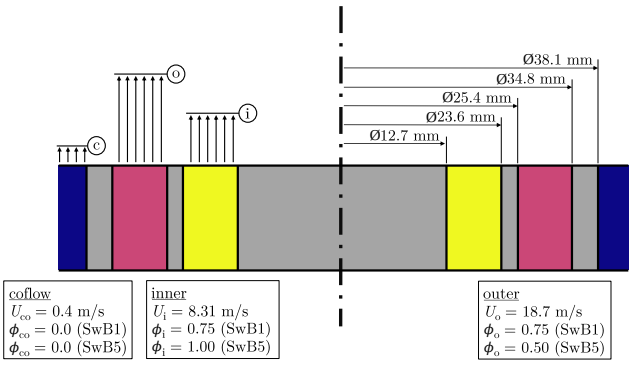

Figure 7.1 Sketch of the nozzle exit of the burner configuration [220]. The streams are characterized by the inner stream velocity U_i, the outer stream velocity U_o and the co-flow velocity U_co.

between the LES- and DNS resolution of 0.1 mm grid size, while providing an adequate amount of cells for the resolution of the burner orifice. This leads to a total amount of 13.4 million cells for the LES. Time-stepping is performed using an explicit low-storage Runge-Kutta method of third order and a CFL number of 0.5. Momentum equations are spatially discretized using second-order central differences, and gridscale- and subgrid-fluxes in additional scalar equations are treated with a Total Variation Diminishing *TVD* method relying on the *CHARM*-limiter [317]. The pressure equation is solved using a successive over-relaxation (*SOR*) Gauss-Seidel solver allowing a maximum residual pressure of 0.1 Pa, continuity is enforced by a pressure correction method embedded in a predictor-corrector scheme. Artificial fluctuations at the inlet were generated using an efficient implementation [120] of Klein's well known filter-based generation of inflow data [133] with an integral lengthscale of $l = 1.0$ mm and a fluctuation level of 10% of the mean velocity for all streams. The subgrid Schmidt-number Sc_t is set to 0.7 and the Lewis number is assumed to be unity for all species.

Including the modeling of the chemical state, the following Favre-filtered equations are solved

$$\frac{\partial \overline{\rho}}{\partial t} + \frac{\partial \overline{\rho}\tilde{u}_\mathrm{j}}{\partial x_\mathrm{j}} = 0 \tag{7.21}$$

$$\begin{aligned} \frac{\partial \overline{\rho}\tilde{u}_\mathrm{i}}{\partial t} + \frac{\partial \overline{\rho}\tilde{u}_\mathrm{i}\tilde{u}_\mathrm{j}}{\partial x_\mathrm{j}} &= -\frac{\partial \overline{p}}{\partial x_\mathrm{i}} \\ + \frac{\partial}{\partial x_\mathrm{j}}\left(\mu\left(\frac{\partial \tilde{u}_\mathrm{i}}{\partial x_\mathrm{j}} + \frac{\partial \tilde{u}_\mathrm{j}}{\partial x_\mathrm{i}} - \frac{2}{3}\frac{\partial \tilde{u}_\mathrm{k}}{\partial x_\mathrm{k}}\delta_\mathrm{ij}\right) - \overline{\rho}\tau_\mathrm{ij}^\mathrm{sgs}\right) \end{aligned} \tag{7.22}$$

$$\frac{\partial \overline{\rho}\tilde{Y}_\mathrm{C}}{\partial t} + \frac{\partial \overline{\rho}\tilde{Y}_\mathrm{C}\tilde{u}_\mathrm{j}}{\partial x_\mathrm{j}} = \frac{\partial}{\partial x_\mathrm{j}}\left(FE\overline{\rho}D\frac{\partial \tilde{Y}_\mathrm{C}}{\partial x_\mathrm{j}} - (1-\Omega)\,\overline{\rho}\tau_\mathrm{j}^\mathrm{sgs}\right) + \frac{E}{F}\dot{\omega}_\mathrm{C} \tag{7.23}$$

This chapter was previously published in Computers and Fluids [60] and is reprinted with permission of the journal.

$$\frac{\partial \overline{\rho}\tilde{Z}}{\partial t} + \frac{\partial \overline{\rho}\tilde{Z}\tilde{u}_\mathrm{j}}{\partial x_\mathrm{j}} = \frac{\partial}{\partial x_\mathrm{j}}\left(\overline{\rho}D\frac{\partial \tilde{Z}}{\partial x_\mathrm{j}} - \overline{\rho}\tau_\mathrm{j}^{\mathrm{sgs}}\right) \tag{7.24}$$

Within the scope of this study, the subgrid-terms, as presented in Sec. 7.2, are treated using Favre-filtering as well. Gravitational effects are neglected to remain consistent with the reference calculations. Following Proch et al. [220–222], the flame modeling is performed using Premixed Flame-Generated Manifolds (*PFGM*) tabulation, as originally developed by van Oijen, de Goey and Bastiaans [286, 288]. Two-dimensional flamelet tables of the chemical state depending on the progress variable Y_C and the mixture fraction Z have been generated using Cantera for a one-dimensional freely-propagating flame and the GRI-3.0 mechanism by Smith et al. [262]. Both independent lookup-variables are obtained by the previously shown corresponding transport equations, allowing for access to density, laminar viscosity, source term of the progress variable, as well as temperature and species mass fractions.

As flame-thicknesses of typical burner-flames can range between 0.1 and 0.5 mm depending on the fuel, pressure and mixture and hence, can be challenging to resolve, typical grids for LES require an artificial thickening of the flame. A dynamical thickening-factor as described by Legier et al. [158] is introduced, to stretch the flame front over a desired amount of cells, while preserving the laminar flame propagation speed. This factor is only applied in the flame-zone and smoothly set to unity outside of the flame to avoid excessive thickening. The flame-zone is determined by the flame-sensor Ω, which yields unity within and zero outside the flame. An overview of the approach is given below, for detailed insights the authors refer to Proch et al. [220].

The flame-sensor Ω is based on the normalized gradient of the progress variable Y_C and has been tabulated using a one-dimensional calculation in Cantera for a given range of progress variables and mixture fractions

$$\Omega\left(Y_\mathrm{C}, Z\right) = \left[\frac{\frac{dY_\mathrm{C}}{dx}}{\max\left(\frac{dY_\mathrm{C}}{dx}\right)}\right]_{\mathrm{1D}} \tag{7.25}$$

The need for flame-thickening is determined by the flame-sensor Ω, which leads to the dynamical formulation for the thickening-factor

$$F = 1 + \Omega\left(F_{\max} - 1\right) \tag{7.26}$$

while the maximum thickening-factor $F_{\max}$ is depending on the desired amount of grid-points n to resolve the flame

$$F_{\max} = \max\left(\frac{n\Delta}{\delta_\mathrm{l}^0}, 1\right) \tag{7.27}$$

with the unstretched laminar flame thickness δ_l^0. The limitation of $F_{\max}$ to minimum values of 1 avoids thinning of the flame. It is suggested by Charlette et al. [36] to resolve the flame

This chapter was previously published in Computers and Fluids [60] and is reprinted with permission of the journal.

using $n = 5$. To account for the loss of flame-wrinkling due to the thickening of the flame, a modified version of Charlette's [36] efficiency function E by Wang et al. [296]

$$E = \left(1 + \min\left[F_{\max} - 1, \Gamma_\Delta\left(F_{\max}, \frac{u'_\Delta}{s_l^0}, Re_\Delta\right)\right]\right)^\beta \tag{7.28}$$

is used. The constant β is chosen as 0.5, following the recommendation by Charlette et al. [36].

The thickening factor F and efficiency function E are applied to the diffusive flux and the source term of the flame progress variable Y_C conservation equation (Eq. 7.23) as

$$\frac{\partial}{\partial x_j}\left(FE\overline{\rho}D\frac{\partial \tilde{Y}_C}{\partial x_j} - (1-\Omega)\,\overline{\rho}\tau_j^{sgs}\right) + \frac{E}{F}\dot{\omega}_C \tag{7.29}$$

The subgrid-contribution is deactivated within the flame using the flame sensor Ω. The influence of the subgrid-fluxes on the transport equation of Y_C are controlled by two different quantities, which may lead to the removal of the subgrid-contribution. The first quantity is the spatial gradient of the progress variable $\partial\tilde{Y}_C/\partial x_j$ (as found in Eq. 7.5, 7.12 and 7.14), which vanishes outside the flame-region due to the gas being either unburnt or fully burnt. The second quantity is the flame sensor Ω, which obtains a value of zero outside and unity within the flame. While the spatial gradient of the flame progress variable leads to the suppression of subgrid-fluxes outside the flame, the flame sensor reduces the fluxes to zero for values within the flame, leaving remaining subgrid-fluxes only in the outer preheat-zone and oxidation-layer of the flame.

7.5 Results of SwB1

The results will be discussed in two sections for the respective cases *SwB1* and *SwB5*.

To provide a first visual impression, Fig. 7.2 shows the instantaneous and time-averaged (*mean*) fields of the equivalence ratio ϕ in the $x-y$ midplane for the LES calculations of the cases *SwB1*.

The equivalence ratio fields show steep gradients between the outer stream and the co-flow. The higher fluctuation level in the outer jet leads to wrinkling in the equivalence ratio field immediately after the nozzle exit. Turbulent mixing occurs in the mixing layer between the inner and outer streams and the air co-flow, forming Kelvin-Helmholtz roll-ups, which grow in thickness when moving downstream. The flame is not influenced by strong turbulent fluctuations in the near region, where it is only moderately wrinkled. Different observations can be made in the far region, where the flame front burns across the shear layer and gets wrinkled more strongly. Fresh gas starts penetrating into the burned region, this results in

This chapter was previously published in Computers and Fluids [60] and is reprinted with permission of the journal.

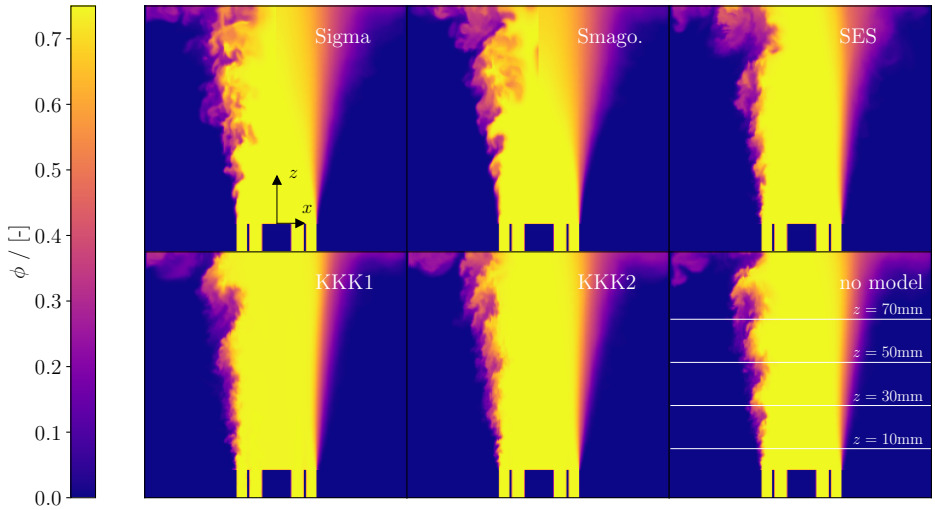

Figure 7.2 Snapshots of the mean and instantaneous equivalence ratio ϕ for *SwB1* in the $x-y$ midplane. The streamwise flow direction points from bottom to top.

unburnt mixture fingers as described in previous works. Also the opposite phenomenon can be observed when narrow regions of burned gas penetrate into the fresh gas, which further downstream leads to regions where pockets of burned gas exist in the fresh gas and regions where fresh gas is surrounded by burned gas in the burner mid-section [221, 21, 214, 215].

The standard eddy-viscosity models reveal distinct differences from the modified *Smagorinsky* and the scale-similarity-type models. The *Smagorinsky* and *Sigma* model feature coarser turbulent structures in the shear-layer and stronger diffusivity - as seen in the mean fields - which is a common problem of standard eddy-viscosity approaches.

Computations for the assessment of five LES subgrid-models including the standard *Smagorinsky*- (denoted as *Smago.*), the Sigma- (*Sigma*), the sensor-enhanced Smagorinsky- (*SES*), the KKK1- (*KKK1*) and the KKK2- (*KKK2*) model, as well as an LES without subgrid-modeling (underresolved DNS, *no model*) have been performed. The *no model* calculations are included to assess if the subgrid-modeling leads to an improvement of the LES results. The respective computational times are displayed in Tab. 7.2 and are normalized by the run-time of the *no model* calculation. The table reveals similar run-times for all calculations, with the standard eddy-viscosity models requiring slightly less computational time than the new models. Further, it can be observed, that the eddy viscosity models require more computational time for the solution of the Poisson equation, which might be interpreted as an indication for the more physical nature of the subgrid-fluxes obtained from the SST models.

This chapter was previously published in Computers and Fluids [60] and is reprinted with permission of the journal.

Table 7.2 Computational times of the performed calculations using different subgrid-models for *SwB1*.

Model	Total computational time	Projection time	Turbulence time
	% - no model	% - Total	% - Total
Sigma	1.05	23.6	2.2
Smagorinsky	1.04	24.9	3.3
SES	1.17	30.1	3.5
KKK1	1.22	20.2	15.0
KKK2	1.16	19.9	12.0
no model	1.00	23.3	0

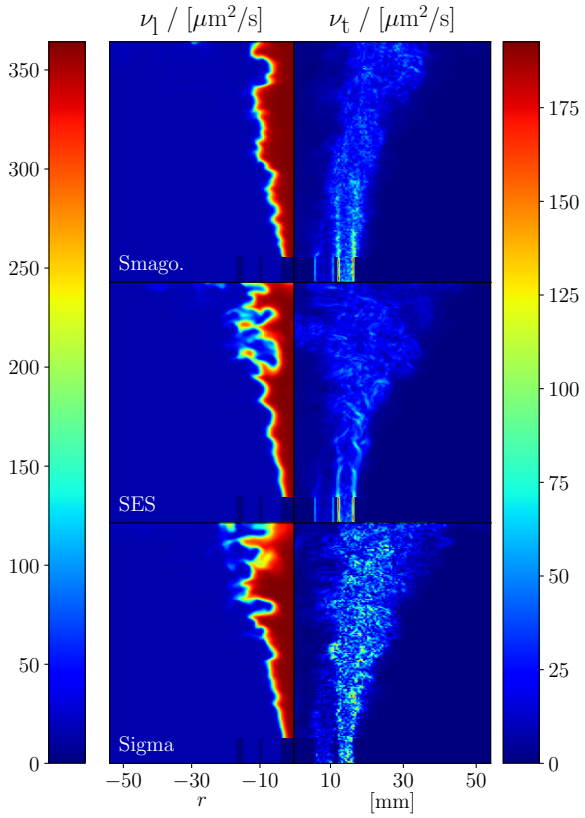

Figure 7.3 Instantaneous snapshots of the laminar (left) ν_l and turbulent (right) ν_t viscosity produced by the eddy-viscosity models (*Smagorinsky*, *SES*, *Sigma*) in the $x-y$ midplane for *SwB1*. The streamwise flow direction points from bottom to top.

This chapter was previously published in Computers and Fluids [60] and is reprinted with permission of the journal.

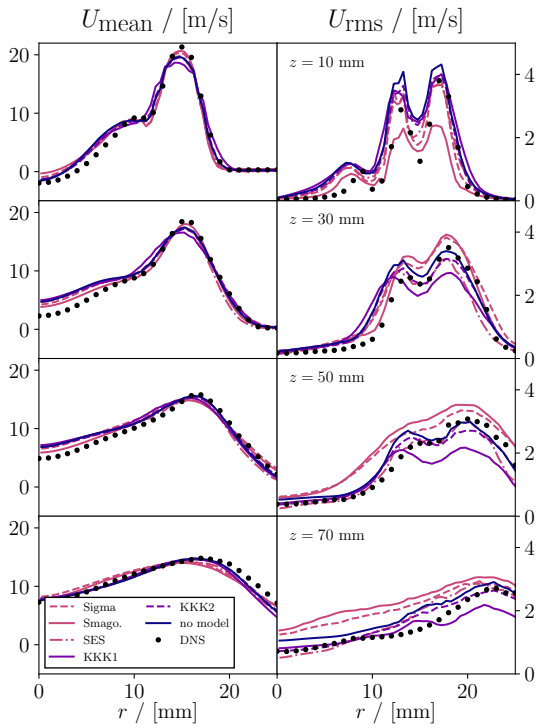

Figure 7.4 Radial profiles of the mean and rms streamwise velocity U at different streamwise positions with 10 mm, 30 mm, 50 mm and 70 mm distance to the nozzle exit for *SwB1*.

Instantaneous fields of the laminar and eddy viscosities of the *Smagorinsky* model without and with the use of the sensor, as well as the *Sigma* model are shown in Fig. 7.3. The structure of the eddy-viscosity fields clearly visualizes the key differences between the three models. While the standard *Smagorinsky* model leads to often criticized high turbulent viscosities, the *SES* model features less excessive turbulent viscosities, which agree with the evolution of the shear layer. The *Sigma* model produces - probably unphysical - high-frequency fluctuations of turbulent viscosity, which is assumed to be a consequence of the eigenvalue calculation in the determination of $\tilde{D}_{\mathrm{m}}$.

Figure 7.4 shows the radial mean and rms value of the streamwise velocity U for four different heights 10, 30, 50 and 70 mm above the burner cap for all calculations, including the flame-resolved results of Proch et al. [221], which have been obtained using the same code. All models are in good agreement with the reference data, while the eddy-viscosity type models appear to resolve the peak velocity slightly better closer the burner and the scale-similarity-type models tend to give better results in the peak region further downstream. It is a common recommendation in literature to use second order statistical moments to assess the performance of numerical simulation, as the comparison of mean values tends to show little differences, which can also be observed in this case. For the streamwise velocity rms, the

This chapter was previously published in Computers and Fluids [60] and is reprinted with permission of the journal.

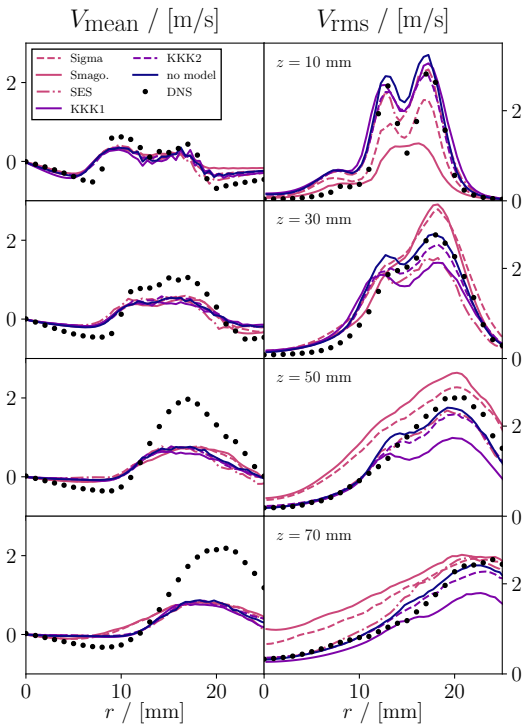

Figure 7.5 Radial profiles of the mean and rms radial velocity V at different streamwise positions with 10 mm, 30 mm, 50 mm and 70 mm distance to the nozzle exit for *SwB1*.

eddy-viscosity models tend to overall overpredict the rms-statistics, while the *KKK1* model tends to underpredict the profiles. The *Sigma* and *Smagorinsky* model are in good agreement with the DNS data at $z = 10$ mm, while all calculations show good visual performance at $z = 30$ mm. The best agreement with the DNS data for larger distances from the burner is shown by the *SES*, the *KKK2* and the *no model* calculation.

The radial profiles of the mean and rms of the radial velocity V are shown in Fig. 7.5. All calculations capture the overall trend of the mean velocity profiles, while the prediction of the peak magnitude worsens with increasing distance from the burner. Again, only little deviation between the different models can be seen for the mean profiles. It can be noted that all calculations show weak oscillations between a radius of 10 and 20 mm at $z = 10$ mm, where the inner and outer streams merge. The rms statistics again reveal considerable overprediction of the reference data by the conventional eddy-viscosity models for distances of $z = 10$ mm and onwards. The best performance is shown by the sensor-enhanced model and the *KKK2* model, as well as the *no model* calculation.

Figure 7.6 shows the radial mean and rms profiles of the temperature T at the given distances from the burner orifice. All calculations struggle to properly capture the temperature

This chapter was previously published in Computers and Fluids [60] and is reprinted with permission of the journal.

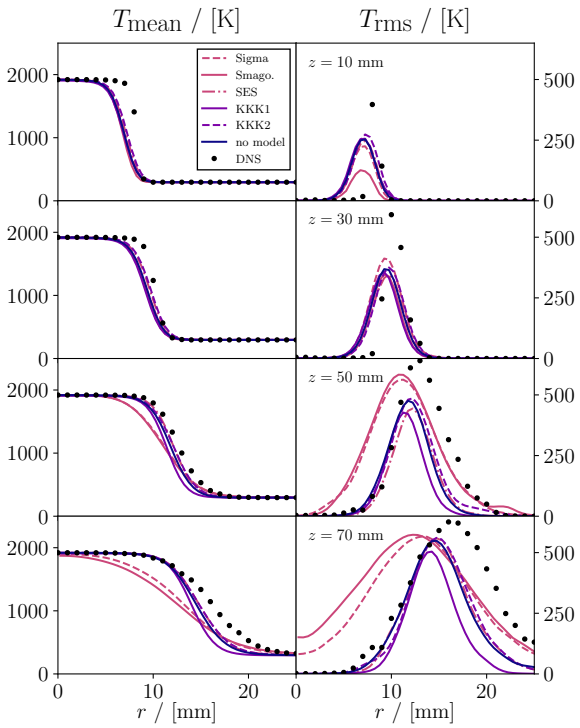

Figure 7.6 Radial profiles of the mean and rms temperature T at different streamwise positions with 10 mm, 30 mm, 50 mm and 70 mm distance to the nozzle exit for *SwB1*.

gradient through the flame front. The standard eddy-viscosity *Smagorinsky* and *Sigma* models show progressive flattening of the profile with increasing distance from the burner, while the *SES* model performs better, like the scale-similarity-type models. The radial rms profiles are underpredicted to the reference data, especially at axial distances of 10 mm and 30 mm. While the prediction of the peak with increasing streamwise distance becomes more accurate, the spreading of the *Smagorinsky* and *Sigma* curve intensifies. Although the boundedness of mean temperature results between unburned and burned temperature is maintained for all models, the agreement of the rms results with the reference data remains quite unsatisfactory. It has to be noted, that the temperature is obtained from the flamelet tables using the mixture fraction and the flame progress variable, with the latter one being influenced by the flame thickening. The thickening affects the flame by stretching the flame front over a desired amount of cells and hence, also flattens the temperature gradient. In this case in particular, the thickening is performed based on the laminar flame thickness, which is obtained from the maximum temperature gradient of the one-dimensional calculation [220]. Applying the thickening then rescales the temperature gradient precisely by the chosen maximum thickening factor, which changes the mean temperature profiles and hence, leads to a misprediction of the rms values as well. Thus, the subgrid-model does not take the responsibility for the deviation in the maximum temperature gradient at least near the burner,

This chapter was previously published in Computers and Fluids [60] and is reprinted with permission of the journal.

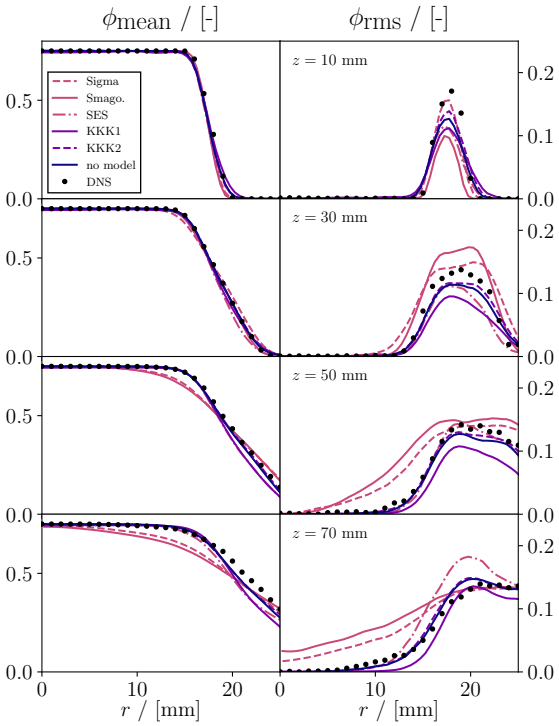

Figure 7.7 Radial profiles of the mean and rms equivalence ratio ϕ at different streamwise positions with 10 mm, 30 mm, 50 mm and 70 mm distance to the nozzle exit for *SwB1*.

however, certainly is the cause for the strong flattening as in the *Sigma* and *Smagorinsky* model calculations.

The mean and rms radial profiles of the equivalence ratio ϕ can be seen in Fig. 7.7 for all streamwise locations. The LES results are in good agreement with the DNS data at $z = 10$ and 30 mm, with the inlet value of $\phi = 0.75$ being maintained well, as ϕ is obtained from the mixture fraction, which is not influenced by the flame thickening. For larger z, the scale-similarity-type models and the *SES* model are in good agreement. The *Sigma* and *Smagorinsky* model show stronger smoothening of the profiles, which can be a consequence of the aforementioned strong diffusivity provided by these models. For the rms profiles, the eddy-viscosity models show strong flattening of the curves from $z = 50$ mm and onwards, while overpredicting the DNS data at $z = 30$ mm. The *SES* and the *KKK* models fail to predict the peak properly for smaller z but show very good agreement for larger distances from the burner cap.

Figure 7.8 shows the CO mass fraction Y_{CO} with radial distance from the centerline. The intermediate species CO has been chosen to allow for insight into the resolution of inner-flame processes. The mean profiles show little difference at distances of 10 mm and 30

This chapter was previously published in Computers and Fluids [60] and is reprinted with permission of the journal.

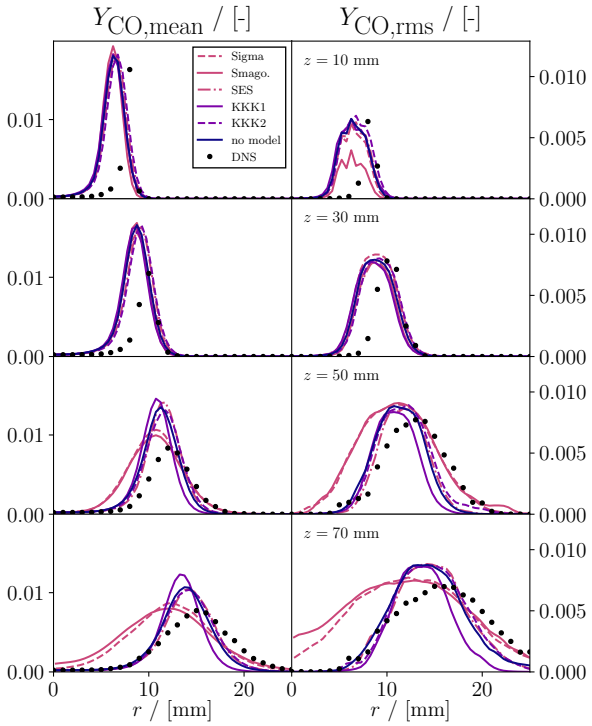

Figure 7.8 Radial profiles of the mean and rms CO mass-fraction Y_{CO} at different streamwise positions with 10 mm, 30 mm, 50 mm and 70 mm distance to the nozzle exit for *SwB1*.

mm above the burner cap. All calculations strongly overpredict the peak mean CO mass fraction. The *Sigma* and standard *Smagorinsky* model manage to capture the peak value for higher distances, but feature strong spreading. The remaining models lead to better resolution of the spreading, but overpredict the peak value. The overall match between the LES and DNS data is better for the rms profiles. The *Sigma* and *Smagorinsky* models manage to resolve the magnitude more accurately, while showing the largest offset. The CO mass fraction is influenced by the flame thickening in a similar manner as the temperature. However, as the thickening is applied in all calculations equally, the differences between the models are caused by the subgrid-model only and hence, may be interpreted in the context of the respective model used.

The total deviation from the DNS data for the *SwB1*-case has been calculated and visualized in Fig. 7.9. The normalized 1-norm (i.e. the sum of the absolute values of the deviations) between the LES and DNS data has been chosen to measure the quantitative error as previous investigation by Klein et al. [140] revealed little difference between different error measures and the 1-norm provided the best agreement between visual inspection of the profiles in Figs. 7.4-7.8 and the quantitative error measures in Figs. 7.9 and 7.10. The velocities are normalized (indicated by index n in Fig. 7.9) using U_i for the mean and $0.1U_i$

This chapter was previously published in Computers and Fluids [60] and is reprinted with permission of the journal.

for the rms values (corresponding to the prescribed inlet fluctuation intensity), while the temperature is normalized with $(T_b - T_u)$ for the mean and $0.1(T_b - T_u)$ for the rms values respectively. The equivalence ratio and the species mass fraction are normalized using unity. The results of the quantitative assessment confirm the findings obtained from the qualitative analysis of the radial profiles from Fig. 7.4 to 7.8. Overall, the standard *Smagorinsky* model shows the largest deviations. The *Sigma* model shows improved behavior compared to the *Smagorinsky* model but features some outliers, which can be avoided by using the *SES* model. The *KKK1* model shows acceptable results, however, the *KKK2* model is preferred over the *KKK1* model as it shows the smallest errors.

Overall, the *KKK1* model shows modest performance. While this case shows more similarities with a jet-flow than a closed channel, it has to be noted, that the tip of the burner is included into the domain and hence, makes walls present for the inflow. Previous studies showed, that the performance of the *KKK1* model deteriorates in the presence of walls [140, 59]. Hence, one might assume that the weaker performance of the *KKK1* model is a consequence of the burner-orifice at the inlet of the domain and that the model might perform better, if no burner geometry is included into the computational domain.

The graphical presentation of the error in Fig. 7.10, which represents the absolute mean error over all axial locations as depicted in Fig. 7.9, shows that the *KKK2* model has the overall best behaviour and also outperforms the simulation without a subgrid model. The *SES* model is the second best model for predicting the fluctuations and considerably better than the other EDV models. The velocity bars of the mean quantities should be interpreted with care because the error is mostly on a small level and the model performance is more or less similar. The overall improved rms predictions of the *KKK2* and *SES* models result in a better mixing behaviour which translates into a better prediction of all mean and rms scalar quantities.

7.6 Results of SwB5

The results of case *SwB5* are discussed in this section. Opposed to *SwB1*, the equivalence ratios of the inner and outer stream differ, leading to stratification of the flame.

The equivalence ratio distributions for this case are shown in Fig. 7.11. The gradient appears more flat in this configuration as the equivalence ratio is first reduced from the inner to the outer stream and then vanishes in the co-flow. Following Proch [220], one can distinguish three characteristic flame regions. The first region is perfectly premixed and characterized by a constant mean flame angle and only moderate broadening of the mean flame brush. The second region starts where the flame enters into the region of equivalence ratio gradients, and is exposed to stratification. The curvature of the gradient-front increases, resulting in a broadening of the mean flame brush. Further onwards the whole flame is exposed to an equivalence ratio gradient. The equivalence ratio at the burnt side of the flame

This chapter was previously published in Computers and Fluids [60] and is reprinted with permission of the journal.

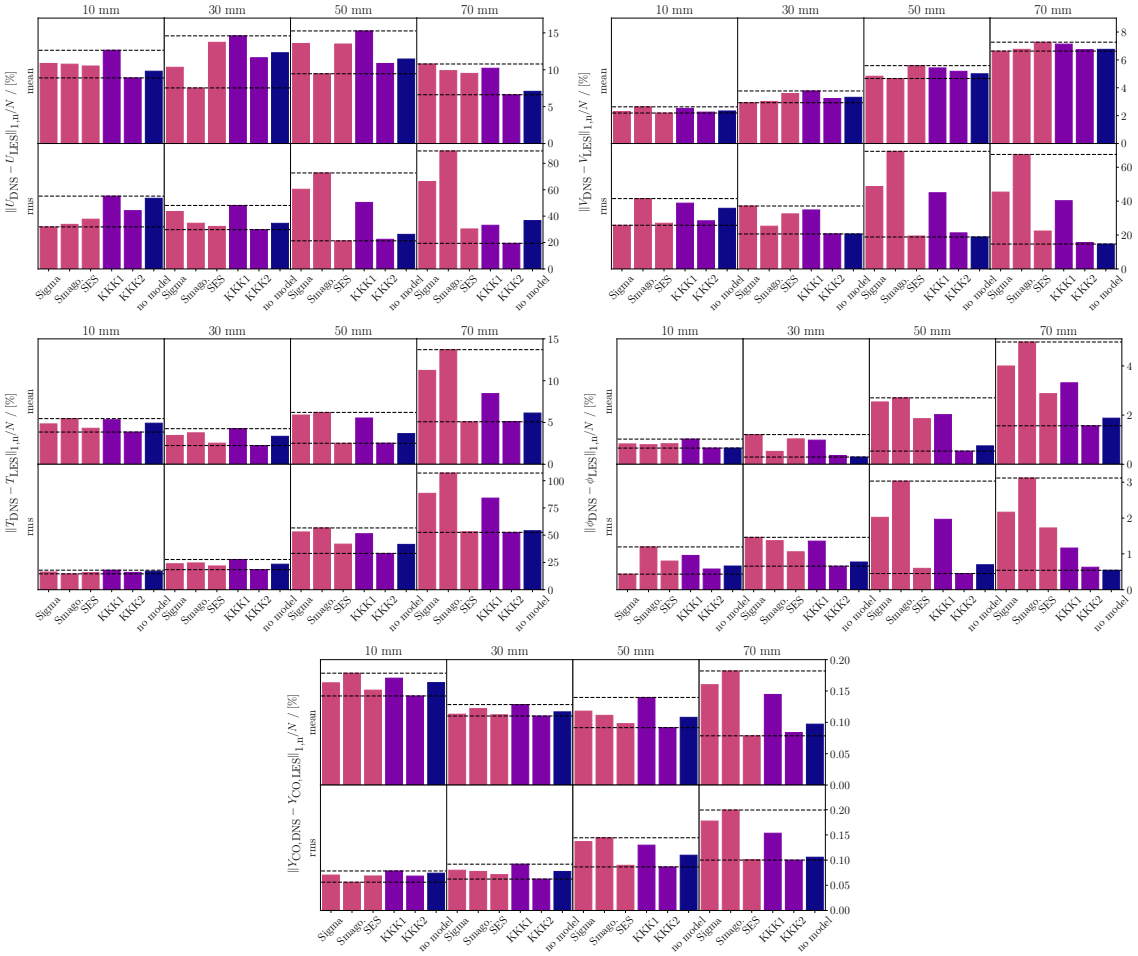

Figure 7.9 Graphical presentation of LES-DNS deviation for *SwB1*. The dashed lines show the smallest and the largest deviation.

This chapter was previously published in Computers and Fluids [60] and is reprinted with permission of the journal.

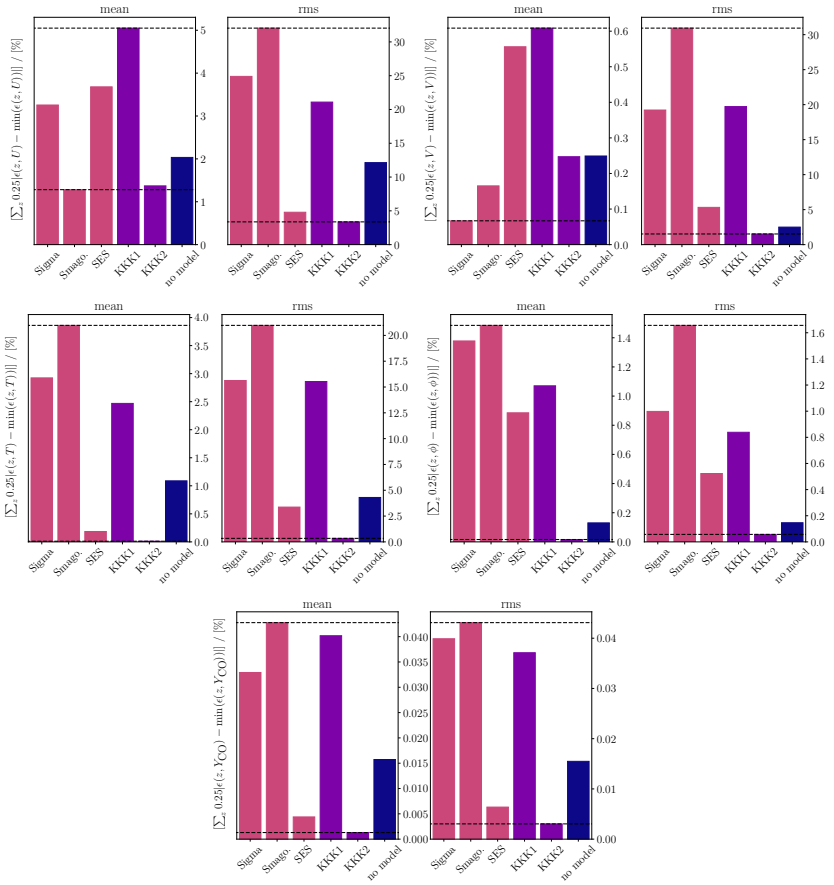

Figure 7.10 Graphical presentation of LES-DNS deviation for *SwB1* summarized over all distances from the nozzle. The dashed lines show the smallest and the largest summarized deviation.

This chapter was previously published in Computers and Fluids [60] and is reprinted with permission of the journal.

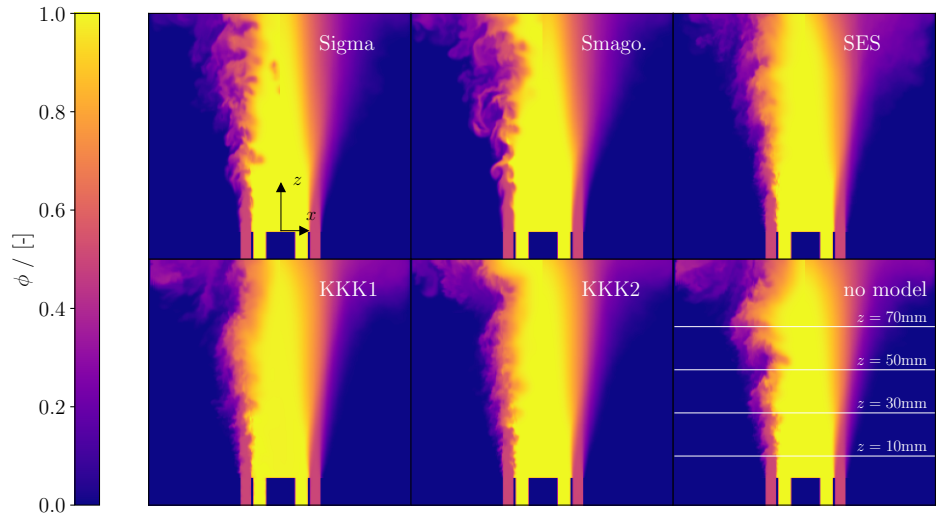

Figure 7.11 Snapshots of the mean and instantaneous equivalence ratio ϕ for *SwB5* in the $x - y$ midplane. The streamwise flow direction points from bottom to top.

Table 7.3 Computational times of the performed calculations using different subgrid-models for *SwB5*.

Model	Total computational time	Projection time	Turbulence time
	% - no model	% - Total	% - Total
Sigma	1.02	22.2	2.2
Smagorinsky	1.01	23.5	3.1
SES	1.18	32.2	3.3
KKK1	1.12	19.7	12.1
KKK2	1.12	19.2	11.9
no model	1.00	22.5	0

converges then towards a value of 0.6, which is the mean of the value at the flammability limit. On the unburnt side of the flame the equivalence ratio converges towards the average value at the inlet, which is 0.75 for all cases. The transition point to the third region is located where the instantaneous flame touches the flammability limit line. Here, the motion of the unburnt side of the flame is determined by the mixing behavior [220].

To allow for the investigation of a different mixture composition, the same analytics have been applied to simulations of the *SwB5* case. The total computational times as well as the computing time spent on the projection-method and the turbulence modeling are documented in Tab. 7.3. Again, the standard eddy-viscosity models require the lowest computational time, while the new models take around ten percent more computational time. The scale-similarity-type models require more computational time for the calculation of the subgrid-fluxes and less time for the projection-method. Figure 7.12 shows instantaneous fields of the laminar ν_l (left) and eddy- ν_t (right) viscosity of the *Sigma*, standard *Smagorinsky*

This chapter was previously published in Computers and Fluids [60] and is reprinted with permission of the journal.

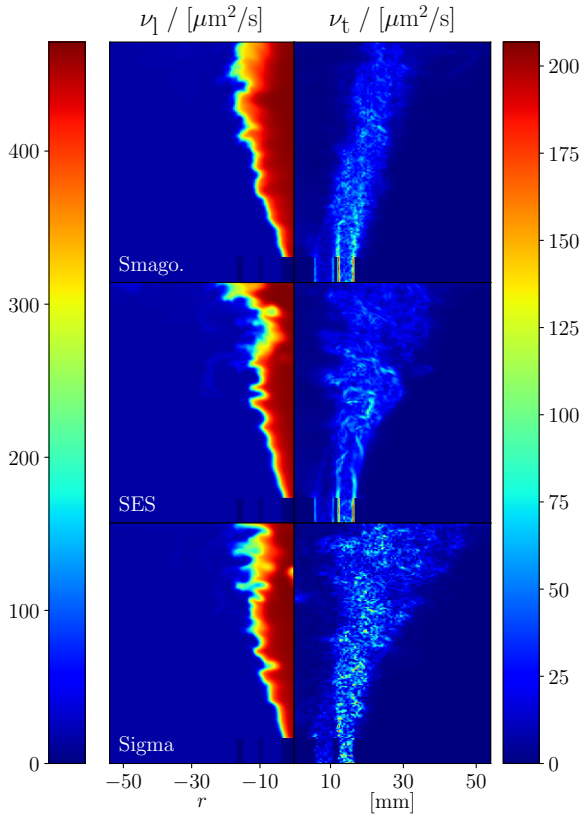

Figure 7.12 Instantaneous snapshots of the laminar (left) ν_l and turbulent (right) ν_t viscosity produced by the eddy-viscosity models (*Smagorinsky*, *SES*, *Sigma*) in the $x-y$ midplane for *SwB5*. The streamwise flow direction points from bottom to top.

This chapter was previously published in Computers and Fluids [60] and is reprinted with permission of the journal.

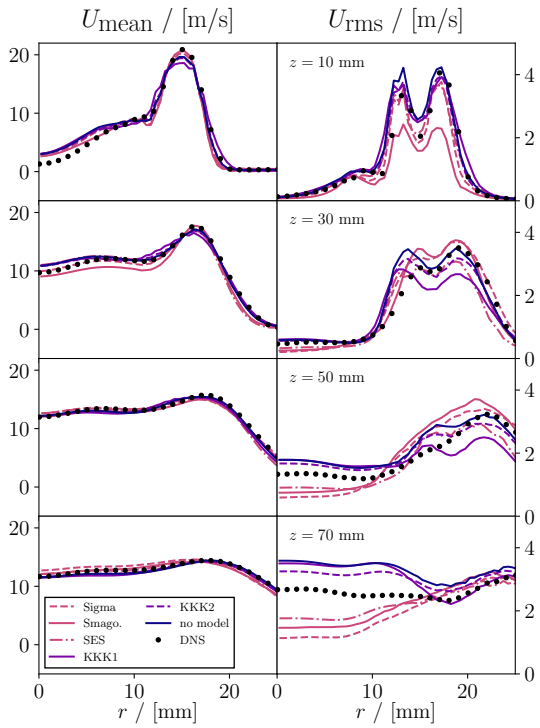

Figure 7.13 Radial profiles of the mean and rms streamwise velocity U at different streamwise positions with 10 mm, 30 mm, 50 mm and 70 mm distance to the nozzle exit for *SwB5*.

and *SES* model. The standard *Smagorinsky* model exhibits high overall viscosities compared to the sensor-enhanced version, which appear more physical than for the *Sigma* model, as coherent structures are well preserved by the *SES* model. The *Sigma* model produces lower viscosity-values, which are non-physically scattered. The standard *Smagorinsky* model appears to show similar physical structures to the *SES* model, which seem to be superimposed by excessive eddy-viscosities however.

Figure 7.13 shows the streamwise velocity U profiles for the given set of streamwise distances from the burner orifice. All mean profiles are in good agreement with the DNS data, however, more distinct differences can be observed for the rms profiles. The scale-similarity models and the *Smagorinsky* models are in good agreement with the DNS data at $z = 10$ mm, while the *Sigma* model shows stronger underprediction than the remaining models. The differences between the models emerge further for longer distances from the burner cap. For lower radii, the eddy-viscosity models appear to underpredict the rms values and the scale-similarity and *no model* calculations tend to overpredict the rms values, which may be interpreted as a result of either too strong or too little dissipation. The models show more similar behavior for $r > 20$ mm with the *KKK1* model tending to underpredict the DNS data.

This chapter was previously published in Computers and Fluids [60] and is reprinted with permission of the journal.

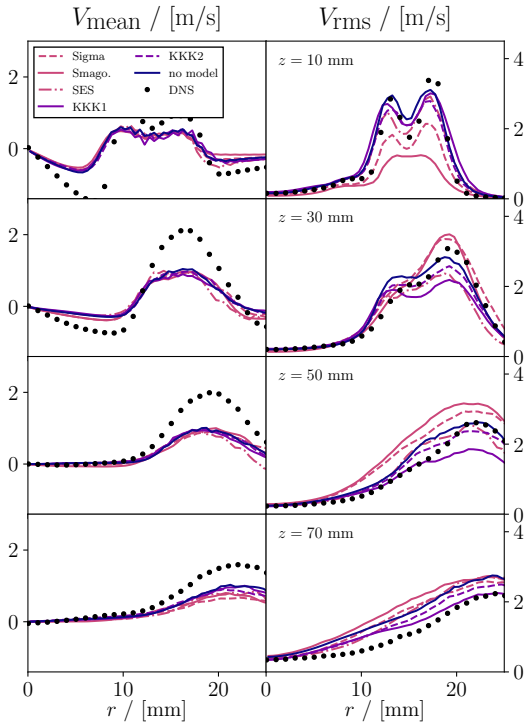

Figure 7.14 Radial profiles of the mean and rms radial velocity V at different streamwise positions with 10 mm, 30 mm, 50 mm and 70 mm distance to the nozzle exit for *SwB5*.

The profiles of the radial velocity V can be seen in Fig. 7.14. The mean profiles feature little difference between the calculations, but the standard eddy-viscosity models appear to show slightly more flattening of the profiles than the remaining models. Similar to the streamwise velocity profiles, the eddy-viscosity models underpredict the rms reference data at $z = 10$ mm and show better agreement for $z = 30$ mm, however, overpredict the data. The *KKK2* as well as the *SES* models are in good overall agreement.

In Fig. 7.15, the temperature T with the radius for the four examined streamwise distances z is shown. The scale-similarity models, the *SES* model and the *no model* calculation are in good agreement with the DNS data for the mean profiles. The agreement of the standard *Sigma* and *Smagorinsky* model with the DNS data worsens with increasing distance z and the radial temperature gradient is significantly smoothened. All calculations underpredict the rms of the reference temperature for smaller streamwise distances, but the agreement improves for larger z. The *Smagorinsky* model stands out at $z = 10$ mm for strongly underpredicting the peak rms of the temperature, but shows very similar performance to the *Sigma* model for the remaining streamwise distances. While their agreement with the peak value at 50 and 70 mm is good, the profiles appear to be radially shifted and feature stronger spread

This chapter was previously published in Computers and Fluids [60] and is reprinted with permission of the journal.

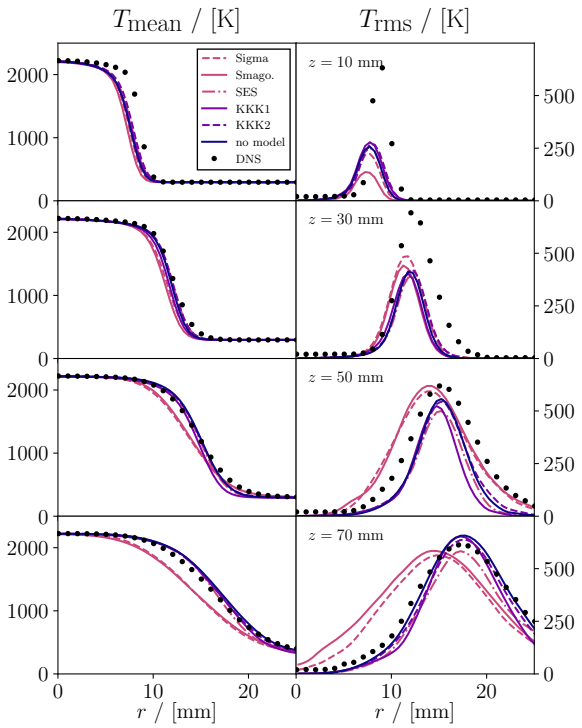

Figure 7.15 Radial profiles of the mean and rms temperature T at different streamwise positions with 10 mm, 30 mm, 50 mm and 70 mm distance to the nozzle exit for *SwB5*.

than the DNS data. The remaining profiles capture the reference data correctly in radial direction but overall underpredict the peak. The best agreement can be found at $z = 70$ mm. Again, it may be argued that the overall mismatch between the maximum temperature gradient at $z = 10$ is not solely caused by the subgrid-model, but more likely consequence of the flame thickening. The excessive smoothening of the temperature gradient, however, may be assumed to be a direct effect of the *Smagorinsky* and *Sigma* subgrid-models.

Due to availability of reference data, the OH mass-fractions are shown in Fig. 7.16. The profiles show all models for the different streamwise locations. The radial mean profiles appear similar for smaller z. For larger z, the standard eddy-viscosity approaches underpredict the DNS data, while the remaining calculations show overprediction of the reference data. All calculations fail to properly capture the peak of the rms of the mass-fractions at $z = 10$ mm and $z = 30$ mm. Again, the standard eddy-viscosity model results appear radially shifted for the largest distances z. The models overpredict the peak value at $z = 50$ and $z = 70$ mm. The *SES* model shows the best agreement with the DNS data at $z = 70$ mm. Again the *KKK2* model outperforms all other models including the *no model* simulation. The *SES* model seems to be the most promising variant of eddy viscosity models.

This chapter was previously published in Computers and Fluids [60] and is reprinted with permission of the journal.

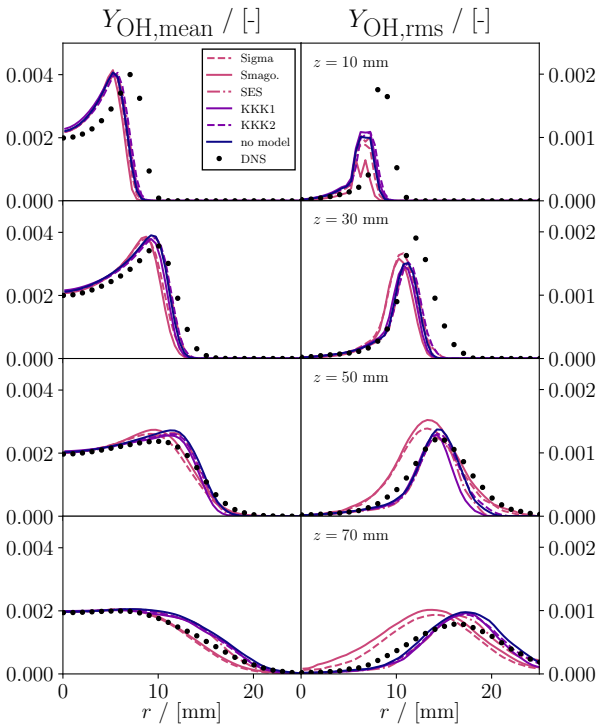

Figure 7.16 Radial profiles of the mean and rms OH mass-fraction Y_{OH} at different streamwise positions with 10 mm, 30 mm, 50 mm and 70 mm distance to the nozzle exit for *SwB5*.

The corresponding quantitative errors are visualized in Fig. 7.17. An error measure to summarize all distances from the model is shown in Fig. 7.18 by averaging the difference of each model error and the minimum error produced by a model at given nozzle distance. The normalization is applied in a similar manner to Fig. 7.9. Both tables quantitatively confirm the insights obtained from the radial profiles.

While the model performance can be categorized in a similar manner to the *SwB1* setup, the overall agreement of the LES and DNS results is worse for *SwB5*. The difference between the cases lies within the different equivalence ratio ϕ, which has a value of 0.75 for the inner and outer burner slot at *SwB1*, but has values of 1.0 for the inner and 0.5 for the outer burner slot in the case of *SwB5*. This leads to stratification of the flame and a greater importance of mixing processes. It can be speculated that the overall decreasing quality of simulation results is a consequence of higher resolution requirements for capturing the mixing process for case *SwB5*. The *KKK2* and *SES* models tend to show the best results but it becomes also apparent that the *no model* calculation performs comparable or better than the other choices of subgrid-models. This observation is more pronounced for the *SwB5* case. It may be concluded in this context, that the flame phenomena and hence the simulation quality strongly depend on the small scale phenomena, which are resolved better in the calculations using less dissipative models.

This chapter was previously published in Computers and Fluids [60] and is reprinted with permission of the journal.

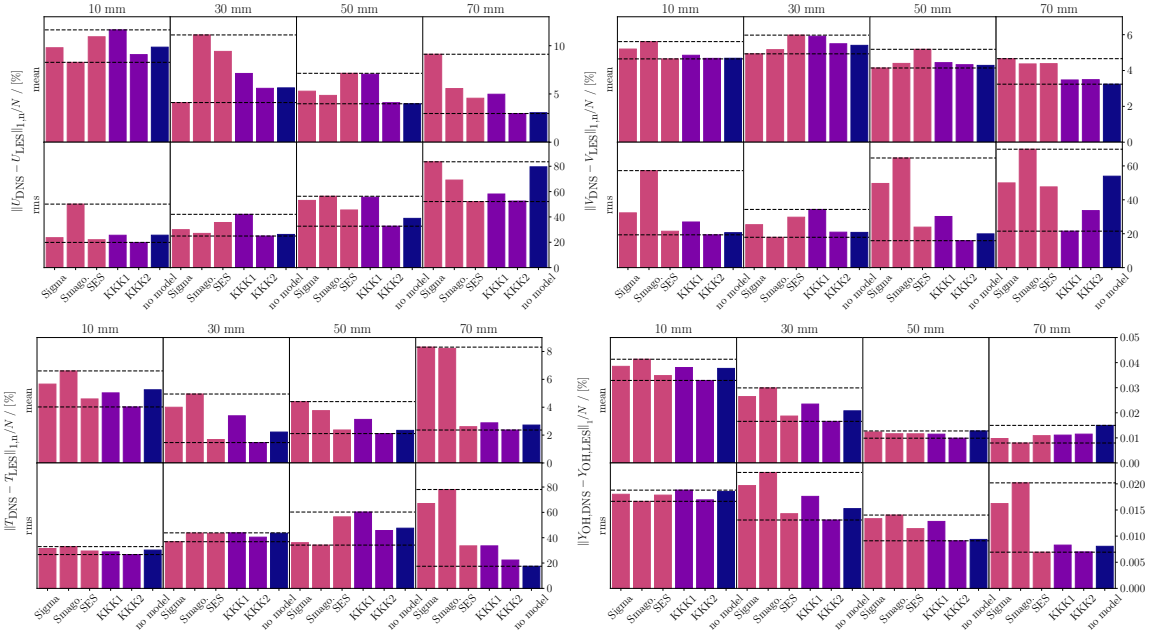

Figure 7.17 Graphical presentation of the absolute LES-DNS deviation for *SwB5*. The dashed lines show the smallest and the largest deviation.

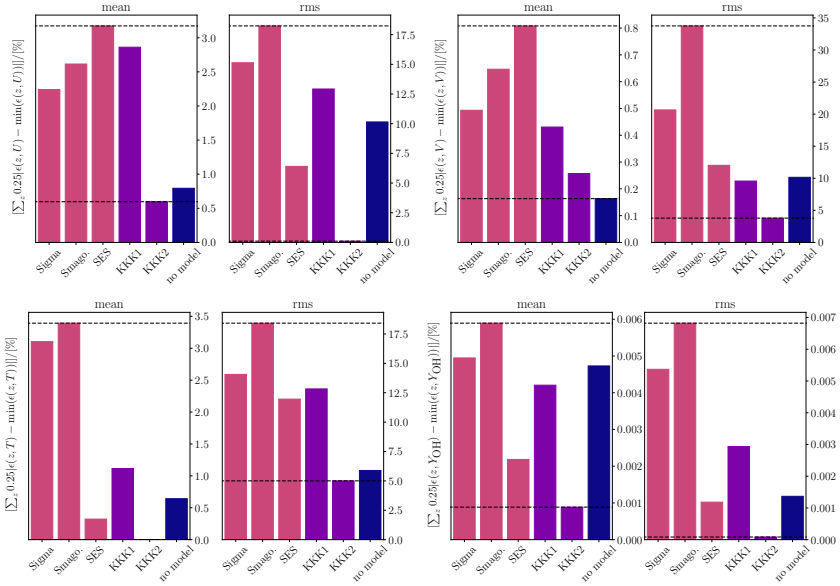

Figure 7.18 Graphical presentation of the absolute LES-DNS deviation for *SwB5* summarized over all distances from the nozzle. The dashed lines show the smallest and the largest summarized deviation.

This chapter was previously published in Computers and Fluids [60] and is reprinted with permission of the journal.

7.7 Prospect

An earlier study by Klein et al. revealed that more advanced subgrid modeling in the case of turbulent premixed combustion might be necessary for the proper prediction of the alignment characteristics of the SGS tensor [135]. Common flames produce increased strain due to thermal expansion while leaving the local vorticity mostly unaffected. Although, the observed additional strain due to thermal expansion is not of turbulent nature, it is mistakenly considered in the calculation of the turbulent viscosity.

An adjustment of the *Smagorinsky* model may be suggested to take into account for the strain-vorticity imbalance within the flame. The operator $\tilde{D}_\mathrm{m}$ can be modified as

$$\tilde{D}_\mathrm{m,f} = \min\left(\sqrt{2\tilde{S}_\mathrm{ab}\tilde{S}_\mathrm{ab}}, 1.1055\sqrt{2\tilde{W}_\mathrm{ab}\tilde{W}_\mathrm{ab}}\right) \tag{7.30}$$

where the value of 1.1055 is the ratio of the strain rate and vorticity, and can be derived from the critical value of the coherent structure function $F_\mathrm{CS} \approx -0.1$ for homogeneous isotropic turbulence [141]. Hence, the modification limits the eddy-viscosity within the flame.

To ensure this modification being applied within the flame region only, a blending for the operator $\tilde{D}_\mathrm{m}$ can be applied using the flame sensor Ω, which is present in many combustion models already, such that

$$\begin{aligned}\tilde{D}_\mathrm{m} = \min\left(\sqrt{2\tilde{S}_\mathrm{ab}\tilde{S}_\mathrm{ab}}, 1.1055\sqrt{2\tilde{W}_\mathrm{ab}\tilde{W}_\mathrm{ab}}\right)\cdot\Omega \\ + \left(\sqrt{2\tilde{S}_\mathrm{ab}\tilde{S}_\mathrm{ab}}\right)\cdot(1-\Omega)\end{aligned} \tag{7.31}$$

Hence, the modification is only applied within the range of $\Omega > 0$. Notable effects may be expected for mildly thickened flames or for flame resolved calculations relying on subgrid-modeling to improve stability. Only small differences have been observed for the flames considered within this work and hence are not reported.

7.8 Summary

Large-Eddy Simulations using six different approaches for the subgrid fluxes have been performed for the operation points *SwB1* and *SwB5* of the Cambridge stratified flame series. The calculations have been compared using the identical numerical setup and the results of the flame resolved direct numerical simulations of Proch and Inanc [221, 222, 109]. A visual analysis of the streamwise velocity fields revealed stronger dissipation of the *Sigma* and *Smagorinsky* models compared to the scale-similarity-type approaches. However, the *SES* model suggested by Hasslberger et al. [96] is an effective way to reduce this excessive dissipation. The new models required overall ten percent more computational time compared

This chapter was previously published in Computers and Fluids [60] and is reprinted with permission of the journal.

to the standard eddy-viscosity models due to more time spent in the turbulence routines, while the costs of the projection method decreased. The relative influence of the turbulence-modeling time reduces if more complex additional physical models (e.g. combustion models) are used. Following the quantitative analysis, especially the *KKK2* and the *SES* model are in good agreement with the reference data. The *Sigma* and *Smagorinsky* model show good results closer to the burner-cap but suffer from the strong dissipation for larger distances. Among the two scale-similarity-type models, the *KKK1* model showed overall inferior behavior compared to the *KKK2* model throughout all results. Previous work [59], however revealed strong performance of the *KKK1* model for free shear flows, while the *KKK1* model results were found to deteriorate in the presence of walls [140]. As a result it can be speculated that the *KKK1* results are dominated by the nozzle flow, an assumption which is underlined by the fact that relatively large deviations occur already close to the nozzle. Overall, the results can be summarized as follows: All models show similar performance for the prediction of mean velocity components but substantially differ in the prediction of velocity rms. Good prediction of velocity fluctuations is responsible for good mixing characteristics and hence the better model performance here can be recovered in all statistics of scalar quantities. It is worth noting that the prediction of scalar quantities is also influenced by the combustion model, such that, for example, the momentum subgrid-closures should not be blamed for not capturing the gradients in the flame front which are decreased due to the use of the flame thickening. Hence, it has to be pointed out, that the performance of the subgrid-closure might change employing a different combustion model due to the interaction of models for different unclosed terms [137]. Further, model constants had to be chosen for the eddy-viscosity models used in this study, which influences the performance of the respective models. Ideally, these model constants need to be known before the simulation. Standard model constants and subgrid Schmidt number have been chosen for this reason and calculations without subgrid-modeling have been included as well. Dynamic determination of the turbulent viscosity is possible, however, has been shown to be misleading if heat release effects overcome the effects of turbulent velocity fluctuations [135]. As some commercial as well as academic codes aim for stability and hence, are based on eddy-viscosity models, the use of the *SES* model is highly recommended since its implementation is straight-forward. For slightly better results the use of the *KKK2* model can be a viable alternative.

7.9 Acknowledgements

The authors gratefully acknowledge the financial support through the state of North Rhine-Westphalia and the supply of computational resources through the Center for Computational Sciences and Simulation (CCSS) of the University of Duisburg-Essen. Support by the German Research Foundation (Deutsche Forschungsgemeinschaft - DFG, GS: FOR-2687) is also gratefully acknowledged.

This chapter was previously published in Computers and Fluids [60] and is reprinted with permission of the journal.

8 Towards the suitability of information entropy as an LES quality indicator

Authors: L. Engelmann, M. Ihme, I. Wlokas, A. Kempf

This chapter including all figures and tables was previously published in *Flow, Turbulence and Combustion, L. Engelmann, M. Ihme, I. Wlokas, A. Kempf, Towards the suitability of information entropy as an LES quality indicator, 2021; 108: 353-385* and is reprinted with permission from Springer. L. Engelmann developed the software for the presented simulations and the post-processing, performed all calculations, wrote the manuscript and generated all figures and tables. M. Ihme, I. Wlokas and A. Kempf contributed corrections, discussions and proofreading. The findings of section 8.4.2 were acquired during the Bachelor's project of L. Engelmann and laid the foundation for the further works presented in this chapter.

Abstract

The Shannon entropy is a rigorous measure that can be applied to evaluate the complexity in dynamical systems. Shannon entropy allows for direct calculation from any set of experimental or numerical data and yields the uncertainty of a given dataset. Originating from information theory, the concept can be generalized from assessing the uncertainty in a *message* to any dynamical system. Following the concept of ergodicity, turbulence forms another class of dynamical systems, which is generally assessed using statistical measures. The quantification of resolution quality is a crucial aspect in the assessment of simulation of turbulent flows. While a vast variety of statistical measures for the evaluation of resolution is available, measures closer representing the dynamics of a turbulent systems, such as Wasserstein metric or Ljapunov exponent become popular.

This study investigates, how the Shannon entropy can lead to useful insights in the quality of simulation of turbulent flows. The Shannon entropy is calculated based on distributions, which enables direct evaluation from unsteady flow simulations or by post-processing. A turbulent channel flow and a plane turbulent jet are used as validation tests. The Shannon entropy is calculated for turbulent velocity- and scalar-fields and correlations with physical quantities such as turbulent kinetic energy and passive scalars are investigated. It is shown

This chapter was previously published in Flow, Turbulence and Combustion [61] and is reprinted with permission of the journal.

that the spatial structure of the Shannon entropy can be related to flow-phenomena. This is illustrated by the investigation of the entropy of the velocity fluctuations, passive scalars and turbulent kinetic energy. Grid studies reveal the Shannon entropy as a converging measure. It is demonstrated, that classical turbulent-kinetic-energy-based quality-measures struggle with the identification of insufficient resolution, while the Shannon entropy might form a solid basis for LES quality assessment.

8.1 Introduction

Turbulence theory has evolved, and many statistical measures are now available for describing turbulence through statistical analysis-tools. Much of our knowledge on turbulence results from Direct Numerical Simulation (DNS) experiments, where the largest available computers generate detailed databases at increasing turbulent Reynolds numbers. Considering these vast data-bases, one may ask about the properties of information in these simulation results, how these properties can be quantified, and what these properties can teach us about turbulence itself. In this context, the concept of *information entropy* is considered, which has been introduced by Shannon [257] for a discrete random variable. The present paper examines, how this concept can be applied to turbulent flows to obtain insight into simulation accuracy.

At this point, Large-Eddy Simulation (LES) can be considered as the state-of-the-art technique for simulations of turbulent flows in engineering systems. However, the assessment of simulation accuracy and quality of LES is in its infancy when it comes to quantifying uncertainty and estimating a simulation's accuracy or quality – in particular from the simulation itself. Several quality estimators have been proposed, often based on energy-related criteria. Given that it is very hard to find a truly sufficient and general quality estimator for LES, it is worth exploring other options that may contribute to a more reliable error estimator. In this context, test concept of information entropy is tested and it is investigated what can be learnt from it about LES-quality.

A large number of statistical quantities can be considered to describe a turbulent flow – including spectral information, spatial correlations, length-scales, structure functions and others – which often require joint measurements or sampling at two different points in space. An overview of commonly used statistical quantities is given in Pope [216] or Wilcox [302]. Several of these quantities are evaluated in the context of resolution quality by Davidson [50].

Easier to use and to consider are one-point statistics, for which the velocity probability density function (PDF) provides the complete picture of the turbulence, but only its first two moments are usually used to quantify turbulence. In LES, the related filtered density function (FDF) provides the distribution of the velocities within a filter volume. The first moments of the PDF are the mean velocities and the Reynolds stresses $\overline{u_\mathrm{i}' u_\mathrm{j}'}$ in Reynolds-Averaged Navier-Stokes (RANS) simulations, the second moment of the FDF (in LES) are the subgrid

This chapter was previously published in Flow, Turbulence and Combustion [61] and is reprinted with permission of the journal.

stresses $\overline{u_\mathrm{i} u_\mathrm{j}} - \overline{u_\mathrm{i}}\ \overline{u_\mathrm{j}}$ in LES. The Reynolds and subgrid stresses emerge as unclosed terms from either averaging or filtering the Navier-Stokes equations and need to be modelled. These stresses can be contracted into a (subgrid) turbulent kinetic energy $\frac{1}{2}\overline{u_\mathrm{i}' u_\mathrm{i}'}$. Higher moments can be derived and may appear in some modeling approaches, but we aim for a different description of the PDF.

To quantify the probability of occurrence of the joint occurrence of two quantities, two-point correlations and auto-correlations can be calculated and integral length scales can be derived. Two-point correlations have been also used as an approximate measure for the resolution of an LES [50].

A Fourier-transformation can also be used to describe a quantity in spectral space. Thus, a function of length is transformed into a function of wavenumber, leading to energy spectra, which are a common tool to assess how energy is distributed over the turbulent scales. To obtain an impression of the quality of a simulation, results are sometimes compared to Kolmogorov's $-5/3$-rule of the inertial subrange [50].

The need for quantitative methods to assess the quality of LES has lead to numerous studies [33, 131, 81]. With implicit (LES) filtering, the physical model for the subgrid scales, the choice of numerical algorithm, grid resolution and filter size determine the quality of an LES [188].

A well-known quality-criterion is attributed to Pope, which uses the ratio of resolved turbulent kinetic energy k_res and the sum of both resolved and modeled turbulent kinetic energy $k_\mathrm{res} + k_\mathrm{sgs}$ as an indicator for LES quality [217]. It is suggested, that the ratio γ should achieve values of at least 80% for the LES to be considered as sufficiently resolved:

$$\gamma = \frac{k_\mathrm{res}}{k_\mathrm{res} + k_\mathrm{sgs}} > 0.8 \tag{8.1}$$

The criterion will indicate high resolution quality if k_sgs is small - even falsely when a low value of k_sgs is caused by a small model constant or a dissipative numerical scheme. [190, 50].

The subgrid-activity parameter s proposed by Geurts and Fröhlich aims to quantify the total amount of modeling and thus the possible modeling error of an LES [81]. The parameter is calculated from the turbulent dissipation rate $\langle \epsilon_t \rangle$ and the molecular dissipation rate $\langle \epsilon_\mu \rangle$:

$$s = \frac{\langle \epsilon_t \rangle}{\langle \epsilon_t \rangle + \langle \epsilon_\mu \rangle} \tag{8.2}$$

A subgrid-activity parameter of $s = 0$ would describe a DNS while a parameter of $s = 1$ represents an LES with infinite Reynolds number [81].

The Index "$\mathrm{LES_{IQ}}$" tries to assess the quality of LES with implicit filtering [33]. The $\mathrm{LES_{IQ}}$ has a similar structure to Pope's approach in utilizing a ratio of the resolved and total turbulent kinetic energy $\mathrm{LES_{IQ}} = k_\mathrm{res}/k_\mathrm{tot}$, but the subgrid scales are treated with

This chapter was previously published in Flow, Turbulence and Combustion [61] and is reprinted with permission of the journal.

Richardson-extrapolation. The total turbulent kinetic energy $k_{\mathrm{tot}} = k_{\mathrm{res}} + \alpha_{\mathrm{k}} h^p$ relies on the grid-size h and the order of the numerical scheme p. The coefficient α_{k} is obtained from the extrapolation, which requires simulations with the grid of interest and a further refined grid [31, 234].

An approach that characterizes the error contributions of numerics and modeling separately was developed by Klein [131, 73]. The strategy is to vary model parameters to control the contribution of the model manually, which yields a different numerical and model error contribution. Both errors are quantified by a Taylor-series expansion of the numerical and modelling error terms. This requires solutions of the investigated LES, an LES with modified model contribution and a coarsened-grid LES [132]. The method holds for a range of applications, but needs to be further evaluated for high Reynolds-number flows and different numerical schemes [131, 73].

Turbulence captured by LES exhibits unsteady behavior and sensitivity to the initial solution, which attracts attention to the treatment of LES as a dynamical system, and hence, putting the general aspect of *information* stored in the flow field into spotlight rather than classical physical quantities. The fact that LES aims to capture turbulent dynamics, might give reason to favor a dynamical measure rather than conventional measures which rather assess the resolved temporal and spatial scales directly. Many quality-measures in common use share the property of comparing a physical-value produced by the LES to an experimental or estimated "true" value, but dynamic measures tend to quantify the frequency of occurrence of a certain solution or the degree of freedom of the solution-state [239, 56, 305].

One example for a dynamical-based measure is the *Lyapunov-exponent*, which assesses the separation of the solution of an LES when the initial solution is perturbated. While the perturbated and unperturbated solution separate until non-linear saturation in a chaotic system, the exponent quantifies the average separation of the solutions. Hence, the Lyapunov-exponent solely remains on the turbulent dynamics in an LES calculation [305, 188].

Another example is the *Wasserstein metric*. The Wasserstein metric is based on the "distance" of two variables of different states in the dynamical system. In the case of random fluctuations the states may be scattered closeby and hence, the distance might fall short. A single state is not meaningful for this set of data and should be replaced by a distribution instead. The Wasserstein metric can be seen as a measure for "dissimilarity" between two different states data [113, 305].

Entropy measures form a popular choice in the study of dynamical systems. The concept of Shannon's entropy was brought into the study of dynamical systems by Andrei Kolmogorov [145]. Although there are plenty of forms of *entropy* in the context of dynamical systems, they are all related together as they assess the *complexity* of a given set. This can be divided into the study of the properties *unpredictability*, *incompressibility*, *asymmetry* and *delayed recurrence* [99, 307].

This chapter was previously published in Flow, Turbulence and Combustion [61] and is reprinted with permission of the journal.

8.2 Shannon Entropy

From classical statistical thermodynamic arguments, the measure for the number of microscopic configurations describing a thermodynamic system comes to mind. Thermodynamical entropy has been used to assess dissipation and heat fluxes of an incompressible turbulent shear flow [144]. The entropy production was used to investigate numerical stability [189, 181, 55]. The question arises, if another form of entropy might lead to further insight into turbulence.

Information entropy was first introduced by Shannon in 1948 to express the term "information" mathematically [257]. In communication theory, any exchange of messages requires a source and a destination. The source contains a defined set of messages of the cardinality N, where each message from $i = 1$ to N has a probability p_i of being sent. Each message has its own value of information I_i, where the gain of information I means removal of uncertainty and less likely messages carry higher values of information.

The value of information of the message i depends on its probability p_i. The distribution of messages i in the set A of a physical quantity X is treated as the alphabet of all *messages* i. The set A can be the result of e.g. a series of measurements. In general, A can be described as a set of tuples of the form $A = \left\{(x_\mathrm{i}, p_\mathrm{i}) | x_\mathrm{i} \in (x_1, ..., x_\mathrm{N}), p_\mathrm{i} \in [0,1] \wedge \sum_{i=1}^{N} p_\mathrm{i} = 1\right\}$, with x_i being the values of X, which occur during the measurement.

Based on these formalities, the value of *information* can be formulated as $I_i = -\log_2 p(x_\mathrm{i})$ with $p_\mathrm{i} = p(x_\mathrm{i})$. By definition, the binary logarithm is chosen to obtain the unit *bit*.

The statistical average of the value of information I_i for $i = 1, ..., N$ leads to the Shannon entropy H. It holds the name entropy because of its formal analogy to the formulation of the entropy in statistical thermodynamics pioneered by Ludwig Boltzmann. Although arbitrary quantities in fluid dynamics are traditionally denoted as ϕ, the symbol X is chosen in this work to stay consistent with literature on information-theory. The Shannon entropy of a quantity X, given in a set A, is defined as

$$H(X) = -\sum_{i=1}^{N} p_\mathrm{i} \log_2 (p_\mathrm{i}) \tag{8.3}$$

Shannon entropy is a rigorous measure of uncertainty. Its calculation is solely based on the probability distribution of the observed quantity X. The Shannon entropy is set to zero for probabilities $p_\mathrm{i} = 0$, to enforce that messages i, which are never sent, lead to no gain of information. As opposed to the standard deviation, the absolute values of x_i do not have any influence on the Shannon entropy.

The information entropy differs from other statistical measures in being a rigorous measure. For the calculation of the entropy only the probability is statistically relevant, while the event itself does not matter. Therefore, the investigated property does not have to be of numerical

This chapter was previously published in Flow, Turbulence and Combustion [61] and is reprinted with permission of the journal.

nature. Information entropy is dependant of the shape of a distribution and invariant to permutation - as demonstrated in Fig. 8.1. Statements about multimodal probability distributions can be derived easily from information entropy, while other statistical measures commonly require high-order statistics. The information entropy can be applied in unsteady and transient flows. It is in dependant of specific models (such as eddy-viscosity models providing a turbulent viscosity) and geometry. The choice of sampling space is free, which also allows application of the information entropy in local parts of the flow. An important aspect of a quality-measure for LES is the additional (computational) effort to be invested into a study, as measures which require additional calculations may be less attractive based on the computational costs. Opposite to some other measures, the presented form of the information entropy is easy to calculate, can be evaluated on-the-fly using a probability mass function based on the present set of samples at negligible computational costs and could be obtained for experimental data even for quantitative comparisons.

To illustrate the link between the Shannon entropy and a physical quantity such as a velocity field, the evolution of a flow field in a mixing layer and its entropy is used as a tangible example. Figure 8.2 shows the development of the flow field for the mixing of three uniform velocity profiles of different magnitude. With increasing distance x from the nozzle, the mixing layer evolves and the velocity-gradients decrease due to shear. The evolution of the flow field shows the formation of a continuous spectrum of velocity values with proceeding state of mixing from originally three discrete velocities. This leads to the occurrence of more velocity values. Defining the feature *velocity value* as the baseline statistical event for the Shannon entropy, the probability of a velocity value to occur in a certain state of mixing can be assessed and the Shannon entropy can be calculated for each velocity profile. The profiles reveal, that a more continuous range of velocities appear with advanced state of mixing, which can be seen as a set of more distributed events, leading to an overall increase of Shannon entropy. In addition, it can be seen that changing the magnitude of the velocities, does not affect the outcome of the entropy, as it is a rigorous measure.

8.3 Numerical techniques and modeling

8.3.1 Demonstration case: Lorenz-attractor

The Lorenz-attractor [170] is a system of non-linear ODEs and arises from the simplified Navier-Stokes equations for a problem of thermal convection between two plates and exhibits chaotic solutions and therefore is interesting for studying uncertainty

This chapter was previously published in Flow, Turbulence and Combustion [61] and is reprinted with permission of the journal.

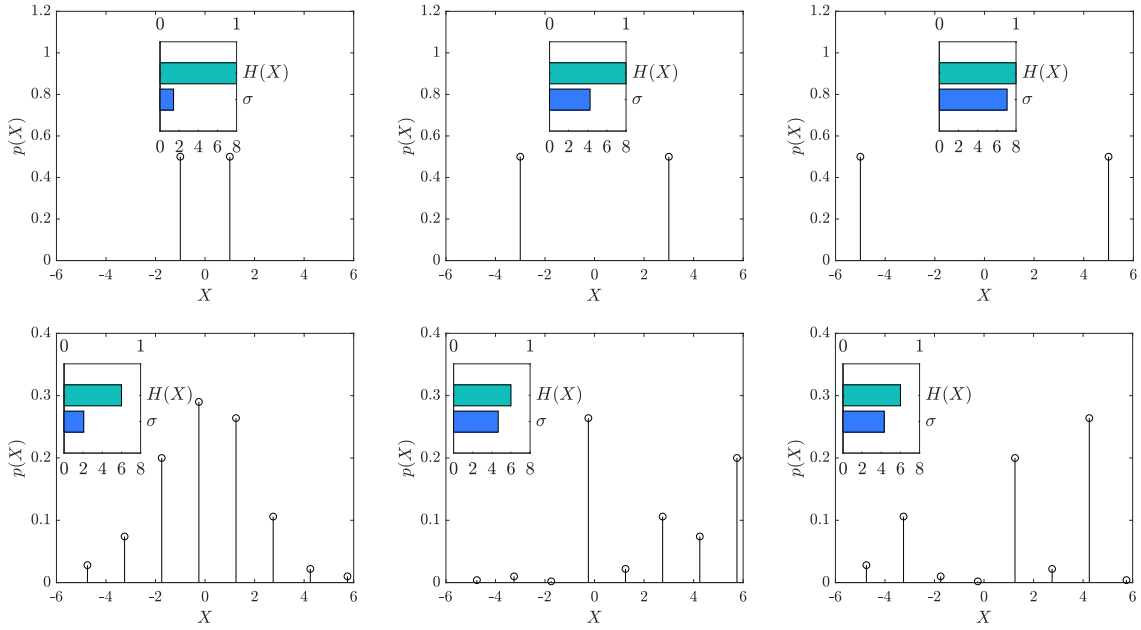

Figure 8.1 Information entropy H and standard deviation σ for a PMF consisting of (top) two Dirac peaks at locations $\{-1, 1\}$, $\{-3, 3\}$ and $\{-5, 5\}$. (bottom) PMF consisting of a Gaussian normal distribution with 8 elements and reassigning their probabilities to other elements randomly. The information entropy reveals information about the structure of the distribution, while standard deviation changes with the mathematical values of the statistic events.

This chapter was previously published in Flow, Turbulence and Combustion [61] and is reprinted with permission of the journal.

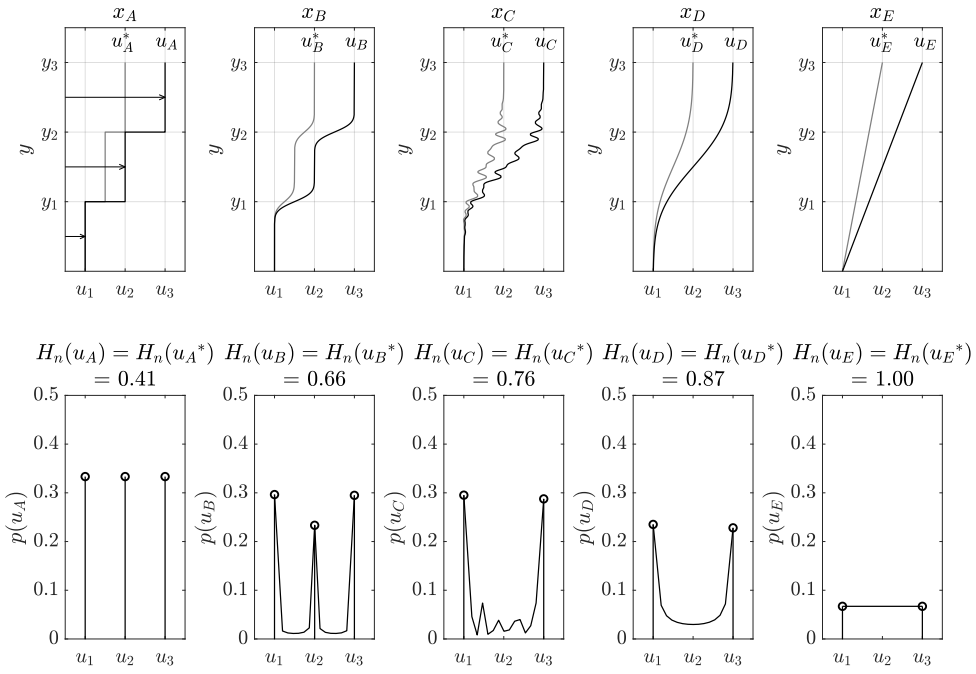

Figure 8.2 Top: Axial velocity profile of a hypothetical shear layer with various downstream locations $x_A < x_B < x_C < x_D < x_E$. Bottom: Probability distributions (PMF) at these locations derived from the velocity profiles. Note the increase of information entropy H with proceeding state of mixing and the Independence of H from the initial velocity value u and u^*.

$$\begin{aligned} \dot{X} &= \alpha(Y - X) \\ \dot{Y} &= X(\beta - Z) \\ \dot{Z} &= XY - \gamma Z \end{aligned} \tag{8.4}$$

The classic set of parameters is $\alpha = 10$, $\beta = 28$ and $\gamma = 8/3$, which result from the non-dimensionalization of the NSE, where α is the Prandtl-number and β is the Rayleigh-number. The temporal derivatives $\dot{X}$, $\dot{Y}$ and $\dot{Z}$ correspond to the velocity components u, v and w. Since the Lorenz-attractor is a simple chaotic system, it is a well suited demonstration case for the calculation- and evaluation-procedure for the information entropy.

The Lorenz-system is solved using a Runge-Kutta method of fourth-order accuracy. A timespan of 300 seconds is chosen to generate the trajectory. The velocities tangential to the trajectory are calculated at every point along the curve and their empirical probabilities $p(\dot{X})$, $p(\dot{Y})$ and $p(\dot{Z})$ are computed. A probability distribution is generated for each velocity-component u, v and w for which the Shannon entropy shall be evaluated. Based on studies of Camesasca, Archambault and Perugini [30, 11, 201], the entropy is normalized with the

This chapter was previously published in Flow, Turbulence and Combustion [61] and is reprinted with permission of the journal.

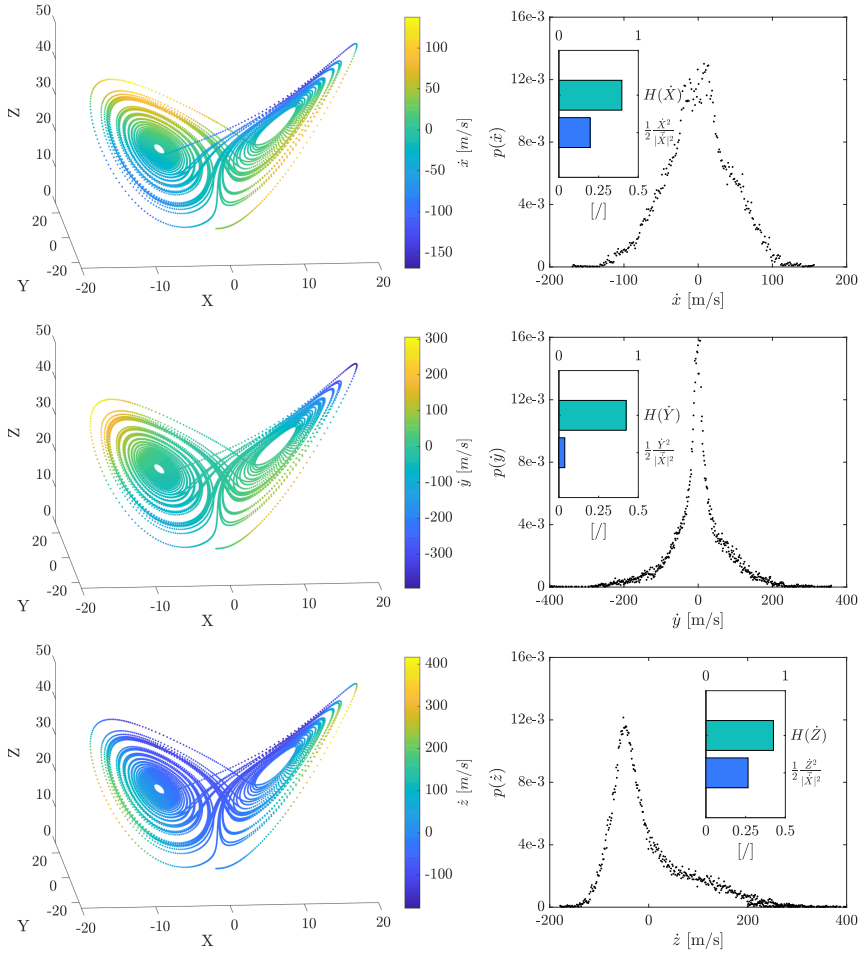

Figure 8.3 Components x, y and z of the solutions of the Lorenz-Attractor with time and their probability distributions. In the right column the entropy of the velocity components $H_\mathrm{n}(\dot{X}_\mathrm{i})$ and the kinetic energy of these components normalized by the squared absolute velocity $\frac{1}{2}\frac{\dot{X}_\mathrm{i}^{\,2}}{|\vec{\dot{X}}|^2}$ can be seen.

binary logarithm of the number of bins . Thus, the influence of the chosen amount of bins can be neglected. Being a scalar quantity, information entropy is calculated for each velocity component u, v and w separately.

The Lorenz-attractor is used as a well-defined reference case for entropy studies in turbulent flows. Figure 8.3 shows the velocity components along the trajectory with their respective probability distributions to give an introducing impression of what probability distributions are used for the calculation of the information entropy and how typical fields of the given case look like. The value of each velocity component along the trajectory is given by the color at the respective point, and the distribution of the respective velocity component is shown on the right-hand side. The bar-plot visualizes the Shannon entropy calculated

This chapter was previously published in Flow, Turbulence and Combustion [61] and is reprinted with permission of the journal.

from the probability distributions and the contribution to the kinetic energy of each velocity component.

The probability distributions of the $\dot{X}$ and $\dot{Y}$ components are symmetric. The distribution of $\dot{Z}$ is skewed, which results from the fast downward motion on the trajectory in the center of the attractor and the slow upward motion on the periphery of the discs. The main propagating direction along the attractor is the Z direction, which leads to the high contribution of $\dot{Z}$ to the total kinetic energy, while the contribution of $\dot{Y}$ to the kinetic energy is low. The attractor features only small motions in Y direction as the attractor can be seen as two merged discs, which hardly expand in Y direction. The X direction shows a medium contribution to the kinetic energy. Velocities are larger on the outer rings of the attractor and slower on the inner rings. The change of velocity on the outer turning points at the ends in X direction show the same change of velocity while the direction is changed. Therefore, the distribution appears to be very symmetrical.

The Shannon entropy is calculated based on the shown distributions for each velocity component, leading to $H_\mathrm{n}(\dot{X})$, $H_\mathrm{n}(\dot{Y})$ and $H_\mathrm{n}(\dot{Z})$. The Shannon entropy of $\dot{X}$ appears to be the lowest, as its probability distribution is relatively narrow compared to the other variables. This leads to a smaller range of statistical events, which indicates lower Shannon entropy. Entropy values $H_\mathrm{n}(\dot{Y})$ and $H_\mathrm{n}(\dot{Z})$ are higher than $H_\mathrm{n}(\dot{X})$, as the probability distributions cover a wider range of statistical events.

The Lorenz-Attractor has been an object of interest for further studies of dynamical measures such as the Lyapunov exponent or the Wasserstein metric, due to its dynamics being representative to these observed in LES and DNS. The Lyapunov exponent is a dynamical measure, which can be used to characterize the dynamical processes in a turbulent system and can lead to statements about the predictability time of a turbulent system. A further analysis can be found in [188, 305].

8.3.2 LES and DNS of a channel flow and Plane jet

The DNS and LES rely on the in-house code *PsiPhi* developed and used at the University of Duisburg-Essen and at Imperial College London. The code is based on a finite-volume technique on equidistant, isotropic Cartesian grids, relying on fourth-order central differencing for transport of momentum, total variation-diminishing (TVD-CHARM) schemes for passive and reactive scalars, pressure correction through a projection method, and a nominally third-order low-storage Runge-Kutta scheme [173] for time-integration at a CFL number of 0.7. Parallelization is achieved through domain decomposition and MPI. The code has been used in many LES studies [267, 205, 231], some of them highly resolved, achieving DNS-resolution away from the burner, [221, 222] and DNS of pulverised coal flame ignition [232]. Turbulent initialisation and inlet data are obtained by an efficient implementation [120] of Klein's well-known inflow data generator [133]. For the LES, Nicoud's Sigma model

This chapter was previously published in Flow, Turbulence and Combustion [61] and is reprinted with permission of the journal.

[192] and the classic Smagorinsky model [259] were tested - the latter for making the finding's more easy to interpret and transferable to other simulations [230].

The channel flow simulations of $Re_\tau = 395$ and $Re_\tau = 934$ have been performed with the grids listed in table 8.1 and 8.2. The DNS of Moser et al. [185] and Hoyas and Jimenez [106] use non-uniform grid spacing in wallnormal direction. In this LES, cubic cells are used, leading to better resolution in streamwise and spanwise direction and hence, providing more samples for the generation of the probability distributions. Periodic boundary conditions are used in streamwise and spanwise direction, while an immersed boundary approach allows for the representation of walls in normalwise direction [202].

A plane turbulent jet at $Re = 10,000$ based on the DNS by Klein [133] serves as a further testing case. The computational domain extends $20D \times 20D \times 6.4D$ in streamwise, normalwise and spanwise dimension, with D being the nozzle width. Periodical boundary conditions are applied in spanwise dimension and the boundaries in normalwise dimension are treated with velocity data of the DNS by Klein. A filter by Anderson and Domaradzki is applied near the outlet boundary in streamwise direction to ensure unperturbated outflow [8]. For further description of the case design, the authors refer to a previous study [59].

Table 8.1 Channel flow grid parameters for $Re_\tau = 395$. The coordinates x, y and z correspond to the streamwise, wallnormal and spanwise directions. N_α refers to the total number of cells.

wall units Δy^+	grid size Δy [mm]	streamwise N_x	spanwise N_y	wallnormal N_z	total N_α [$\times 10^6$]
52.8	8.0	48	24	16	0.016
39.6	6.0	64	32	21	0.043
26.4	4.0	96	48	32	0.131
13.2	2.0	192	96	64	1.049
6.6	1.0	384	192	128	8.392
3.3	0.5	768	384	256	67.136

Table 8.2 Channel flow grid parameters for $Re_\tau = 934$. The coordinates x, y and z correspond to the streamwise, wallnormal and spanwise directions. N_α refers to the total number of cells.

wall units Δy^+	grid size Δy [mm]	streamwise N_x	spanwise N_y	wallnormal N_z	total N_α [$\times 10^6$]
93.4	6.0	64	32	21	0.043
62.3	4.0	96	48	32	0.131
31.1	2.0	192	96	64	1.049
15.6	1.0	384	192	128	8.392
7.8	0.5	768	384	256	67.136
3.9	0.25	1536	768	512	134.272

This chapter was previously published in Flow, Turbulence and Combustion [61] and is reprinted with permission of the journal.

Table 8.3 Jet flow grid parameters. The coordinates x, y and z correspond to the streamwise, wallnormal and spanwise directions. N_α refers to the total number of cells.

cells/nozzle N_D	grid size Δy [mm]	streamwise N_x	spanwise N_y	wallnormal N_z	total N_α [$\times 10^6$]
5	2.0	100	32	100	0.32
10	1.0	200	64	200	2.56
20	0.5	400	128	400	20.48

8.3.3 Calculation of the Information entropy

The Shannon entropy is based on a discrete probability distribution, which requires a probability mass function (PMF - probability distribution with finite bins). To calculate a probability distribution, a field of any physical quantity is sufficient. The PMF is generated on a single plane using histograms of the desired quantity, which decomposes the continuous range of real values into a number of N discrete bins. The binning requires a width to separate the continuous range of physical values into discrete intervals. However, choosing any bin width appears to be arbitrary and violates the idea of finding an independent measure. Hence, the information entropy is normalized with the binary logarithm of the number of bins N [30, 201], so that the possible entropy values range between 0 and 1 using

$$H_n(X) = -\sum_{i=1}^{N} p_\mathrm{i} \cdot \log_2(p_\mathrm{i}) / \log_2(N) \tag{8.5}$$

Another aspect is the choice of mathematical borders, between which the binning is performed. While physical quantities can range between $(-\infty, +\infty)$, a given field of a physical quantity will be limited by the highest and lowest value X_{max} and X_{min} occurring in the field. Applying histograms for values in the intervals $(-\infty, X_{min})$ and $(X_{max}, +\infty)$ will lead to empty bins and hence, probabilities of zero, which - by definition - do not contribute to the value of entropy. Therefore, bins will only be applied within $[X_{min}, X_{max}]$. Although different fields will feature different values of X_{min} and X_{max}, the entropy of a set of fields X remains comparable as values outside of this interval cannot influence the entropy since the values inside of this interval are converged with the number of bins. An algorithm is used to calculate the normalized entropy for gradually refined bin widths. The converged value of the entropy is then chosen to represent the distribution. A short summary of the necessary steps can be found in table 8.4.

This chapter was previously published in Flow, Turbulence and Combustion [61] and is reprinted with permission of the journal.

Table 8.4 Instruction for calculation of the normalized Shannon entropy $H_n(X)$ for a quantity of interest X.

1. Perform the simulation of a chosen resolution up to temporally fully converged state
2. Choose a quantity X for calculation of the entropy $H_n(X)$
3. Choose a physically meaningful field of X
4. Apply histograms within the range $[X_{min}, X_{max}]$ with n_b bins on the chosen field and divide by the total number of values in the field to obtain PMF
5. Calculate information entropy $H_\mathrm{n}(X)$ for the PMF using Eq. 8.5
6. Increase n_b and repeat steps 4 to 6 until $\Delta H_n(X)$ vanishes
7. Sample $H_n(X)$ over multiple timesteps

8.4 Results

8.4.1 A-priori study of the JHU channel flow at $Re_\tau = 1,000$

The skill of models and indicators in LES is typically measured by their performance in a-posteriori calculations. However, to investigate the convergence of information-entropy-based measures with respect to the resolution, a-priori studies are a suitable method. Hence, the DNS of the turbulent channel flow at $Re_\tau = 1,000$ by Graham et al. [90] is used as a basis for the a-priori investigation. The data is openly accessible and provided by the John-Hopkins University (JHU) Turbulence Database. It has to be noted, that a-priori cases might give limited insight into the true nature of a model in a-posteriori applications, a prominent example affected by this being scale-similarity-type subgrid models for LES [140].

The friction Reynolds number for the database is $Re_\tau = 1,000$ and the velocity-based Reynolds number is approximately $Re = 40,000$. The domain consists of approximately $1.6 \cdot 10^9$ cells with a non-uniform grid spacing of $\Delta_x \approx 13$ and $\Delta_z = 7$ viscous wall units, while Δ_y follows a hyperbolic tangent profile. Hence, filtering was applied following the classical channel flow literature, e.g. Clark et al. [42] and Piomelli et al. [209] applying a Gaussian filter kernel in streamwise and spanwise directions.

The DNS data is compared with a-priori evaluations using filter-widths of $\overline{\Delta} = 1, 2, 5$ and $10\Delta_z$.

Figure 8.4 shows an instantaneous slice parallel to the wall in the channel center of the original calculation (top-left) and the a-priori filtered fields (indicated by the annotated filter-width $\overline{\Delta}$). The images reveal an increased blurring-effect with progressive increasing of the filter-width. The removal of velocity fluctuations can also be observed with the decrease of the total magnitude of the fluctuations in the field as shown in the colorbars and in the probability distributions. Further, the probabilities of the fluctuation values close to zero decrease, which is assumed to be a consequence of the filtering. In this context, it has to be noted that the application of a filter on a strong velocity fluctuation in a velocity field

This chapter was previously published in Flow, Turbulence and Combustion [61] and is reprinted with permission of the journal.

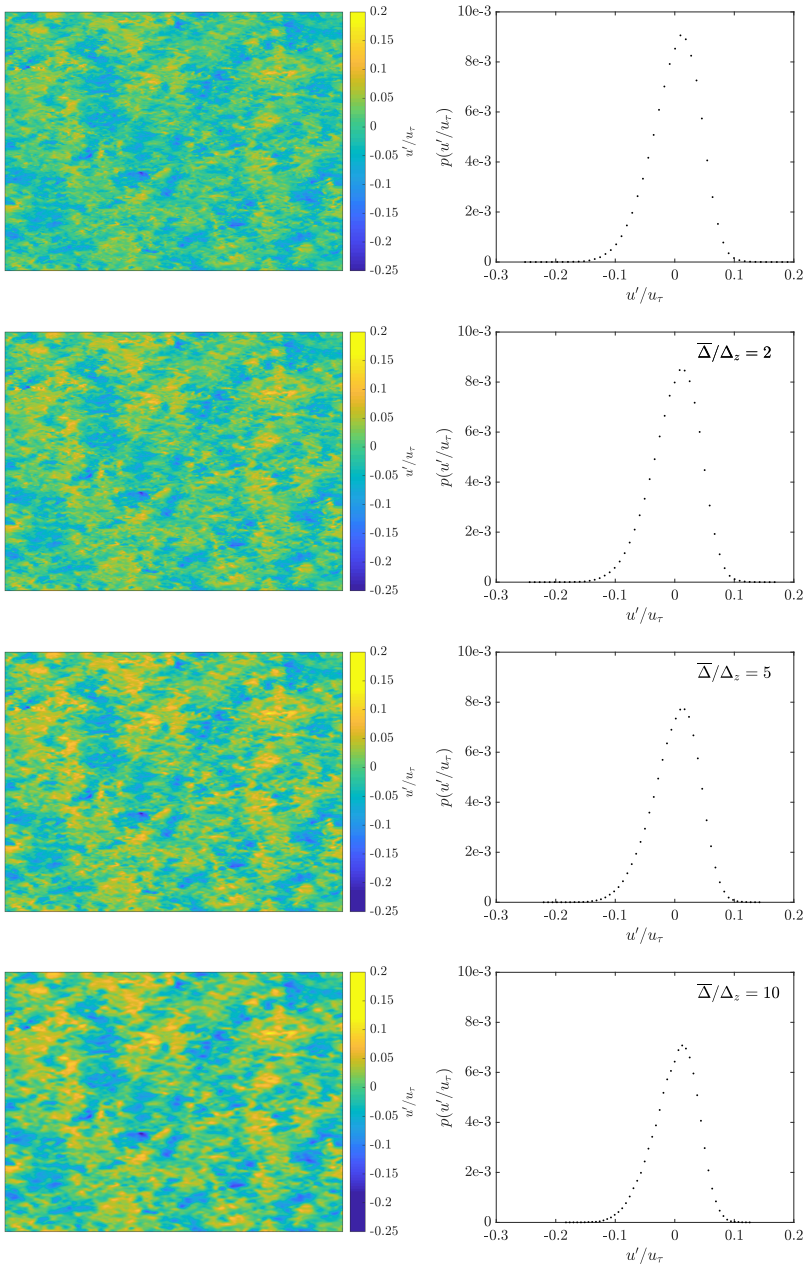

Figure 8.4 Instantaneous streamwise velocity fluctuation u' normalized with the friction velocity u_τ and the probability distributions based on the shown field of instantaneous streamwise velocity fluctuations at the channel center for the JHU turbulent channel flow at $Re_\tau = 1,000$ unfiltered and with filter-widths $\overline{\Delta} = 2, 5$ and $10\Delta_z$.

This chapter was previously published in Flow, Turbulence and Combustion [61] and is reprinted with permission of the journal.

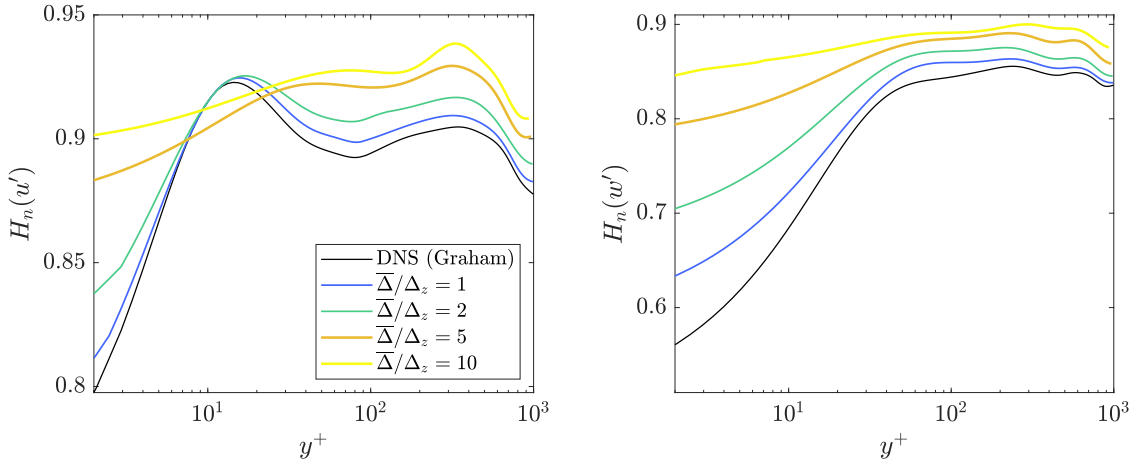

Figure 8.5 Profiles of a-priori calculated entropies $H_\mathrm{n}(u'')$ and $H_\mathrm{n}(w'')$ with the wall distance y^+ in viscous units. The y^+ axis is cropped to allow for good visualization of the channel center and near-wall region.

can be compared to the filtering of a pulsed top-hat type signal with a low on/off-time ratio. Sampling a top-hat type signal is a representative case for generating a bi-modal distribution, as the signal is characterized by the alternating low and high values only. Applying a filter on the top-hat-signal leads to smoothing of the flanks, which is achieved by decreasing and increasing the values at the flanks respectively, thus increasing the total amount of values characterizing the signal and therefore introducing more modes into the signal-distribution. The generation of more modes in a distribution leads to a decrease of the probabilities of the already present modes and hence will increase the entropy. This effect is enforced with increasing the filter-width, however will be counteracted by the progressive decrease of the signal amplitudes, which eventually will reduce the entropy due to the removal of modes from the distribution. Therefore, filters are able to both increase and decrease the entropy of a signal, depending if either the generation of mode outweighs their removal or vice versa.

Results of the a-priori analysis can be found in Fig. 8.5. The entropies of the wall-parallel velocity-component fluctuations $H_\mathrm{n}(u')$ and $H_\mathrm{n}(w')$ were chosen as an generic example. The y^+ axis was cropped to allow for a better visualization of the near-wall and centerline regions and comparison with the following a-posteriori calculations, while still showing the overall entropy-behavior approaching the wall further. Both profiles reveal progressive deviation from the unfiltered DNS data with increasing filtering width. The entropy of the streamwise velocity fluctuations reveal a local maximum at $y^+ \approx 10$, which is approximately where the production term of the turbulent kinetic energy reaches its maximum [28, 185]. This region is governed by eddies with high turnover-velocities compared to the rest of the flow, which by tendency lead to greater velocity-fluctuation magnitudes and therefore extend

This chapter was previously published in Flow, Turbulence and Combustion [61] and is reprinted with permission of the journal.

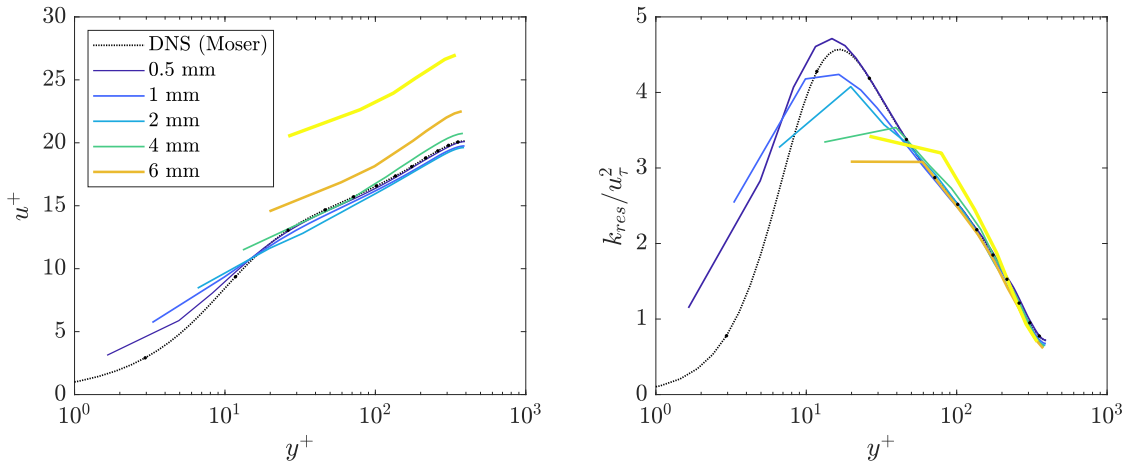

Figure 8.6 Profiles of viscous normalized streamwise velocity u^+ and the resolved turbulent kinetic energy k_{res} with the wall distance y^+ in viscous units at $Re_\tau = 395$. The underresolution (coarse grids) is intended to obtain simulations of different quality.

the interval of possible fluctuation values (- the absolute values in this interval span from zero to the highest value of velocity fluctuation) [171]. The mean flow occurs in streamwise direction and statistically no mean flow in spanwise direction occurs. This implicates that only little differences in the spanwise momentum occur compared to the streamwise direction, leading to absolute spanwise velocity fluctuations being smaller than absolute streamwise velocity fluctuations. Hence, the turbulent kinetic energy is mostly driven by the streamwise velocity fluctuations, which is in accordance with the findings of Moser et al. or Rieth et al. [185, 230]. Therefore, the peak is more pronounced for the entropy of the streamwise velocity fluctuations. The entropy begins to decrease close to the wall due to the vanishing of the turbulent kinetic energy. The entropy shows an overall increasing trend with the increasing filtering width. This is assumed to be a consequence of the overall introduction of modes by the filter, as discussed before.

8.4.2 A-posteriori LES of the channel flow at $Re_\tau = 395$

An LES is performed for six consecutively coarsened grids using Nicoud's Sigma model [192], the resulting mean velocity and turbulent kinetic energy profiles are shown in Fig. 8.6. The results of the original DNS of Moser et al. [185] are added for reference and validation of the simulation.

A good agreement with the DNS data can be achieved on the 0.5 mm, 1 mm and 2 mm grids, while grids with 4 mm size and coarser show progressively increasing deviations from the reference data. Still, these grids were chosen intentionally to assess if the Shannon entropy can indicate major differences in the quality of the results.

This chapter was previously published in Flow, Turbulence and Combustion [61] and is reprinted with permission of the journal.

On the left-hand side of Fig. 8.7, the instantaneous streamwise velocity fluctuation u' can be seen on a wall-parallel slice at the channel half-height δ. The right-hand side shows the probability distributions of u' obtained by applying the binning algorithm from table 8.4 on the respective slices. The small line-plot features the value of the Shannon entropy for the shown distributions. The flow fields feature stronger blurring with increased gridspacing. The corresponding probability distributions feature stronger skew and extend further towards negative velocity fluctuations on the fine grid. This extend may be assumed to be a consequence of the field being located in the channel center. The turbulent mean velocity profile predicts the maximum velocity at this location, which - following Prandtl's mixing-length hypothesis - leads to momentum exchange with regions closer to the wall due to turbulent transport statistically favoring momentum deficits in the center of the channel. The growth of the left flat part of the distribution in direction of negative values is assumed to be a consequence of the increased grid resolution, allowing for more and smaller turbulent structures in the flow field. The distributions appear more symmetric on the coarser grids.

The Shannon entropy of the resolved fluctuating velocity components u', v' and w' is calculated and the information entropy values of the streamwise component $H(u')$, the wallnormal component $H(v')$ and the spanwise component $H(w')$ are obtained. Sufficient resolution of the near-wall stresses is crucial to achieve a good agreement for channel flow LES and DNS. The information entropy is calculated in dependence of the wall distance utilizing wall parallel slices of the domain, to assess if statements about resolution quality can be derived from this quantitiy.

The results are shown in Fig. 8.8 for six resolution levels. Particularly coarse grids are used to examine if the entropy is able to show poor resolution through characteristic features. The graphs of $H_\mathrm{n}(v')$ and $H_\mathrm{n}(w')$ feature a similar shape, since the entropy first rises with the wall distance and peaks after around 100 non-dimensional wall units. The profile of $H_\mathrm{n}(u')$ features a maximum at 10 viscous wall units for the fine resolved simulations, the entropy values decrease approaching the centerline further. The shape of the curve becomes less distinct the coarser the grid becomes. $H_\mathrm{n}(v')$ and $H_\mathrm{n}(w')$ show a similar behavior for larger y^+, but stronger sensitivity in the near-wall region. This similarity may be assumed to be a consequence of the similar behavior of statistics in these periodical directions. The resolution quality of the near-wall region is vital for the quality of the simulation, which might make the information entropy suitable for assessing simulation quality.

In boundary-layer theory it is postulated that the flow is laminar close to the wall [248]. Hence, the velocity profile is not affected by the turbulent fluctuations, which transform a single value velocity into a distribution. In the fully evolved case, the flow can be seen as orderly. For wall distances within the laminar sublayer, there is no uncertainty of which velocity value is found as only one velocity value can be found. Thus $H_\mathrm{n}(u') = 0$ for a

This chapter was previously published in Flow, Turbulence and Combustion [61] and is reprinted with permission of the journal.

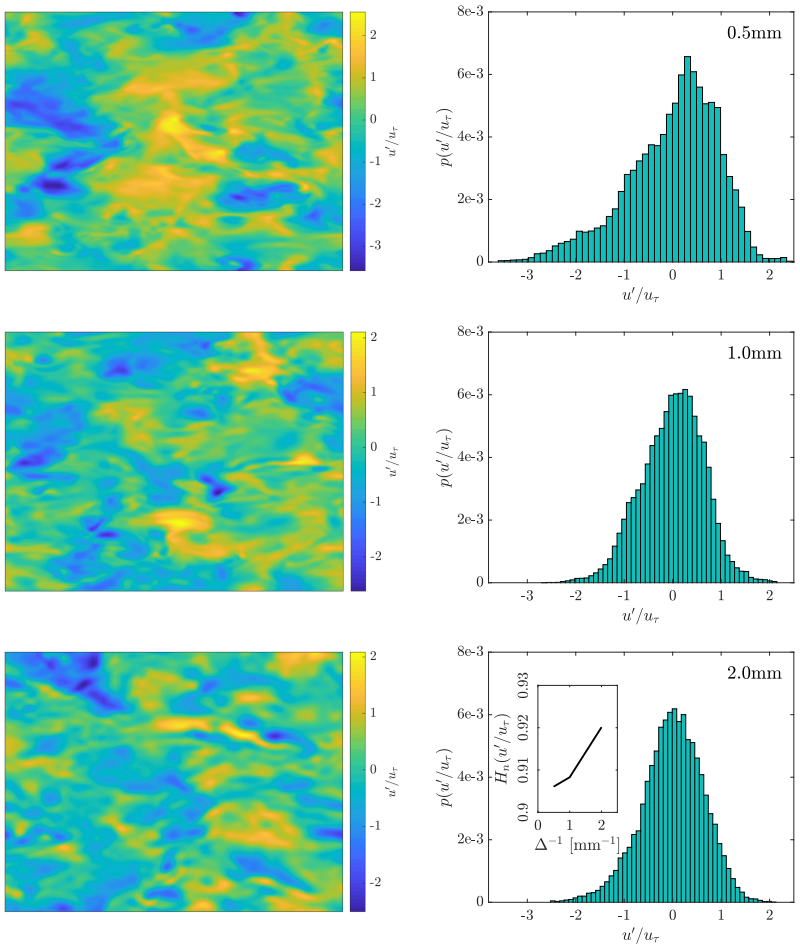

Figure 8.7 Instantaneous streamwise velocity fluctuation u' normalized with the friction velocity u_τ and the probability distributions based on the shown field of instantaneous streamwise velocity fluctuations at the channel half-height layer (x-y plane) for the grid widths $0.5, 1$ and 2mm at $Re_\tau = 395$. The additional set of axis shows the entropy $H_\mathrm{n}(u')$ of the three given fields arranged by grid size.

This chapter was previously published in Flow, Turbulence and Combustion [61] and is reprinted with permission of the journal.

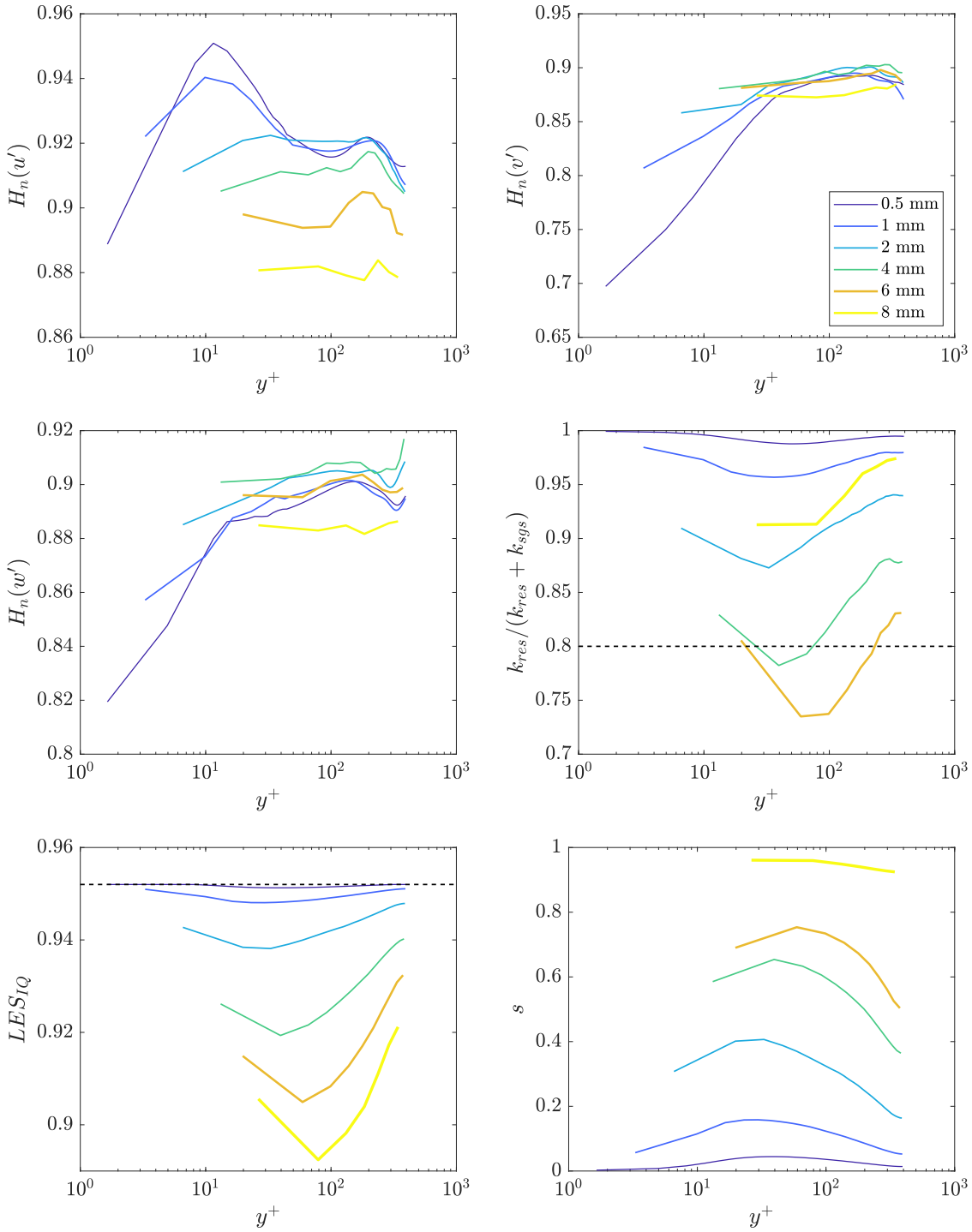

Figure 8.8 Entropy results $H_\mathrm{n}(u')$, $H_\mathrm{n}(v')$, $H_\mathrm{n}(w')$, the ratio of resolved and total kinetic energy $\gamma = k_\mathrm{res}/(k_\mathrm{res}+k_\mathrm{sgs})$ based on Eq. 8.1, the $\mathrm{LES_{IQ}}$ by Celik et al. [33] and the subgrid-activity parameter s suggested by Geurts and Fröhlich [81] with the wall distance y^+ in viscous units at $Re_\tau = 395$.

This chapter was previously published in Flow, Turbulence and Combustion [61] and is reprinted with permission of the journal.

plane parallel to the wall with a fixed wall distance in the laminar sublayer. Increasing the wall distance and leaving the laminar sublayer, small turbulent structures arise, starting to superimpose the velocity profile [216]. The mean velocity is then superimposed by weak fluctuations induced by eddies of small size. For sufficient resolution of the near wall region, the fluctuations lead to a greater number of velocity values besides the mean value and widen the distribution. This leads to a rising uncertainty and therefore an increase of the Shannon entropy $H_n(u') > 0$.

The graph on the middle-right side of Fig. 8.8 shows an evaluation of the turbulent kinetic energy ratio, where the subgrid turbulent kinetic energy was calculated following ideas of Yoshizawa, Lilly and Vreman [310, 164, 292] based on the turbulent viscosity obtained from the Sigma model. The ratio γ is shown versus y^+ to investigate the relation between resolution and wall distance. Following the - commonly used but often misleading - recommendation of $\gamma > 0.8$ for sufficient LES quality, all grids would lead to satisfactory results except from the 4 mm grid at a wall distance of around 100 wall units. Furthermore, it may be concluded, that sampling of γ in wallnormal direction would have lead to an overall ratio $\gamma > 0.8$ for all simulations, which would imply sufficient resolution of even the coarse grids, which has been proven wrong during the evaluation of Fig. 8.6. Even though the ratio indicates the right trend of resolution and result quality for the fine 0.5, 1 and 2 mm grids, the criterion fails to warn against actual poor resolution - a key property for a useful quality indicator.

The $\mathrm{LES_{IQ}}$ is shown in the down left graph. A value of greater than 0.8 is suggested for an LES to be considered properly resolved, while a value of 0.952 resembles a fully resolved DNS. The finely resolved simulation of 0.5 mm grid size achieve the highest values, almost reaching a constant value of 0.952, which would imply DNS-like resolution. This finding however cannot be fully confirmed by the velocity and turbulent kinetic energy profile. Since the very poorly resolved grids show lower values above 0.8, it might be concluded that the $\mathrm{LES_{IQ}}$ struggles with strong underresolution. However, compared to the energy ratio, the $\mathrm{LES_{IQ}}$ shows some form of convergence for the poorly resolved grids. The down right graph shows the subgrid-activity parameter s. The parameter s shows stronger sensitivity towards the subgrid model contribution for the fine grids. The overall behavior of the two indicators appears very similar with respect to the curvature of the graphs, with the subgrid-activity parameter being stretched over a larger range of values. Hence it may be considered, that similar insights can be obtained from both measures.

To further investigate the connection between the Shannon entropy and the turbulent kinetic energy, the entropy of the absolute velocity $H_\mathrm{n}(|\vec{u'}|)$ is plotted over the resolved turbulent kinetic energy k_res in Fig. 8.9. Both quantities are obtained from the wall-parallel cross-sections for each distance from the wall, up to the channel half height. The behavior of both quantities is linked as the entropy grows with increasing turbulent kinetic energy. The resolved turbulent kinetic energy $k_\mathrm{res} = \frac{1}{2}\overline{u'_\mathrm{i} u'_\mathrm{i}}$ is dominated by the streamwise velocity

This chapter was previously published in Flow, Turbulence and Combustion [61] and is reprinted with permission of the journal.

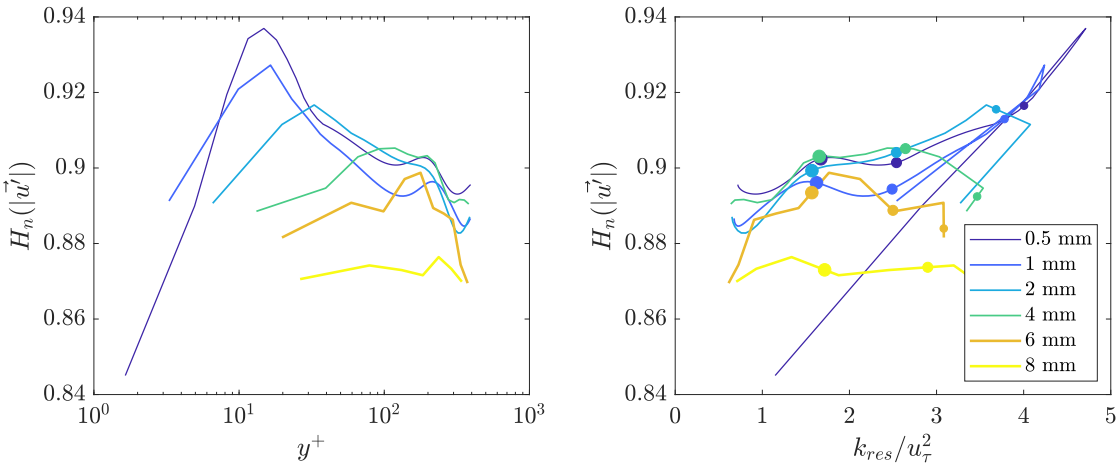

Figure 8.9 Profile of the entropy of the absolute velocity fluctuations $H_\mathrm{n}(|\vec{u'}|)$ with the wall distance y^+ (left) and dependency between the entropy of the absolute of velocity fluctuations $H_\mathrm{n}(|\vec{u'}|)$ and the resolved turbulent kinetic energy k_res (right) at $Re_\tau = 395$ - the marker size (from large to small) indicates the proximity to the wall in viscous wall units for a discrete chosen set of points with $y^+ = 30, 100, 200$.

fluctuations [230]. It has been discussed before, that uncertainty reaches its maximum for the strongest turbulent kinetic energy. Therefore, the entropy $H_\mathrm{n}(|\vec{u'}|)$ and the energy k_res share a similar contour while plotted versus the wall distance and must show some correlation.

While a correlation between the entropy $H_\mathrm{n}(|\vec{u'}|)$ and the turbulent kinetic energy k_res has been postulated, the location of both the maximum entropy and energy occur at around 10 viscous wall units on the fine grids. Both measures rely on the rms of the velocity fluctuations in streamwise, wallnormal and spanwise direction. As the turbulent kinetic energy in a channel flow is dominated by the streamwise velocity fluctuation, the location of the maximum of k_res is dictated by u' [50]. The maximum of $H_\mathrm{n}(|\vec{u'}|)$ however only depends on the range of different fluctuation values that can be observed at a given wall distance. $H_\mathrm{n}(|\vec{u'}|)$ will reach large values, if a wide set of different fluctuation values $|\vec{u'}|$ can be observed. Thus, the entropy increases, if u', v' and w' contribute from different magnitudes. Therefore, the information entropy $H_\mathrm{n}(|\vec{u'}|)$ reaches a minimum value in the isotropic case. The velocity fluctuations u', v' and w' tend to achieve values of similar magnitude closer to the center line and can be considered more isotropic than closer to the wall [216, 130]. This also shows agreement with the decrease of $H_\mathrm{n}(|\vec{u'}|)$ for wall distances $y^+ > 100$. At the wall, the velocity fluctuations approach zero due to the no-slip condition. Increasing the wall distance, the velocity fluctuations u', v' and w' start to grow with different rates and differ more. This also leads to a wider range of events which matches with the rising slope of $H_\mathrm{n}(|\vec{u'}|)$.

The link between the Shannon entropy and the turbulent kinetic energy is visualized in Fig. 8.9. The entropy of the magnitude of the vector of velocity fluctuations is plotted

This chapter was previously published in Flow, Turbulence and Combustion [61] and is reprinted with permission of the journal.

as a function of the turbulent kinetic energy - the wall distance acts as variable along the profile. Small distances to the wall are indicated with larger dots. The more fine grids reveal a proportional increase between the entropy and turbulent kinetic energy, as can be expected due to the similar behavior in the near wall region, leading to a straight line behaving similar to an angle bisector. The curve then proceeds towards lower energies with comparably higher entropies. Hence, the fine grids tend to reveal a higher value of entropy for similar values of turbulent kinetic energy.

8.4.3 A-posteriori LES of the channel flow at $Re_\tau = 934$

To substantiate the findings from the previous subsection 8.4.2, another set of simulations has been carried out at higher Reynolds number $Re_\tau = 934$ using the same setup. A refined grid of 0.25 mm width has been added to take into account for the decreased boundary layer thickness, achieving a resolution of 3.9 viscous wall units, while the coarsest grid of 8 mm is neglected in this case.

Figure 8.10 shows the viscous normalized velocity profile and the turbulent kinetic energy with the wall distance in viscous wall units featuring the reference data of Hoyas and Jimenez [106]. The grids of up to 2 mm width show good agreement with the DNS data, while the coarser grids lead to a stronger overprediction of the velocity profile. All grids manage to predict the resolved turbulent kinetic energy well, with the wall-nearest point on the coarser grids showing stronger deviations. Again, the results from (too) grids are kept to also show the effect of poor resolution.

In Fig. 8.11 visualizations of the flow field of the instantaneous streamwise velocity fluctuations u' along with the corresponding probability distribution in the channel center are shown for the three finest grids in the same manner as in Fig. 8.7. The flow fields appear more blurred for the coarser grids, however the overall effect is not as distinctive as for the lower Reynolds number. The obtained probability distribution shows a stronger skew towards negative fluctuations on the finely resolved 0.25 mm grid opposed to the coarser grid, where the distribution appears rather symmetrical.

Figure 8.12 shows the profiles of the information entropy of $H_\mathrm{n}(u')$, $H_\mathrm{n}(v')$ and $H_\mathrm{n}(w')$ as well as the ratio of the resolved and modeled turbulent kinetic energy $k_\mathrm{res}/(k_\mathrm{res} + k_\mathrm{sgs})$, the $\mathrm{LES_{IQ}}$ and the subgrid-activity parameter s. The entropy of the streamwise velocity fluctuations $H_\mathrm{n}(u')$ features a similar shape compared to the lower Reynolds number with one maximum at $y^+ \approx 10$ and a local maximum closer to the channel center. The entropies of the normalwise and spanwise velocity fluctuations $H_\mathrm{n}(v')$ and $H_\mathrm{n}(w')$ show an increase from lower to higher wall distances. Again the entropy of the normalwise fluctuation reveals a strong drop closer to the wall, which is a consequence of the conservation of mass prohibiting wallnormal velocity components close to the wall and hence reducing the normalwise velocity fluctuations.

This chapter was previously published in Flow, Turbulence and Combustion [61] and is reprinted with permission of the journal.

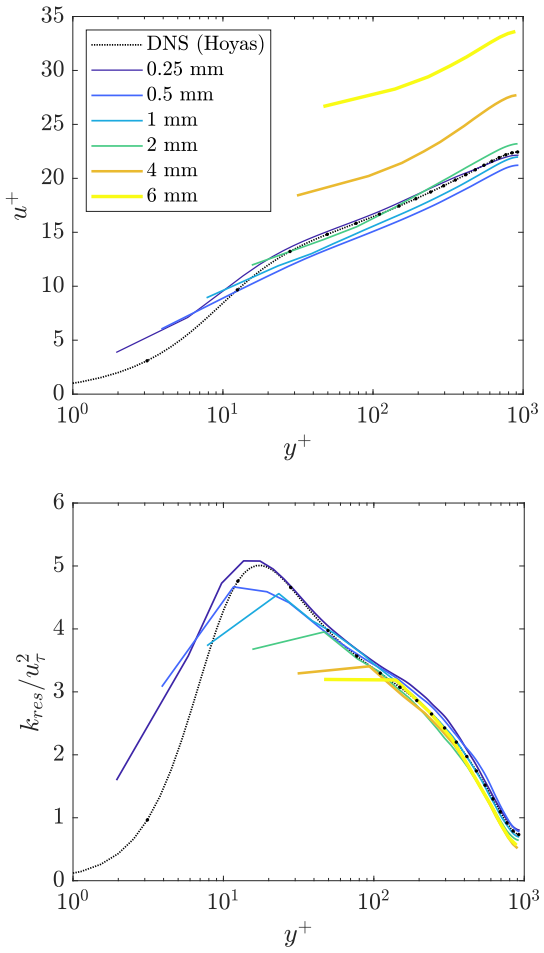

Figure 8.10 Profiles of viscous normalized streamwise velocity u^+ and the resolved turbulent kinetic energy k_{res} with the wall distance y^+ in viscous units at $Re_\tau = 934$. The underresolution (coarse grids) is intended to obtain simulations of different quality.

This chapter was previously published in Flow, Turbulence and Combustion [61] and is reprinted with permission of the journal.

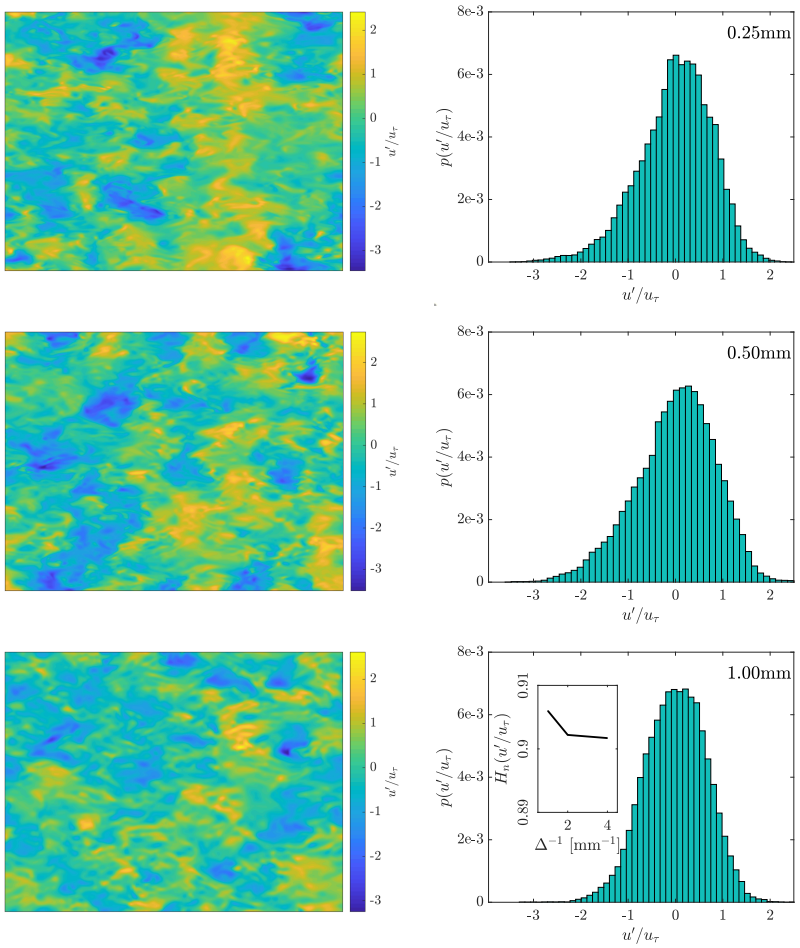

Figure 8.11 Instantaneous streamwise velocity fluctuation u' normalized with the friction velocity u_τ and the probability distributions based on the shown field of instantaneous streamwise velocity fluctuations at the channel half-height layer (x-y plane) for the grid widths $0.25, 0.5$ and 1mm at $Re_\tau = 934$. The additional set of axis shows the entropy $H_\mathrm{n}(u')$ of the three given fields arranged by grid size.

This chapter was previously published in Flow, Turbulence and Combustion [61] and is reprinted with permission of the journal.

The shape of the entropy curves become less distinct with reduced grid resolution, however especially the $H_n(u')$ and $H_n(v')$ profiles feature a clear trend of curve-development when increasing the grid resolution.

The ratio of the resolved and the modeled turbulent kinetic energy can be found in the center-right plot. The finely resolved grids reveal very low contributions of the modeled turbulent kinetic energy. The ratio of resolved turbulent kinetic energy decreases progressively with coarsening the grid. Following the recommendation of the resolved turbulent kinetic energy making up at least 0.8 of the total kinetic energy, the coarsest grids can only be considered well resolved near the centerline or close to the wall. As revealed by the velocity profile in Fig. 8.10, the resolution of both grids can be considered overall poor for all wall distances. The $\mathrm{LES_{IQ}}$ reveals a similar trend, with the finest grid achieving very high values close to 0.952 which can be considered *DNS*-resolution. Celik et al. [33] suggest a value of at least 0.8 for a LES to be well resolved and all calculations achieve values of at least 0.86 for all wall distances. The subgrid-activity parameter can be found in the bottom-right plot. It features a similar trend to the ratio of kinetic energy and $\mathrm{LES_{IQ}}$ with the finest grid revealing the lowest subgrid-activity. While the subgrid indicator is often used as a measure for assessing the contribution of the subgrid model, especially the criteria based on the turbulent kinetic energy ratio and the $\mathrm{LES_{IQ}}$ do not fully represent the findings from the velocity profile in Fig. 8.10 as the agreement with the DNS results does not necessarily improve with grid refinement.

To assess the link between the turbulent kinetic energy and the information entropy, the entropy of the norm of the fluctuation vector and the turbulent kinetic energy can be found in Fig. 8.13. The curve of the entropy $H_n(|\vec{u'}|)$ features a maximum at $y^+ \approx 10$ and an overall decrease for larger distances from the wall, similar to the findings for the lower Reynolds number. Plotting the entropy versus the turbulent kinetic energy again reveals a bisector-like behavior for the lower wall distances on the finer grids. After the peak values of energy and entropy, the proportional behavior changes and leads to a weaker increase of entropy with increasing kinetic energy as already observed in Fig. 8.13.

All entropy profiles shown in Figs. 8.8/8.12 & 8.9/8.13 reveal dependence on the grid size and - more importantly - show a trend with decreasing (e.g. poorer) resolution: While the single entropies of u', v' and w' served as an introduction example, it may be argued, that the entropy of the absolute fluctuation value $H_n(|\vec{u'}|)$ is a more suitable representative for generating statements about the simulation. Indeed the simulations, which can be considered sufficiently resolved for the channel-flow, feature similar behavior in the peak-region and show the predicted decrease of entropy for closer wall distances for $H_n(|\vec{u'}|)$. While measures based on the turbulent kinetic energy are often criticized for generating misleading statements about the simulation quality [50, 190] - as emphasized in Figs. 8.6/8.10 - an entropy-measure

This chapter was previously published in Flow, Turbulence and Combustion [61] and is reprinted with permission of the journal.

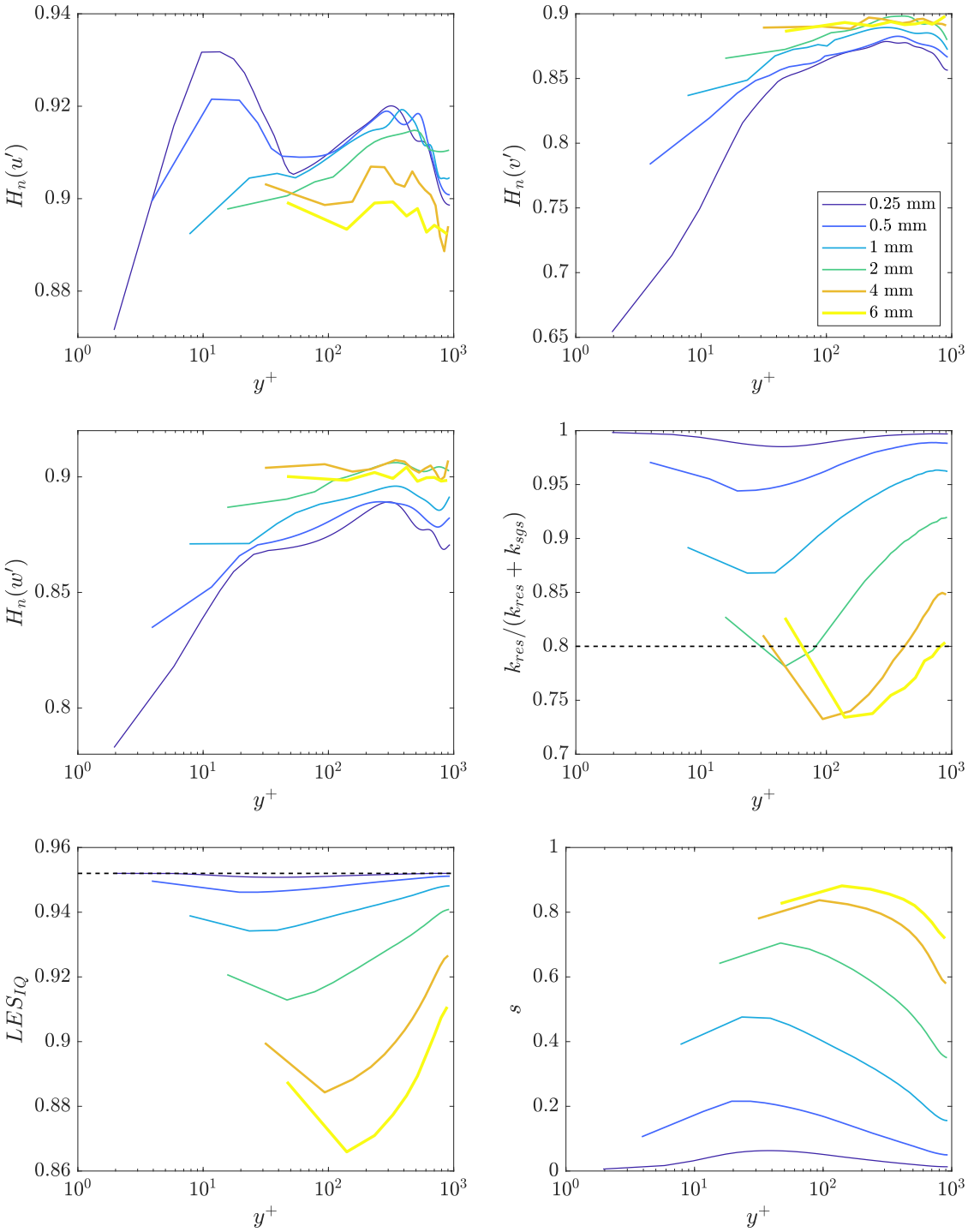

Figure 8.12 Entropy results $H_\mathrm{n}(u')$, $H_\mathrm{n}(v')$, $H_\mathrm{n}(w')$ and the ratio of resolved and total kinetic energy $\gamma = k_\mathrm{res}/(k_\mathrm{res} + k_\mathrm{sgs})$ based on Eq. 8.1, the $\mathrm{LES_{IQ}}$ by Celik et al. [33] and the subgrid-activity parameter s suggested by Geurts and Fröhlich [81] with the wall distance y^+ in viscous units at $Re_\tau = 934$.

This chapter was previously published in Flow, Turbulence and Combustion [61] and is reprinted with permission of the journal.

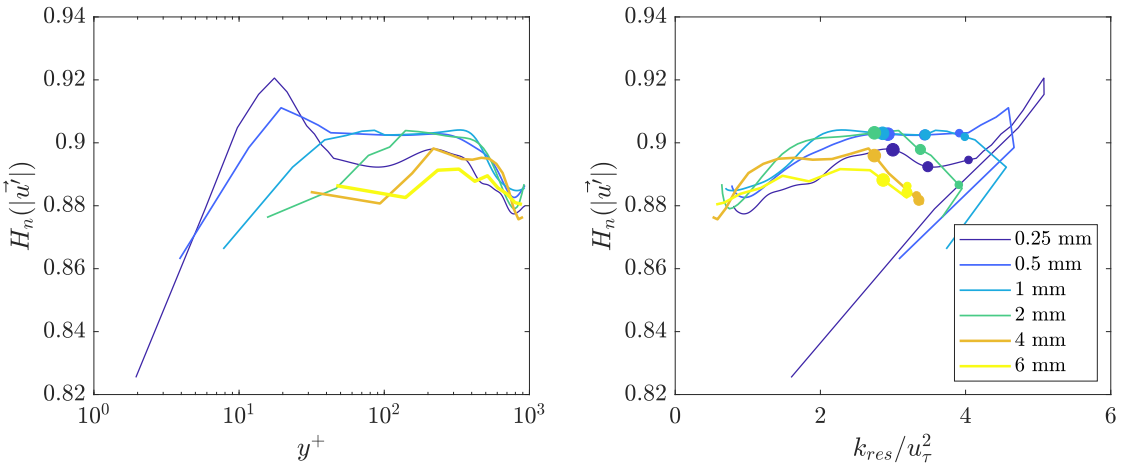

Figure 8.13 Profile of the entropy of the absolute velocity fluctuations $H_\mathrm{n}(|\vec{u'}|)$ with the wall distance y^+ (left) and dependency between the entropy of the absolute of velocity fluctuations $H_\mathrm{n}(|\vec{u'}|)$, the resolved turbulent kinetic energy k_res (right) at $Re_\tau = 934$ - the marker size (from large to small) indicates the proximity to the wall in viscous wall units for a discrete chosen set of points with $y^+ = 50, 100, 200$

based on the total fluctuation value may be considered, as it obtains its information about the flow physics rather from the statistical structure of the flow field than from absolute values.

8.4.4 A-posteriori LES of the plane turbulent jet

Figure 8.14 gives a visual impression of the jet for different mesh qualities and shows the distributions used for the calculation of entropy, instantaneous fields of the passive scalar ϕ and the corresponding probability distributions, along with the information entropy calculated from the distributions. The finest grid with 20 cells per nozzle height D reveals the finest structures in the flow field, which gradually disappear while coarsening the mesh to ten and five points - again, a coarse grid has been used intentionally for testing the behavior of information entropy. The LES resolution is chosen to allow for a sufficient scale separation between LES and DNS and at the same time, provide a sufficient resolution of the shear layer.

Figure 8.15 shows the streamwise velocity fluctuations $\sqrt{u'u'}$ and passive scalar fluctuations $\sqrt{\phi'\phi'}$ over the normalwise distance y/D from the centerline. Profiles of mean quantities $\langle u \rangle$ and $\langle \phi \rangle$ are commonly considered as easy to predict, so that the focus lies on the fluctuations that provide a more challenging test for the simulation. The agreement with the DNS data gets worse with coarser grids, characterized by high fluctuation values for larger distances from the centerline. While there is little difference between the 0.5 and 1 mm grids, deviations

This chapter was previously published in Flow, Turbulence and Combustion [61] and is reprinted with permission of the journal.

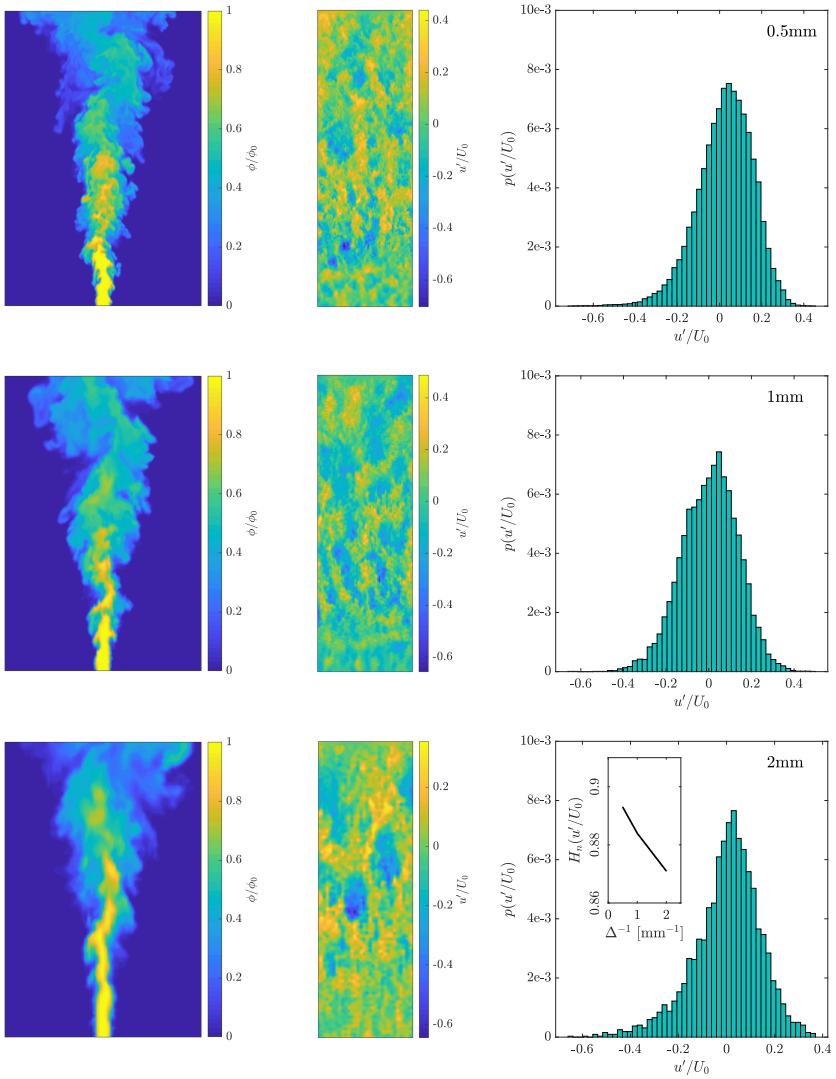

Figure 8.14 Instantaneous passive scalar field ϕ/ϕ_0 (x-y plane), streamwise velocity fluctuations u' normalized by the bulk velocity U_0 (x-z plane), the probability distributions of u' and information entropy for the turbulent plane jet at grids using 0.5 mm, 1 mm and 2 mm cells arranged by grid size.

This chapter was previously published in Flow, Turbulence and Combustion [61] and is reprinted with permission of the journal.

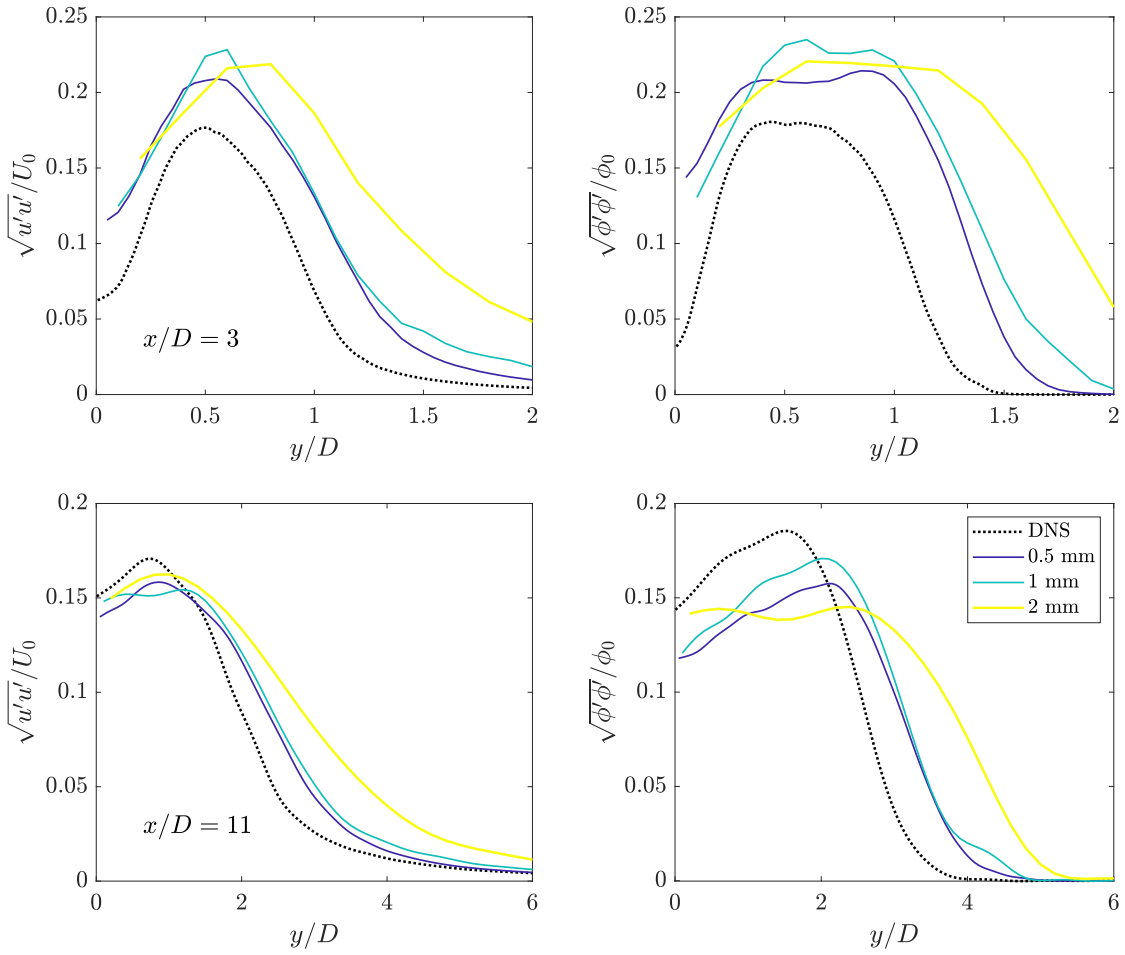

Figure 8.15 Profiles of streamwise velocity $\sqrt{u'u'}$ and passive scalar $\sqrt{\phi'\phi'}$ fluctuations with the normalwise distance y/D from the centerline.

from the DNS data are significantly stronger for the 2 mm grid. Given the fact that simulation results for the two finer grids show a similar match with DNS data and doubling the gridsize leads to a notable drop in quality, the 2 mm grid may be considered insufficiently resolved.

The information entropy has been evaluated for the streamwise velocity fluctuations u', the absolute value of the velocity fluctuation vector $|\vec{u'}|$ and the passive scalar fluctuations ϕ'. The results are shown in Fig. 8.16 and the turbulent-kinetic-energy-based criterion (Eq. 8.1) has been added. Due to access to the complete DNS database, results of the Shannon entropy for DNS resolution have been added.

The overall impression from the results reveals the entropy as an actual converging measure, since differences between DNS and LES results decrease with grid refinement. Strong differences for the velocity-fluctuation-based entropies $H_\mathrm{n}(u')$ and $H_\mathrm{n}(|\vec{u'}|)$ can be observed between the fine and coarse grids. The velocity-fluctuation-based entropies reveal high values near the centerline, representing the strong shear also found in the previous

This chapter was previously published in Flow, Turbulence and Combustion [61] and is reprinted with permission of the journal.

fluctuation profiles, which goes in hand with higher overall fluctuation values and hence, more possible velocity values, leading to a wider range of events and an increase in information entropy. With decreasing shear, the entropy also reduces, but increases again at larger distances y/D, which are governed by large-scale vortices that lead to an increase of entropy. The decrease of entropy near $y/D = 10$ is considered to be the result of the boundary conditions and hence, is not discussed any further. The entropy profile $H_{\mathrm{n}}(\phi')$ shows a decrease with increasing centerline-distance. This is assumed to be a result of vortices in the region of strong shear, transporting fluid of high ϕ values from the nozzle in normalwise direction. The continuous mixing with the ambient fluid leads to progressive increase of cells with values of $\phi = 0$, which again reduces the possible set of values for ϕ and hence, causes a decay of information entropy.

The profile of $k_{\mathrm{res}}/(k_{\mathrm{res}} + k_{\mathrm{sgs}})$ shows strong differences between all three mesh resolutions. While quantitative deviations between the 0.5 and 1 mm grid have been shown to be small in Fig. 8.15, the criterion states strong differences in resolution quality up to medium distances from the centerline. The gridsize of 2 mm achieves values of γ below the suggested limit of 0.8 for $y/D < 2$, but considers the simulation to be resolved sufficiently for larger distances from the centerline. Similar observations can be made for the subgrid-activity parameter s, which predicts overall lower subgrid contributions for a finer grid. A different trend can be observed for the $\mathrm{LES_{IQ}}$. The $\mathrm{LES_{IQ}}$ claims overall better resolution with coarser grids, which contradicts the findings from Fig. 8.15 - especially on the 2 mm grid. This indicator predicts more poor resolution for larger distances y/D, while the actual agreement between the LES and DNS data is improving according to Fig. 8.15.

8.5 Summary and conclusion

The utility of the Shannon entropy has been studied for different flow variables in different canonical flows in LES. Calculations over a wide range of grid resolutions have been performed to provide a set of differently resolved simulations, for which the Shannon entropy has been evaluated. The Shannon entropy is a simple measure, which can be calculated during a simulation or post-processed, without the need of performing further simulations with modified parameters or grid sizes. The Shannon entropy obtains its information about the flow physics rather from the statistical structure of the PMF and the underlying flow field than from its absolute values, which provides a different view-point.

General observations about the Shannon entropy are that a) it drops off approaching the wall and towards the center of a channel, with the finest simulations achieving the lowest information entropy values at the wall, and that b) in a free shear layer information entropy seems to drop with grid resolution, so that overall, achieving a low Shannon entropy may imply a good resolution. For the underlying PMF, this would require a multimodal probability distribution. This would imply that the probability distribution features characteristics such

This chapter was previously published in Flow, Turbulence and Combustion [61] and is reprinted with permission of the journal.

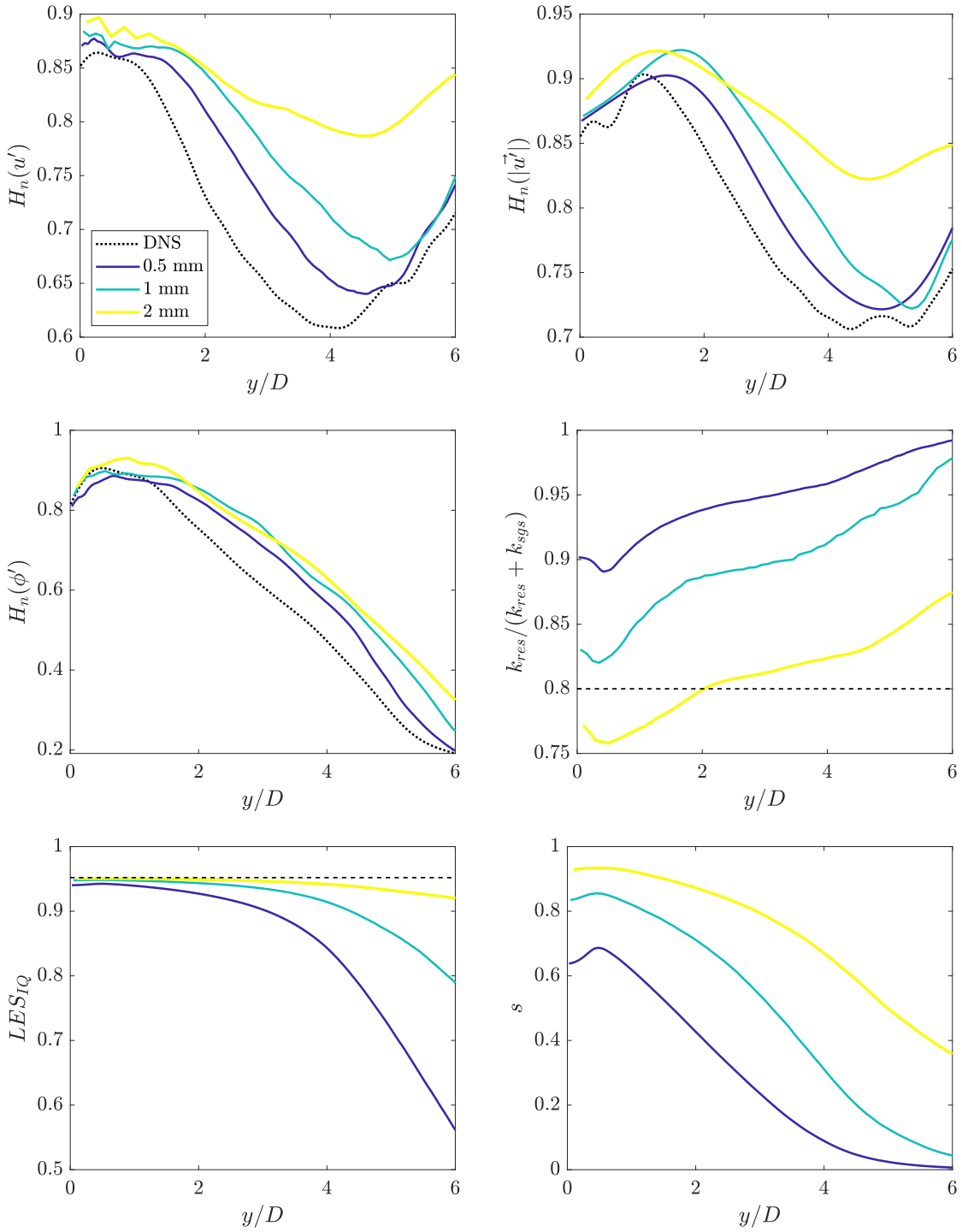

Figure 8.16 Entropy results $H_\mathrm{n}(u')$, $H_\mathrm{n}(|\vec{u}'|)$, $H_\mathrm{n}(\phi')$, the ratio of resolved and total kinetic energy $\gamma = k_\mathrm{res}/(k_\mathrm{res} + k_\mathrm{sgs})$ based on Eq. 8.1, the $\mathrm{LES_{IQ}}$ by Celik et al. [33] and the subgrid-activity parameter s as suggested by Geurts and Fröhlich [81] with the normalwise distance y/D from the centerline. H_n has been calculated on fields in homogeneous and streamwise direction for each y/D.

This chapter was previously published in Flow, Turbulence and Combustion [61] and is reprinted with permission of the journal.

as a characteristic state of mixing, a flow field being characterized by vortices of a certain length-scale or a state of thermal equilibrium.

Low values of information entropy are achieved for distributions which are governed by only few modes with high probabilities. Looking at a flow field, such a field would correspond to locally identical values which can be considered as "steps" in spatial profiles - this is with strongly localized gradients and curvature: relatively large zones of constant value must be separated by thin layers of steep gradients and strong curvature to achieve a low entropy. Requiring locally either very strong or low gradients, it may be argued that also the gradient field must be composed of only few modes. An extreme example of such a low-entropy field would be a very thin shear layer, right at a splitter plate, where only a very thin interface separates a fast fluid A from a slow fluid B. After some mixing, the homogeneous zones of values of just A or B will be separated by a thicker mixing layer - generating more states of mixture and hence, a higher entropy. - Thinking about LES-quality, such a field can only be maintained by very good numerical resolution - maintaining steps requires much better numerical resolution than just maintaining minima and maxima. In that sense, entropy could be seen as a more stringent quality criterion than resolved energy. In fact, low-entropy "steps" require that multiple neighbouring cells take almost the same value - for example, by sharing the same eddy. This implies that low entropy can only be achieved if eddies (of homogeneous states) are resolved by two or more points - a sensible requirement for an LES! One therefore might argue that information entropy could indicate whether a grid can actually resolve eddy structures - which may be more than other criteria can provide.

Two test cases for a-posteriori LES were chosen to cover two common canonical flows established for the assessment of new models, with the turbulent channel flow representing wall-bounded flows and the plane turbulent jet representing free shear flows. The cases were designed in such a way, that no effects of different boundary conditions or additional modeling such as wall-modeling may be observed. In the case of the channel flow, wall-modeling might be required for coarse grids. It might be argued that this error is introduced not by the lack of an additional wall-model, but by the lack of sufficient resolution in the near wall region. Therefore, in this study the resulting error is treated as a consequence of underresolution, which in fact was intended to achieve on the coarse grids to demonstrate its effect on the information entropy. Both cases feature Reynolds numbers which are considered to be lower than in typical technical applications. Nevertheless, the turbulent channel flows at the present Reynolds numbers form a popular choice in the context of LES modeling assessment [209, 140, 96], as they allow for good resolution of the near wall region at moderate computational costs using Cartesian grids and therefore allow for an affordable and broad spectrum of grid qualities. Plane turbulent jets are a canonical case featuring the prominent challenge of the choice of the right boundary treatment due to the presence of entrainment phenomena. While there are several cases available in literature [133, 265], possible differences in boundary treatment may introduce additional undesired errors [59]. To avoid these errors,

This chapter was previously published in Flow, Turbulence and Combustion [61] and is reprinted with permission of the journal.

a simple DNS case has been designed and all calculations have been performed using identical numerical settings. While the Reynolds number in this case is moderate in comparison with technical applications, the case is considered relevant for canonical LES studies and the computation on a Cartesian grid remains affordable.

Considering the potential of Shannon entropy as a future LES quality indicator, we note that Shannon entropy profiles reveal a converging trend with resolution increasing (towards the limit of DNS), whereas the ratio of resolved and total turbulent kinetic energy struggled with assessing the poor simulations, yet we do want to mention that other insights might be obtained from vorticity- or enstrophy-based criteria, which were not in the focus of this study. This may imply that besides being an interesting quantity for analyzing and interpreting turbulent flows, Shannon entropy could help to assess the quality of LES. We would however like to point out that much further research will be needed for establishing a reliable quality criterion. At the same time, all statements about quality of resolution derived from the Shannon entropy in this early state have to be assessed with care.

8.6 Acknowledgements

The authors gratefully acknowledge the financial support through the state of North Rhine-Westphalia and the supply of computational resources through the Center for Computational Sciences and Simulation (CCSS) of the University of Duisburg-Essen. Further computational resources for this project have been provided by the Gauss Centre for Supercomputing/Leibniz Supercomputing Centre under grant no. pn68nu. Support by the German Research Foundation (Deutsche Forschungsgemeinschaft - DFG, GS: FOR-2687) is also gratefully acknowledged.

8.7 Appendix: Simplified introduction to information entropy

The information entropy H can be seen as a measure quantifying the predictability of a discrete statistical experiment, which is also referred to as the *uncertainty* of the experiment. Statistical experiments with only one outcome may be considered fully predictable or experiments with no uncertainty of the outcome. A statistical experiment may be seen as least predictable or most uncertain if every outcome has the same probability.

For sake of simplicity, assume having a set of marbles only differing by color. A simple experiment can be conducted by filling a bag with five marbles. In case A (Fig. 8.17 left) the bag shall be filled with five marbles of the same color. While reaching for a marble from the bag, the outcome of the experiment is already known. As only blue marbles exist in the bag, the result *blue marble* is fully predictable and hence, may be seen as without uncertainty. Equation 8.5 can be used to assess the value of entropy for this experiment. The number of statistical events N equals 1, as there is only the event *blue marble* and the respective

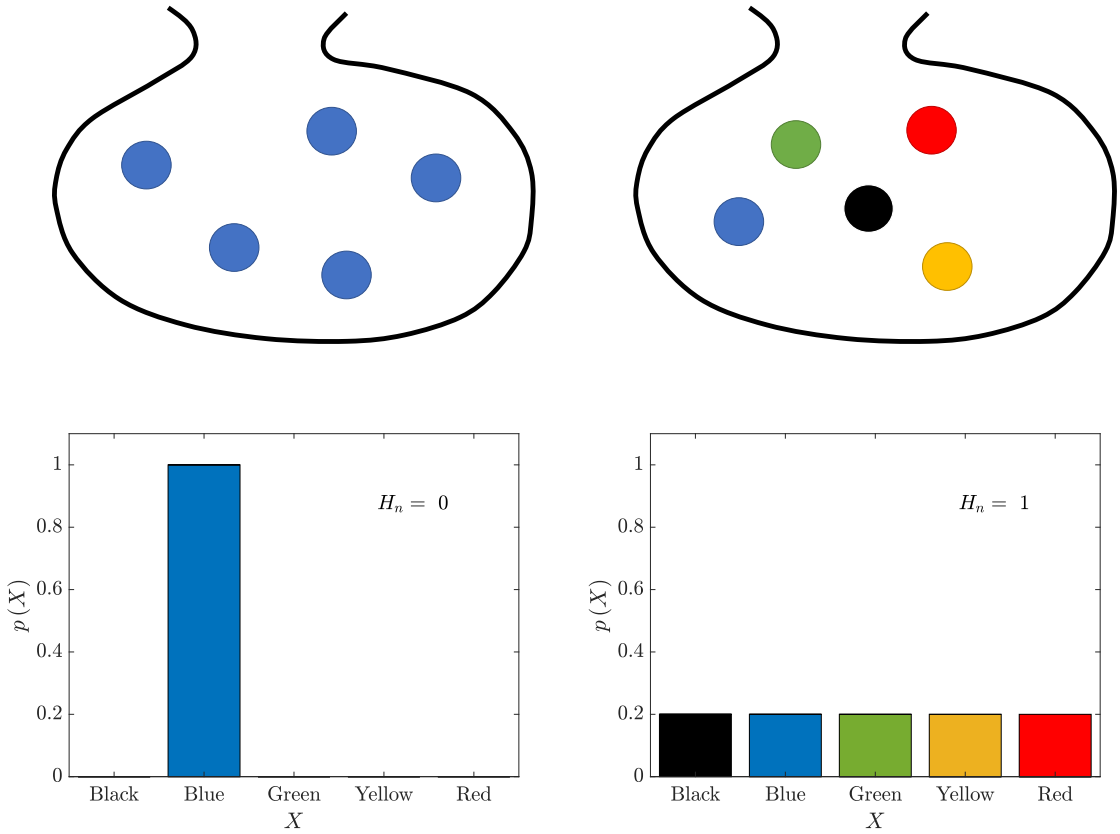

Figure 8.17 Discrete statistical experiment: Bag filled with five marbles. Case A: every marble has the same color - the outcome is fully predictable. Case B: every marble has a different color - the outcome is non-predictable.

probability is $p = 1$. Hence, $H_\mathrm{n} = -1 \cdot \log_{10}(1) / \log_{10}(1) = 0$. This result can be interpreted as zero uncertainty over the outcome of the experiment.

The opposite scenario can be achieved by filling the bag with five marbles of different color, which is referred to as case B (Fig. 8.18 right). The new setup leaves no tendency for a certain colored marble as all colors appear with the same probability. For this setup using five marbles, the predictability reaches a minimum and the uncertainty of the outcome reaches its maximum. Hence, the information entropy as a measure for this uncertainty reaches a maximum using Eq. 8.5, as $H_\mathrm{n} = 5 \cdot [-0.2 \cdot \log_{10}(0.2) / \log_{10}(5)] = 1$.

It can be observed from cases A and B, that the value of entropy increases with more equal distribution of the statistical events - which is represented by adding more marbles of different colors. A more equal distribution can be achieved by adding more statistical events to the experimental setup, as demonstrated in Fig. 8.18. To the original five blue marbles, a purple marble is be added, which reduces the predictability in the experiment. Drawing from the bag now leaves a small uncertainty of the outcome, since a purple marble

This chapter was previously published in Flow, Turbulence and Combustion [61] and is reprinted with permission of the journal.

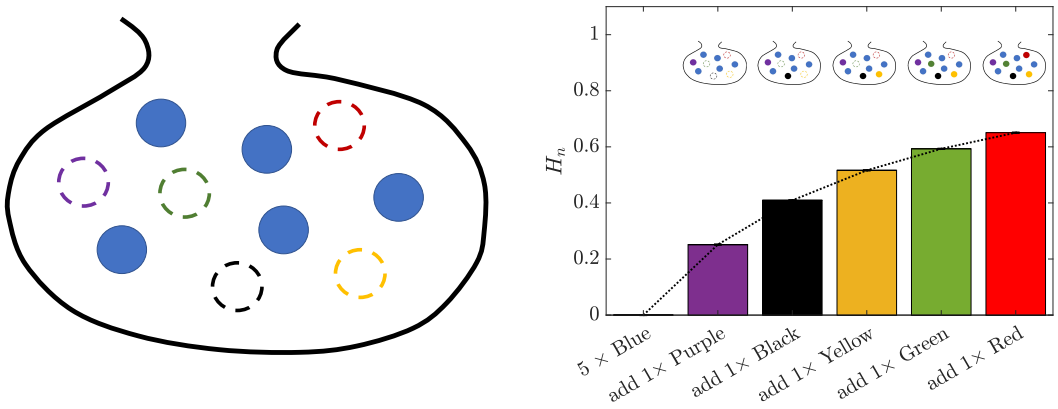

Figure 8.18 Discrete statistical experiment: Bag filled with five blue marbles. Case C: marbles of a new color are added incrementally to the bag and H_n is calculated at each step for the bag filled with the current set of marbles.

might be the result of drawing. This uncertainty is represented by an increase of information entropy. Adding another marble of a different color to the bag decreases the probability of drawing a blue marble further and hence, increases information entropy. The addition of more marbles of different colors continuously reduces the original significance of the blue marbles by reducing the difference between the probabilities of drawing a blue marble and drawing another marble.

The difference between the standard deviation and the information entropy in statistics might be guessed already by the nature of the example chosen to introduce the information entropy. The information entropy is also referred to as rigorous due to its ignorance towards the nature of the statistical event. In the context of information entropy it does not matter if the statistical event is the amount of prize money in a tombola, hitting a certain number at a dice roll or receiving a specific marble while drawing from a bag. The standard deviation is always bound to the mathematical value of a statistical event (a prize money, the number of eyes rolled with a dice, the age of a person picked for a social study) and scales with the orders of magnitude covered by all statistical events. Hence, it may be concluded that information entropy is only influenced by the spreading of the statistical events. The standard deviation depends on the spreading as well as on the mathematical value of the event.

This chapter was previously published in Flow, Turbulence and Combustion [61] and is reprinted with permission of the journal.

9 A temporal fluid-parcel backwards-tracing method for Direct-Numerical and Large-Eddy Simulation employing Lagrangian particles

Authors: L. Engelmann, C. Welch, M. Schmidt, D. Meller, P. Wollny, B. Boehm, A. Dreizler, A. Kempf

This chapter including all figures and tables was previously published in *Applied Energy: L. Engelmann, C. Welch, M. Schmidt, P. Wollny, D. Meller, B. Boehm, A. Dreizler, A. Kempf, A temporal fluid-parcel backwards-tracing method for Direct-Numerical and Large-Eddy Simulation employing Lagrangian particles* and is reprinted with permission from Elsevier. L. Engelmann developed the software for the presented simulations and the post-processing, performed all calculations, wrote the manuscript and generated all figures and tables. The experimental measurements were performed by C. Welch and M. Schmidt. P. Wollny, D. Meller, B. Boehm, A. Dreizler and A. Kempf contributed corrections, discussions and proofreading.

Abstract

In this study, a method which allows for causal backtracing of turbulent flow phenomena is suggested. Key events in technical processes based on turbulent mixing can thereby be studied by their detailed temporal and spatial convective history. As a demonstration case for this method, a study of cyclic variations in internal combustion engines is used. Since it is assumed that major influences on cyclic variations are transported convectively, a set of Lagrangian tracer particles is generated at the start of a simulation run. The simulation is performed until the point where an arbitrary phenomenon of interest is observed and the simulation run is cancelled. The method then identifies particles in the neighboring region and saves their identification. Subsequently, the simulation is restarted using the same exact initial flow conditions for artificial turbulence generation and recreates the previous run.

This chapter is under review in Applied Energy.

However, in the second run, only the identified particles are simulated and their spatial and temporal trajectories are logged and observed in detail. The trajectory provides information on pressure, temperature, velocities and mixture composition to reconstruct the causes of the phenomenon of interest. This approach offers an efficient work-around of computational memory and input/output problems, which occur in modern computational fluid dynamics while also saving temporal and spatial information of small parts in the computational domain. The presented method can be of fundamental value in the research of cyclical processes with complex flows.

9.1 Introduction

In the context of technical flows, turbulence is a desirable phenomenon for applications involving the mixing of fluids. Many reactive and non-reactive turbulent flows in the field of energy and process engineering serve the purpose of setting a certain concentration or mixing ratio between two or more substances. As the precision of adjusted mixing ratio is crucial for the material or energetic output of processes like pharmaceutical reactors or energy conversion units using both, redox reactions and direct combustion, a detailed understanding of the turbulent pathways of fluid parcels involved in key events, e.g., initiation reactions in chemical reactors or ignition in combustion engines, is required. The prediction and manipulation of the fluid parcels involved in these phenomena provide further control of technical processes and offer further potential for efficiency. Therefore, fluid parcels have to be tracked spatially and temporally over the whole process and all influences on the parcel have to be assessed.

Direct-Numerical (DNS) and Large-Eddy Simulation (LES) form a basis for forward- and backward-tracing in physical domains of reasonable sizes due to the accessibility of key data to reconstruct spatial and temporal trajectories of single fluid parcels. To trace a flow backwards in time, fluid and thermodynamical data need to be saved for each time-step, which requires vast amounts of computational memory and hence, is not affordable on most computational systems. Starting a simulation from a key event and enforcing time-stepping to proceed temporally backwards causes negative diffusion and dissipation, which is numerically unstable. Hence, the total amount of data stored while tracing has to be reduced. It is evident that only the trajectories of the fluid parcels involved in key events are of interest, which reduces the required memory drastically. However, these parcels can only be identified after the key event has already happened.

Model development for computational fluid dynamics (CFD) have benefited from the increase of computational power and powerful schemes as well as models have become more affordable for the simulation of reactive and non-reactive flows. In the context of reactive flows, early studies employed LES of premixed and non-premixed combustion and have proven its suitability for the simulation of modern combustion systems [53, 210, 207, 77, 121].

Unsteady Reynolds-averaged Navier–Stokes (URANS) is the most cost-efficient and widely used approach for internal combustion engine (ICE) simulation in industry and research applications. Numerous works have employed URANS for the simulation of ICE – some with respect to cycle-to-cycle variations (CCV) [229, 72, 308, 247, 49, 200]. Nonetheless, the discussion about the suitability of URANS for the analysis of CCV is still controversial. It is commonly argued that URANS is lacking the presence of the small scale turbulent influences, which are only captured in DNS and highly-resolved LES. Hence, a popular makeshift for the study of CCV within the URANS community is the use of hybrid URANS-LES approaches to achieve the resolution of small scale structures in the regions where the URANS resolution is considered insufficient. In particular, their suitability was the subject of several studies, e.g. by Hasse et al. [95], Krastev et al. [148, 149], Buhl et al. [27] and Celik et al. [34] in a more general manner. Hybrid methods are considered state-of-the-art and are utilized in numerous works.

The transition of engine simulation from URANS to LES was discussed by Celik et al.[32], Richards et al. [228] and Rutland [241]. Flows in ICEs are characterized by different turbulent length scales from the large tumble and swirl vortices to the small dissipative structures. The resolution of these vortices is crucial for the correct description of the mixing processes of fuel and oxidizer, which is the key for the prediction of the combustion and emissions. LES allows for the resolution of the larger vortices, scaling with the characteristic geometry, which is an important basis for the prediction of mixing processes. The simulation of mixing through the gas exchange process was analyzed by Ameen et al. [6] and detailed flow field investigations relevant to such processes were performed by Janas et al. [112]. The availability of modern computational resources makes LES an attractive tool for the study of cyclic variations, which requires the simulation of multiple cycles. Earlier studies of CCV were performed by Vermorel et al. [290], Enaux et al. [58], Granet et al. [91] and d'Adamo et al. [48].

While still considered niche, with computational power increasing, the DNS of ICE processes is slowly gaining importance. DNS of engine-like assemblies and conditions were extensively studied by Schmitt et al. [251, 253, 252]. With the most critical issues of engine DNS being addressed by Frouzakis et al. [76], recent DNS works for selected problems in ICE were performed by Keskinen et al. [125, 126] as well as Giannakopolous et al. [83], which particularly focus on the near-wall physics such as boundary layers and heat transfer.

The LES and DNS approaches are of particular importance for this work. Overall, recent advances within LES and DNS have been made in the field of Lattice-Boltzmann methods, e.g., for large scale [180] and complex geometry flows [97] – with the latter work applying the framework to engine simulation –, machine learning methods to improve the overall efficiency of CFD [143] or for sub-grid closure [226, 199], detailed chemistry of single [40] and multi-component fuels [78, 277] as well as environmental and urban flows [79, 153].

Lagrangian–Eulerian frameworks have become the state of the art in LES and DNS due to their versatility and efficiency. Techniques with relevance to the study case of this work include the description of liquid sprays – a detailed mathematical overview is given by Stiesch [270]. Numerous extensions for this method exist, e.g., the extension to high-pressure flows [20], improvement of the droplet-turbulence interaction [193] or the description of the spray-wall interaction [314, 281]. Another common application of Lagrangian–Eulerian frameworks in this context are the description of complex moving geometries by arbitrary Lagrangian–Eulerian methods (ALE). Since their development [104], several extensions, e.g., adaptive mesh refinement, were made and a summary with relevance to engine applications was given by Barlow et al. [17]. Lagrangian–Eulerian frameworks serving for tracking methods are of high relevance to the present work. Lagrangian–Eulerian tracking methods can be directly coupled to physical particles that they aim to assess, such as soot [197], atmospheric particles [263] or liquid droplets [245], but also fluid parcels such as transported passive scalars, as demonstrated by Bonnani et al. [24] or within those of this work. While the employment of Lagrangian tracers within LES is not novel, the present approach bridges the gap between spatial and temporal causation for stationary and unsteady processes. The proposed method uses the stochastic nature of LES and the deterministic nature of random number generation in turbulence initialization and particle seeding and thus, allows for the analysis of events that occur just once or in a repetitive nature.

In this study, a method employing Lagrangian tracer particles is proposed, allowing for temporal backwards tracing of the causes of key events. The studied application case is an ICE, which features the known problem of cyclic variation, making it a well-suited test case for this method. However, this method is universally applicable and not only restricted to combustion problems.

While new potential energy converters for electrical power supply and propulsion emerge, many of these technologies are not yet mature enough to be reliable alternatives to ICEs for the broad mass market. Internal combustion engines running on renewable fuels are expected to play an important role during the energy transition and in future heavy-duty applications. Hence, an efficient and clean operation of engines is required. Reducing CCV of in-cylinder flows is one of the biggest challenges in engine design as CCV lead to significant variations in mixture formation and flame propagation, reducing the overall performance of the engine. Due to its ability to resolve the major scales of the turbulent energy cascade, LES has proven itself to be a powerful tool in the assessment of CCV. Large-Eddy Simulations aiming for the assessment of CCV with respect to the mixing and combustion process were performed by Goryntsev et al. [88], Truffin et al. [282], Zhao et al. [315] and Ameen et al. [7].

The causes of CCV can be assessed using different measures obtained from experiment and simulation. Goryntsev et al. [88] used common mean and RMS statistics to analyze the air-fuel ratio as well as the flow velocities under direct-injection operation. Truffin et al. [282] made use of the coefficient of variability and the Bravais–Pearson coefficient to

study the correlation of different turbulent and thermodynamic quantities. Advances in the experimental assessment of CCV were made by employing elaborate tools and analysis. With machine learning (ML) methods becoming more popular in model development and post-processing of results, Hanuschkin et al. [92] and Dreher et al. [54] utilized ML to assess combustion variations in engines and were able to predict high energy cycles based on partial flame topology from one snapshot of the flame propagation and based on flow field features, respectively. An approach based on bivariate 2D empirical mode decomposition was proposed by Sadeghi et al. [242], which attempted to separate instantaneous flow fields into large scale structures and turbulent fluctuations and therefore, gives insight into the CCV of the in-cylinder flow. A similar procedure aiming for the identification of coherent structures and their effects on CCV relying on proper orthogonal decomposition was suggested by Wu et al. [306]. Furthermore, analysis based on conditional statistics as suggested by Krueger et al. [150] and correlation maps as presented by Bode et al. [23] revealed that the in-cylinder flow can correlate to the ignition and the indicated mean effective pressure.

Measures of engine CCV typically assess correlation instead of the actually desired causation. To thoroughly link correlation and causation, a large set of variables must be evaluated, as shown by Welch et al. [300], who found that conditional statistics were required in addition to multivariate correlations to obtain deeper insights into the causal chain of ICE CCV. Ultimately, in the case of simulation, this leads to a large set of variables to be computed over a large number of cycles and the need for expensive simultaneous data measurements in the case of an experiment. This is supported by a study by Chu et al. [39], who found that a high number of cycles were required to obtain correlations above the significance level. Furthermore, ML approaches are more commonly trained using even more cycles, leading to these techniques being applied more commonly to experimental rather than simulation data. Similar to the correlation techniques, ML approaches require the dependencies between several sets of data or variables to be able to give insights into causation. The proposed technique is applied in-situ, which couples it directly to the physics observed in the simulation. This not only allows for the direct insight into causation within a set of data but also for the full control of data sets to be investigated without expensive post-processing techniques. Furthermore, due to not being formulated as a black box model, the proposed method can be validated using known physical phenomena, leaving less room for speculation within the observations. Nevertheless, the method is not seen as a replacement but as a useful addition to known approaches. While this method is demonstrated for the study of engine CCV, it is not restricted to only this field.

The present method is complementary to the state-of-the-art tools to examine CCV, as it not only allows for the analysis of convectively transported phenomena, but also for the precise temporal tracing of fluid particles. The method potentially extends the works of Krueger and Bode [150, 23] by providing even more information. Stiehl et al. [269] investigated the influence of the intake port geometry on the in-cylinder flow. Furthermore,

Desantes et al. [52] and Balz et al. [14] assessed the influence of the spray nozzle geometry on ignition and combustion. The present method can extend these studies by revealing which regions of the intake manifold are likely to have fluid reaching the spark plug or the spray nozzle. Further, the particles can be assigned to spray droplets revealing which injector holes are likely to produce droplets reaching the walls or piston gap. Phenomena such as intake, injection or ignition can be assessed requiring little modification of this flexible method.

9.2 Modeling strategy

The proposed strategy is based on three assumptions:

⇒ Convective transport is significant for the observed phenomena

⇒ The performed simulation run is deterministic

⇒ The statistics obtained from the tracers converge with the number of tracers used

Lagrangian tracer particles are used to investigate the temporal evolution of the thermochemical and fluid dynamical state of fluid parcel elements. The proposed methods require two simulation runs of identical settings on the same machine to ensure a deterministic setup. During the first simulation run, the tracer particles are initialized randomly at the inlet boundary during the intake stroke and have no mass. Hence, the tracers are transported passively based on the local flow velocity. During a key event – for this study ignition at the spark plug – all tracer particles in close proximity to the event's source – in this study the spark plug – are saved and the simulation run is terminated. The run is then restarted with only tracer particles which were saved in the previous run simulated and the variables of state and space are stored with time to reconstruct the thermochemical states each tracked fluid parcel has transitioned through. The number of tracer particles used per simulation run is variable and more significant statistics are obtained employing a higher number of tracers. However, the number of tracers is limited by the memory at hand on the respective computing system.

9.3 Experimental test bench

To validate the numerical simulation, experiments were performed in the four-stroke single-cylinder spark-ignition optically accessible research engine at TU Darmstadt. The Darmstadt engine (AVL) is equipped with a four-valve spray-guided pent-roof cylinder head configuration with a compression ratio of 8.7:1 and a bore and stroke of 86 mm each. Optical access is provided by an optical-grade fused-silica cylinder liner and a flat fused-silica piston window, which is connected to a Bowditch piston extension for mirror access. In the spray-guided

Table 9.1 Engine specifications for the reference case as presented by Schmidt et al. [249].

Data	Value
Engine Speed	1500 rpm
Bore	86 mm
Stroke	86 mm
Compression ratio	8.7 : 1
Crank angle range	$-360/+360°$ CA
Top dead center (TDC)	0° CA
Intake valve open (IVO)	325° CA
Intake valve close (IVC)	−125° CA
Exhaust valve open (EVO)	105° CA
Exhaust valve close (EVC)	−345° CA
Ignition/Tracing	−14.2° CA
Intake Pressure	0.95 bar
Intake Temperature	308 K

cylinder configuration, the top 55 mm of the stroke and an additional 8 mm in the pent-roof are visible. The engine runs under controlled boundary conditions for consistent operation. Mass flow and pressure perturbations are damped by large plenums in the intake and exhaust. For further details of the engine test bench, the authors refer to studies by Welch et al. [299] and Baum et al. [19]. Figure 9.1 shows a cross-sectional representation of the engine and the intake and exhaust ports. The operating conditions of the experimental test bench can be found in Tab. 9.1.

The long intake pipe allows fuel for port fuel injection and seed particles for particle image velocimetry (PIV) to homogeneously mix with the air before entering the combustion chamber. Within the intake pipe, two relative pressure sensors (GU21C, AVL, referenced to PMP4070, Kistler) measure the pressure just downstream of the noise reduction plenum and just before the intake valves. For clarity, the same nomenclature as in the underlying experimental works is used. Thus, the crank angles in this work range between −360°CA for the beginning of the intake stroke and +360°CA for the end of the exhaust stroke, where 0°CA indicates compression top dead center (TDC).

9.4 Numerical methods

The in-house code *PsiPhi* was used to perform all simulations. It was developed at the University of Duisburg-Essen and Imperial College London. *PsiPhi* has been utilized in many LES calculations – some of which have been highly resolved up to DNS resolutions – of reactive and non-reactive flows [232, 221, 59]. A finite volume method (FVM) and a cubic, equidistant grid allow for the solution of mass, momentum and a variable number of

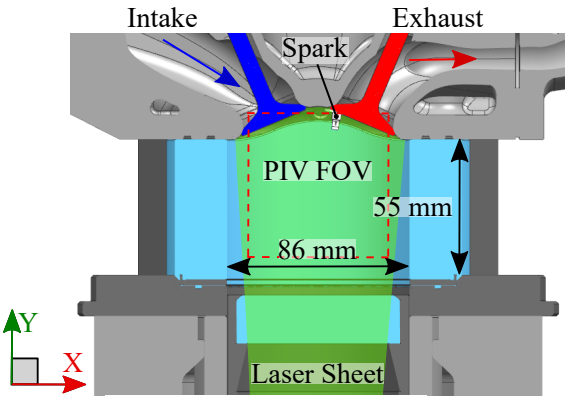

Figure 9.1 Cross-sectional display of the experimental test bench.

scalar transport equations. The momentum equations are spatially discretized using eighth-order central differencing (CDS) and tenth-order filtering to avoid spurious high-frequency fluctuations following Chen et. al. [37, 122], while the discretization order is reduced successively approaching the walls, and total variation diminishing (TVD) with the CHARM limiter treat additional scalar transport equations [317]. *PsiPhi* expresses fixed and moving walls with immersed boundaries [202], the latter being reduced to an ensemble of Lagrangian particles with prescribed motion profiles, as proposed by Nguyen et al. [191]. Conservation of the transported quantities such as momentum, mass and energy at the moving boundaries is enforced by applying the mirror-flow technique proposed by Forrer [71]. The immersed boundary cells are obtained by importing the geometry CAD data during the initialization of the simulation and applying a voxelizer with the desired resolution, leading to approximately 30 million fluid cells within this study at bottom dead center, which corresponds to a cell edge length of $\Delta x = 0.39$ mm. Good results have been obtained using this resolution and the same software framework in previous works [191, 190, 62]. The import of the geometry data is parallelized using the message passing interface (MPI) and leads to a negligible invested time at the beginning of the simulation and no additional computational effort during the simulation run. Time-stepping is achieved by a low-storage third-order accurate Runge–Kutta scheme [304]. A distributed memory domain decomposition approach, utilizing MPI and a non-blocking implementation for simultaneous computations and exchange of data, yield high parallel efficiency.

The following fully compressible, Favre-filtered transport equations are solved:

$$\frac{\partial \overline{\rho}}{\partial t} + \frac{\partial \overline{\rho} \tilde{u}_\mathrm{j}}{\partial x_\mathrm{j}} = 0 \tag{9.1}$$

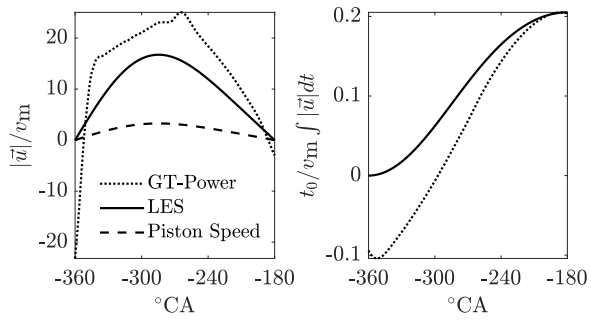

Figure 9.2 Velocity magnitude and its direction for the inflow boundary condition and GT-Power results by Welch et al. [299].

$$\frac{\partial\overline{\rho}\tilde{u}_\mathrm{i}}{\partial t}+\frac{\overline{\rho}\tilde{u}_\mathrm{i}\tilde{u}_\mathrm{j}}{\partial x_\mathrm{j}}=-\frac{\partial\overline{p}}{\partial x_\mathrm{i}} +\frac{\partial}{\partial x_\mathrm{j}}\left(\mu\left(\frac{\partial\tilde{u}_\mathrm{i}}{\partial x_\mathrm{j}}+\frac{\partial\tilde{u}_\mathrm{j}}{\partial x_\mathrm{i}}-\frac{2}{3}\frac{\partial\tilde{u}_\mathrm{k}}{\partial x_\mathrm{k}}\delta_\mathrm{ij}\right)-\overline{\rho}\tau_\mathrm{ij}^\mathrm{sgs}\right) \tag{9.2}$$

$$\frac{\overline{\rho}\tilde{E}}{\partial t}+\frac{\partial\overline{\rho}\tilde{u}_\mathrm{j}\left(\tilde{E}+\overline{p}/\overline{\rho}\right)}{\partial x_\mathrm{j}}=\lambda\frac{\partial^2\overline{T}}{\partial x_\mathrm{j}^2} +\frac{\partial}{\partial x_\mathrm{j}}\tilde{u}_\mathrm{j}\left(\mu\left(\frac{\partial\tilde{u}_\mathrm{i}}{\partial x_\mathrm{j}}+\frac{\partial\tilde{u}_\mathrm{j}}{\partial x_\mathrm{i}}-\frac{2}{3}\frac{\partial\tilde{u}_\mathrm{k}}{\partial x_\mathrm{k}}\delta_\mathrm{ij}\right)\right)-\frac{\partial}{\partial x_\mathrm{j}}\overline{\rho}\tau_\mathrm{j}^\mathrm{sgs}(\tilde{E}) \tag{9.3}$$

$$\frac{\partial\overline{\rho}\tilde{\phi}}{\partial t}+\frac{\partial\overline{\rho}\tilde{u}_\mathrm{j}\tilde{\phi}}{\partial x_\mathrm{j}}=\frac{\partial}{\partial x_\mathrm{j}}\left(\frac{\mu}{Sc}\frac{\partial\tilde{\phi}}{\partial x_\mathrm{j}}\right)-\frac{\partial}{\partial x_\mathrm{j}}\overline{\rho}\tau_\mathrm{j}^\mathrm{sgs}(\tilde{\phi}) \tag{9.4}$$

with the density $\overline{\rho}$, the velocity $\tilde{u}_\mathrm{i}$, the absolute total energy $\tilde{E}$ and the pressure $\overline{p}$. Hereby, $(\tilde{\cdot})$ denotes the Favre-filtered variables. A passive scalar quantity ϕ is used to identify old and fresh gas. The momentum and scalar sub-grid fluxes $\tau_\mathrm{ij}^\mathrm{sgs}$ and $\tau_\mathrm{j}^\mathrm{sgs}$ are treated using an improved eddy-viscosity approach as suggested by Hasslberger et al. [96] featuring reduced dissipativeness and improved scaling behavior closer to the walls compared to the standard static Smagorinsky model. The computational domain is kept compact due to the choice of an equidistant, cubic grid and the immersed boundary approach. Hence, only a small part of the intake and exhaust ports are included in the domain (50 mm in x-direction for each port, also see Fig. 9.3). The resulting boundaries are treated using the Navier–Stokes characteristic boundary approach as presented by Poinsot [213], where the intake and exhaust ports are treated with non-reflecting inlet boundaries during the intake stroke and non-reflecting outlet boundaries during the compression and exhaust stroke. The respective target values are obtained from velocity estimates based on the port cylinder cross-section ratio and the piston velocity, and pressure measurements in the ports. The boundary condition is switched dynamically depending on the mean flow direction within the respective ports.

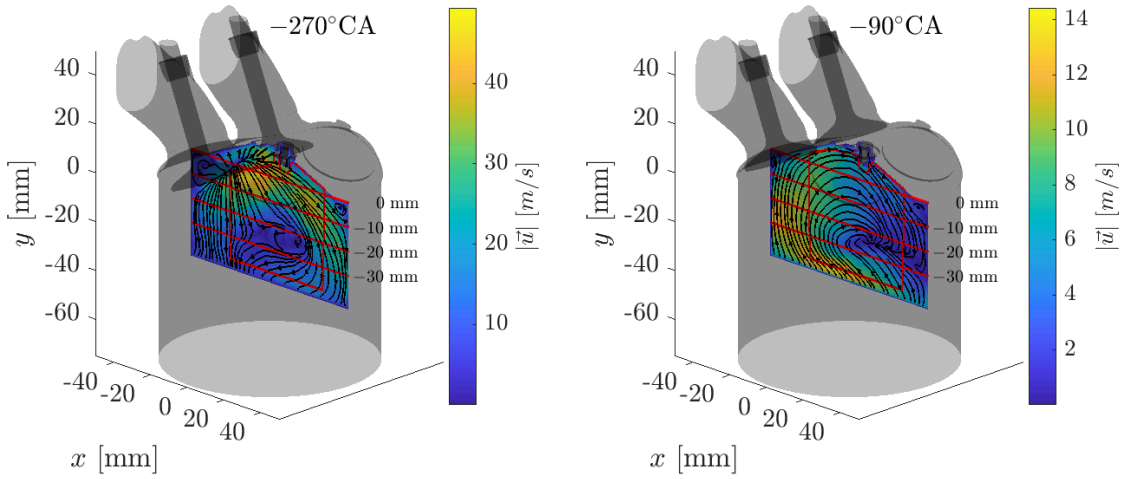

Figure 9.3 Magnitudes of the averaged velocity calculated from the x- (u) and y-component (v) of the velocities in the tumble plane at $= -270°$ CA and $= -90°$ CA obtained from the simulation. The red contour gives the outline of the PIV-measurement area and the lines indicate the sampling area used for the statistics.

Figure 9.2 shows the velocity magnitude imposed at the boundary based on the piston velocity, as well as the integrated velocity to indicate the filling of the cylinder. Both, 1D-simulations of the engine (GT-Power) and experiments (not shown) feature a back flow – indicated by the negative velocities – at the beginning of the cycle caused at the start of the intake stroke by a negative pressure differential. While the model based on the piston velocity profile is not able to take pressure oscillations in the intake pipe into account, the qualitative agreement for the rest of the cycle remains acceptable and the total inflow of gas is captured well.

9.5 Results

9.5.1 Validation of the global flow field

To ensure a reliable computational basis for the presented method, a sufficient prediction of the flow field is required as the tracer particles are transported purely convectively. Simulations of motored operation (unfired) are performed for a total set of 30 cycles. The calculations can be performed without ignition, since the key event considered in this study is ignition and no combustion occurs until that point. Statistics are obtained by neglecting the first two cycles to ensure that all effects of the initialization are removed.

The experimental and numerical flow fields used for the comparisons are obtained in the tumble plane (Fig. 9.3). The figure includes the intake ports and valves to allow for better

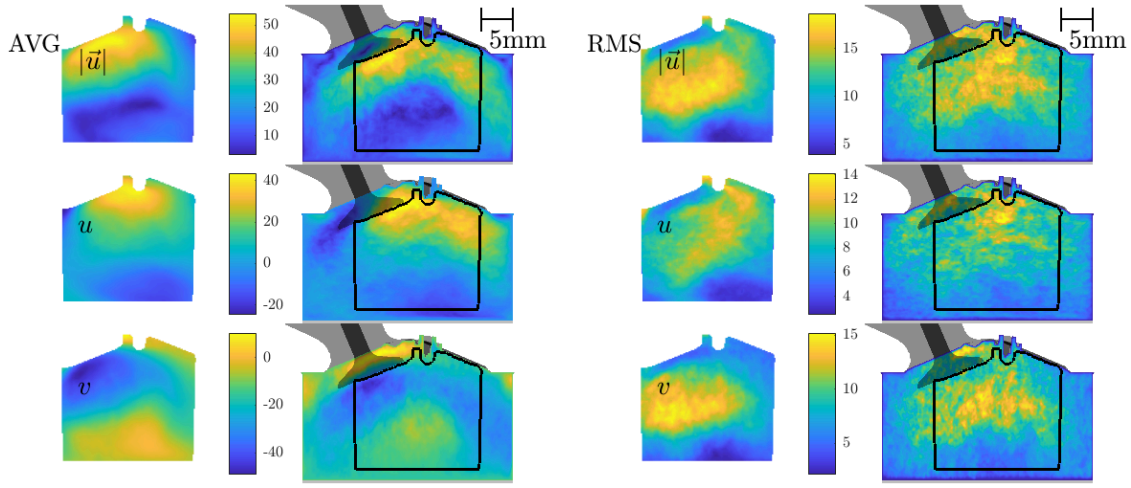

Figure 9.4 Averaged flow fields of the x-component (u) and the y-component (v) of the velocities in the tumble plane at $= -270°$ CA obtained from the experiment (left column) and simulation (right column).

orientation and to give an estimate of the features included in the computational domain. The exhaust ports and valves were excluded from this figure to improve the visibility of the flow field. Two crank angles of $-270°$ CA and $-90°$ CA (after TDC) were chosen to represent both the intake and the compression stroke, as these are critical for particle movement. The flow fields show the velocity magnitudes calculated from the velocity components in horizontal (x) and vertical (y) direction within the image plane. Streamlines are superimposed to represent the flow direction, which is dominated by the wake turbulence behind the valves during the intake stroke ($-270°$ CA) and the tumble vortex during the compression stroke ($-90°$ CA).

The flow pattern obtained during the intake stroke is illustrated in Fig. 9.4 and compared to the experimental measurements. The figure shows row-wise the magnitude of the two-dimensional flow velocity $\sqrt{u^2 + v^2}$, the x-velocity component u and the y-velocity component v. Furthermore, the experimental measurements are shown on the left side. The borders of the PIV measurement region are represented by a black outline, which was superimposed on the numerical flow fields. Capturing the correct in-cylinder flow during the intake stroke is essential since the turbulence is mainly generated in this stage and then later affects the mixture formation for direct injection cases or the flame propagation during combustion. Despite the exclusion of the complex flow dynamics induced by intake flow oscillations in the experiment, the intake flow is well-represented by the simulation. The good agreement for the averaged velocities found in the comparison between the numerical results and the measurement at $-270°$ CA demonstrates the capability of the used approach to capture the complex flow behavior as it was demonstrated by Nguyen et al. [191]. The RMS values of the velocities, however, are under-predicted. As the RMS values represent fluctuations due

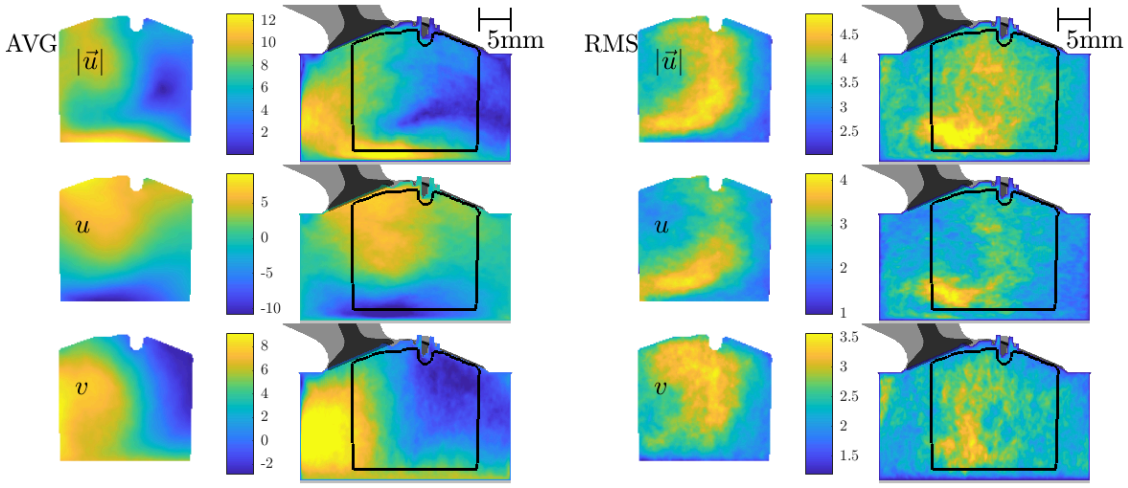

Figure 9.5 Averaged flow fields of the x-component (u) and the y-component (v) of the velocities in the tumble plane at $= -90°$CA obtained from the experiment (left column) and simulation (right column).

to turbulence and variations of coherent structures, the RMS values serve as an indicator for the predicted local turbulent energy. The under-prediction of these values is assumed to have multiple causes. First, the simulation is not fully capturing the cyclic and turbulent variation of all structures, which might be a consequence of too-strong numerical dissipation caused by under-resolution or numerical modeling. Second, possible over-prediction by the experiment due to noise and third, lack of cycles for a fully converged RMS field in the simulation.

Fig. 9.5 shows the x- and y-velocity components (u and v) as well as the magnitude in the tumble plane for the experimental and computational results at $-90°$ CA. Contrary to the intake flow field, which is driven by high velocities emerging from the pressure difference between the intake ports and cylinder, the in-cylinder flow during the compression stroke is dominated by the remaining inertia of the flow and the compression by the piston motion. Undergoing recirculation, interactions between tumble, eddies, moving walls, and the dissipation of kinetic energy make the dynamics of the flow under compression difficult to predict. Therefore, capturing the correct velocity fields at $-90°$ CA is challenging. The experimental and numerical results show a similar distribution of the low- and high-velocity areas of magnitude, u and v. Some deviations can be seen in a region to the left below the spark plug, where v is slightly under-predicted. Previous calculations with similar resolution showed that the flow behavior during compression is sensitive and requires a large number of cycles to converge towards the ensemble mean flow [191, 190].

The insights of the presented velocity fields must be further assessed by a quantitative analysis to ensure proper validation of the proposed simulation method. For a quantitative

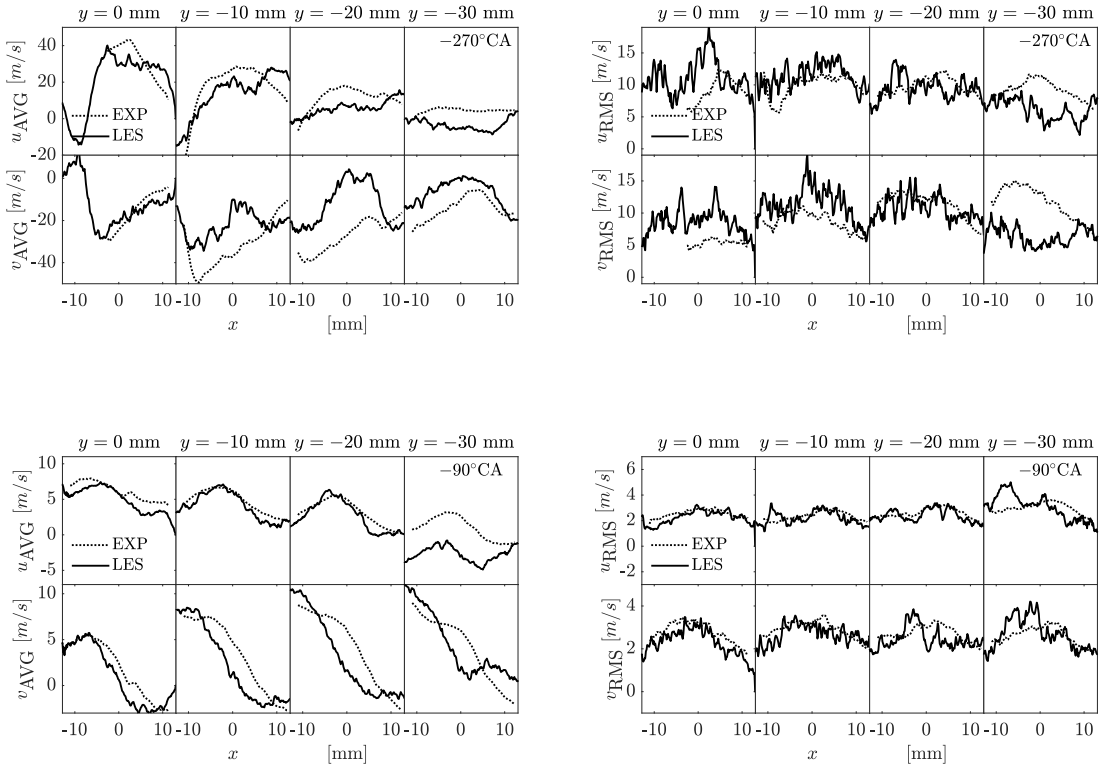

Figure 9.6 Averaged flow field statistics of the x-component (u) and the y-component (v) of the velocities in the tumble plane at $= -270°$ CA and $= -90°$ CA obtained from the experiment and simulation. The profiles are obtained along four sampling lines within the cylinder.

comparison, the u and v velocity components are obtained along straight lines within the tumble plane at the presented CA of $-270°$ and $-90°$, as displayed in Fig. 9.3. The figure shows the four chosen sampling lines with a spacing of 10 mm inside the tumble plane. Fig. 9.6 shows the velocity profiles of the horizontal (u) and vertical (v) components in the tumble plane at a CA of $-270°$ and $-90°$. The agreement for the u velocity component at $-270°$ CA improves with distance from the valve. However, the agreement of the v velocity components is less pronounced and no clear trend of improvement can be observed as for the u component. This can be assumed to be a consequence of the complex flow field and highly turbulent downward velocity of the intake flow forming due to the wake region below the valve disc. The flow at this stage is driven by the intake boundary condition leading to similar qualitative profiles but wrong prediction of magnitude. Due to the complex flow field and highly turbulent downward velocity of the intake flow, agreement between the measurement and the computation is difficult to reach, in particular for line plots. Nevertheless, the overall agreement at $-90°$ CA is better than for the earlier CA. Similar observations are made for the qualitative flow fields and it is hypothesized that this is a consequence of the reduced complexity and hence, easier to predict tumble flow driven by the piston when compared to the valve and piston-induced flow characteristic of the intake stroke. For this CA, the agreement diminishes with increasing distance from the cylinder roof. The tumble typically has to be predicted in both, shape and location. The slight incorrect prediction of these may lead to a great disagreement for line profiles, while flow fields still appear to match well. This is in particular supported by the negative values of the computed profile at $y = -30$ mm, while the measured profile still remains positive. Thus, it can be concluded that the simulation predicts the tumble center to be slightly higher than in the experiments, leading to the occurrence of the negative horizontal velocity values at $y = -30$ mm. The agreement of the lower distances might be compensated by over-predicting the shape of the tumble vortex within this direction. Nonetheless, the profiles can still be considered to be captured well in a qualitative and quantitative sense.

In Fig. 9.7, the volume-averaged velocity profiles within the reduced region of interest (ROI) of the spark plug, obtained from the simulation, can be seen. The ROI is a spherical region around the spark plug, which serves for the detection of tracing particles. The results are phase-averaged over all cycles with the grey envelope showing the maximum deviation from the mean value. These velocities are crucial for the flame formation and propagation in fired operation and in this study are indicators for the preferred direction from which particles approach the spark plug.

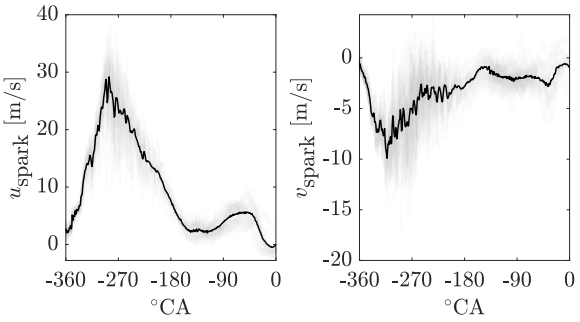

Figure 9.7 Phase-averaged velocities of the x-component (u) and the y-component (v) in the region of interest (ROI)
around the spark plug for the simulation. The grey color shows the envelope of curves around the averaged curve.

9.5.2 Generation of tracer trajectories

A set of spatial tracer particle trajectories for two variants of different sized spherical target regions is shown in Fig. 9.8. The spherical ROIs are defined around the spark plug to visualize the motion path from the point of tracer generation until the occurrence of the key event: the *ignition* at $-14.2°$ CA. Tracer particles inside the spherical ROI around the spark plug at ignition timing are chosen for trajectory generation (a small part of the spherical ROI is outside of the engine geometry and can not be reached by the tracer particles. This part is of no relevance for the particle detection). A three-dimensional perspective as well as x-z and x-y projections are shown to give better insight into the spatial trajectories. Further, the engine geometry is displayed transparently to reveal the trajectory of the tracer particles seeded between $-345°$ CA and $-270°$ CA. The black round markers within the spherical ROI indicate the end of the trajectory to reveal the particles' location during ignition. The particle seeding was performed homogeneously over the two intake ports by choosing random locations within the port cross-section for each time-step. The time frame of seeding the particles is variable but was set to this window of CAs within this study. The variation of the ROI size was performed to assess whether the results are sensitive to the number of tracer particles. Using the full ROI, a number of ≈ 2000 tracer particles was detected per cycle at the spark plug during ignition and their trajectories are tracked during the second run. For the reduced ROI ≈ 500 tracer particles were detected per cycle. However, only a fraction of the tracer trajectories are shown to ensure readability of the displayed trajectories. The choice of the presented trajectories is arbitrary and serves the purpose of providing a first insight. Furthermore, the trajectories are given different colors for better differentiation based on the CA at which the particle was seeded. A few observed particles were trapped in recirculation zones near rather complex geometry features and are not considered for evaluation.

The particles follow the in-flowing air stream through the intake ports into the cylinder. Due to the narrow valve gap, particles are launched into the cylinder with high velocities. Depending on the particle seeding time and entry location in the valve gap, the particle trajectory varies due to the particle's exposure to the tumble vortex, which can be seen by the different shape of the trajectories shown. The particles seeded at earlier times (indicated by darker colors) feature strong interaction with the turbulence generated in the wake behind the valve disc as soon as the valve gap is passed – this is more apparent in the $x-y$ projection. The use of the larger ROI reveals that most of the trajectories follow a tumble-like motion, which itself is governed by the intake momentum meeting the bounds of the cylinder and the piston wall. Towards the end of the trajectory, the tracers approach the spark plug due to the direction of the piston motion. A reduction of the ROI radius by 50% confirms this observation. Overall, it can be observed that particles from the whole interval can potentially reach the spark plug at ignition. Additionally, the particles traverse most of the in-cylinder volume, indicating the occurrence of strong mixing.

9.5.3 Influence of numerical modeling

While the presented approach focuses on convectively transported phenomena, in general, diffusive processes might change the relevance of the results.

Figure 9.9-a) reveals the ratio of the turbulent viscosity ν_t produced by the LES sub-grid model and the laminar viscosity ν_l experienced by each tracer particle. During the intake stroke, the ratio is between 1 and 10 as the turbulent viscosity succeeds the laminar viscosity on average. Then this ratio reduces to a value less than ten during the late intake and the compression stroke. During the late compression stage, however, the factor increases again. This reveals, that the diffusion observed in the simulation is mainly of a modeling nature and should reduce with grid refinement.

Based on the figure of the profile of the viscosity, the role of diffusion in the context of the fluid particle tracing is investigated. For that reason, the Peclét number experienced by each tracer particle based on the total diffusivity D_{tot} of the Euler phase is shown in Fig. 9.9-b). As already observed in Fig. 9.9-a), the profiles are dominated by the turbulent contribution. The total diffusivity-based Peclét number reveals intense dark coloring along all lines at all CA. This indicates that the trajectories are superimposed by a strong fluctuation, which is caused by the sub-grid viscosity. The overall values of the Peclét number hold magnitudes up to a hundred, which indicates relevancy of the diffusive transport within this calculation. Due to the early intake and the influence of compression, the convection is up to a hundred times greater than the diffusion, while during the late compression, the ratio holds values between 0.1 and 10. This also affects the ability of this approach to predict reality considering the diffusion of momentum and scalars of the fluid parcels. The diffusion in this study is further affected by the sub-grid model due to the contribution of turbulent viscosity.

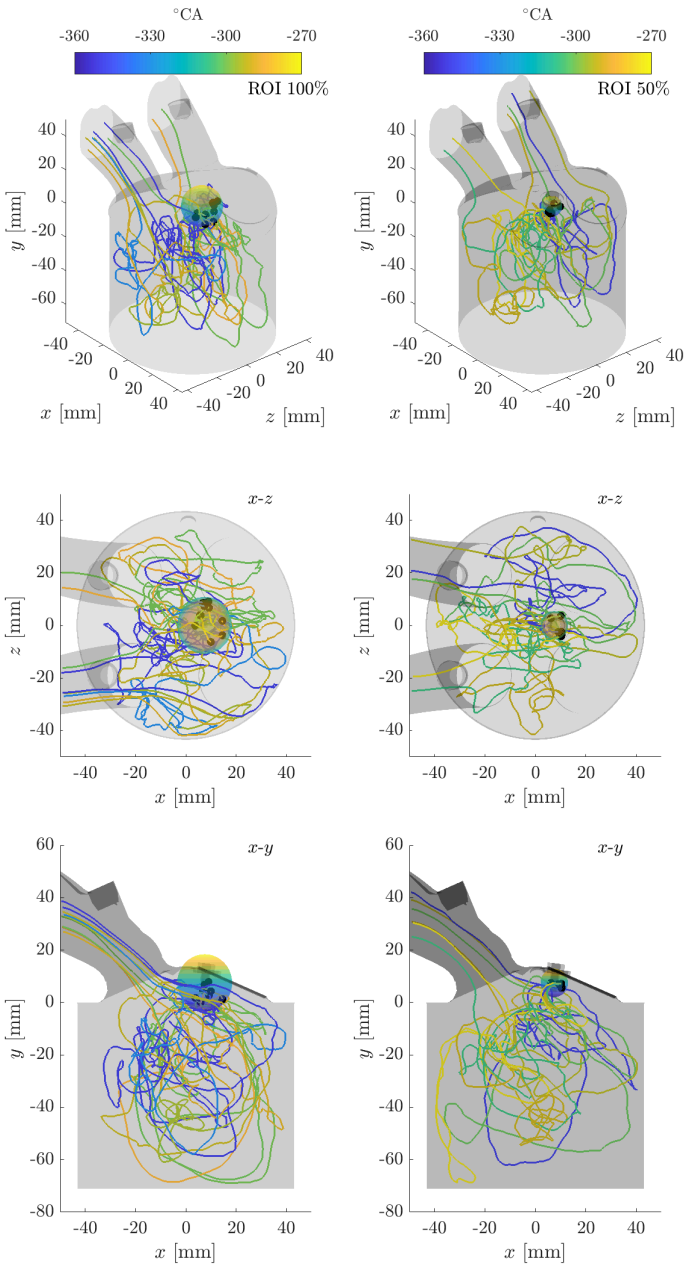

Figure 9.8 Three-dimensional projection of the tracer trajectories for the full and the reduced size of the ROI around the spark plug.

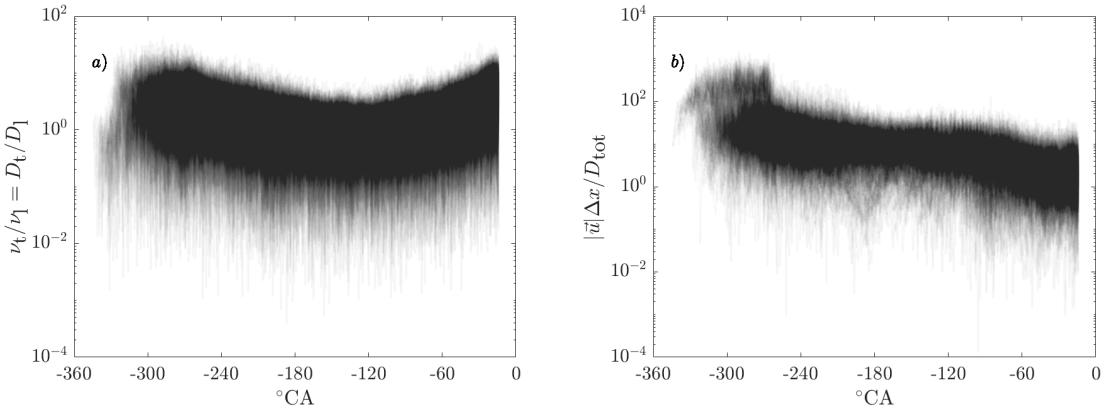

Figure 9.9 a) Ratio of the turbulent viscosity ν_t and the laminar viscosity ν_l experienced by the tracer particles. b) Peclét number experienced by the tracer particles based on the total diffusion of the Euler phase.

From a numerical perspective, it has to be noted that a major part of this modeled diffusion is formed by suppressed convective phenomena, such as small-scale turbulent transport or numerical schemes. In this context, the grid resolution is a crucial parameter when it comes to controlling the influence of the modeled diffusion, as the numerical error vanishes with the order of the numerical scheme and the resolution determines the contribution of the sub-grid model. Hence, increasing the resolution will reduce the total diffusion and thus, also improve the ability of the presented method to predict the flow.

9.5.4 Assessment of tracer trajectories

In the following section, the quantities observed by the tracers are analyzed with respect to the flow physics. Figure 9.10-a) shows a cross-section of the intake manifold, in which the tracer particles are seeded. The color of the local features of the cross-section shows the probability density of a point to produce a particle that ends up in the ROI at the spark plug during ignition. The probability density was obtained by sampling the number of particles spawned in each seeding position over all tracer particles captured at the spark plug from all simulated cycles. The number of tracers originating from each seeding position was normalized such that integration over all cells inside the cross-section (including both intake ports) yields a value of unity.

While the colored regions show the presence of tracer particles, the white regions imply the absence of particles reaching the spark plug. In addition, the grey regions represent the wall-geometry. The regions with particles reaching the spark plug form a kidney-like shape. Particles seeded near the walls seem to not reach the spark plug. Interactions with the intake

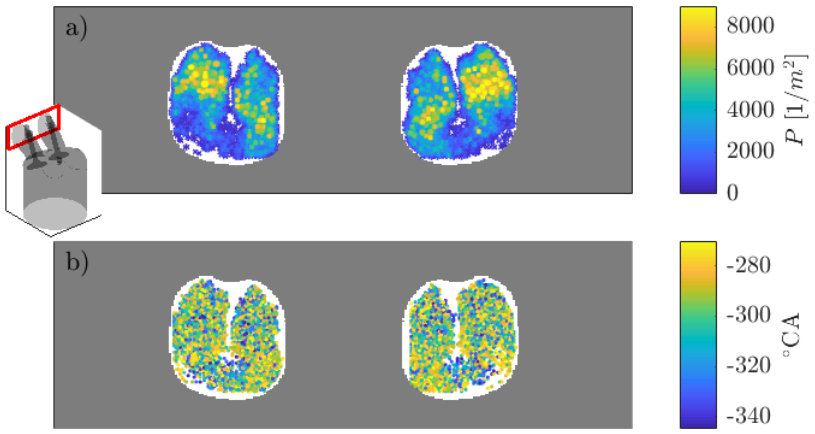

Figure 9.10 a) Probability density in the intake manifolds to produce a tracer particle that ends up in the ROI of the spark plug during ignition. b) Crank angle and seeding positions in the intake manifolds to generate a tracer particle that ends up in the ROI of the spark plug during ignition. The detailed view on the left shows the location of the seeding plane within the engine geometry.

valve stems appear to have the same effect, as can be observed by the white gaps in the center of the intake manifold. Conversely, the regions with higher particle yield appear more distinct and are concentrated in a rather narrow space. The high-probability regions form diagonals through the ports, appearing in a V-shape stretched over both left and right intake ports. The outer-top regions are the most likely to end at the spark plug. This might be a consequence of the corresponding streamlines avoiding initial recirculation zones below the valves. These zones appear mostly between and under the valves due to the mixing of the streams from the two manifolds and the low-magnitude velocities below the valve disc. Therefore, higher seeding locations in the cross-section allow the particles to find streamlines that lead away from these turbulent zones and walls where the particles might get trapped and hence, not reach the spark plug. The lower parts of the cross section are characterized by low to zero probabilities of particles reaching the spark plug. Again, this is assumed to be a consequence of the flow being highly dominated by walls, since the flow entering the cylinder from this side of the valve is deflected by the valves, the cylinder walls and the piston during the early intake stage.

Figure 9.10-b) shows the same cross-section as Fig. 9.10-a), however, it visualizes the seeding CA of the tracer particles reaching the ROI of the spark plug. It can be noted, that at the lower walls of the intake plane, two kernels of particle-seeding early CA are forming within the ports as indicated by the blue-color zones.

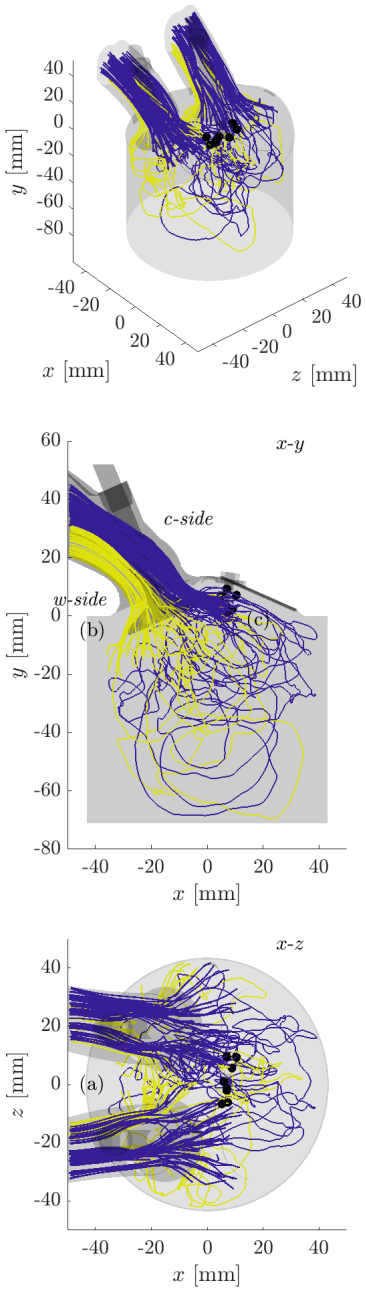

Figure 9.11 Three-dimensional projection of the tracer trajectories in the intake manifold and valve gap. The trajectories are cut after the particles have passed the valve gap. The coloring is chosen to indicate the *upper* and *lower* half of the intake manifolds. Features of the flow are indicated as *a*, *b* and *c*.

Given the insights of Fig. 9.8 and 9.10, it is assumed that the particles being seeded in the lower half of the intake cross-section pass the intake valve disc closer to the cylinder walls (*w-side*) and the particles being seeded in the upper half of the cross section pass the intake valve disc closer to the cylinder axis (*c-side*). To further investigate this hypothesis, the tracer trajectories of the particles from the time of seeding until the passing through the valve gap – this takes ≈ 8 ° CA – are shown in Fig. 9.11. The particles being seeded in the *upper* half of the intake manifold, colored in blue, remain on their respective side of the intake manifold until they enter the cylinder. A similar observation can be made for the particles being seeded in the *lower* half of the intake manifold. Furthermore, more particles traverse the *c-side* (blue) of the manifold compared to the *w-side* (yellow). The flow feature *a* from Fig. 9.11 reveals that the trajectories moving past the *w-side* tend to leave the valve disc in the z-direction, rather than towards the cylinder liner (feature *b*). This leaves a smaller number of particles going past the *w-side* and eventually reaching the spark plug. The flow through the intake port evolves with increasing CA and flow velocities are lower for earlier CA. It may be assumed that this allows the particles to follow the free flow on the *w-side* of the valve more easily, as the streamlines can form freely and provide a sufficient distance from the walls, reducing the chance of the particles getting stuck in low-velocity regions near the wall. However, it is still interesting that these particles reach the spark plug, despite their tendency to develop in a trajectory opposed to the tumble-dominated flow.

With the progressing intake stroke, high velocities occur in the valve gap, which form smooth streamlines from the intake boundary into the cylinder flowing past the *c-side* of the valve disc to enter the cylinder. At these high velocities, the flow on the *w-side* of the valve disc is governed by wall impingement and curvature, and particles are likely to be flushed into the wake region (feature *b*) behind the valve or collide with the wall. This is assumed to strongly decrease the chances of a particle ending up near the spark plug, as most particles are observed to travel deeply through the cylinder before reaching the spark plug. The flow past the *c-side* near feature *c* appears to yield the highest success rate of tracer particles reaching the spark plug, as the flow geometry is less complex and the trajectories follow the natural tendency of the streamlines to form a tumble. This ultimately brings particles back to the cylinder roof after impinging on the cylinder and then the piston walls. Furthermore, this also agrees with the findings from Fig. 9.10.

Figure 9.12 shows the total cumulative travelled distance of the tracer particles with time in crank angle degrees normalized with the mean piston velocity v_m and the reference timescale $t_0 = 1s$. The initial slope of the travelled distance becomes steeper with later seeding times, as the piston accelerates and hence, induces higher velocities in the intake manifold. Likewise, the slope reaches a maximum when the particles travel through the valve gap due to the high velocities experienced there. This is further represented by the addition of the small figure showing the magnitude of the tracer velocity (derivative of travelled distance).

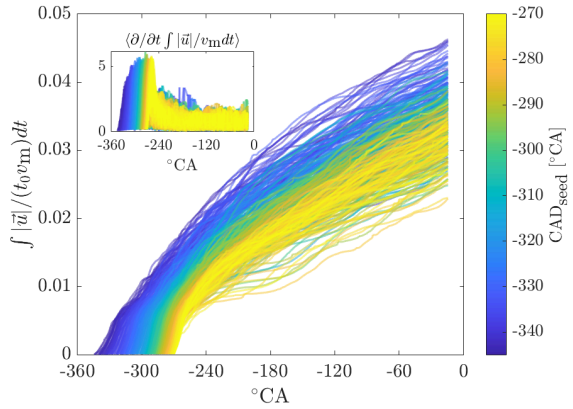

Figure 9.12 Total travelled distance and the tracer particle velocity with time. The color of the curve represents the seeding time of the particle with a brighter color indicating later seeding times.

The gradient likely increases for particles seeded at later times due to the increasing piston velocity in those intervals, which causes a greater pressure ratio at the valve gap. The curves then progressively flatten down due to the overall decrease of the kinetic energy.

This trend can be observed also in the profile of the kinetic energy. Figure 9.13 shows the resolved kinetic energy experienced by each tracer particle with time. The trajectories were filtered to focus on the medium- and large-scale physical behavior. The plot is shown using a logarithmic axis to emphasize the different energy magnitudes in the flow field. The high transparency of the lines is used to focus the collective behavior of the particles, which is now visible by the density and intensity of the line color. furthermore, the color of the trajectories indicates the total travelled distance at the time of ignition; red colors indicate higher travelled distance and blue colors indicate less travelled distance. All particles appear to experience the highest kinetic energy within the intake manifold and the valve gap, as can be observed by the initial peaks of the energy at the early CA. Due to few fluctuations of the lines, it may be assumed that the particles are exposed to little turbulence within the manifold. However, the fluctuations increase as the kinetic energy level decreases after the particles have passed the valve gap. These fluctuations indicate an increase in the number of turbulent structures that the particles pass. These early fluctuations pass and are caused in a rather small volume, as the piston is still close to TDC. Thus, flow phenomena in the cylinder are mostly governed by the turbulence generated due to the valve flow. As the piston expands further and the volume increases, there is more space for the particles and they follow the major tumble to further depth into the cylinder leaving the highly turbulent zone near the valves. During compression of the piston, the two averages of high and low distance split between -120 and $-60°$ CA (the averages are indicated by the *high* and *low* annotation in Fig. 9.13). A diverging colormap is chosen to emphasize the separation between the particles

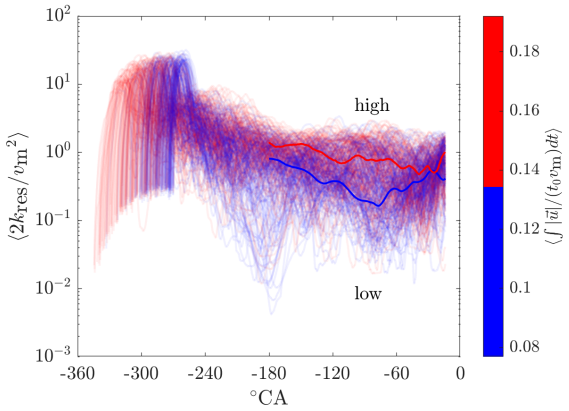

Figure 9.13 Experienced filtered kinetic energy by the tracer particles. The coloring of the filtered trajectory indicates the total travelled distance of the particle at the time of ignition; dark blue indicates lower distances and red indicates higher distances.

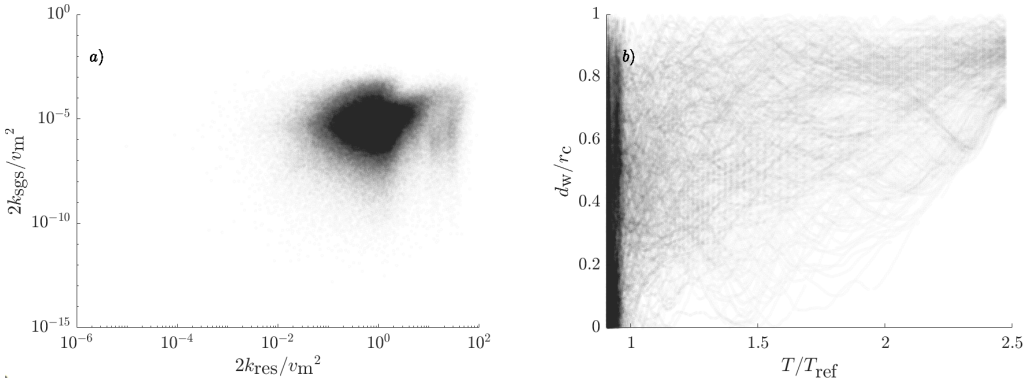

Figure 9.14 a) Experienced resolved kinetic energy k_{res} and sub-grid kinetic energy k_{sgs}. b) Experienced distance from the cylinder liner walls and temperature.

of lower and higher travelled distance. The trajectories of the lower traveling distance show more fluctuations than the particles of higher traveling distance. The two parts of the curve eventually merge at around $-60°$ CA, as the piston approaches TDC further. This is likely a consequence of the tumble vortex breakup, which removes the large and directed structures from the flow and leaves smaller turbulent structures behind. Furthermore, particles converge onto the same location around the spark plug and consequently experience more similar conditions. Both, the spatial homogenization of turbulent energy and spatial proximity agree with the merging of red and blue lines.

Figure 9.14-a) shows the scattering of the resolved kinetic energy and the sub-grid kinetic energy normalized with the average piston velocity $v_{\mathrm{m}} = 2ns$ (with the engine speed n and

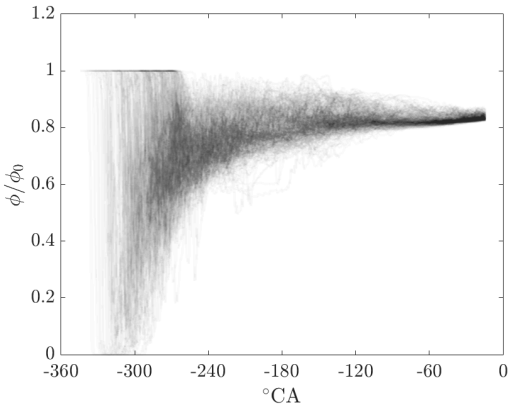

Figure 9.15 Experienced passive scalar by the tracer particles.

the stroke s). The inflow into the cylinder can be observed by the vertical structure on the right hand side, due to the high values of kinetic energy and the comparably small range of sub-grid energy values. Therefore, the flow through the intake manifold gets perturbed as the particles pass the valve. Both quantities appear mostly uncorrelated, as the kinetic energy is not necessarily an indicator for turbulence.

Figure 9.14-b) shows the temperature within the cylinder normalized by the reference intake temperature $T_{\text{ref}} = 308\text{K}$ versus the distance from the cylinder bounding walls normalized by the radius of the bore r_C. However, it should be noted that the spark plug is not treated as a wall in this analysis. The plot reveals a dense streak of scattered values for the low temperatures, which is assumed to be a consequence of the nearly constant temperature during the intake stroke. As the tracer particles move completely freely, they cover major parts of the geometry and hold all possible distances from the cylinder wall. This changes, however, when the compression starts and the intake valves close, as the temperature then increases. Hence, the temperature during the compression stroke may also be seen as a measure of time. With ongoing compression, the tracked particles hold larger distances from the walls, as they slowly converge towards the location of the spark plug. Particles being transported too close to the wall or near the crevice region get stuck in stagnant regions and can not be picked up again by the tumble vortex. Therefore, these particles will not reach the spark plug. Yet, the highest density is not achieved at a value of unity, as the spark plug is located slightly off-centered from the cylinder axis.

At each cycle, a bounded scalar of the value of unity is seeded at the inflow boundary within the intake manifold, while the scalar field of the residual gas within the cylinder is assigned to a value of zero. This scalar is transported passively as described earlier by Eq. 9.4 and may be used in a similar manner as quantities such as the fresh residual gas mixture, fuel

mixture fractions or chemical tracers. The tracer particles experience the field of the passive scalar on their path through the cylinder and the recorded values can be found in Fig. 9.15. The curves of the single particles are colored using high transparency to move the focus from the single particles' behavior to the collective behavior of the particles. The particles seeded within the intake manifold undergo scalar values of unity, as can be seen by the horizontal line during the particle seeding time. The particles seeded at earlier CA quickly encounter scalar values near zero, as indicated by the steep jump of the curves. Consequently, mixing within the cylinder proceeds and increases the overall scalar value within the cylinder, which ultimately leads to smaller jumps when the particles leave the intake manifold. This leads to the displayed convergence of each curve, which is underlined by the increasing density of the curves. The graph also reveals the present homogeneity of the mixture when assuming the particles spread widely over the cylinder, which is confirmed by Fig. 9.8. As the curves converge to a very narrow range of values between 0.8 and 0.85, the scalar distribution may be assumed to be homogeneous.

To investigate the relation between location and scalar value for a set of selected tracers reaching the spark plug, Fig. 9.16 displays the streamlines colored by the scalar value ϕ and their absolute time derivative $\partial\phi/\partial t$. The graph starts with values of unity as shown in Fig. 9.15. However, a few trajectories with a dark blue color can be observed and it is likely that these belong to the first particles seeded in the cycle. The particles are seeded inside the intake manifold and ride along the fluid, which is initialized with scalar values of unity. Figure 9.15 reveals a quick transition from the scalar values to the value of final mixture, which can also be observed visually in Fig. 9.16, as there is only a small region of green values around the valve plate. Therefore, it is concluded that this is where major mixing processes occur. To investigate the scalar mixing, the time derivative of the scalar experienced by each tracer particle is visualized along the spatial trajectories in the lower section of Fig. 9.16. The gradient is multiplied with the reference timescale $t_0 = 1s$ to non-dimensionalize the graph. As expected, the strongest mixing occurs in the jet leaving the valve gap. Further, small kernels with a low-high-low gradient transition can be observed on single tracer trajectories, especially on the ones which reach deep into the cylinder. Only weak gradients are revealed near the spark plug and between the valves as well as below the valves, which is interpreted as a result of little mixing after the intake valves have closed.

To further investigate the correlations between the passively transported scalar and other quantities, scatter-plots obtained from the trajectories are shown. Figure 9.17-a) assesses the correlation between the passive scalar and the resolved kinetic energy. The transparency of the markers is chosen to highlight the collective behavior of the tracers. Furthermore, the scalar values range between the bounds of 0 and 1. From a temporal point of view (with Fig. 9.15), the plot is formed from the edges on the left and right side to the center. At the

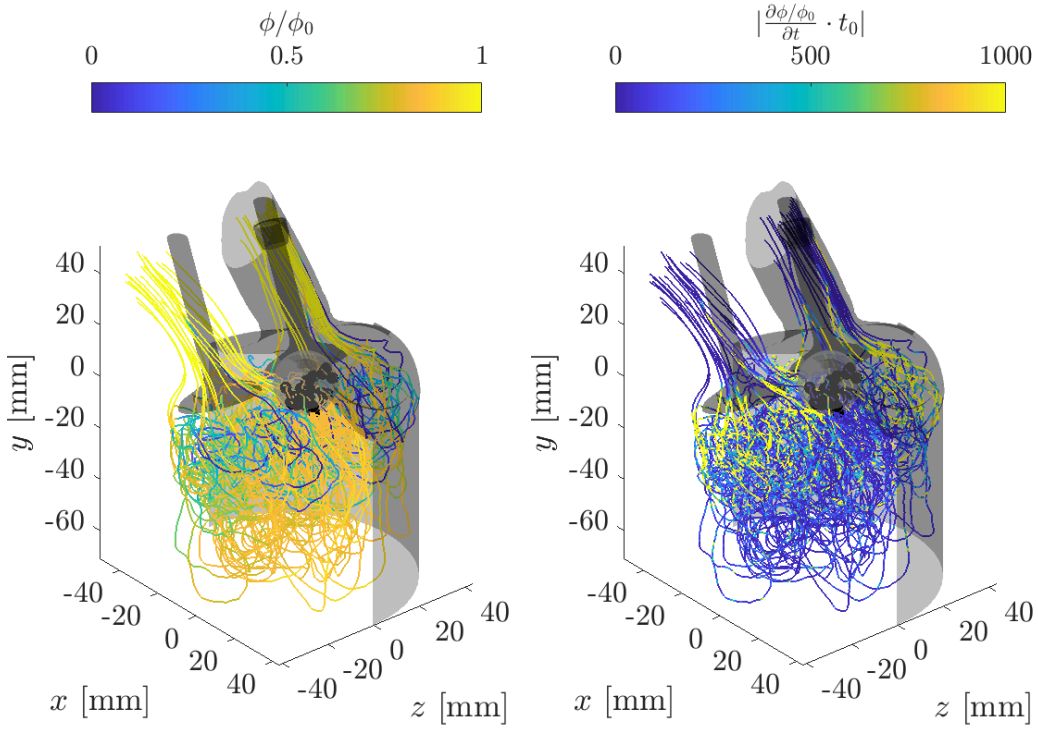

Figure 9.16 Experienced passive scalar and experienced passive scalar time derivative by the tracer particles for a set of trajectories.

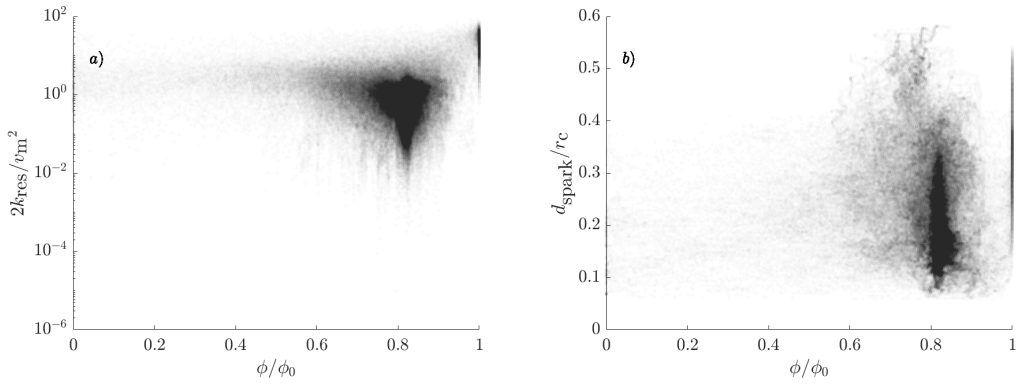

Figure 9.17 a) Scatter-plot of the experienced passive scalar versus resolved kinetic energy. b) Experienced passive scalar versus normalized distance to spark plug.

beginning of the cycle, only scalar values of zero in the cylinder and values of unity at the inflow boundary exist. The thin zone on the right-hand side with scalar values of unity and the highest energies is a result of the particles traveling through the intake manifold and valve gap. In this region, only fresh fluid is present and high velocities occur. Subsequently, the passive scalar on the left side increases steadily due to the proceeding mixing within the cylinder. The scalar values of zero vanish quickly, which can also be seen in the very low color intensity within the graph and in the temporal history of the experienced scalar by the tracers in Fig. 9.15. The low scalar values also only occur for the highest kinetic energies, implying that the particles still hold a high kinetic energy from reaching the cylinder through the valve gap more recently. The values then approach the center of the scatter-plot from both sides and form a more color-intensive region for scalars between 0.6 and 0.9. This range narrows down to a final scalar value of 0.8, which is achieved in late-stage compression and also indicated by a larger range of energies. This agrees with Fig. 9.15 and is assumed to be a consequence of the tumble breakdown, which produces turbulent structures of medium and smaller scale and hence, lowers the kinetic energy of the particles. As the flow during the compression stroke is governed by the large tumble vortex feeding energy to smaller turbulent structures, the presence of smaller and medium sized structures at earlier times is revealed by the spikes towards lower energies in the interval between 0.6 and 0.9. However, the spikes show rather low color intensity, which is a consequence of the flow being dominated by the large structures, which are rich in energy, and the interaction of the particles with the smaller structures being comparably small.

In Fig. 9.17-b) the correlation between the experienced passive scalar and the tracer particles' distance from the spark plug is presented in the form of a scatter plot. Again, a similar behavior can be observed for the scalar component, as the kernel in the center of

the graph is formed by the tracers undergoing progressive mixing. The kernel reveals high color intensity for a range of distances from the spark plug, which indicates a good mixture homogeneity for the late-stage compression.

9.6 Summary

An efficient Lagrangian particle-based method for causal back-tracing of physical phenomena was proposed and evaluated. Simulations of the Darmstadt optically accessible engine under motored operation were performed and compared with experimental results at different CA. Good agreement was achieved and a valid basis for the investigation of the proposed method was formed. The performed LES captured the physics of the internal aerodynamics sufficiently and the proposed method was used for further analysis. Spatial particle trajectories were investigated and the influence of the seeding location on the success rate of the particles to reach the spark plug was analyzed. The travelled distance, passive scalar values (representing residual gas) and the experienced kinetic energy were used to interpret the tracer trajectories. It was found that the regions on a diagonal line through the manifolds are most likely to produce particles reaching the spark plug. The flexibility of the presented method allows for future studies on the causation of various phenomena such as injection or knock.

Acknowledgments

The authors gratefully acknowledge the financial support through the state of North Rhine-Westphalia and the computational resources of the Center for Computational Sciences and Simulation (CCSS) of the University of Duisburg-Essen. Further computational resources for this project were provided by the Gauss Centre for Supercomputing/Leibniz Supercomputing Centre under Grant No. pn68nu. Support by the German Research Foundation (Deutsche Forschungsgemeinschaft–DFG) FOR-2687 “Cyclic variations in highly optimized spark-ignition engines: experiment and simulation of a multi-scale causal chain” – project numbers 423192870 and 423224402 – is kindly acknowledged.

Data Availability Statement

The data that support the findings of this study are available from the corresponding author upon reasonable request.

10 Cyclic variations in the flame propagation in a spark-ignited engine: multi cycle Large Eddy Simulation supported by imaging diagnostics

Authors: L. Engelmann, J. Laichter, P. Wollny, M. Klein, S. Kaiser, A. Kempf

This chapter including all figures and tables was previously published in *Flow, Turbulence and Combustion: L. Engelmann, J. Laichter, P. Wollny, M. Klein, S. Kaiser, A. Kempf, Cyclic variations in the flame propagation in a spark-ignited engine: multi cycle Large Eddy Simulation supported by imaging diagnostics, 2023; 110: 91-104* and is reprinted with permission from Springer. L. Engelmann developed the software for the presented simulations and the post-processing, performed all calculations, wrote the manuscript and generated all figures and tables. The experimental measurements were performed by J. Laichter. P. Wollny, M. Klein, S. Kaiser and A. Kempf contributed corrections, discussions and proofreading.

Abstract

Experimental measurements and multi-cycle Large Eddy Simulation (LES) are performed in an optically accessible four-stroke spark-ignition engine to investigate Cycle-to-Cycle Variations (CCV). High-speed combustion imaging is used to measure the early flame propagation and obtain the flame radius and centroids. Large Eddy Simulation generates data-bases for the flame propagation as well as the kinetic energy in the cylinder and confirms the observations from the two-dimensional fields by three-dimensional simulation results. Experiment and simulation are compared with respect to the strength and distribution of CCV. Both approaches reveal CCV causing similar statistics of maximum pressures and combustion speeds. The cycles are categorized as slow and fast cycles using the crank angle of ten percent burnt fuel-mixture. Analysis of the flame centroids shows that slow cycles move further towards the intake-side of the engine compared to fast cycles. The kinetic energy during combustion is averaged for the slow and fast cycles based on the samples being

in unburnt and burnt mixture. Studying the kinetic energy level in the unburnt and burnt mixture reveals higher turbulent kinetic energy for the fast cycles as well as larger separation between the global kinetic and the turbulent kinetic energy for the slow cycles, providing evidence for a source of the CCV variations observed in this engine.

10.1 Introduction

Cycle-to-Cycle Variations (*CCV*) form a major uncertainty and obstacle for achieving better power and lower pollutant output from internal combustion engines, resulting in a high demand to further the understanding of their origin. It is expected that inhibiting or manipulating the variation of the mixture-quality and flame development could reduce the potential of misfire and abnormal combustion, as well as improve the overall combustion performance [198, 235].

Multiple sources for CCV exist, including the in-cylinder flow processes, the formation of the mixture, the evolution of the early flame kernel and the flame propagation. The flame propagation was object of detailed experimental [174, 4, 5, 204] studies. Deviations in the early flame kernel development and flame propagation are considered to cause up to 50% of the CCV [105, 273]. The early flame kernel is sensitive towards the flow field, and different modes of combustion may appear, depending on the operating conditions of the engine [203]. Turbulence may be considered a crucial phenomenon driving CCV, not only by controlling the speed of combustion due to flame wrinkling, but also by introducing small-scale variations to the flow field, influencing the mixing-process and flame-propagation.

Three-dimensional Large Eddy Simulation (*LES*) forms a suitable and mature tool to complement the experimental analysis, especially in the context of CCV. High-fidelity LES was performed by Vermorel et al. [289, 290], Kazmouz et al. [116], and Richard et al. [228], as well as Goryntsev et al. [87, 89] demonstrating the suitability of LES for analyzing CCV in engine combustion.

In addition to classic pressure-based metrics, such as heat release analysis or multi-dimensional measures, further metrics were introduced in the recent years to characterize CCV relying on different data input. A bivariate 2D empirical-mode-decomposition was employed by Sadeghi et al. [242] to identify CCV within the in-cylinder 2D flow fields. Jung et al. [115] showed that the spark discharge energy and the in-cylinder turbulence level influence the combustion stability. Hanuschkin et al. [92] followed a machine-learning based approach to predict high- and low-energy cycles by analyzing the shape and position of the early flame kernel. A joint evaluation of flow fields and heat-release data was performed by Zeng et al. [313] to quantitatively compare the difference in flow and flame development between fast and slow burning cycles. The different approaches taken to investigate CCV are due to its complexity and suggest that both experimental and numerical techniques are required to further its understanding.

This chapter was previously published in Flow, Turbulence and Combustion and is reprinted with permission of the journal.

This work studies the CCV of the flame propagation in an optical research engine in a joint approach of experimental observations and simulation data. A port fuel-injection (*PFI*) strategy was used to allow for a high homogeneity of the fuel-air mixture. Thus, mixture effects on the flame may be neglected. This reduces the number of phenomena influencing the CCV. This study focuses on the turbulent effects on the early flame-propagation. In a first step, pressure traces and flame-radii will be analyzed to ensure a reliable basis. Then, the early evolution of the flame and the turbulence level in the cylinder will be investigated.

10.2 Methods

10.2.1 Experiments

The measurements and simulations were conducted for an optically accessible four-stroke single-cylinder SI engine with port fuel-injection. The engine was operated at 1500 rpm, using iso-octane as fuel. Table 10.1 summarizes the operating conditions. Optical access is provided by a flat piston window and a quartz glass cylinder liner. In the experiments, to minimize the potential influence of residual gas on CCV and to decrease the thermal load, each fired cycle was followed by two motored cycles. Combining three subsequent measurements of 71 fired cycles lead to a data set of 213 cycles with short interruptions in between. The pressure was measured using a piezoelectric pressure sensor. A high-speed camera captured the line-of-sight integrated combustion luminosity (CH*) at a frame rate of 43 kHz. To extract the apparent burnt area the images were segmented by a predictor-corrector scheme [258]. Afterwards the equivalent flame radius was calculated [4, 5]. With a field-of-view (*FOV*) of 23 x 34 mm, only the region around the spark plug was imaged, and the recording was performed from ignition timing at -20°CA until $+5$°CA[1].

10.2.2 Simulation

Corresponding computations were carried out with the inhouse LES-solver *PsiPhi*. The Favre-filtered conservation equations for mass, momentum, total internal energy, flame-progress variable and mixture fraction were solved in a density-based framework. The finite volume method was used to discretize the equations on an isotropic equidistant grid of 0.39 mm size and a total of 38 Mio. cells. Convective fluxes were interpolated with an eighth-order central differencing scheme (*CDS*) supported by a tenth-order filter for momentum, at Mach numbers below 0.2. The CDS fluxes were blended linearly with a total variation diminishing (*TVD*) scheme with the non-linear CHARM limiter for $0.1 < \mathrm{Ma} < 0.2$ and the full TVD fluxes were used for higher Mach numbers. Scalar fluxes were discretized using TVD. Time integration was performed with a low-storage third order Runge–Kutta scheme. The boundaries were

[1]This work assigns 0°CA to compression top-dead centre, i.e., crank angles during intake and compression are negative.

This chapter was previously published in Flow, Turbulence and Combustion and is reprinted with permission of the journal.

Table 10.1 Engine operating conditions.

Engine speed	1500 rpm
Bore	84 mm
Stroke	90 mm
Compression ratio	9 : 1
Intake valve open (IVO)	316°CA
Intake valve close (IVC)	−112°CA
Exhaust valve open (EVO)	252°CA
Exhaust valve close (EVC)	−326°CA
Ignition timing	−20°CA
Fuel	Iso-octane
Relative air/fuel ratio	1.1
Intake pressure	1 bar
Intake temperature	328.15 K
IMEP	7.7 bar
COV of IMEP	1%

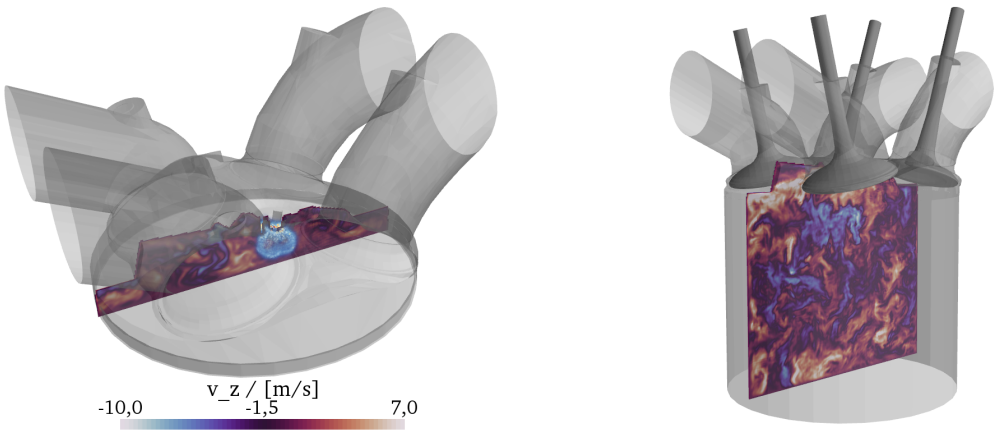

Figure 10.1 Computational domain included in the simulation. Top: flame kernel and image-normal velocity during early combustion phase (−17°CA). Bottom: image-normal velocity component during intake stroke (−120°CA).

This chapter was previously published in Flow, Turbulence and Combustion and is reprinted with permission of the journal.

treated using the Navier-Stokes Characteristic Boundary Conditions, supplied by pressure measurements inside the intake manifold and velocities obtained from GT-Power calculations for the corresponding target values. The extend of the ports included into the computational domain is shown in Fig. 10.1. All walls and moving parts of the engine follow a Lagrangian-Particle and immersed boundary-based framework first described by Nguyen et al. [191]. The Sigma model by Nicoud et al. [192] with $C_\mathrm{m} = 1.5$ was employed to take into account the subfilter transport along with a turbulent Schmidt number of $\mathrm{Sc_t} = 0.7$. The simulation was performed over a total of 30 cycles for sampling, discarding the first two cycles to not include initial transient effects (different numbers of cycles for sampling can be found in literature, typically ranging between 10 and 30 [289, 89, 191, 295]). To reduce costs and reproduce the effect of the skip firing, the cycles were simulated consecutively without ignition. The fired results were obtained from restarting and running the simulation separately from short before ignition. Overall up to two cycles have been achieved on 1024 cores within 24 hours, offering a good speed for an engine LES.

10.2.3 Combustion Modeling

The Flame-Surface Density (*FSD*) approach is employed within this work. FSD models aim for the closure of the combined filtered laminar diffusion and reaction rate term using a transport equation for the reaction progress variable c. The reaction progress variable ranges between values of zero and unity, indicating fully unburnt mixture and completely burnt mixture, respectively. In this study, the Favre-filtered reaction progress variable c is transported using

$$\begin{aligned}\frac{\partial \overline{\rho}\tilde{c}}{\partial t} + \frac{\partial \overline{\rho}\tilde{c}\tilde{u}_\mathrm{j}}{\partial x_\mathrm{j}} + \frac{\partial \overline{\rho}\left(\tilde{c}\tilde{u}_\mathrm{j} - \widetilde{cu_\mathrm{j}}\right)}{\partial x_\mathrm{j}} \\ = \overline{\frac{\partial}{\partial x_\mathrm{j}}\left(\rho D \frac{\partial c}{\partial x_\mathrm{j}}\right) + \dot{\omega}_c}\end{aligned} \tag{10.1}$$

with the diffusivity D and the reaction rate $\dot{\omega}_c$. The Favre filtering of a general quantity Q is denoted as $\tilde{Q}$ and the LES filtering as $\overline{Q}$, respectively. The unclosed reaction and diffusion terms may be rewritten using the flame-surface density

$$\overline{\frac{\partial}{\partial x_\mathrm{j}}\left(\rho D \frac{\partial c}{\partial x_\mathrm{j}}\right) + \dot{\omega}_c} = \overline{(\rho_0 s_\mathrm{d})}_\mathrm{s} \Sigma_\mathrm{gen} \tag{10.2}$$

where ρ_0 indicates the unburnt density, s_d the flame displacement speed on the flame surface s and the generalized flame-surface density Σ_gen, which combines the diffusion and source terms. A popular choice to calculate Σ_gen is a modified transport-equation based model by Colin and Truffin [43], which takes into account the subgrid-behavior of the early flame kernel. The numerical framework used in the present study relies on the algebraic model by

This chapter was previously published in Flow, Turbulence and Combustion and is reprinted with permission of the journal.

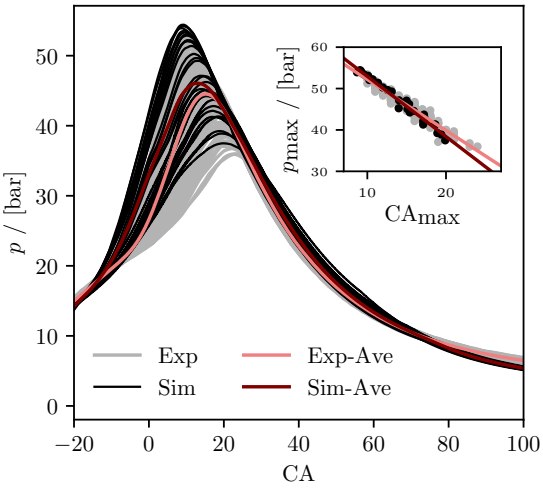

Figure 10.2 Experimentally and numerically obtained pressure traces from all cycles. Averages are given by the colored lines. The insert shows the correlation between the peak pressure and the crank angle at which peak pressure occurs.

Muppala et al. [187]. Following this modeling philosophy, the flame-surface density may be approximated as

$$\overline{(\rho_0 s_\mathrm{d})}_\mathrm{s} \Sigma_\mathrm{gen} \approx \rho_\mathrm{u} s_\mathrm{l} \Xi |\nabla \tilde{c}| \tag{10.3}$$

The model gives the wrinkling factor Ξ based on

$$\Xi = \left(1 + \frac{0.46}{\mathrm{Le}} \mathrm{Re}_\Delta^{0.25} \left(\frac{u'_\Delta}{s_\mathrm{l}}\right)^{0.3} \left(\frac{p}{p_0}\right)^{0.2}\right) \tag{10.4}$$

with the Lewis number Le assumed as unity, the laminar flame speed s_l and the pressure p. Here p_0 represents the ambient pressure. Re_Δ refers to the turbulent Reynolds number that can be rewritten using the turbulent lengthscale l_t and the laminar flame thickness δ_l as $\approx 4\,(l_\mathrm{t}/\delta_\mathrm{l})\,(u'_\Delta/s_\mathrm{l})$. The turbulent lengthscale in the context of LES is assumed as $l_\mathrm{t} = \Delta$. The subfilter velocity fluctuations u'_Δ are calculated using the $OP1$ formulation following Colin et al. [44]. The laminar flame speed s_l and flame thickness δ_l are obtained from tabulation, which was generated using calculations of one-dimensional freely propagating flames with varying pressure, temperature and equivalence ratio in Cantera [86]. The ignition was simulated by initializing a spherical kernel of burnt gas of 1.5 mm radius at the spark plug.

This chapter was previously published in Flow, Turbulence and Combustion and is reprinted with permission of the journal.

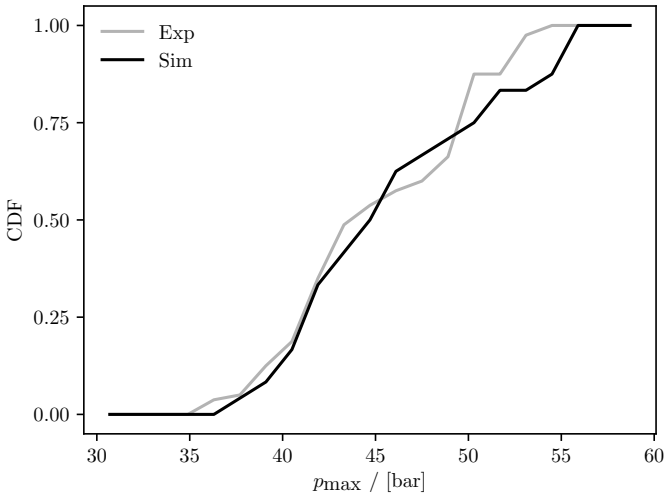

Figure 10.3 Experimentally and numerically obtained cumulative distribution function of peak pressures from all cycles

10.3 Results

10.3.1 Comparison of experimental and numerical indicator quantities

Figure 10.2 shows the experimental and numerical pressure traces over the crank angle interval of combustion. The overall agreement of the traces is good, even if the slowest cycles are not fully reproduced by the simulation. The crank angle of the maximum pressure shifts with the peak pressure-value, as indicated by the insert in Fig. 10.2. Linear regression lines were obtained by the least-squares method for the measured and simulated results and are displayed as lines. The scatter around the regression lines shows only little deviation, which was found to indicate stable combustion cycles [175]. The slope of the numerical data is slightly below that of the experiments. The lack of predictability of the slow cycles is a known topic in engine simulation. A common practice is the use of one-step chemistry for combustion modeling due to its robustness and efficiency, some works even applying sophisticated additional modeling for the capture of the spark and early flame development, that as a drawback have several sensitive calibration parameters. However, a shortcoming of these models is their incapability to capture the sensitive chemistry, in particular after ignition. It is possible that a spark model might improve the prediction of the slow cycles although even works including this philosophy revealed difficulties with this issue [228, 282, 295].

In Fig. 10.3, the cumulative distribution function (CDF) for the experimental and numerical samples is presented. The CDF reveals that the simulation indeed manages to predict some of the weaker cycles. The agreement between the measured and simulated CDF may be seen as an indicator for the simulation to contain a sufficient amount of cycles to allow for a reasonable comparison with the experiment.

This chapter was previously published in Flow, Turbulence and Combustion and is reprinted with permission of the journal.

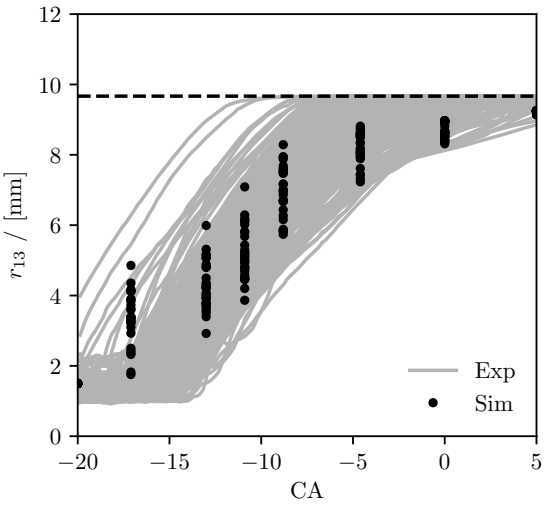

Figure 10.4 Experimentally and numerically obtained equivalent flame radii, calculated from the two-dimensional projection along the camera line-of-sight axis. The maximum flame radius produced by the simulation is indicated by the dashed line.

Figure 10.4 presents the values of the equivalent flame radius obtained from experiment and simulation. The experiments yield the line-of-sight integrated light emissions within the flame and the burnt gases. The projected area A_{2D} of the two-dimensional region was calculated, and the equivalent radius of a circle of the same area was computed as $r = (A_{2D}/\pi)^{0.5}$. In the simulation, the progress variable field was projected in the same direction, and the resulting image was processed following the same procedure. The initial radii appear constant within the first crank angles. This is a consequence of the overexposure caused by the ignition spark and the size of the initialized flame-kernel in the simulation. After approximately four crank angle degrees – which may be interpreted as the time of the early flame kernel development – the flame radii increase but with substantial variation across the cycles. The spreading weakens as parts of the flame run into less turbulent regions closer to the cylinder wall. Eventually, the flame encounters the wall, where further growth is inhibited. The simulation exhibits somewhat stronger growth for the earlier crank angles and slower growth for the later crank angles compared to the experiment. The strong initial growth might be partially caused by the employed combustion model. A similar behavior was discussed by Colin and Truffin [43], who proposed a modification to better consider the initial flame curvature in the context of transported FSD-type models.

In Fig. 10.5, the equivalent flame radius r_{13} 13°CA after ignition (calculated using the projected aria in the imaging region as discussed in the previous paragraph) is plotted versus the crank angle CA_{10}, at which ten percent of the fuel mass are burnt. The figure reveals a linear decrease of the flame radius and CA_{10} for experimental and numerical results. While the slope is similar, with a slight underprediction indicating smaller CA_{10}, the numerical

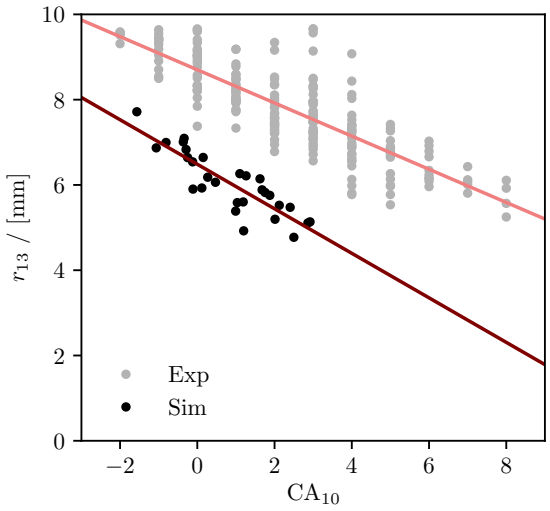

Figure 10.5 Correlation between the equivalent flame radius r_{13} 13°CA after ignition and the crank angle CA_{10} of 10% percent fuel mass burnt for the experiment and the simulation.

values are shifted towards lower radii, as also shown by the linear regression lines. This, in comparison with the experiment, may be interpreted as the simulation slightly underpredicting the flame speed. Considering the findings from Fig. 10.2, the correlation confirms that the simulation is struggling with reproducing the slowest cycles.

The metrics presented in Fig. 10.5 form the foundation for the classification of *slow* and *fast* cycles. The equivalent flame radius at 13°CA after ignition is an optically measured quantity, which indicates the quality of the combustion and correlates with the pressure. Both r_{13} and CA_{10} form a plausibility check for properly capturing the combustion physics in the experiment and simulation [4, 5]. The value of CA_{10} is chosen to identify the slowest and fastest of the obtained cycles. As the propagation speed of the flame is crucial for the combustion of ten percent fuel mass, the terms *slow* and *fast* were chosen.

10.3.2 Flame propagation and kinetic energy

Figure 10.6 shows the volume-rendered flame surface density Σ_{gen} projected along the cylinder axis and the camera line-of-sight. The figure shows the averages, which were obtained for the five fastest and slowest cycles. The images show crank angles until 30°CA to give insight into the progression of the flame through the cylinder. It can be seen that the flames in the fast cycles (columns two and four) are significantly faster than in the slow cycles (columns one and three), showing almost complete combustion at 20°CA already. The flames are initialized as a spherical kernel at the time of ignition. The flame then propagates and exhibits progressive wrinkling with increasing crank angle. The flames are not fully circular but oval-shaped, which causes the flame to take more time to reach the left side of the cylinder walls.

This chapter was previously published in Flow, Turbulence and Combustion and is reprinted with permission of the journal.

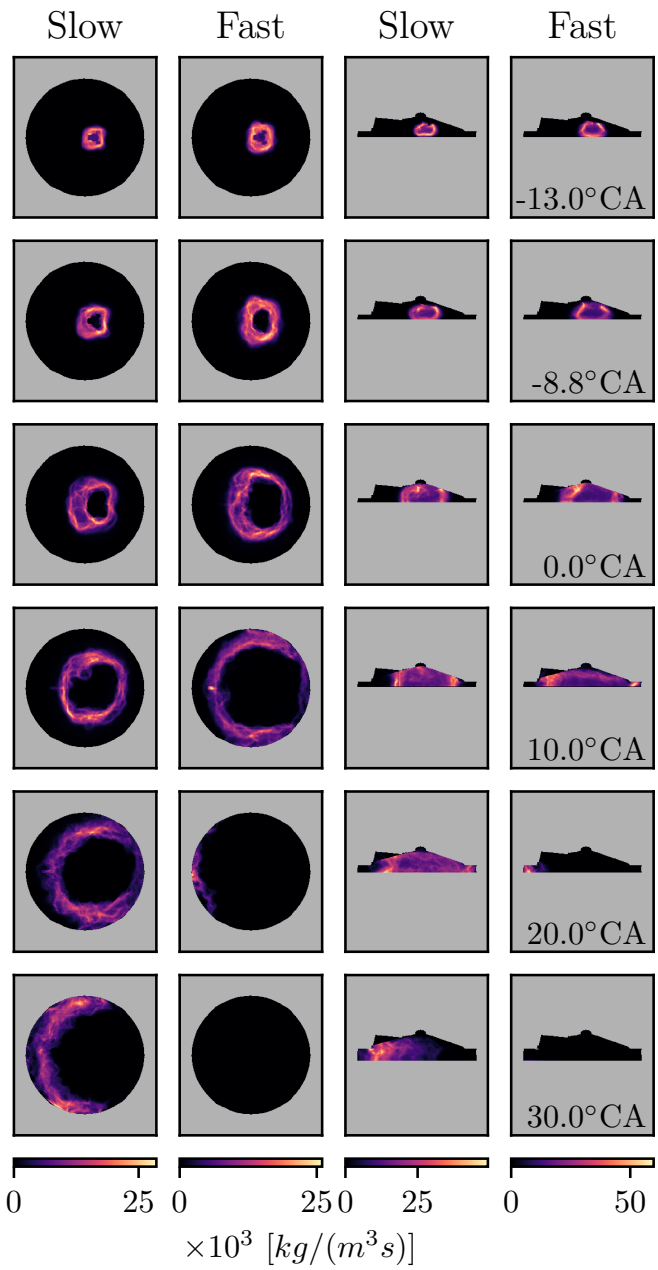

Figure 10.6 Average of the volume-rendered flame surface density Σ_{gen} projected along the cylinder axis (left column) and the camera line-of-sight (right column) for different crank angles visualizing the progress of combustion. The averaging was performed using slow and fast cycles separately.

This chapter was previously published in Flow, Turbulence and Combustion and is reprinted with permission of the journal.

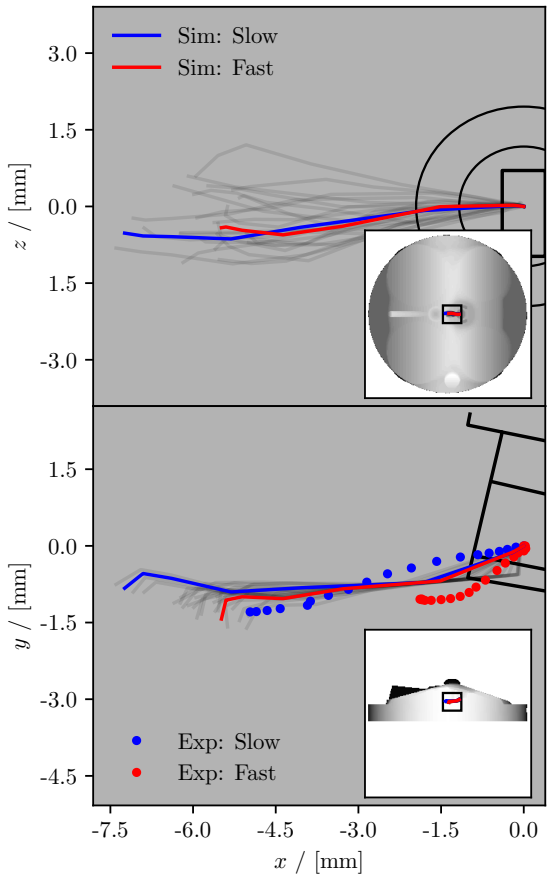

Figure 10.7 Experimentally and numerically obtained centroids of the flame for crank angles up to 10°CA after TDC conditioned for slow and fast cycles.

This chapter was previously published in Flow, Turbulence and Combustion and is reprinted with permission of the journal.

Fig. 10.7 presents the projections of the flame centroids obtained from experiment and simulation. The viewing direction is indicated by the insert in the bottom right corner. The location and size of the region shown in the figure is given by the rectangle within the insert. The coordinate axis are moved to give values of zero at the location of ignition. The experimental centroids are only found in the lower graph, due to lack of information about the third dimension. The mean for the centroids of the slowest and fastest cycles were obtained and are displayed by blue (slow) and red (fast) lines. The lines start at the spark plug and extend towards the left side, as also observed from Fig. 10.6. The centroids overall behave symmetrically in the z direction, only deviating by a millimeter. The flame centroids move in negative y direction. The flames of the slow cycles travel further to the left than the fast cycles. The slow cycles travel significantly further in the direction of negative x values than in the experiment. The difference between fast and slow cycles, however, is similar. In both experiment and simulation, the centroids of the weaker cycles traveled further. One should note, however, that the centroids are a sensitive and challenging quantity to assess. Overall, some deviations between the experiment and the simulation can be observed. Possible reasons for these deviations are the predicted flow field and the flame propagation as a result of the interaction of several numerical aspects including subgrid modeling, grid resolution, reaction modeling and discretization. Other potential causes are the precision of the experimental boundary conditions, the timing of ignition or the errors involved in the imaging of the flame kernel.

Figure 10.8 shows the kinetic energies during the early combustion phase, using different sampling methods. The figure shows the volume-averaged global kinetic energy (GKE) $k_\mathrm{g} = \int \tilde{u}_\mathrm{i}\tilde{u}_\mathrm{i}/2 \; dV/V$ and the turbulent kinetic energy (TKE) $k_\mathrm{t} = \int u'_\mathrm{i}u'_\mathrm{i}/2 \; dV/V$ with the velocity fluctuation $u'_\mathrm{i} = \tilde{u}_\mathrm{i} - \langle\tilde{u}_\mathrm{i}\rangle$ based on the instantaneous velocity $\tilde{u}_\mathrm{i}$ and the phase-averaged velocity $\langle\tilde{u}_\mathrm{i}\rangle$, which were obtained using the entire three-dimensional domain (denoted 3D) and a two-dimensional slice in the central tumble plane of the cylinder (2D). The employed definition of TKE using the phase-average differs from the classical definition, as it may include coherent structures that vary from cycle to cycle. The energies were calculated with and without using the image-normal velocity component v_z ($v_\mathrm{x,y,z}$ and $v_\mathrm{x,y}$). Also, the statistics are conditioned by using the energies in the fresh gas mixture $Y_\mathrm{C} = 0$ for the first set and the energies of the burnt gas $Y_\mathrm{C} = 1$ for the second set to perform the averaging. The colored values are the averages of the five fastest (red) and slowest (blue) cycles, the rest indicates the remaining cycles (grey). All values are obtained from the simulation.

Overall, the fast cycles exhibit higher TKE than the slow cycles, indicating stronger turbulence within the flow field, which potentially speeds up the flame propagation and causes the fast cycles. The slow cycles feature a higher separation between the GKE and TKE. This may be interpreted as a poorer distribution of the overall energy between the turbulent and large scale structures. As a result, the energy of the turbulent structures is

This chapter was previously published in Flow, Turbulence and Combustion and is reprinted with permission of the journal.

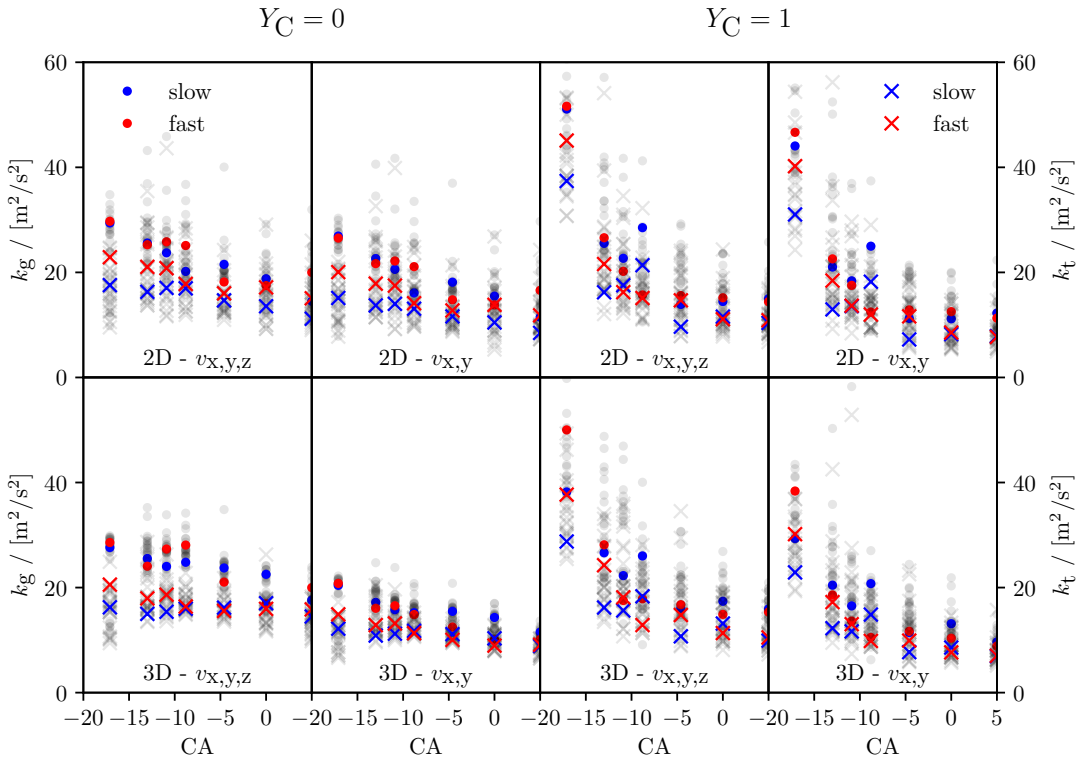

Figure 10.8 Simulated global kinetic energy k_g (dots) and turbulent kinetic energy k_t (crosses) during early combustion for all cycles, as well as averaged for fast and slow cycles based on different sampling methods: Conditioned for a progress variable Y_C of 1 and 0 for the whole domain (3D) as well as the central tumble plane (2D).

This chapter was previously published in Flow, Turbulence and Combustion and is reprinted with permission of the journal.

comparably smaller, which leaves less turbulence to increase the flame speed than in the fast cycles. The GKE of the fast and slow cycles has similar values, revealing turbulence to be the main driver of the observed CCV. While few differences for the GKE between fast and slow cycles can be found, it is expected that a greater number of simulated cycles will reduce these differences further. Consideration of the image-normal velocity component only slightly increases the amplitudes of the shown energies without any change of the qualitative findings, as only minor transport can be expected along the tumble axis. This indicates that the typically two-dimensional experimental imaging techniques would capture similar physics without significant loss of information for this setup.

For the samples within the unburnt mixture, the energy values obtained from the 2D slice appear more scattered than for the 3D sampling. This results from the 3D sampling being based on more samples and including regions nearby walls, where the flow field energy is dampened. The decrease of GKE and TKE using the unburnt samples is low compared to the burnt samples, which is assumed to be a consequence of the high density and low viscosity. The GKE is overall decreasing until TDC for fast and slow cycles, which is assumed to be a result of the tumble collapse and the decay of directed flow as a consequence thereof. In the curves including the image-normal velocity component, the decrease between -15 and -5°CA is interrupted by a slight increase of GKE, which is assumed to be a consequence of the tumble collapse, leading to a less organized rotational but more unordered flow. The TKE of the slow cycles remains constant. The fast cycles reveal decreasing TKE with increasing crank angle. This might indicate that the fast cycles have experienced a stronger conversion of GKE to TKE during the tumble collapse, which is now dissipating.

The samples conditioned for the burnt mixture exhibit decreasing energies with increasing crank angle. This implies strong turbulence around the spark plug. The strong decay of energy is interpreted as a consequence of the ongoing tumble collapse. The separation between the GKE and TKE fades with increasing crank angle.

10.4 Conclusion

In the present study, the cyclical variation of the flame propagation in a port fuel-injected, spark-ignited engine was studied by experiment and simulation. The pressure traces revealed that both experiment and simulation are in good agreement for the peak pressure and its timing. The flame radii evolved at a similar rate. The burnt fuel fraction was used to classify slow and fast cycles.

The second part investigated the flame surface density terms for slow-burning and fast-burning cycles, revealing a notable difference in the flame speeds. The simulated flame was found to burn in an oval shape. Trajectories of the flame centroids showed that the flame is traveling towards intake ports. Interestingly, the flame moved further in the slow cycles, consistently in simulation and experiment. Finally, the global kinetic energy and turbulent

This chapter was previously published in Flow, Turbulence and Combustion and is reprinted with permission of the journal.

kinetic energy was evaluated separately for slow and fast cycles, using samples of the unburnt and burnt mixture to examine if the turbulence affects the strength of a cycle. Negligible qualitative differences were observed between a two and three-dimensional sampling space, indicating that for this configuration the same findings can be made using either two or three-dimensional diagnostics. It was also found, that the differences between turbulent kinetic energy and global kinetic energy are larger for slow than for fast cycles. As expected, fast cycles were found to higher turbulent kinetic energies than slow cycles. The kinetic energy conditioned on the burned state showed very high initial values, likely due to high turbulence levels at the spark plug.

In this work, the simulation took PFI to simply mean a perfectly homogeneous mixture. In reality, this is not the case, and slight mixture gradients occur that may influence CCV and might have caused some of the difference between experiment and simulation. Overall, the experiment and simulation have succeeded in demonstrating that much of the difference in cycle strength can be explained by the turbulence levels – within the two-dimensional tumble plane and outside of the plane.

10.5 Acknowledgments

The authors acknowledge funding by the Deutsche Forschungsgemeinschaft (DFG, German Research Foundation) within the Research Unit FOR 2687, project numbers 423192870 and 423271400. The authors also gratefully acknowledge the computing time granted by the Center for Computational Sciences and Simulation (CCSS) of the Universitaet of Duisburg-Essen and provided on the supercomputer magnitUDE (DFG grants INST 20876/209-1 FUGG, INST 20876/243-1 FUGG) at the Zentrum fuer Informations- und Mediendienste (ZIM).

This chapter was previously published in Flow, Turbulence and Combustion and is reprinted with permission of the journal.

11 Summary and Conclusion

11.1 Summary

This comprehensive study delved into the impact of subgrid models on the simulation quality of Large-Eddy Simulation using Direct Numerical Simulation, with the aim of providing reliable and accurate results. Through extensive simulations with a range of well-known and recently developed models, as well as without any subgrid models, the suitability of various subgrid models was identified and validated against data from fully- and underresolved Direct Numerical Simulation obtained from an identical numerical framework. The study revealed that the influence of subgrid models on the simulation quality was non-trivial and highlighted the importance of assessing both reactive and non-reactive cases of canonical and lab-scale nature to ensure accurate results.

Furthermore, the study proposed a novel procedure for quantifying simulation quality relying on an entropy-based measure, which was applied to simulations performed at different resolutions. In contrast to several known quality indicators, this proposed measure demonstrated a converging trend with improved simulation quality in both a-priori and a-posteriori studies, which emphasizes its reliability in quantifying simulation quality.

The study also introduced a temporal backtracking method-based on a Lagrangian framework for the reconstruction of fluid parcel paths in turbulent reactive technical systems. The accuracy of this method depends on the quality of the simulation, which was validated by comparing the simulations with experimental data. The proposed method was also compared with known physical phenomena to assess its correctness. Finally, the study found that high-fidelity numerical tools provide a reliable alternative to additional modeling for underresolved physical phenomena, further emphasizing the importance of accurate simulation results.

11.2 Conclusion

The assessment of subgrid models presented in this work is a critical analysis of algebraic approaches in Large-Eddy Simulation. While other possible approaches were outlined, this study focuses on the strengths and weaknesses of the proposed strategies, particularly in terms of the quality of the results and the computational resources invested. However, it's

important to note that the numerical implementation of these algorithms must be considered for a wider application of these models, especially given the variety of codes and frameworks available, which greatly affect the applicability of a model. Thus, the findings of this work are an important contribution to identifying appropriate modeling strategies for a given numerical framework.

The assessment of the grid resolution quality for canonical cases was conducted using simulation data, providing valuable insights into the potential of the proposed approach. Although only trends were observed, the importance of using experimental or simulation data for evaluating simulation quality cannot be overemphasized, particularly given the general lack of experimental data and the high cost of Direct Numerical Simulation. Therefore, further studies in this area should be intensified to improve our understanding of the subject.

The assessment of cyclic variability in spark-ignited optical research engines presented a challenging physics problem that required a high-quality framework to obtain satisfactory results. An essential finding of this study was that high-order numerics can compensate for the use of supplementary models that account for small-scale physics of ignition, underscoring the need for high-fidelity software for simulating turbulent reactive systems. Unfortunately, many simulations of such systems are performed using frameworks primarily designed to maintain numerical stability, which may not lead to satisfactory results, as the predictive abilities of these methods are greatly reduced. To compensate for these impairments, additional modeling often featuring several parameters is employed, leading to simulation results that require calibration with respect to reference data. Such practices are not high-fidelity and render these simulations somewhat redundant. Hence, it is crucial to develop and use high-fidelity numerical frameworks capable of accurately simulating complex phenomena.

Bibliography

[1] K. Abe. An improved anisotropy-resolving subgrid-scale model with the aid of a scale-similarity modeling concept. *International Journal of Heat and Fluid Flow*, 39: 42–52, 2013.

[2] N. A. Adams, S. Hickel, and S. Franz. Implicit subgrid-scale modeling by adaptive deconvolution. *Journal of Computational Physics*, 200(2):412–431, 2004.

[3] J. E. Akin. *Finite element analysis with error estimators: An introduction to the FEM and adaptive error analysis for engineering students.* Elsevier, 2005.

[4] P. G. Aleiferis, A. Taylor, J. H. Whitelaw, K. Ishii, and Y. Urata. Cyclic variations of initial flame kernel growth in a Honda VTEC-E lean-burn spark-ignition engine. *SAE Technical Paper*, 2000-01-1207:1340–1380, 2000.

[5] P. G. Aleiferis, A. Taylor, K. Ishii, and Y. Urata. The nature of early flame development in a lean-burn stratified-charge spark-ignition engine. *Combustion and Flame*, 136(3): 283–302, 2004.

[6] M. M. Ameen, X. Yang, T.-W. Kuo, Q. Xue, and S. Som. LES for simulating the gas exchange process in a spark-ignition engine. In *Internal Combustion Engine Division Fall Technical Conference*, volume 57281, page V002T06A001. American Society of Mechanical Engineers, 2015.

[7] M. M. Ameen, M. Mirzaeian, F. Millo, and S. Som. Numerical prediction of cyclic variability in a spark-ignition engine using a parallel Large-Eddy Simulation approach. *Journal of Energy Resources Technology*, 140(5), 2018.

[8] B. W. Anderson and J. A. Domaradzki. A subgrid-scale model for Large-Eddy Simulation based on the physics of interscale energy transfer in turbulence. *Physics of Fluids*, 24(6):065104, 2012.

[9] D. Anderson, J. C. Tannehill, and R. H. Pletcher. *Computational Fluid Mechanics and Heat Transfer.* Taylor & Francis, 2016.

[10] B. Andersson, R. Andersson, L. Håkansson, M. Mortensen, R. Sudiyo, and B. Van Wachem. *Computational Fluid Dynamics for Engineers.* Cambridge University Press, 2011.

[11] M. R. Archambault. A maximum entropy moment closure approach to modeling the evolution of spray flows, 1999.

[12] S. Arrhenius. Über die Dissociationswärme und den Einfluss der Temperatur auf den Dissociationsgrad der Elektrolyte. *Zeitschrift für physikalische Chemie*, 4(1):96–116, 1889.

[13] S. Arrhenius. Influence of temperature on the rate of inversion of sucrose. *Zeitschritt für Physikalische Chemie*, 4:226, 1889.

[14] R. Balz, G. Bernardasci, B. von Rotz, and D. Sedarsky. Influence of nozzle geometry on spray and combustion characteristics related to large two-stroke engine fuel injection systems. *Fuel*, 294:120455, 2021.

[15] J. Bardina. Improved turbulence models based on Large-Eddy Simulation of homogeneous, incompressible, turbulent flows, 1983.

[16] J. Bardina, J. Ferziger, and W. C. Reynolds. Improved subgrid-scale models for Large-Eddy Simulation. In *13th fluid and plasmadynamics conference*, page 1357, 1980.

[17] A. J. Barlow, P.-H. Maire, W. J. Rider, R. N. Rieben, and M. J. Shashkov. Arbitrary lagrangian–eulerian methods for modeling high-speed compressible multimaterial flows. *Journal of Computational Physics*, 322:603–665, 2016.

[18] G. K. Batchelor. Small-scale variation of convected quantities like temperature in turbulent fluid part 1. General discussion and the case of small conductivity. *Journal of Fluid Mechanics*, 5(1):113–133, 1959.

[19] E. Baum, B. Peterson, B. Böhm, and A. Dreizler. On the validation of LES applied to internal combustion engine flows: Part 1: comprehensive experimental database. *Flow, Turbulence and Combustion*, 92(1-2):269–297, 2014.

[20] P. Beard, J.-M. Duclos, C. Habchi, G. Bruneaux, K. Mokaddem, and T. Baritaud. Extension of Lagrangian-Eulerian spray modeling: Application to high pressure evaporating Diesel sprays. *SAE transactions*, pages 1417–1434, 2000.

[21] J. Bell, M. Day, J. Grcar, and M. Lijewski. Active control for statistically stationary turbulent premixed flame simulations. *Communications in Applied Mathematics and Computational Science*, 1(1):29–51, 2007.

[22] R. W. Bilger, S. H. Stårner, and R. J. Kee. On reduced mechanisms for methane-air combustion in nonpremixed flames. *Combustion and Flame*, 80(2):135–149, 1990.

[23] J. Bode, J. Schorr, C. Krüger, A. Dreizler, and B. Böhm. Influence of three-dimensional in-cylinder flows on cycle-to-cycle variations in a fired stratified disi engine measured by time-resolved dual-plane piv. *Proceedings of the Combustion Institute*, 36(3):3477–3485, 2017.

[24] M. Bonanni, A. Norris, and M. Ihme. Eulerian-lagrangian LES analysis of residence time in a scramjet cavity combustor. *Bulletin of the American Physical Society*, 2022.

[25] J. Boussinesq. Theorie de l'ecoulement tourbillant. *Mémoires de l'Académie impériale des sciences de St. Pétersbourg*, 23:46, 1877.

[26] M. Breuer and W. Rodi. Large-Eddy Simulation of turbulent flow through a straight square duct and a 180 bend. In *Direct and Large-Eddy Simulation I*, pages 273–285. Springer, 1994.

[27] S. Buhl, F. Dietzsch, C. Buhl, and C. Hasse. Comparative study of turbulence models for scale-resolving simulations of internal combustion engine flows. *Computers & Fluids*, 156:66–80, 2017.

[28] M. H. Buschmann and M. Gad-el Hak. Structure of the canonical turbulent wall-bounded flow. *AIAA journal*, 44(11):2500–2504, 2006.

[29] J. C. Butcher. *Numerical methods for ordinary differential equations*. John Wiley & Sons, 2016.

[30] M. Camesasca, M. Kaufman, and I. Manas-Zloczower. Quantifying fluid mixing with the Shannon entropy. *Macromolecular Theory and Simulations*, 15(8):595–607, 2006.

[31] I. B. Celik and O. Karatekin. Numerical experiments on application of Richardson extrapolation with nonuniform grids. *Journal of Fluids Engineering*, 119(3):584–590, 1997.

[32] I. B. Celik, I. Yavuz, and A. Smirnov. Large-Eddy Simulations of in-cylinder turbulence for internal combustion engines: a review. *International Journal of Engine Research*, 2 (2):119–148, 2001.

[33] I. B. Celik, Z. N. Cehreli, and I. Yavuz. Index of resolution quality for Large-Eddy Simulations. *Journal of Fluids Engineering*, 127(5):949–958, 2005.

[34] I. B. Celik, M. Klein, M. Freitag, and J. Janicka. Assessment measures for URANS/DES/LES: an overview with applications. *Journal of Turbulence*, 7:N48, 2006.

[35] S. Chapman and T. G. Cowling. *The mathematical theory of nonuniform Gases: an account of the kinetic theory of viscosity, thermal conduction, and diffusion in gases*. Cambridge University Press, 1970.

[36] F. Charlette, C. Meneveau, and D. Veynante. A power-law flame wrinkling model for LES of premixed turbulent combustion Part I: non-dynamic formulation and initial tests. *Combustion and Flame*, 131(1-2):159–180, 2002.

[37] J. H. Chen, A. Choudhary, B. De Supinski, M. DeVries, E. R. Hawkes, S. Klasky, W.-K. Liao, K.-L. Ma, J. Mellor-Crummey, and N. Podhorszki. Terascale Direct Numerical Simulations of turbulent combustion using S3D. *Computational Science & Discovery*, 2 (1):015001, 2009.

[38] M. Chrigui, J. Gounder, A. Sadiki, A. R. Masri, and J. Janicka. Partially premixed reacting acetone spray using LES and FGM tabulated chemistry. *Combustion and Flame*, 159(8):2718–2741, 2012.

[39] H. Chu, C. Welch, H. Elmestikawy, S. Cao, M. Davidovic, B. Böhm, A. Dreizler, and H. Pitsch. A combined numerical and experimental investigation of cycle-to-cycle variations in an optically accessible spark-ignition engine. *Flow, Turbulence and Combustion*, pages 1–27, 2022.

[40] W. T. Chung, N. Ly, and M. Ihme. LES of HCCI combustion of iso-octane/air in a flat-piston rapid compression machine. *Proceedings of the Combustion Institute*, 2022.

[41] M. Ciardi, P. Sagaut, M. Klein, and W. N. Dawes. A dynamic finite volume scheme for Large-Eddy Simulation on unstructured grids. *Journal of Computational Physics*, 210 (2):632–655, 2005.

[42] R. A. Clark, J. H. Ferziger, and W. C. Reynolds. Evaluation of subgrid-scale models using an accurately simulated turbulent flow. *Journal of Fluid Mechanics*, 91(1):1–16, 1979.

[43] O. Colin and K. Truffin. A spark-ignition model for Large-Eddy Simulation based on an FSD transport equation (ISSIM-LES). *Proceedings of the Combustion Institute*, 33 (2):3097–3104, 2011.

[44] O. Colin, F. Ducros, D. Veynante, and T. Poinsot. A thickened flame model for Large-Eddy Simulations of turbulent premixed combustion. *Physics of Fluids*, 12(7): 1843–1863, 2000.

[45] K. A. Connors. *Chemical kinetics: the study of reaction rates in solution*. Wiley-VCH Verlag GmbH, 1990.

[46] R. Courant, K. Friedrichs, and H. Lewy. Über die partiellen Differenzengleichungen der mathematischen Physik. *Mathematische Annalen*, 100(1):32–74, 1928.

[47] J. Crank and P. Nicolson. A practical method for numerical evaluation of solutions of partial differential equations of the heat-conduction type. In *Mathematical Proceedings of the Cambridge Philosophical Society*, volume 43, pages 50–67. Cambridge University Press, 1947.

[48] A. d'Adamo, S. Breda, S. Fontanesi, and G. Cantore. LES modelling of spark-ignition cycle-to-cycle variability on a highly downsized DISI engine. *SAE International Journal of Engines*, 8(5):2029–2041, 2015.

[49] A. d'Adamo, S. Breda, S. Fontanesi, A. Irimescu, S. S. Merola, and C. Tornatore. A RANS knock model to predict the statistical occurrence of engine knock. *Applied energy*, 191:251–263, 2017.

[50] L. Davidson. Large-Eddy Simulations: How to evaluate resolution. *International Journal of Heat and Fluid Flow*, 30(5):1016 – 1025, 2009. ISSN 0142-727X. The 3rd International Conference on Heat Transfer and Fluid Flow in Microscale.

[51] P. A. Davidson. An introduction to magnetohydrodynamics. *Applied Mechanics Reviews*, 55(6):B114–B115, 2002.

[52] J. Desantes, J. M. García-Oliver, J. Pastor, and J. G. Ramírez-Hernández. Influence of nozzle geometry on ignition and combustion for high-speed direct injection Diesel engines under cold start conditions. *Fuel*, 90(11):3359–3368, 2011.

[53] P. Domingo, L. Vervisch, and K. Bray. Partially premixed flamelets in LES of non-premixed turbulent combustion. *Combustion Theory and Modelling*, 6(4):529, 2002.

[54] D. Dreher, M. Schmidt, C. Welch, S. Ourza, S. Zündorf, J. Maucher, S. Peters, A. Dreizler, B. Böhm, and A. Hanuschkin. Deep feature learning of in-cylinder flow fields to analyze cycle-to-cycle variations in an SI engine. *International Journal of Engine Research*, page 1468087420974148, 2020.

[55] P. Dutt. Stable boundary conditions and difference schemes for Navier-Stokes equations. *SIAM Journal on Numerical Analysis*, 25(2):245–267, 1988.

[56] J.-P. Eckmann and D. Ruelle. Ergodic theory of chaos and strange attractors. In *The theory of chaotic attractors*, pages 273–312. Springer, 1985.

[57] G. K. El Khoury, P. Schlatter, A. Noorani, P. F. Fischer, G. Brethouwer, and A. V. Johansson. Direct Numerical Simulation of turbulent pipe flow at moderately high Reynolds numbers. *Flow, Turbulence and Combustion*, 91(3):475–495, 2013.

[58] B. Enaux, V. Granet, O. Vermorel, C. Lacour, C. Pera, C. Angelberger, and T. Poinsot. LES study of cycle-to-cycle variations in a spark-ignition engine. *Proceedings of the combustion Institute*, 33(2):3115–3122, 2011.

[59] L. Engelmann, M. Klein, and A. Kempf. A-posteriori LES assessment of subgrid-scale closures for bounded passive scalars. *Computers & Fluids*, page 104840, 2021.

[60] L. Engelmann, J. Hasslberger, E. Inanc, M. Klein, and A. Kempf. A-posteriori assessment of Large-Eddy Simulation subgrid-closures for momentum and scalar fluxes in a turbulent premixed burner experiment. *Computers & Fluids*, 240:105441, 2022.

[61] L. Engelmann, M. Ihme, I. Wlokas, and A. Kempf. Towards the suitability of information entropy as an LES quality indicator. *Flow, Turbulence and Combustion*, 108(2):353–385, 2022.

[62] L. Engelmann, J. Laichter, P. Wollny, M. Klein, S. Kaiser, and A. Kempf. Cyclic variations in the flame propagation in an spark-ignited engine: Multi cycle Large-Eddy Simulation supported by imaging diagnostics. *Flow, Turbulence and Combustion*, pages 1–14, 2022.

[63] G. Erlebacher, M. Y. Hussaini, C. G. Speziale, and T. A. Zang. Towards the Large-Eddy Simulation of compressible turbulent flows. *Journal of Fluid Mechanics*, 238:155–185, 1992.

[64] A. Ern and V. Giovangigli. *Multicomponent transport algorithms*, volume 24. Springer Science & Business Media, 1994.

[65] L. Euler. *Institutiones calculi integralis*, volume 1. impensis Academiae imperialis scientiarum, 1792.

[66] A. J. Favre. The equations of compressible turbulent gases. Technical report, AIX-Marseille University Institute Mecanique Statistique de la Turbulence, 1965.

[67] C. L. Fefferman. Existence and smoothness of the Navier-Stokes equation. *The millennium prize problems*, 57:67, 2000.

[68] J. H. Ferziger. Large-Eddy Simulation. In *Simulation and modeling of turbulent flows*. Oxford University Press, 1996.

[69] J. H. Ferziger, M. Perić, and R. L. Street. *Computational methods for fluid dynamics*, volume 3. Springer, 2002.

[70] B. Fiorina, O. Gicquel, L. Vervisch, S. Carpentier, and N. Darabiha. Approximating the chemical structure of partially premixed and diffusion counterflow flames using FPI flamelet tabulation. *Combustion and Flame*, 140(3):147–160, 2005.

[71] H. Forrer and M. Berger. Flow simulations on cartesian grids involving complex moving geometries. In *Hyperbolic problems: theory, numerics, applications*, pages 315–324. Springer, 1999.

[72] C. Forte, E. Corti, G. M. Bianchi, S. Falfari, and S. Fantoni. A RANS CFD 3D methodology for the evaluation of the effects of cycle by cycle variation on knock tendency of a high performance spark-ignition engine. *SAE Technical Paper*, (2014-01-1223), 2014.

[73] M. Freitag and M. Klein. An improved method to assess the quality of Large-Eddy Simulations in the context of implicit filtering. *Journal of Turbulence*, 7:N40, 2006.

[74] H. Frezat, G. Balarac, J. Le Sommer, R. Fablet, and R. Lguensat. Physical invariance in neural networks for subgrid-scale scalar flux modeling. *Physical Review Fluids*, 6(2): 024607, 2021.

[75] U. Frisch and A. N. Kolmogorov. *Turbulence: the legacy of A.N. Kolmogorov*. Cambridge University Press, 1995.

[76] C. E. Frouzakis, G. Giannakopoulos, Y. Wright, K. Boulouchos, M. Schmitt, and A. G. Tomboulides. Direct Numerical Simulations for internal combustion premixed gas engines: first steps, challenges and prospects. *Motorische Verbrennung: aktuelle Probeme und moderne Lösungsansätze:(XIII. Tagung)*, 17:267–284, 2017.

[77] C. Fureby. A fractal flame-wrinkling Large-Eddy Simulation model for premixed turbulent combustion. *Proceedings of the Combustion Institute*, 30(1):593–601, 2005.

[78] M. Gadalla, J. Kannan, B. Tekgül, S. Karimkashi, O. Kaario, and V. Vuorinen. Large-Eddy Simulation of tri-fuel combustion: Diesel spray assisted ignition of methanol-hydrogen blends. *international Journal of Hydrogen Energy*, 46(41):21687–21703, 2021.

[79] C. García-Sánchez, J. van Beeck, and C. Gorlé. Predictive Large-Eddy Simulations for urban flows: Challenges and opportunities. *Building and Environment*, 139:146–156, 2018.

[80] M. Germano, U. Piomelli, P. Moin, and W. H. Cabot. A dynamic subgrid-scale eddy viscosity model. *Physics of Fluids A: Fluid Dynamics*, 3(7):1760–1765, 1991.

[81] B. J. Geurts and J. Fröhlich. A framework for predicting accuracy limitations in Large-Eddy Simulation. *Physics of Fluids*, 14(6):L41–L44, 2002.

[82] S. Ghosal. An analysis of numerical errors in Large-Eddy Simulations of turbulence. *Journal of Computational Physics*, 125(1):187–206, 1996.

[83] G. K. Giannakopoulos, K. Keskinen, J. Koch, C. E. Frouzakis, Y. M. Wright, and K. Boulouchos. Characterizing the evolution of boundary layers in IC engines by combined Direct Numerical and Large-Eddy Simulations. *Flow, Turbulence and Combustion*, pages 1–30, 2022.

[84] R. G. Gilbert, K. Luther, and J. Troe. Theory of thermal unimolecular reactions in the fall-off range. II. weak collision rate constants. *Berichte der Bunsengesellschaft für physikalische Chemie*, 87(2):169–177, 1983.

[85] D. J. Glaze and S. H. Frankel. Stochastic inlet conditions for Large-Eddy Simulation of a fully turbulent jet. *AIAA journal*, 41(6):1064–1073, 2003.

[86] D. G. Goodwin, H. K. Moffat, and R. L. Speth. Cantera: An object-oriented software toolkit for chemical kinetics, thermodynamics, and transport processes. *Caltech, Pasadena, CA*, 124, 2009.

[87] D. Goryntsev, A. Sadiki, M. Klein, and J. Janicka. Large-Eddy Simulation based analysis of the effects of cycle-to-cycle variations on air–fuel mixing in realistic DISI IC-engines. *Proceedings of the Combustion Institute*, 32(2):2759–2766, 2009.

[88] D. Goryntsev, A. Sadiki, M. Klein, and J. Janicka. Analysis of cyclic variations of liquid fuel–air mixing processes in a realistic DISI IC-engine using Large-Eddy Simulation. *International Journal of Heat and Fluid Flow*, 31(5):845–849, 2010.

[89] D. Goryntsev, A. Sadiki, and J. Janicka. Analysis of misfire processes in realistic direct injection spark-ignition engine using multi-cycle Large-Eddy Simulation. *Proceedings of the Combustion Institute*, 34(2):2969–2976, 2013.

[90] J. Graham, K. Kanov, X. Yang, M. Lee, N. Malaya, C. Lalescu, R. Burns, G. Eyink, A. Szalay, and R. Moser. A web services accessible database of turbulent channel flow and its use for testing a new integral wall model for LES. *Journal of Turbulence*, 17(2): 181–215, 2016.

[91] V. Granet, O. Vermorel, C. Lacour, B. Enaux, V. Dugué, and T. Poinsot. Large-Eddy Simulation and experimental study of cycle-to-cycle variations of stable and unstable operating points in a spark-ignition engine. *Combustion and Flame*, 159(4):1562–1575, 2012.

[92] A. Hanuschkin, S. Zündorf, M. Schmidt, C. Welch, J. Schorr, S. Peters, A. Dreizler, and B. Böhm. Investigation of cycle-to-cycle variations in a spark-ignition engine based on a machine learning analysis of the early flame kernel. *Proceedings of the Combustion Institute*, 38(4):5751–5759, 2021.

[93] F. H. Harlow and E. J. Welch. Numerical calculation of time-dependent viscous incompressible flow of fluid with free surface. *The Physics of Fluids*, 8(12):2182–2189, 1965.

[94] A. Harten. On a class of high resolution total-variation-stable finite-difference schemes. *SIAM Journal on Numerical Analysis*, 21(1):1–23, 1984.

[95] C. Hasse, V. Sohm, and B. Durst. Numerical investigation of cyclic variations in gasoline engines using a hybrid URANS/LES modeling approach. *Computers & Fluids*, 39(1):25–48, 2010.

[96] J. Hasslberger, L. Engelmann, A. Kempf, and M. Klein. Robust dynamic adaptation of the Smagorinsky model based on a sub-grid activity sensor. *Physics of Fluids*, 33(1): 015117, 2021.

[97] M. Haussmann, F. Ries, J. B. Jeppener-Haltenhoff, Y. Li, M. Schmidt, C. Welch, L. Illmann, B. Böhm, H. Nirschl, and M. J. Krause. Evaluation of a near-wall-modeled Large-Eddy Lattice-Boltzmann method for the analysis of complex flows relevant to IC engines. *Computation*, 8(2):43, 2020.

[98] S. Hickel, N. A. Adams, and N. N. Mansour. Implicit subgrid-scale modeling for Large-Eddy Simulation of passive-scalar mixing. *Physics of Fluids*, 19(9):095102, 2007.

[99] C. Hillman. All entropies agree for an sft, 1998.

[100] C. Hirsch. *Numerical computation of internal and external flows: The fundamentals of computational fluid dynamics*. Elsevier, 2007.

[101] J. O. Hirschfelder, C. F. Curtiss, and R. B. Bird. Molecular theory of gases and liquids. *Molecular theory of gases and liquids*, 1964.

[102] C. W. Hirt. Heuristic stability theory for finite-difference equations. *Journal of Computational Physics*, 2(4):339–355, 1968.

[103] C. W. Hirt and B. D. Nichols. Volume of fluid (VOF) method for the dynamics of free boundaries. *Journal of Computational Physics*, 39(1):201–225, 1981.

[104] C. W. Hirt, A. Amsden, and J. L. Cook. An arbitrary Lagrangian-Eulerian computing method for all flow speeds. *Journal of Computational Physics*, 135(2):203–216, 1997.

[105] K. Holmström and I. Denbratt. Cyclic variation in an SIengine due to the random motion of the flame kernel. *SAE Technical Paper*, 961152:36–47, 1996.

[106] S. Hoyas and J. Jiménez. Scaling of the velocity fluctuations in turbulent channels up to $\mathrm{Re}_\tau = 2003$. *Physics of Fluids*, 18(1):011702, 2006.

[107] M. Ihme, L. Shunn, and J. Zhang. Regularization of reaction progress variable for application to flamelet-based combustion models. *Journal of Computational Physics*, 231(23):7715–7721, 2012.

[108] E. Inanc, F. Proch, and A. Kempf. Studying transient jet flames by high-resolution LES using premixed flamelet chemistry. In *Direct and Large-Eddy Simulation XI*, pages 237–243. Springer, 2019.

[109] E. Inanc, A. M. Kempf, and N. Chakraborty. Effect of sub-grid wrinkling factor modelling on the large eddy simulation of turbulent stratified combustion. *Combustion Theory and Modelling*, 25(5):911–939, 2021.

[110] A. Iserles. *A first course in the numerical analysis of differential equations*, volume 44. Cambridge University Press, 2009.

[111] T. Ishihara, T. Gotoh, and Y. Kaneda. Study of high-Reynolds number isotropic turbulence by Direct Numerical Simulation. *Annual Review of Fluid Mechanics*, 41(1): 165–180, 2009.

[112] P. Janas, I. Wlokas, B. Böhm, and A. Kempf. On the evolution of the flow field in a spark-ignition engine. *Flow, Turbulence and Combustion*, 98(1):237–264, 2017.

[113] R. Johnson, H. Wu, and M. Ihme. A general probabilistic approach for the quantitative assessment of LES combustion models. *Combustion and Flame*, 183:88–101, 2017.

[114] W. P. Jones and B. E. Launder. The prediction of laminarization with a two-equation model of turbulence. *International Journal of Heat and Mass Transfer*, 15(2):301–314, 1972.

[115] D. Jung, K. Sasaki, and N. Iida. Effects of increased spark discharge energy and enhanced in-cylinder turbulence level on lean limits and cycle-to-cycle variations of combustion for SI engine operation. *Applied Energy*, 205:1467–1477, 2017.

[116] S. J. Kazmouz, D. C. Haworth, P. Lillo, and V. Sick. Large-Eddy Simulations of a stratified-charge direct-injection spark-ignition engine: Comparison with experiment and analysis of cycle-to-cycle variations. *Proceedings of the Combustion Institute*, 38 (4):5849–5857, 2021.

[117] R. J. Kee, M. E. Coltrin, and P. Glarborg. *Chemically reacting flow: theory and practice*. John Wiley & Sons, 2005.

[118] F. Kemm. A comparative study of TVD-limiters – well-known limiters and an introduction of new ones. *International Journal for Numerical Methods in Fluids*, 67(4): 404–440, 2011.

[119] A. Kempf. Large-Eddy Simulation of non-premixed turbulent flames, 2003.

[120] A. Kempf, M. Klein, and J. Janicka. Efficient generation of initial-and inflow-conditions for transient turbulent flows in arbitrary geometries. *Flow, Turbulence and Combustion*, 74(1):67–84, 2005.

[121] A. Kempf, P. Lindstedt, and J. Janicka. Large-Eddy Simulation of a bluff-body stabilized nonpremixed flame. *Combustion and Flame*, 144(1-2):170–189, 2006.

[122] C. A. Kennedy. *Comparison of several numerical methods for simulation of compressible shear layers*, volume 3484. NASA, Langley Research Center, 1997.

[123] C. A. Kennedy and M. H. Carpenter. Several new numerical methods for compressible shear-layer simulations. *Applied Numerical Mathematics*, 14(4):397–433, 1994.

[124] C. A. Kennedy, M. H. Carpenter, and R. M. Lewis. Low-storage, explicit Runge-Kutta schemes for the compressible Navier-Stokes equations. *Applied Numerical Mathematics*, 35(3):177–219, 2000.

[125] K. Keskinen, J. Koch, Y. M. Wright, M. Schmitt, M. Nuutinen, O. Kaario, V. Vuorinen, M. Larmi, and K. Boulouchos. Numerical assessment of wall modelling approaches in scale-resolving in-cylinder simulations. *International Journal of Heat and Fluid Flow*, 74:154–172, 2018.

[126] K. Keskinen, G. Giannakopoulos, M. Bolla, J. Koch, Y. M. Wright, C. Frouzakis, K. Boulouchos, M. Schmidt, B. Böhm, and A. Dreizler. Novel insight into engine near-wall flows and wall heat transfer using Direct Numerical Simulations and high-fidelity experiments. In *21. Internationales Stuttgarter Symposium*, pages 377–394. Springer, 2021.

[127] S. Ketterl and M. Klein. A-priori assessment of subgrid scale models for Large-Eddy Simulation of multiphase primary breakup. *Computers & Fluids*, 165:64–77, 2018.

[128] S. Ketterl, M. Reißmann, and M. Klein. Large-Eddy Simulation of multiphase flows using the volume of fluid method: Part 2 — a-posteriori analysis of liquid jet atomization. *Experimental and Computational Multiphase Flow*, 1(3):201–211, 2019.

[129] J. Kim and P. Moin. Application of a fractional-step method to incompressible Navier-Stokes equations. *Journal of Computational Physics*, 59(2):308–323, 1985.

[130] J. Kim, P. Moin, and R. Moser. Turbulence statistics in fully developed channel flow at low Reynolds number. *Journal of Fluid Mechanics*, 177:133–166, 1987.

[131] M. Klein. An attempt to assess the quality of Large-Eddy Simulations in the context of implicit filtering. *Flow, Turbulence and Combustion*, 75(1-4):131–147, 2005.

[132] M. Klein. Towards LES as an engineering tool, 2008.

[133] M. Klein, A. Sadiki, and J. Janicka. A digital filter based generation of inflow data for spatially developing Direct Numerical or Large-Eddy Simulations. *Journal of Computational Physics*, 186(2):652–665, 2003.

[134] M. Klein, A. Sadiki, and J. Janicka. Investigation of the influence of the Reynolds number on a plane jet using Direct Numerical Simulation. *International Journal of Heat and Fluid Flow*, 24(6):785–794, 2003.

[135] M. Klein, C. Kasten, Y. Gao, and N. Chakraborty. A-priori Direct Numerical Simulation assessment of sub-grid scale stress tensor closures for turbulent premixed combustion. *Computers & Fluids*, 122:1–11, 2015.

[136] M. Klein, N. Chakraborty, and Y. Gao. Scale similarity based models and their application to subgrid scale scalar flux modelling in the context of turbulent premixed flames. *International Journal of Heat and Fluid Flow*, 57:91–108, 2016.

[137] M. Klein, N. Chakraborty, and M. Pfitzner. Analysis of the combined modelling of sub-grid transport and filtered flame propagation for premixed turbulent combustion. *Flow, Turbulence and Combustion*, 96(4):921–938, 2016.

[138] M. Klein, C. Kasten, and N. Chakraborty. A-priori Direct Numerical Simulation assessment of models for generalized sub-grid scale turbulent kinetic energy in turbulent premixed flames. *Computers & Fluids*, 154:123–131, 2017.

[139] M. Klein, S. Ketterl, and J. Hasslberger. Large-Eddy Simulation of multiphase flows using the volume of fluid method: Part 1 - governing equations and a priori analysis. *Experimental and Computational Multiphase Flow*, 1(2):130–144, 2019.

[140] M. Klein, S. Ketterl, L. Engelmann, A. Kempf, and H. Kobayashi. Regularized, parameter free scale similarity type models for Large-Eddy Simulation. *International Journal of Heat and Fluid Flow*, 81:108496, 2020.

[141] H. Kobayashi. The subgrid-scale models based on coherent structures for rotating homogeneous turbulence and turbulent channel flow. *Physics of Fluids*, 17(4):045104, 2005.

[142] H. Kobayashi. Improvement of the SGS model by using a scale-similarity model based on the analysis of SGS force and SGS energy transfer. *International Journal of Heat and Fluid Flow*, 72:329–336, 2018.

[143] D. Kochkov, J. A. Smith, A. Alieva, Q. Wang, M. P. Brenner, and S. Hoyer. Machine learning–accelerated computational fluid dynamics. *Proceedings of the National Academy of Sciences*, 118(21):e2101784118, 2021.

[144] F. Kock and H. Herwig. Local entropy production in turbulent shear flows: a high-Reynolds number model with wall functions. *International Journal of Heat and Mass Transfer*, 47(10-11):2205–2215, 2004.

[145] A. Kolmogorov. Three approaches to the quantitative definition of information. *Problems of Information Transmission*, 1(1):1–7, 1965.

[146] A. N. Kolmogorov. Equations of turbulent motion in an incompressible fluid. In *Dokl. Akad. Nauk SSSR*, volume 30, pages 299–303, 1941.

[147] A. N. Kolmogorov. The local structure of turbulence in incompressible viscous fluid for very large Reynolds numbers. *Proceedings of the USSR Academy of Sciences*, 30: 301–305, 1941.

[148] V. K. Krastev, G. Di Ilio, G. Falcucci, and G. Bella. Notes on the hybrid URANS/LES turbulence modeling for internal combustion engines simulation. *Energy Procedia*, 148: 1098–1104, 2018.

[149] V. K. Krastev, A. d'Adamo, F. Berni, and S. Fontanesi. Validation of a zonal hybrid URANS/LES turbulence modeling method for multi-cycle engine flow simulation. *International Journal of Engine Research*, 21(4):632–648, 2020.

[150] C. Krüger, J. Schorr, F. Nicollet, J. Bode, A. Dreizler, and B. Böhm. Cause-and-effect chain from flow and spray to heat release during lean gasoline combustion operation using conditional statistics. *International Journal of Engine Research*, 18(1-2):143–154, 2017.

[151] K. K. Kuo. *Principles of combustion*. Elsevier Science Pub. Co. Inc., New York, NY, 1986.

[152] W. Kutta. Beitrag zur naherungsweisen integration totaler Differentialgleichungen. *Zeitschrift für Mathematik und Physik*, 46:435–453, 1901.

[153] Y. Kuwata and Y. Kawaguchi. Direct Numerical Simulation of turbulence over systematically varied irregular rough surfaces. *Journal of Fluid Mechanics*, 862:781–815, 2019.

[154] B. E. Launder and N. D. Sandham. *Closure strategies for turbulent and transitional flows*. Cambridge University Press, 2002.

[155] C. Le Ribault, S. Sarkar, and S. A. Stanley. Large-Eddy Simulation of a plane jet. *Physics of Fluids*, 11(10):3069–3083, 1999.

[156] G. Lecocq, S. Richard, O. Colin, and L. Vervisch. Gradient and counter-gradient modeling in premixed flames: Theoretical study and application to the LES of a lean premixed turbulent swirl-burner. *Combustion Science and Technology*, 182(4-6): 465–479, 2010.

[157] S. Lee, S. K. Lele, and P. Moin. Simulation of spatially evolving turbulence and the applicability of taylor's hypothesis in compressible flow. *Physics of Fluids A: Fluid Dynamics*, 4(7):1521–1530, 1992.

[158] J.-P. Legier, T. Poinsot, and D. Veynante. Dynamically thickened flame LES model for premixed and non-premixed turbulent combustion. In *Proceedings of the summer program*, volume 12, pages 157–168. Center for Turbulence Research Stanford, CA, 2000.

[159] S. K. Lele. Compact finite difference schemes with spectral-like resolution. *Journal of Computational Physics*, 103(1):16–42, 1992.

[160] A. Leonard. Energy cascade in Large-Eddy Simulations of turbulent fluid flows. In *Advances in geophysics*, volume 18, pages 237–248. Elsevier, 1975.

[161] W. K. Lewis. The evaporation of a liquid into a gas. *Transactions of the American Society of Mechanical Engineers*, 44:325–340, 1922.

[162] H. Li, Y. Zhao, J. Wang, and R. D. Sandberg. Data-driven model development for Large-Eddy Simulation of turbulence using gene-expression programing. *Physics of Fluids*, 33(12):125127, 2021.

[163] D. Lilly. The representation of small-scale turbulence in numerical simulation experiments (manuscript no. 281). *National Center for Atmospheric Research*, 1966.

[164] D. K. Lilly. The representation of small-scale turbulence in numerical simulation experiments. *IBM Form*, pages 195–210, 1967.

[165] D. K. Lilly. A proposed modification of the germano subgrid-scale closure method. *Physics of Fluids A: Fluid Dynamics*, 4(3):633–635, 1992.

[166] F. A. Lindemann, S. Arrhenius, I. Langmuir, N. Dhar, J. Perrin, and W. C. Lewis. Discussion on "the radiation theory of chemical action". *Transactions of the Faraday Society*, 17:598–606, 1922.

[167] J. T. Lipkowicz, D. Nativel, S. Cooper, I. Wlokas, M. Fikri, E. Petersen, C. Schulz, and A. Kempf. Numerical investigation of remote ignition in shock tubes. *Flow, Turbulence and Combustion*, pages 1–28, 2020.

[168] S. Liu, C. Meneveau, and J. Katz. On the properties of similarity subgrid-scale models as deduced from measurements in a turbulent jet. *Journal of Fluid Mechanics*, 275: 83–119, 1994.

[169] Y. Liu, P. G. Tucker, and R. M. Kerr. Linear and nonlinear model Large-Eddy Simulations of a plane jet. *Computers & fluids*, 37(4):439–449, 2008.

[170] E. N. Lorenz. Deterministic nonperiodic flow. *Journal of the Atmospheric Sciences*, 20 (2):130–141, 1963.

[171] A. Lozano-Durán, J. H. Bae, and M. P. Encinar. Causality of energy-containing eddies in wall turbulence. *Journal of Fluid Mechanics*, 882, 2020.

[172] T. S. Lund, X. Wu, and K. D. Squires. Generation of turbulent inflow data for spatially-developing boundary layer simulations. *Journal of Computational Physics*, 140(2): 233–258, 1998.

[173] R. Man and P. Moin. Direct simulations of turbulent flow using finite-difference schemes. In *27th Aerospace Sciences Meeting*, page 369, 1991.

[174] M. Mansour, N. Peters, and L.-U. Schrader. Experimental study of turbulent flame kernel propagation. *Experimental Thermal and Fluid Science*, 32(7):1396–1404, 2008.

[175] F. A. Matekunas. Modes and measures of cyclic combustion variability. *SAE Technical Paper*, 830337:1139–1156, 1983.

[176] B. J. McBride, S. Gordon, and M. A. Reno. Coefficients for calculating thermodynamic and transport properties of individual species. Technical report tm-4513, NASA, 1993.

[177] D. Meller, L. Engelmann, P. Wollny, K. Tainaka, H. Watanabe, P. Debiagi, O. T. Stein, and A. M. Kempf. Evaluation of ammonia co-firing in the criepi coal jet flame using a three mixture fraction fpv-les. *Proceedings of the Combustion Institute*, 2022.

[178] C. Meneveau, T. S. Lund, and W. H. Cabot. A lagrangian dynamic subgrid-scale model of turbulence. *Journal of Fluid Mechanics*, 319:353–385, 1996.

[179] F. R. Menter. Two-equation eddy-viscosity turbulence models for engineering applications. *AIAA Journal*, 32(8):1598–1605, 1994.

[180] L. Merlier, J. Jacob, and P. Sagaut. Lattice-boltzmann Large-Eddy Simulation of pollutant dispersion in complex urban environment with dense gas effect: Model evaluation and flow analysis. *Building and Environment*, 148:634–652, 2019.

[181] M. L. Merriam. An entropy-based approach to nonlinear stability. Technical report, Ames Research Center, 1989.

[182] J. Meyers, B. J. Geurts, and P. Sagaut. A computational error-assessment of central finite-volume discretizations in Large-Eddy Simulation using a smagorinsky model. *Journal of Computational Physics*, 227(1):156–173, 2007.

[183] P. Moin and J. Kim. Numerical investigation of turbulent channel flow. *Journal of Fluid Mechanics*, 118:341–377, 1982.

[184] P. Moin, K. Squires, W. Cabot, and S. Lee. A dynamic subgrid-scale model for compressible turbulence and scalar transport. *Physics of Fluids A: Fluid Dynamics*, 3 (11):2746–2757, 1991.

[185] R. D. Moser, J. Kim, and N. N. Mansour. Direct Numerical Simulation of turbulent channel flow up to re τ= 590. *Physics of Fluids*, 11(4):943–945, 1999.

[186] M. E. Mueller. Physically-derived reduced-order manifold-based modeling for multi-modal turbulent combustion. *Combustion and Flame*, 214:287–305, 2020.

[187] R. Muppala, N. K. Aluri, F. Dinkelacker, and A. Leipertz. Development of an algebraic reaction rate closure for the numerical calculation of turbulent premixed methane, ethylene, and propane/air flames for pressures up to 1.0 MPa. *Combustion and Flame*, 140(4):257–266, 2005.

[188] G. Nastac, J. W. Labahn, L. Magri, and M. Ihme. Lyapunov exponent as a metric for assessing the dynamic content and predictability of Large-Eddy Simulations. *Physical Review Fluids*, 2(9):094606, 2017.

[189] G. F. Naterer and J. A. Camberos. Entropy and the second law fluid flow and heat transfer simulation. *Journal of Thermophysics and Heat Transfer*, 17(3):360–371, 2003.

[190] T. M. Nguyen and A. Kempf. Investigation of numerical effects on the flow and combustion in LES of ICE. *Oil & Gas Science and Technology–Revue d'IFP Energies nouvelles*, 72(4):25, 2017.

[191] T. M. Nguyen, F. Proch, I. Wlokas, and A. Kempf. Large-Eddy Simulation of an internal combustion engine using an efficient immersed boundary technique. *Flow, Turbulence and Combustion*, 97(1):191–230, 2016.

[192] F. Nicoud, H. B. Toda, O. Cabrit, S. Bose, and J. Lee. Using singular values to build a subgrid-scale model for Large-Eddy Simulations. *Physics of Fluids*, 23(8):085106, 2011.

[193] W. Ning, R. D. Reitz, R. Diwakar, and A. M. Lippert. An Eulerian-Lagrangian spray and atomization model with improved turbulence modeling. *Atomization and Sprays*, 19(8), 2009.

[194] Y.-S. Niu, L. Vervisch, and P. D. Tao. An optimization-based approach to detailed chemistry tabulation: Automated progress variable definition. *Combustion and Flame*, 160(4):776–785, 2013.

[195] W. F. Noh and P. Woodward. SLIC (simple line interface calculation). In *Proceedings of the fifth international conference on numerical methods in fluid dynamics June 28–July 2, 1976 Twente University, Enschede*, pages 330–340. Springer, 1976.

[196] A. G. Novoselov, C. E. Lacey, B. A. Perry, and M. E. Mueller. Large-Eddy Simulation of a turbulent lifted flame using multi-modal manifold-based models: Feasibility and interpretability. *Proceedings of the Combustion Institute*, 38(2):2581–2588, 2021.

[197] J. C. Ong, K. M. Pang, J. H. Walther, J.-H. Ho, and H. K. Ng. Evaluation of a lagrangian soot tracking method for the prediction of primary soot particle size under engine-like conditions. *Journal of Aerosol Science*, 115:70–95, 2018.

[198] N. Ozdor, M. Dulger, and E. Sher. Cyclic variability in spark-ignition engines a literature survey. *SAE Technical Paper*, 940987:1514–1552, 1994.

[199] J. Park and H. Choi. Toward neural-network-based Large-Eddy Simulation: Application to turbulent channel flow. *Journal of Fluid Mechanics*, 914, 2021.

[200] A. Pati, D. Paredi, C. Welch, M. Schmidt, C. Geschwindner, B. Böhm, T. Lucchini, G. D'Errico, and C. Hasse. Numerical and experimental investigations of the early injection process of spray g in a constant volume chamber and an optically accessible DISI engine. *International Journal of Engine Research*, 23(12):2073–2093, 2022.

[201] D. Perugini, C. P. De Campos, M. Petrelli, D. Morgavi, F. P. Vetere, and D. B. Dingwell. Quantifying magma mixing with the shannon entropy: Application to simulations and experiments. *Lithos*, 236:299–310, 2015.

[202] C. S. Peskin. The immersed boundary method. *Acta Numerica*, 11:479–517, 2002.

[203] N. Peters. Laminar flamelet concepts in turbulent combustion. *Proceedings of the Combustion Institute*, 21(1):1231–1250, 1988.

[204] B. Peterson, D. L. Reuss, and V. Sick. High-speed imaging analysis of misfires in a spray-guided direct injection engine. *Proceedings of the Combustion Institute*, 33(2): 3089–3096, 2011.

[205] M. Pettit, B. Coriton, A. Gomez, and A. Kempf. Large-Eddy Simulation and experiments on non-premixed highly turbulent opposed jet flows. *Proceedings of the Combustion Institute*, 33(1):1391–1399, 2011.

[206] S. Pfadler, F. Beyrau, F. Dinkelacker, and A. Leipertz. A-priori testing of an eddy viscosity model for the density-weighted subgrid scale stress tensor in turbulent premixed flames. *Experiments in Fluids*, 49(4):839–851, 2010.

[207] C. D. Pierce and P. Moin. Progress-variable approach for Large-Eddy Simulation of non-premixed turbulent combustion. *Journal of Fluid Mechanics*, 504:73–97, 2004.

[208] U. Piomelli and J. Liu. Large-Eddy Simulation of rotating channel flows using a localized dynamic model. *Physics of Fluids*, 7(4):839–848, 1995.

[209] U. Piomelli, P. Moin, and J. H. Ferziger. Model consistency in Large-Eddy Simulation of turbulent channel flows. *The Physics of Fluids*, 31(7):1884–1891, 1988.

[210] H. Pitsch and D. De Lageneste. Large-Eddy Simulation of premixed turbulent combustion using a level-set approach. *Proceedings of the Combustion Institute*, 29(2): 2001–2008, 2002.

[211] R. H. Pletcher, J. C. Tannehill, and D. Anderson. *Computational fluid mechanics and heat transfer*. CRC press, 1997.

[212] T. Poinsot and D. Veynante. *Theoretical and numerical combustion*. RT Edwards, Inc., 2005.

[213] T. J. Poinsot and S. K. Lele. Boundary conditions for direct simulations of compressible viscous flows. *Journal of Computational Physics*, 101(1):104–129, 1992.

[214] A. Y. Poludnenko and E. S. Oran. The interaction of high-speed turbulence with flames: Global properties and internal flame structure. *Combustion and Flame*, 157(5): 995–1011, 2010.

[215] A. Y. Poludnenko and E. S. Oran. The interaction of high-speed turbulence with flames: Turbulent flame speed. *Combustion and Flame*, 158(2):301–326, 2011.

[216] S. B. Pope. *Turbulent flows*. Cambridge University Press, 2000.

[217] S. B. Pope. Ten questions concerning the Large-Eddy Simulation of turbulent flows. *New Journal of Physics*, 6(1):35, 2004.

[218] W. H. Press, S. A. Teukolsky, W. T. Vetterling, and B. P. Flannery. Numerical recipes in c^{++}. *The Art of Scientific Computing*, 2:1002, 2007.

[219] F. Proch. Highly-resolved numerical simulation of turbulent premixed and stratified combustion under adiabatic and non-adiabatic conditions with tabulated chemistry, 2017.

[220] F. Proch and A. Kempf. Numerical analysis of the cambridge stratified flame series using artificial thickened flame LES with tabulated premixed flame chemistry. *Combustion and Flame*, 161(10):2627–2646, 2014.

[221] F. Proch, P. Domingo, L. Vervisch, and A. Kempf. Flame resolved simulation of a turbulent premixed bluff-body burner experiment. Part I: Analysis of the reaction zone dynamics with tabulated chemistry. *Combustion and Flame*, 180:321–339, 2017.

[222] F. Proch, P. Domingo, L. Vervisch, and A. Kempf. Flame resolved simulation of a turbulent premixed bluff-body burner experiment. Part II: A-priori and a-posteriori investigation of sub-grid scale wrinkling closures in the context of artificially thickened flame modeling. *Combustion and Flame*, 180:340–350, 2017.

[223] U. Prüfert, S. Hartl, F. Hunger, D. Messig, M. Eiermann, and C. Hasse. A constrained control approach for the automated choice of an optimal progress variable for chemistry tabulation. *Flow, Turbulence and Combustion*, 94(3):593–617, 2015.

[224] W. E. Ranz and W. R. Marshall. Evaporation from droplets. *Chemical Engineering Progress*, 48(3):141–146, 1952.

[225] J. Ray, C. A. Kennedy, S. Lefantzi, and H. N. Najm. Using high-order methods on adaptively refined block-structured meshes: derivatives, interpolations, and filters. *SIAM Journal on Scientific Computing*, 29(1):139–181, 2007.

[226] M. Reissmann, J. Hasslberger, R. D. Sandberg, and M. Klein. Application of gene expression programming to a-posteriori LES modeling of a Taylor-Green vortex. *Journal of Computational Physics*, 424:109859, 2021.

[227] C. M. Rhie and W.-L. Chow. Numerical study of the turbulent flow past an airfoil with trailing edge separation. *AIAA journal*, 21(11):1525–1532, 1983.

[228] S. Richard, O. Colin, O. Vermorel, A. Benkenida, C. Angelberger, and D. Veynante. Towards Large-Eddy Simulation of combustion in spark-ignition engines. *Proceedings of the combustion institute*, 31(2):3059–3066, 2007.

[229] K. Richards, D. Probst, E. Pomraning, P. K. Senecal, and R. Scarcelli. The observation of cyclic variation in engine simulations when using RANS turbulence modeling. In *Internal Combustion Engine Division Fall Technical Conference*, volume 46179, page V002T06A010. American Society of Mechanical Engineers, 2014.

[230] M. Rieth, F. Proch, O. T. Stein, M. Pettit, and A. Kempf. Comparison of the Sigma and Smagorinsky LES models for grid generated turbulence and a channel flow. *Computers & Fluids*, 99(Supplement C):172 – 181, 2014. ISSN 0045-7930.

[231] M. Rieth, A. G. Clements, M. Rabaçal, F. Proch, O. T. Stein, and A. Kempf. Flamelet LES modeling of coal combustion with detailed devolatilization by directly coupled CPD. *Proceedings of the Combustion Institute*, 36(2):2181–2189, 2017.

[232] M. Rieth, A. Kempf, A. Kronenburg, and O. T. Stein. Carrier-phase DNS of pulverized coal particle ignition and volatile burning in a turbulent mixing layer. *Fuel*, 212:364–374, 2018.

[233] A. Rittler, F. Proch, and A. Kempf. LES of the sydney piloted spray flame series with the PFGM/ATF approach and different sub-filter models. *Combustion and Flame*, 162 (4):1575–1598, 2015.

[234] P. J. Roache. *Verification and validation in computational science and engineering*. Hermosa, 1998.

[235] A. Robert, S. Richard, O. Colin, L. Martinez, and L. De Francqueville. LES prediction and analysis of knocking combustion in a spark-ignition engine. *Proceedings of the Combustion Institute*, 35(3):2941–2948, 2015.

[236] H. H. Robertson. The solution of a set of reaction rate equations. *Numerical analysis: an introduction*, 178182, 1966.

[237] P. L. Roe. Approximate Riemann solvers, parameter vectors, and difference schemes. *Journal of Computational Physics*, 43(2):357–372, 1981.

[238] P. L. Roe. Characteristic-based schemes for the euler equations. *Annual Review of Fluid Mechanics*, 18(1):337–365, 1986.

[239] D. Ruelle. Ergodic theory of differentiable dynamical systems. *Publications Mathematiques de l'Institut des Hautes Etudes Scientifiques*, 50(1):27–58, 1979.

[240] C. Runge. Über die numerische Auflösung von Differentialgleichungen. *Mathematische Annalen*, 46(2):167–178, 1895.

[241] C. J. Rutland. Large-Eddy Simulations for internal combustion engines – a review. *International Journal of Engine Research*, 12(5):421–451, 2011.

[242] M. Sadeghi, K. Truffin, B. Peterson, B. Böhm, and S. Jay. Development and application of bivariate 2d-EMD for the analysis of instantaneous flow structures and cycle-to-cycle variations of in-cylinder flow. *Flow, Turbulence and Combustion*, 106(1):231–259, 2021.

[243] P. G. Saffman. A model for inhomogeneous turbulent flow. *Proceedings of the Royal Society of London. A. Mathematical and Physical Sciences*, 317(1530):417–433, 1970.

[244] P. Sagaut. *Large-Eddy Simulation for incompressible flows: an introduction*. Springer Science & Business Media, 2006.

[245] M. Sanjosé, J. M. Senoner, F. Jaegle, B. Cuenot, S. Moreau, and T. Poinsot. Fuel injection model for Euler-Euler and Euler-Lagrange Large-Eddy Simulations of an evaporating spray inside an aeronautical combustor. *International Journal of Multiphase Flow*, 37(5):514–529, 2011.

[246] F. Sarghini, G. De Felice, and S. Santini. Neural networks based subgrid scale modeling in Large-Eddy Simulations. *Computers & fluids*, 32(1):97–108, 2003.

[247] R. Scarcelli, K. Richards, E. Pomraning, P. K. Senecal, J. M. Sevik, and T. Wallner. Cycle-to-cycle variations in multi-cycle engine RANS simulations. Technical report, Argonne National Lab.(ANL), Argonne, IL (United States), 2016.

[248] H. Schlichting and K. Gersten. *Boundary-layer theory*. Springer, 2016.

[249] M. Schmidt, C.-P. Ding, B. Peterson, A. Dreizler, and B. Boehm. Near-wall flame and flow measurements in an optically accessible SI engine. *Flow, Turbulence and Combustion*, 106:597–611, 2021.

[250] F. G. Schmitt. About Boussinesq's turbulent viscosity hypothesis: historical remarks and a direct evaluation of its validity. *Comptes Rendus Mécanique*, 335(9-10):617–627, 2007.

[251] M. Schmitt, C. E. Frouzakis, Y. M. Wright, A. G. Tomboulides, and K. Boulouchos. Investigation of cycle-to-cycle variations in an engine-like geometry. *Physics of Fluids*, 26(12):125104, 2014.

[252] M. Schmitt, C. E. Frouzakis, A. G. Tomboulides, Y. M. Wright, and K. Boulouchos. Direct Numerical Simulation of the effect of compression on the flow, temperature and composition under engine-like conditions. *Proceedings of the Combustion Institute*, 35 (3):3069–3077, 2015.

[253] M. Schmitt, C. E. Frouzakis, Y. M. Wright, A. G. Tomboulides, and K. Boulouchos. Direct Numerical Simulation of the compression stroke under engine-relevant conditions: Evolution of the velocity and thermal boundary layers. *International Journal of Heat and Mass Transfer*, 91:948–960, 2015.

[254] U. Schumann. Subgrid scale model for finite difference simulations of turbulent flows in plane channels and annuli. *Journal of Computational Physics*, 18(4):376–404, 1975.

[255] J. Sellmann, I. Rahinov, S. Kluge, H. Jünger, A. Fomin, S. Cheskis, C. Schulz, H. Wiggers, A. Kempf, and I. Wlokas. Detailed simulation of iron oxide nanoparticle forming flames: Buoyancy and probe effects. *Proceedings of the Combustion Institute*, 37(1): 1241–1248, 2019.

[256] J. Sellmann, P. Wollny, S.-J. Baik, S. Suleiman, F. Schneider, C. Schulz, H. Wiggers, I. Wlokas, and A. Kempf. LES of nanoparticle synthesis in the SpraySyn burner: A comparison against experiments. *Powder Technology*, 404:117466, 2022.

[257] C. E. Shannon. A mathematical theory of communication. *Mobile Computing and Communications Review*, 5(1):3–55, 2001.

[258] S. Shawal, M. Goschutz, M. Schild, S. Kaiser, M. Neurohr, J. Pfeil, and T. Koch. High-speed imaging of early flame growth in spark-ignited engines using different imaging systems via endoscopic and full optical access. *SAE Technical Paper*, 2:704–718, 2016.

[259] J. Smagorinsky. General circulation experiments with the primitive equations: I. the basic experiment. *Monthly Weather Review*, 91(3):99–164, 1963.

[260] J. Smagorinsky, S. Manabe, and L. J. Holloway. Numerical results from a nine-level general circulation model of the atmosphere. *Monthly Weather Review*, 93(12):727–768, 1965.

[261] A. Smirnov, S. Shi, and I. Celik. Random flow generation technique for Large-Eddy Simulations and particle-dynamics modeling. *Journal of Fluids Engineering*, 123(2): 359–371, 2001.

[262] G. P. Smith, D. M. Golden, M. Frenklach, N. W. Moriarty, B. Eiteneer, M. Goldenberg, T. C. Bowman, R. K. Hanson, S. Song, and W. C. Gardiner Jr. Gri 3.0 mechanism. *Gas Research Institute (http://www. me. berkeley. edu/gri_mech)*, 1999.

[263] I. Sölch and B. Kärcher. A large-eddy model for cirrus clouds with explicit aerosol and ice microphysics and Lagrangian ice particle tracking. *Quarterly Journal of the Royal Meteorological Society*, 136(653):2074–2093, 2010.

[264] C. G. Speziale, G. Erlebacher, T. A. Zang, and M. Y. Hussaini. The subgrid-scale modeling of compressible turbulence. *The Physics of Fluids*, 31(4):940–942, 1988.

[265] S. Stanley, S. Sarkar, and J. P. Mellado González. A study of the flow-field evolution and mixing in a planar turbulent jet using Direct Numerical Simulation. *Journal of Fluid Mechanics*, 450:377–407, 2002.

[266] O. Stein. Large-Eddy Simulation of combustion in swirling and opposed jet flows, 2009.

[267] O. T. Stein, B. Böhm, A. Dreizler, and A. Kempf. Highly-resolved LES and PIV analysis of isothermal turbulent opposed jets for combustion applications. *Flow, Turbulence and Combustion*, 87(2):425–447, 2011.

[268] P. H. Stewart, C. W. Larson, and D. M. Golden. Pressure and temperature dependence of reactions proceeding via a bound complex. 2. application to 2CH3→ C2H5+ H. *Combustion and Flame*, 75(1):25–31, 1989.

[269] R. Stiehl, J. Bode, J. Schorr, C. Krüger, A. Dreizler, and B. Böhm. Influence of intake geometry variations on in-cylinder flow and flow–spray interactions in a stratified direct-injection spark-ignition engine captured by time-resolved particle image velocimetry. *International Journal of Engine Research*, 17(9):983–997, 2016.

[270] G. Stiesch. *Modeling engine spray and combustion processes*. Springer Science & Business Media, 2003.

[271] S. Stolz and N. A. Adams. An approximate deconvolution procedure for Large-Eddy Simulation. *Physics of Fluids*, 11(7):1699–1701, 1999.

[272] S. Stolz, N. A. Adams, and L. Kleiser. An approximate deconvolution model for Large-Eddy Simulation with application to incompressible wall-bounded flows. *Physics of Fluids*, 13(4):997–1015, 2001.

[273] R. Stone, A. G. Brown, and P. Beckwith. Cycle-by-cycle variations in spark-ignition engine combustion - part II: Modelling of flame kernel displacements as a cause of cycle-by-cycle-variations. *SAE Technical Paper*, 960613:133–141, 1996.

[274] P. K. Sweby. High resolution schemes using flux limiters for hyperbolic conservation laws. *SIAM journal on numerical analysis*, 21(5):995–1011, 1984.

[275] M. S. Sweeney, S. Hochgreb, M. J. Dunn, and R. S. Barlow. The structure of turbulent stratified and premixed methane/air flames I: Non-swirling flows. *Combustion and Flame*, 159(9):2896–2911, 2012.

[276] M. S. Sweeney, S. Hochgreb, M. J. Dunn, and R. S. Barlow. The structure of turbulent stratified and premixed methane/air flames II: Swirling flows. *Combustion and Flame*, 159(9):2912–2929, 2012.

[277] B. Tekgül, H. Kahila, S. Karimkashi, O. Kaario, Z. Ahmad, É. Lendormy, J. Hyvönen, and V. Vuorinen. Large-Eddy Simulation of spray assisted dual-fuel ignition under reactivity-controlled dynamic conditions. *Fuel*, 293:120295, 2021.

[278] F. O. Thomas and V. W. Goldschmidt. Structural characteristics of a developing turbulent planar jet. *Journal of Fluid Mechanics*, 163:227–256, 1986.

[279] K. W. Thompson. Time dependent boundary conditions for hyperbolic systems I. *Journal of Computational Physics*, 68(1):1–24, 1987.

[280] K. W. Thompson. Time-dependent boundary conditions for hyperbolic systems II. *Journal of Computational Physics*, 89(2):439–461, 1990.

[281] R. Torelli, R. Scarcelli, S. Som, X. Zhu, S.-Y. Lee, J. Naber, D. Markt, and M. Raessi. Toward predictive and computationally affordable Lagrangian-Eulerian modeling of spray-wall interaction. *International Journal of Engine Research*, 21(2):263–280, 2020.

[282] K. Truffin, C. Angelberger, S. Richard, and C. Pera. Using Large-Eddy Simulation and multivariate analysis to understand the sources of combustion cyclic variability in a spark-ignition engine. *Combustion and Flame*, 162(12):4371–4390, 2015.

[283] H. A. Van der Vorst. Parallel iterative solution methods for linear systems arising from discretized PDE's. *Special Course on parallel Computing in CFD*, 1995.

[284] E. R. Van Driest. On turbulent flow near a wall. *Journal of the aeronautical Sciences*, 23(11):1007–1011, 1956.

[285] B. Van Leer. Towards the ultimate conservative difference scheme. ii. monotonicity and conservation combined in a second-order scheme. *Journal of Computational Physics*, 14(4):361–370, 1974.

[286] J. A. Van Oijen and P. De Goey. Modelling of premixed laminar flames using flamelet-generated manifolds. *Combustion Science and Technology*, 161(1):113–137, 2000.

[287] J. A. Van Oijen and P. De Goey. Modelling of premixed counterflow flames using the flamelet-generated manifold method. *Combustion Theory and Modelling*, 6(3):463–478, 2002.

[288] J. A. Van Oijen, R. Bastiaans, and P. De Goey. Low-dimensional manifolds in Direct Numerical Simulations of premixed turbulent flames. *Proceedings of the Combustion Institute*, 31(1):1377–1384, 2007.

[289] O. Vermorel, S. Richard, O. Colin, C. Angelberger, A. Benkenida, and D. Veynante. Multi-cycle LES simulations of flow and combustion in a PFI SI 4-valve production engine. *SAE Technical Paper*, 2007-01-0151:152–164, 2007.

[290] O. Vermorel, S. Richard, O. Colin, C. Angelberger, A. Benkenida, and D. Veynante. Towards the understanding of cyclic variability in a spark ignited engine using multi-cycle LES. *Combustion and Flame*, 156(8):1525–1541, 2009.

[291] H. K. Versteeg and W. Malalasekera. *An introduction to computational fluid dynamics: the finite volume method*. Pearson Education, 2007.

[292] B. Vreman, B. Geurts, and H. Kuerten. Realizability conditions for the turbulent stress tensor in Large-Eddy Simulation. *Journal of Fluid Mechanics*, 278:351–362, 1994.

[293] B. Vreman, B. Geurts, and H. Kuerten. Large-Eddy Simulation of the turbulent mixing layer. *Journal of Fluid Mechanics*, 339:357–390, 1997.

[294] B. Vreman, B. A. Albrecht, J. A. Van Oijen, P. De Goey, and R. Bastiaans. Premixed and nonpremixed generated manifolds in Large-Eddy Simulation of Sandia flame D and F. *Combustion and Flame*, 153(3):394–416, 2008.

[295] S. Wadekar, P. Janas, and M. Oevermann. Large-Eddy Simulation study of combustion cyclic variation in a lean-burn spark-ignition engine. *Applied Energy*, 255:113812, 2019.

[296] G. Wang, M. Boileau, and D. Veynante. Implementation of a dynamic thickened flame model for Large-Eddy Simulations of turbulent premixed combustion. *Combustion and Flame*, 158(11):2199–2213, 2011.

[297] Z. Warhaft. Passive scalars in turbulent flows. *Annual Review of Fluid Mechanics*, 32 (1):203–240, 2000.

[298] A. Wehrfritz, O. Kaario, V. Vuorinen, and B. Somers. Large-Eddy Simulation of n-dodecane spray flames using flamelet generated manifolds. *Combustion and Flame*, 167:113–131, 2016.

[299] C. Welch, M. Schmidt, K. Keskinen, G. Giannakopoulos, K. Boulouchos, A. Dreizler, and B. Boehm. The effects of intake pressure on in-cylinder gas velocities in an optically accessible single-cylinder research engine. *SAE Technical Paper*, 2020-01-0792, 2020.

[300] C. Welch, M. Schmidt, L. Illmann, A. Dreizler, and B. Böhm. The influence of flow on cycle-to-cycle variations in a spark-ignition engine: a parametric investigation of increasing exhaust gas recirculation levels. *Flow, Turbulence and Combustion*, pages 1–24, 2022.

[301] H. G. Weller, G. Tabor, H. Jasak, and C. Fureby. A tensorial approach to computational continuum mechanics using object-oriented techniques. *Computers in Physics*, 12(6): 620–631, 1998.

[302] D. C. Wilcox. *Turbulence modeling for CFD*, volume 2. DCW industries La Canada, CA, 1998.

[303] F. A. Williams. *Combustion theory*. CRC Press, 2018.

[304] J. H. Williamson. Low-storage Runge-Kutta schemes. *Journal of Computational Physics*, 35(1):48–56, 1980.

[305] H. Wu, P. C. Ma, Y. Lv, and M. Ihme. Lyapunov exponent and Wasserstein metric as validation tools for assessing short-time dynamics and quantitative model evaluation of Large-Eddy Simulation. In *2018 AIAA Aerospace Sciences Meeting*, page 0440, 2018.

[306] S. Wu, S. Patel, and M. Ameen. Investigation of cycle-to-cycle variations in internal combustion engine using proper orthogonal decomposition. *Flow, Turbulence and Combustion*, pages 1–23, 2022.

[307] A. D. Wyner. Typical sequences and all that: Entropy, pattern matching, and data compression. In *Proceedings of 1994 IEEE International Symposium on Information Theory*, page 1. IEEE, 1994.

[308] X. Yang, S. Gupta, T.-W. Kuo, and V. Gopalakrishnan. RANS and Large-Eddy Simulation of internal combustion engine flows — a comparative study. *Journal of Engineering for Gas Turbines and Power*, 136(5), 2014.

[309] X. Yang, S. Zafar, J. Wang, and H. Xiao. Predictive large-eddy-simulation wall modeling via physics-informed neural networks. *Physical Review Fluids*, 4(3):034602, 2019.

[310] A. Yoshizawa. A statistically-derived subgrid model for the Large-Eddy Simulation of turbulence. *The Physics of Fluids*, 25(9):1532–1538, 1982.

[311] A. Yoshizawa. Statistical theory for compressible turbulent shear flows, with the application to subgrid modeling. *The Physics of Fluids*, 29(7):2152–2164, 1986.

[312] Y. Zang, R. L. Street, and J. R. Koseff. A dynamic mixed subgrid-scale model and its application to turbulent recirculating flows. *Physics of Fluids A: Fluid Dynamics*, 5 (12):3186–3196, 1993.

[313] W. Zeng, S. Keum, T.-W. Kuo, and V. Sick. Role of large scale flow features on cycle-to-cycle variations of spark-ignited flame-initiation and its transition to turbulent combustion. *Proceedings of the Combustion Institute*, 37(4):4945–4953, 2019.

[314] Y. Zhang, M. Jia, H. Liu, and M. Xie. Development of an improved liquid film model for spray/wall interaction under engine-relevant conditions. *International Journal of Multiphase Flow*, 79:74–87, 2016.

[315] L. Zhao, A. A. Moiz, S. Som, N. Fogla, M. Bybee, S. Wahiduzzaman, M. Mirzaeian, F. Millo, and J. Kodavasal. Examining the role of flame topologies and in-cylinder flow fields on cyclic variability in spark-ignited engines using Large-Eddy Simulation. *International Journal of Engine Research*, 19(8):886–904, 2018.

[316] Y. Zhiyin. Large-Eddy Simulation: Past, present and the future. *Chinese Journal of Aeronautics*, 28(1):11–24, 2015.

[317] G. Zhou. *Numerical simulations of physical discontinuities in single and multi-fluid flows for arbitrary Mach numbers*. Chalmers University of Technology, 1995.

[318] R. Zhou, S. Balusamy, M. S. Sweeney, R. S. Barlow, and S. Hochgreb. Flow field measurements of a series of turbulent premixed and stratified methane/air flames. *Combustion and Flame*, 160(10):2017–2028, 2013.

A Assessment of liquid injection in piston engines

A.1 Introduction

The description of multiphase flows forms one of the most important applications of Large-Eddy Simulation (LES). Liquids and solids may occur as a dispersion in a gaseous flow and hence, may alter the behavior of the flow. A plethora of technical systems relies on the injection of liquids for, e.g. cooling, cleansing or firing, all of which aim to disperse the respective liquid phase in the gaseous flow. Thus, the appropriate description of the dispersed phase and the numerical treatment of the gaseous phase are of great importance in order to achieve satisfactory reproduction of the desired physics.

A common way to describe the dispersed phase which is of particular relevance to this work, is the Euler-Lagrangian framework. In this framework, the dispersed phase is treated as Lagrangian particles, while the surrounding gaseous phase is described by transport equations in the Eulerian framework. Since the Lagrangian particles typically represent spherical droplets, it can be concluded that these methods are only able to capture all the physical processes after the secondary breakup of the injected liquid jet, and the effects of the primary breakup have to be modeled by other means.

A purely Eulerian formulation is provided by the Volume of Fluid (VOF) approach which has been introduced by Noh and Woodward [195] and further developed by Hirt and Nichols [103]. The VOF methods track down fluid-fluid interfaces by introducing a fraction function C. The values of C range between 0 and 1 to distinguish between the two fluid phases present in the domain where values of 0 indicate the pure presence of the one phase and values of 1 represent the other phase. A pure convection equation is solved for the fraction function and its values are used to calculate the density and viscosity required for the solution of the momentum equations. A detailed overview of the VOF method was provided recently by Klein et al. [139] and Ketterl et al. [128].

Table A.1 Engine operating conditions.

Engine speed	1500 rpm
Bore	84 mm
Stroke	90 mm
Compression ratio	9 : 1
Intake valve open (IVO)	316°CA
Intake valve close (IVC)	−112°CA
Exhaust valve open (EVO)	252°CA
Exhaust valve close (EVC)	−326°CA
Ignition timing	−20°CA
Fuel	Iso-octane
Relative air/fuel ratio	1.2
Intake pressure	1 bar
Intake temperature	333.15 K
Injection pressure	200 bar
1. Injection timing	−330°CA
1. Injection duration	13.7°CA
1. Injection mass	21.6 mg
2. Injection time	−56°CA
2. Injection duration	6.2°CA
2. Injection mass	10.0 mg

A.2 Experiments

The measurements and simulations were performed on an optically accessible four-stroke single-cylinder SI engine with direct fuel-injection. The engine was operated at 1500 rpm and was fueled using iso-octane. Table A.1 summarizes the operating conditions. Optical access is provided by a flat piston window and a quartz glass cylinder liner. In the experiments, to minimize the potential influence of residual gas on CCV and to reduce the thermal load, each fired cycle was followed by two motored cycles. Combining three subsequent measurements of 71 fired cycles resulted in a data set of 213 cycles with short interruptions in between. The pressure was measured using a piezoelectric pressure sensor. A high-speed camera captured the line-of-sight integrated combustion luminosity (CH*) at a frame rate of 43 kHz. With a field-of-view (FOV) of 23x34 mm, only the region around the spark plug was imaged, and the recording was performed from ignition timing at −20°CA until +5°CA. This work assigns 0°CA to compression top-dead center, i.e., crank angles during intake and compression are negative.

A.3 Numerical Modeling

Computations were carried out with an in-house LES-solver. The Favre-filtered conservation equations for mass, momentum, total internal energy and fuel mixture fraction were solved in

a density-based solver framework. The finite volume method (*FVM*) was used to discretize the equations on an isotropic equidistant grid of 0.39 mm size, leading to a total amount of 38 Mio. cells. Convective fluxes were interpolated with an eighth-order central difference scheme (*CDS*) supported by a tenth-order filter for momentum for Mach numbers Ma below 0.2. The CDS fluxes were blended with a total variation diminishing (*TVD*) scheme with the nonlinear CHARM limiter for $0.2 < \mathrm{Ma} < 0.3$ and the full TVD fluxes were used for higher Mach numbers. All scalar-fluxes were discretized using TVD. Time integration was performed with a low-storage Runge–Kutta scheme of third-order. All walls and moving parts of the engine follow a Lagrangian particle and immersed boundary based framework given by Nguyen [191]. The sensor-enhanced Smagorinsky model of Hasslberger [96] was employed to take into account for the subfilter transport along with a turbulent Schmidt number of $\mathrm{Sc_t} = 0.7$.

A.4 Modeling of the liquid phase

The liquid phase is described in an Euler-Lagrangian framework which has been developed and applied for the employed code successfully [233, 256] and for the detailed description of the dispersed phase the reader is referred to the respective works. The droplets are described employing equations for position $x_{\mathrm{i,d}}$, velocity $u_{\mathrm{i,d}}$, mass m_{d} and temperature T_{d} of Lagrangian form:

$$\frac{dx_{\mathrm{i,d}}}{dt} = u_{\mathrm{d,i}} \tag{A.1}$$

$$\frac{du_{\mathrm{i,d}}}{dt} = \frac{f_1}{\tau_{\mathrm{d}}}(\tilde{u}_{\mathrm{i}} - u_{\mathrm{i,d}}) + \left(1 - \frac{\overline{\rho}}{\rho_{\mathrm{d}}}\right) \tag{A.2}$$

$$\frac{dm_{\mathrm{d}}}{dt} = -\frac{\mathrm{Sh}}{3\mathrm{Sc}}\frac{m_{\mathrm{d}}}{\tau_{\mathrm{d}}}\log\left(1 + B_{\mathrm{m}}\right) \tag{A.3}$$

$$\frac{dT_{\mathrm{d}}}{dt} = \frac{\mathrm{Nu}}{3\mathrm{Pr}}\frac{c_{\mathrm{p}}}{c_{\mathrm{p,d}}}\frac{(T - T_{\mathrm{d}})}{\tau_{\mathrm{d}}}\frac{\log\left(1 + B_{\mathrm{h}}\right)}{B_{\mathrm{h}}} + \frac{L_{\mathrm{v,d}}}{m_{\mathrm{d}}c_{\mathrm{p,d}}}\frac{dm_{\mathrm{d}}}{dt} \tag{A.4}$$

In addition to the previously introduced gas phase quantities, these equations require the droplet density ρ_{d}, the isobaric heat capacity $c_{\mathrm{d,p}}$ and the latent heat $L_{\mathrm{v,d}}$.

The drag force f_1 is obtained from the droplet Reynolds number:

$$f_1 = 1 + \frac{3}{20}\mathrm{Re_d}^{0.687} \tag{A.5}$$

Where the droplet Reynolds number is evaluated based on the velocity of the droplet relative to the carrier phase:

$$\mathrm{Re_d} = \frac{\rho|\tilde{u}_{\mathrm{i}} - u_{\mathrm{d,i}}|d_{\mathrm{d}}}{\mu} \tag{A.6}$$

The characteristic droplet timescale τ_d can be calculated using the droplet diameter d_d and the gas phase viscosity μ as:

$$\tau_\mathrm{d} = \frac{\rho_\mathrm{d} d_\mathrm{d}^2}{18\mu} \tag{A.7}$$

The Schmidt number Sc, the Sherwood number Sh, the Nusselt number Nu, the Spalding mass transfer number $\mathrm{B_m}$ and the Spalding heat transfer number $\mathrm{B_h}$ are needed to calculate the above quantities. While the Schmidt number can be considered given for the respective flow by experience, the Sherwood and Nusselt numbers are typically determined using empirical correlations, which one of the most important ones being that of Ranz and Marshall [224]:

$$\mathrm{Sh} = 2 + 0.552 \mathrm{Re_d}^{1/2} \mathrm{Sc}^{1/3} \tag{A.8}$$

$$\mathrm{Nu} = 2 + 0.552 \mathrm{Re_d}^{1/2} \mathrm{Pr}^{1/3} \tag{A.9}$$

The Spalding mass transfer number is defined based on the mass fraction of the liquid dissolved in the gas phase Y as:

$$\mathrm{B_m} = \frac{Y^\mathrm{S} - Y^\infty}{1 - Y^\mathrm{S}} \tag{A.10}$$

Where Y^S denotes the mass fraction directly on the droplet surface and Y^∞ indicates the mass fraction in the distant gas phase. The mass fraction at the droplet surface Y^S is found under the assumption of equal ratios of mole fractions X and partial pressures for the evaporated liquid phase and the gas phase:

$$Y^\mathrm{S} = \frac{X^\mathrm{S}}{X^\mathrm{S} + (1 - X^\mathrm{S}) \frac{W}{W_\mathrm{d}}} \tag{A.11}$$

With the molar mass of the gas phase W and the molar mass of the liquid droplet W_d. The respective molar fraction at the surface is obtained from the Clausius-Clapeyron equation:

$$X^\mathrm{S} = \exp\left(\frac{L_\mathrm{v,d}}{R_\mathrm{m}/W}\left(\frac{1}{T_\mathrm{b}} - \frac{1}{T_\mathrm{d}^\mathrm{S}}\right)\right) \tag{A.12}$$

Which requires the boiling temperature of the droplet T_b and the surface temperature of the droplet T_d^S – within this work it is assumed that the temperature of the droplet is homogeneous and hence $T_\mathrm{d}^\mathrm{S} = T_\mathrm{d}$:

$$\mathrm{B_h} = \frac{c_\mathrm{p}}{L_\mathrm{v,d}} \left(T - T_\mathrm{d}\right) \tag{A.13}$$

To establish the coupling between the liquid and gaseous phases, a source term is included in the conservation equations. As it directly indicates the evaporated liquid, the conservation

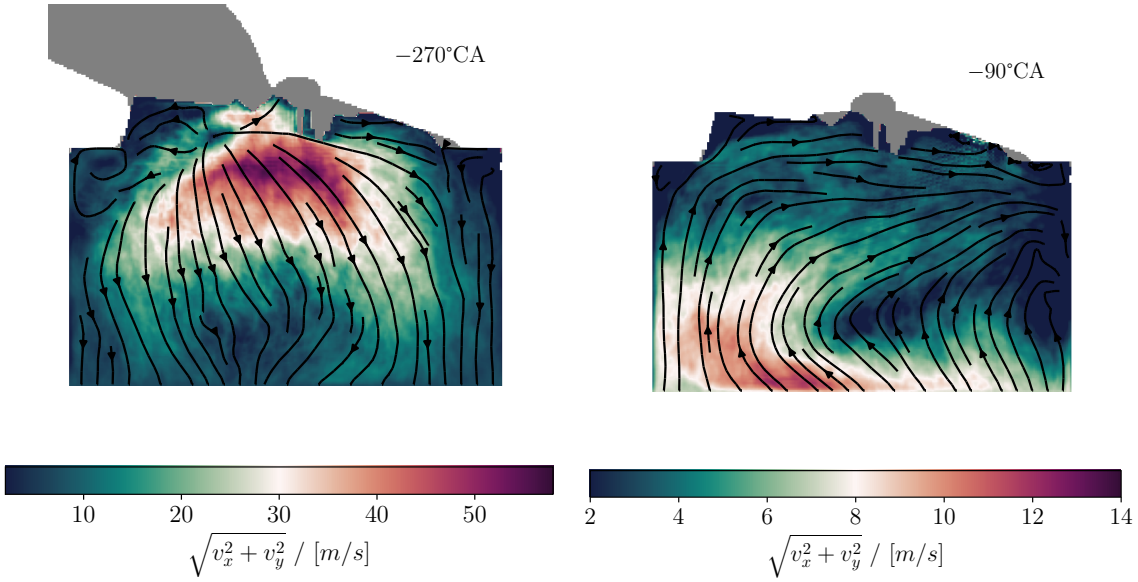

Figure A.1 Averaged flow fields at crank angles of −270°CA and −90°CA in the tumble plane.

equation of the mixture fraction featuring the corresponding source term shall be given:

$$\frac{\partial \overline{\rho}\tilde{Z}}{\partial t} + \frac{\partial \overline{\rho}\tilde{Z}\tilde{u}_\mathrm{j}}{\partial x_\mathrm{j}} = \frac{\partial}{\partial x_\mathrm{j}}\left(\overline{\rho}D\frac{\partial \tilde{Z}}{\partial x_\mathrm{j}} - \overline{\rho}\tau_\mathrm{j}^{\mathrm{sgs}}\right) + \dot{\Gamma}_{\rho\tilde{Z}} \tag{A.14}$$

Where the source term $\dot{\Gamma}_{\rho\tilde{Z}}$ is calculated from the evaporated droplet mass per timestep.

The droplets are treated in the simulation using the equations described above. Since the Lagrangian-Eulerian framework does not allow for the description of atomization, the droplets must be seeded in the simulation after the breakup stage. This requires a priorly performed DNS of the near field of the injector employing the VOF method. Droplet statistics are sampled from this preprocessing simulation and then seeded into the carrier phase LES.

A.5 Results

A.5.1 Flow Fields

For a qualitative insight into the dynamics of the mixing the flow fields in the tumble plane are shown at two crank angles of −270°CA and −90°CA representing compression. The left image features the intake flow, which is the basis for the mixing during and after the first injection stage. The flow is characterized by strong motion into the cylinder, which creates a strong wake region below the valves. While mixing is affected by this wake region, the strong flow into the cylinder will spread the fuel to different regions in the cylinder. As the piston enters the compression stroke and the valves are closed, the tumble motion

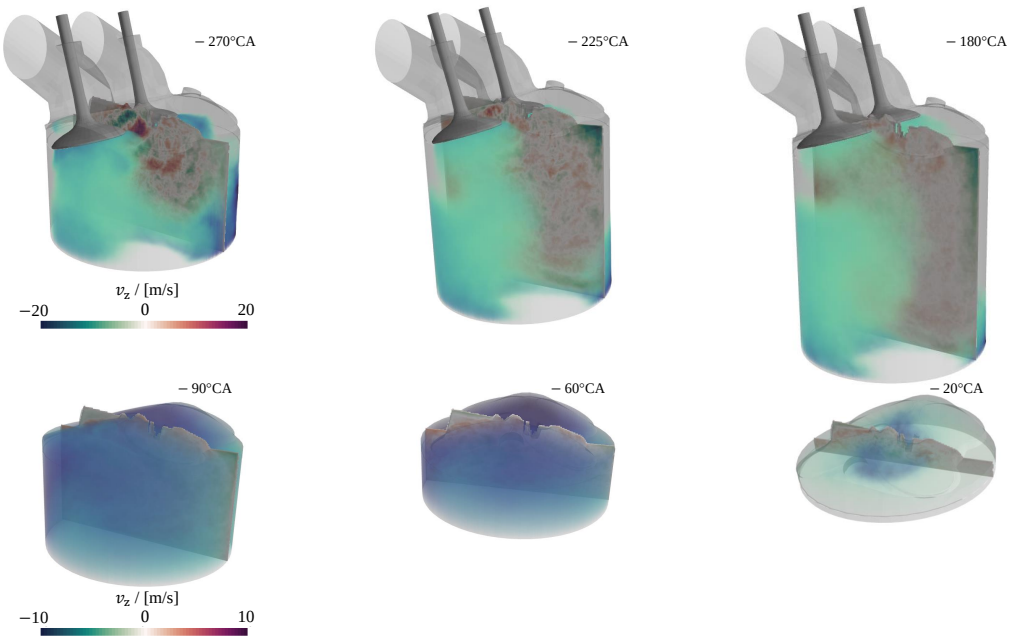

Figure A.2 Visualization of the averaged three-dimensional mixture fields within the engine geometry. The tumble plane is indicated by the averaged image-normal velocity component.

is forming, ultimately resulting in strong mixing. The tumble motion is the basis for a homogeneous mixture. As the valves are closed, the internal geometry is greatly simplified by the elimination of narrow gaps and wake regions, allowing for the flow to better reach previously unmixed areas of the cylinder. The second injection takes place during the late stage of compression before the tumble breakdown. This results in partial mixing of the fuel and achieves the residual stratification that is the objective of the two-stage injection.

A.5.2 Spray topology

To assess the distribution of the evaporated fuel in the gas-phase three-dimensional fields of the averaged equivalence ratio ϕ are shown in Fig. A.2 at different crank angles. Crank angles during intake, early and late compression are shown to cover both injection phases and to describe the spatial evolution of the mixture in time. The engine geometry is included in the visualization for orientation purpose.

The vaporized spray is qualitatively visualized as a green cloud, with the blue shades indicating a richer mixture and the transparent areas representing pure air. At a crank angle of −270°CA, a dense parcel of rich mixture can be found below the intake valves as they are protected from the inflowing air. Due to the isolation by the wake region around the valve, this mixture is isolated from the surrounding pure air. Another dense kernel of rich mixture can be found below the exhaust valves, close to the piston, due to the liquid spray

hitting the piston with great force. The evaporating spray is pushed into this area by the intake flow, resulting in the formation of this kernel. With ongoing intake stroke, this kernel moves to the side of the intake valves where it is diluted by the progressing inflow of air. The increased lift of the intake valves reduces the magnitude of the inflow velocity in the valve gap, which leads to a weaker wake region and better mixing of the rich mixture below the intake valve. Finally, at −180°CA, the piston motion stops and the intake flow reverses, eliminating the wake region below the intake valve. Despite the loss of mixture due to the outflow, this results in better mixing as the piston begins to progressively push the rich and lean regions together.

A more homogeneous mixture can be observed during the compression stroke which is characterized by a dense mixture as a consequence of the tumble motion and the progressively decreasing volume. This is highlighted by the uniform coloration during −90°CA and −60°CA. As a consequence of the second injection, the equivalence ratios at −20°CA feature less homogeneity. While reducing the overall mixture inhomogeneity, the goal of the second injection is the stratification of the charge. The last crank angle −20°CA confirms the stratification of the charge near the spark-plug as seen by the dense kernel of mixture around the spark-plug area.

It can be summarized that compared to the common hypothesis of a homogeneous mixture in spark-ignited piston engines, the actual simulated mixture features notable inhomogeneities. In particular, the second injection leads to a richer mixture in close proximity to the spark-plug which is typically desired in stratified charge operation.

A.5.3 Spray Statistics

Line plots of the averaged equivalence ratio are generated in the tumble plane to provide a more quantitative insight into the fuel distribution. Four lines are evaluated from the tumble plane as illustrated in Fig. A.3 where the line center $x = 0$ corresponds to the cylinder axis. The lines are shifted vertically along the y axis in steps of 10 mm. Six crank angles are evaluated with three representing the intake and another three representing compression respectively. The lines for different crank angles are kept within the same plot to better visualize the temporal evolution of the mixture at each location. The profiles reveal little evolution of the profiles obtained from the compression stroke with the −90°CA and −60°CA particularly revealing homogeneous mixtures. The −20°CA profile can only be found at $y = 0$ mm as the piston is already close to TDC, causing all the remaining space in the cylinder to vanish. This line features strong inhomogeneity due to the second injection closely before TDC, which aims at stratifying the mixture. The lines of crank angles during the intake stroke show strong variations which is a consequence of the more intense flow dynamics during the intake. Due to the increasing domain and the variation of the intake jet above the valve and the corresponding wake region forming below the valve, the intensity of the mixing

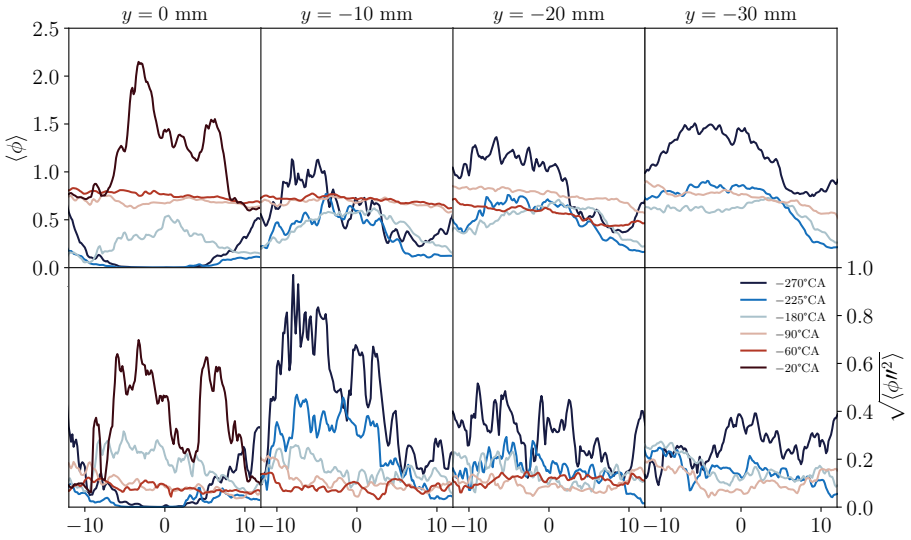

Figure A.3 Averaged flow profiles and their respective standard deviation of the equivalence ratio ϕ in the tumble plane.

process strongly increases as the intake stroke progresses. These observations are supported by the standard deviations of the equivalence ratio. The early crank angles feature an overall higher level of variation. During the compression stroke, the crank angle of −20°CA has to be noticed, which again shows high variation due to the late injection which is interacting with the tumble breakdown.

DOI: 10.17185/duepublico/78840
URN: urn:nbn:de:hbz:465-20230821-155037-9